

**AN INVESTIGATION IN THE MECHANISM OF $[\text{Ru}(\text{tpy})(\text{bpy})(\text{H}_2\text{O})]^{2+}$
AND $[\text{Ru}(\text{bpy})_2(\text{bpyNO})]^{2+}$ WITH THE EMPHASIS ON THE N-OXIDE: A
REDOX ACTIVE LIGAND**

by

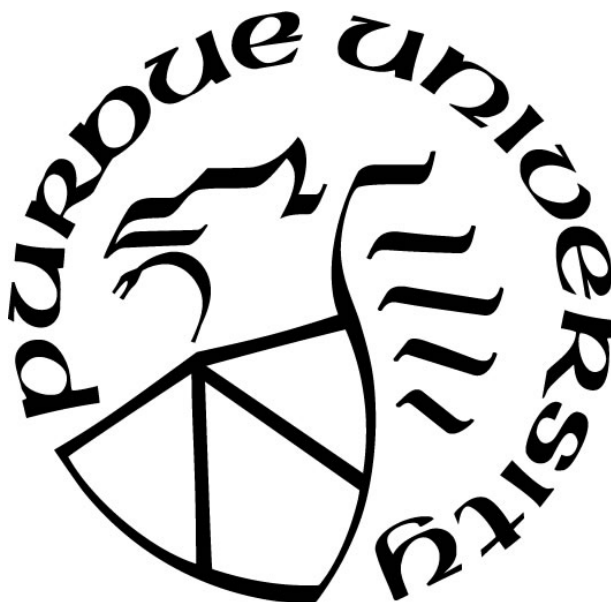
Alireza Karbakhsh Ravari

A Dissertation

Submitted to the Faculty of Purdue University

In Partial Fulfillment of the Requirements for the degree of

Doctor of Philosophy



Department of Physics and Astronomy

West Lafayette, Indiana

December 2020

THE PURDUE UNIVERSITY GRADUATE SCHOOL
STATEMENT OF COMMITTEE APPROVAL

Dr. Yulia Pushkar, Chair

Department of Physics and Astronomy

Dr. Paul Muzikar

Department of Physics and Astronomy

Dr. Sergei Savikhin

Department of Physics and Astronomy

Dr. Lyudmila Slipchenko

Department of Chemistry

Dr. Martin Kruczynski

Department of Physics and Astronomy

Approved by:

Dr. John P. Finley

*To my Mother,
for all she did, and I never appreciated it until it was too late*

ACKNOWLEDGMENTS

I like to thank Prof. Yulia Pushkar for being an excellent and encouraging advisor.

Also, I would like to mention all the prof. Pushkar's group members, in particular, Daniel Hartzler for his help with setting up the Raman experiment. Other group members include Gabe Bury, Alexander Huynh, Brenden Sullivan, Yuliana Pineda Galvan, Scott Jensen, Sergei Shmakov, and Darren Erdman.

TABLE OF CONTENTS

LIST OF TABLES	8
LIST OF FIGURES	9
LIST OF ABBREVIATIONS.....	13
ABSTRACT.....	14
CHAPTER 1. PHOTOSYNTHESIS.....	18
1.1 Motivation.....	18
1.2 Photosynthesis and the role of photosystem II.	19
1.3 Artificial Photosynthesis.....	21
1.4 Non-ruthenium-based catalysts and important concepts	24
1.5 Ru-based WOCs.....	26
CHAPTER 2. INTRODUCTION TO METHODS.....	30
2.1 The Theory of Raman Scattering.....	30
2.1.1 Why Raman Spectroscopy.....	30
2.1.2 The classical description of Raman Scattering.....	30
2.1.3 Non-classical description of Raman spectroscopy	33
2.1.4 Raman Scattering intensity	35
2.1.6 Resonance Raman Scattering	37
2.1.7 Fluorescence	40
2.1.8 Raman experiment.....	41
2.2 An introduction to Electron Paramagnetic Resonance (EPR) spectroscopy	43
2.2.1 Why EPR	43
2.2.2 Theory of EPR.....	44
2.2.3 EPR spectrum	46
2.2.4 More on the g-factor with an example.....	47
2.2.5 Hyperfine interaction.	48
2.2.6 Instrumentation.	49
2.3 Computational calculations.....	51
2.3.1 Why Computational calculations.....	51
2.3.2 DFT.....	51

CHAPTER 3. UNRAVELING THE MECHANISM OF CATALYTIC WATER OXIDATION VIA DE NOVO SYNTHESIS OF REACTIVE INTERMEDIATE	56
3.1 Abstract.....	56
3.2 Introduction.....	56
3.3 Results and discussion	62
3.4 Conclusions.....	76
3.5 Materials and methods	85
CHAPTER 4. INSIGHTS INTO MOF REACTIVITY: CHEMICAL WATER OXIDATION CATALYSIS BY A $[\text{Ru}(\text{TPY})(\text{DCBPY})\text{OH}_2]^{2+}$ MODIFIED METAL-ORGANIC FRAMEWORK	94
4.1 Abstract.....	94
4.2 Introduction.....	94
4.3 Results and Discussion	96
4.4 Experimental Section	102
4.4.1 Materials	102
4.4.2 <i>Fabrication of Ru-UiO-67 MOF powder</i>	102
4.4.3 <i>FTRaman</i>	103
4.4.4 <i>RRaman</i>	103
4.4.5 <i>Oxygen evolution measurement</i>	103
4.5 Conclusions.....	104
CHAPTER 5. FACILE LIGHT INDUCED TRANSFORMATION OF $[\text{Ru}^{\text{II}}(\text{BPY})_2(\text{BPYNO})]^{2+}$ TO $[\text{Ru}^{\text{II}}(\text{BPY})_3]^{2+}$	105
5.1 Abstract.....	105
5.2 Introduction.....	106
5.3 Experimental section.....	106
5.3.1 Synthesis:.....	106
5.3.2 Sample illumination:.....	107
5.3.3 Raman Spectroscopy:	107
5.3.4 EPR Spectroscopy:	107
5.3.5 Oxygen-evolution measurement:.....	108
5.3.6 DFT:.....	108

5.3.7 Nuclear magnetic resonance spectroscopy:	108
5.4 Results.....	109
5.4.1 Redox behavior:.....	109
5.4.2 Spectroscopic Study.....	115
5.4.3 Discussion of the mechanism of the light induced transformation.....	120
5.5 Conclusions.....	127
REFERENCES	128

LIST OF TABLES

Table 2-1. The Character table for point group T_d . E and C_n and S_n are symmetry elements.....	37
Table 3-1. g-factors comparison for $Ru^V=O$ species.....	63
Table 3-2. Lorentzian fit parameters for resonance Raman spectra of (1) and (2) . $H_2^{18}O$ and $H_2^{16}O$ are presented in separate sections and peaks sensitive to oxygen isotope substitution are highlighted by dark gray (Ru=O) and light gray (Ru-N-O).....	68
Table 3-3. Delay (lag phase) (seconds) in O_2 evolution in 0.1 M HNO_3	69
Table 3-4. Key thermodynamic parameters computed using DFT.	77
Table 3-5. $[Ru^{II}(EtO-tpy)(bpy)H_2O]^{2+}$ theoretical free energy and other intermediates and molecules that are necessary to explain our ligand oxidation model. All the theoretical energies are calculated by DFT.....	86
Table 3-6. Theoretical Analysis of Oxidation, Oxygen Atom Transfer and O-O bond formation in $[Ru^{II}(EtO-tpy)(bpy)(H_2O)]^{2+}$ water oxidation catalyst. Number in parenthesis are the experimental values	88
Table 3-7. $[Ru^{II}(tpy)(bpy)(H_2O)]^{2+}$ theoretical free energy and other intermediates and molecules that are necessary to explain our ligand oxidation model. All the theoretical energies are calculated by DFT	89
Table 3-8. Theoretical Analysis of Oxidation, Oxygen Atom Transfer and O-O bond formation in $[Ru^{II}(tpy)(bpy)H_2O]^{2+}$ water oxidation catalyst.	91
Table 5-1. Redox properties of $[Ru^{II}(bpy)_2(bpyNO)]^{2+}$ and $[Ru^{II}(bpy)_3]^{2+}$ from DFT analysis ^a	112
Table 5-2. Relative energies and ^{14}N hfs for selected configuration of $[Ru(bpy)_2(bpyNO)]^{1+}$ species.	113
Table 5-3. Calculated energies of light driven reactions with DFT (the photon energy is not explicitly entered in the calculations) ^a	126
Table 5-4. (1-NO) and possible intermediates theoretical free energy by DFT	127

LIST OF FIGURES

- Figure 1-1.** Schematic of photosynthesis reaction. Carbon dioxide and water are reactants; oxygen and glucose are the products. Solar energy provides the essential energy to run this reaction. ... 19
- Figure 1-2.** Thylakoid membrane is shown with the essential components for the electron transport chain path and its reactions. 20
- Figure 1-3.** Kok's cycle. S_1 is the dark-adapted state and each photon drives the cluster one step ahead. The exact dynamics of the process is still debated. 22
- Figure 1-4.** Gibbs free energy of water splitting reaction is shown. The role of a catalyst is to lower the activation energy barrier. 25
- Figure 1-5.** Blue dimer (A) and $[\text{Ru}(\text{bpy})_3]^{2+}$ (B), two of the most studied catalysts in the field of artificial photosynthesis. (C) common geometries in Ru-based WOC and their corresponding orbital energies. (D) Depiction of two possible mechanisms for water splitting that are studied in this thesis. 29
- Figure 2-1.** An example of a linear molecule shown in the equilibrium state(A); and an electric field induced stretched state, (B) 32
- Figure 2-2.** The curves represent electronic states and the horizontal lines inside the curves represent vibrational states. (A) Raman (nonresonance) scattering process; note that the energy that the electron gains is less than the energy gap between two electronic states. A virtual state is added to the figure to clarify this point. (B) RRaman scattering process; here the energy that an electron gains is close to the energy gap between two electronic states. This resonance effect enhances the signal significantly. (C) Fluorescence process; the excited electron relaxes first on the vibrational states of the electronic excited state before it decays into the electronic ground state. 34
- Figure 2-3.** Two of the vibrational modes of CO_2 . (A) represents a symmetric mode while (B) represents an anti-symmetric vibrational mode. 36
- Figure 2-4.** Schematic explanation of absorption spectroscopy. The top left is the spectrum of white light. The middle top curve is the absorption spectrum which is calculated from the subtraction of the top right spectrum (the portion of the light that went through the sample) and the white light spectrum. 38
- Figure 2-5.** Setup of Raman spectrometer and its laser sources. 42
- Figure 2-6.** internal structure of the spectrometer that is used in the setup of this report. 43
- Figure 2-7.** Energy splitting of an electron in the presence of an external magnetic field. 45
- Figure 2-8.** Different orbitals with different shape and orientation and their correspondence absorption and derivative of the absorption. 47
- Figure 2-9.** hyperfine effect cause splitting in the absorption spectrum. 49

Figure 2-10. (A) the potential energy of a diatomic molecule. (B) the potential surface energy of two molecule bonds. (C) a local and global minimum for a potential surface energy 55

Figure 3-1. Activated Ru-based species capable of O-O bond formation and oxygen atom transfer. A) Formation of the activated $[\text{Ru}^{\text{IV}}, \text{Ru}^{\text{V}}=\text{O}]$ intermediate in the blue dimer is achieved via PCET. B) $\text{Ru}^{\text{II}}(\text{L})_2(\text{bda})$ class of WOCs form 7-coordinate $\text{Ru}^{\text{V}}=\text{O}$ intermediate via coordination sphere expansion and PCET. Catalysts with variety of axial ligands were investigated, two typical axial ligands (L_1) are shown. C) 7-coordinate $[\text{Ru}^{\text{V}}=\text{O}(\text{L})_2(\text{dpp})]^{3+}$ intermediate with neutral dpp ligand is stable in solutions on a minute time scale due to ligand protection of the $\text{Ru}^{\text{V}}=\text{O}$ fragment. Activation occurs via oxygen atom transfer with formation of dpp-N-oxides. D) Overview of ligand modifications in $[\text{Ru}^{\text{II}}(\text{bpy})(\text{tpy})(\text{H}_2\text{O})]^{2+}$ family of catalysts. It has been shown that ethoxy (EtO-) and methoxy (MeO-) substituents increase the rate of O_2 evolution..... 58

Figure 3-2. Catalytic cycle of $[\text{Ru}^{\text{II}}(\text{5N-ligands})\text{H}_2\text{O}]^{2+}$ family of catalysts, **Figure 3-1D**. There is ~95% of $[\text{Ru}^{\text{IV}}=\text{O}(\text{bpy})(\text{tpy})]^{2+}$ in the catalytic steady state. Involvement of the $\text{Ru}^{\text{V}}=\text{O}$ and proposed O-O bond formation via WNA (blue arrows) currently lacks reaction with water (middle insert). The lag phase in the onset of O_2 evolution indicates an additional step of catalyst activation (yellow box)..... 61

Figure 3-3. A) EPR spectra of **(1)** (orange) and **(2)** (magenta) in 0.1 M HNO_3 after addition of one equiv of Ce^{IV} (solid lines) and after addition of 20 equiv of Ce^{IV} (dash lines) B) Zoom ($\times 20$) into low intensity EPR signals from solutions generated by adding 20 equiv of Ce^{IV} in 0.1 M HNO_3 to **(1)** (orange) and to **(2)** (magenta). All samples were frozen within 30 s..... 64

Figure 3-4. The selected frequency range of resonance Raman (532 nm) of **(1)** and **(2)** 1mM solutions in 0.1 M HNO_3 mixed with 20 equiv of Ce^{IV} (one minute after oxidation) in H_2^{16}O and H_2^{18}O , Figure S1, Table S2. Two isotope sensitive vibrations were assigned to $\text{Ru}^{\text{IV}}=\text{O}$ ($\sim 800 \text{ cm}^{-1}$) and Ru-O-N ($\sim 830 \text{ cm}^{-1}$)..... 65

Figure 3-5 Fits to the room temperature RR spectra (532 nm) of **(1)** and **(2)** 1 mM dissolved in H_2^{18}O (final H_2^{18}O content $\sim 85\%$) and H_2^{16}O in 0.1 M HNO_3 upon oxidation with 20 equiv of Ce^{IV} . Bands marked with ‘*’ did not shift after isotope substitution while those marked with ‘+’ and are oxygen isotope sensitive..... 66

Figure 3-6. A Raman spectrum of $[(\text{tpy})\text{Ru}^{\text{VI}}=\text{O}_2(\text{OH})]^+$ with ^{18}O and ^{16}O . The insert is the Raman calculated by DFT. B Raman spectra of **(1)**, concentration of 1 mM and 2 mM in 0.1 M HNO_3 recorded 30 min after oxidation with 20 equiv of Ce^{IV} . Two spectra are normalized to the same height for bands around 800 cm^{-1} . Formation of dimeric species is evident by new bands at $300\text{-}400 \text{ cm}^{-1}$ corresponding to Ru-O-Ru bridging unit.¹⁻³ Increase in concentration stimulates dimer formation, a second order process. Loss or partial de-coordination of bpy ligand might facilitate formation of dimeric species..... 67

Figure 3-7. A) Representative oxygen evolution profiles for 0.1mM $[\text{Ru}^{\text{II}}(\text{bpy})(\text{tpy-EtO})(\text{H}_2\text{O})]^{2+}$ in 0.1 M HNO_3 with different equiv of Ce^{IV} added at $t = 0$ s. B) Oxygen evolution after addition of indicated amount of 10% $[\text{Ru}(\text{tpy})(\text{bpyNO})(\text{H}_2\text{O})]^{2+}$ / 90% $[\text{Ru}(\text{tpy})(\text{bpy})(\text{H}_2\text{O})]^{2+}$ at $t = 0$ to 20 mM solution of Ce^{IV} oxidant in 0.1 M HNO_3 . Rate was determined over the linear slope and was shown to be first order in catalyst. 70

Figure 3-8 Spectroscopic and catalytic properties of the $[\text{Ru}(\text{tpy})(\text{bpy-NO})(\text{H}_2\text{O})]^{2+}$ (1-NO) intermediate. A) UV-Vis absorption of (1), *trans*-(1-NO) and *cis*-(1-NO). Ethanol solutions contain *trans*- and *cis*- $[\text{Ru}(\text{tpy})(\text{bpy-NO})\text{Cl}]^+$ correspondingly. In $[\text{Ru}(\text{tpy})(\text{bpy-NO})\text{Cl}]^+$ Cl undergoes fast exchange in water. B) FTIR of (1) and (1-NO) powders. Insert shows FTIR of pure ligands. C) Cyclic voltammetry of 0.5 mM (1) and *cis*-(1-NO) in 0.1 M HNO_3 , scan rate 0.1 V/sec. The insert shows the $\text{Ru}^{\text{II}}/\text{Ru}^{\text{III}}$ and $\text{Ru}^{\text{III}}/\text{Ru}^{\text{IV}}$ couples. D) Oxygen evolution of (1), (2) and *cis*-(1-NO) prepared by mixing of 1 mL of 0.2 mM of the solution and 40 equiv of Ce^{IV} in 0.1 M HNO_3 74

Figure 3-9. Latimer Frost diagram of $[\text{Ru}^{\text{II}}(\text{tpy})(\text{bpy})(\text{H}_2\text{O})]^{2+}$. This diagram is focused on bpy ligand oxidation. 79

Figure 3-10. Latimer Frost diagram of $[\text{Ru}^{\text{II}}(\text{tpy})(\text{bpy})(\text{H}_2\text{O})]^{2+}$. This diagram is focused on tpy ligand oxidation. 80

Figure 3-11. Latimer Frost diagram of $[\text{Ru}^{\text{II}}(\text{EtO-tpy})(\text{bpy})(\text{H}_2\text{O})]^{2+}$. This diagram is focused on bpy ligand oxidation. 81

Figure 3-12. Latimer Frost diagram of $[\text{Ru}^{\text{II}}(\text{tpy})(\text{bpy})(\text{H}_2\text{O})]^{2+}$. This diagram is focused on EtO-tpy ligand oxidation. 82

Figure 3-13. (A) Spin density of $[\text{Ru}^{\text{IV}}=\text{O}(\text{tpy})(\text{bpyNO}^+_{\text{out}})(\text{OH})]^{2+}$ in three different views. (B) DFT computed $\text{Ru}^{\text{V}}=\text{O}$ redox potentials (**Table 3-1**) do not correlate with the rate of O_2 evolution. We found that redox potentials for ligand oxidation (dashed lines) correlate better with O_2 evolution rates. Transient ligand oxidation with the formation of the ligand-N-oxide lowers the oxidation potential of the ligand, allowing it to store the third hole needed for water activation. 83

Figure 3-14. HOMO orbitals of the (1); (2) and (1-NO) in $[\text{Ru}^{\text{IV}}=\text{O}]^{2+}$ state. Delocalization to EtO-tpy and bpyNO ligands is evident. Thus, these ligands can delocalize hole upon oxidation.84

Figure 4-1. FT-Raman ($\lambda_{\text{ex}} = 1064 \text{ nm}$) of (A, black) $[\text{Ru}(\text{tpy})(\text{dcbpy})\text{Cl}]\text{Cl}$, (B, blue) Ru-UiO-67 and (C, red) UiO-67. 97

Figure 4-2. RRaman ($\lambda_{\text{ex}}=532 \text{ nm}$) spectra of a) $[\text{Ru}(\text{tpy})(\text{bpy})\text{Cl}]\text{Cl}$, b) Ru-UiO-67, and c) UiO-67..... 98

Figure 4-3. RRaman ($\lambda_{\text{ex}}=532 \text{ nm}$) of Ru complex under CAN treatment (100 equivalents of CAN in nitric acid pH 1) at (A) the beginning, (B) 30 minutes, (C) 1 hour and (D) 2 hours later..... 99

Figure 4-4. RRaman ($\lambda_{\text{ex}}=532 \text{ nm}$) spectra of Ru-UiO-67 at a) $t=0 \text{ min}$ and after 100 mm CAN treatment (in nitric acid, pH 1): b) 0–20 min, c) 20–40 min, and d) 2 h. e) $[\text{Ru}(\text{tpy})(\text{bpy})(\text{OH}_2)]^{2+}$ solution incubated with CAN (100 equiv.) for 2 h. f) Untreated UiO-67. Spectral signatures of the Ru–O–Ru bridges were observed in $300\text{--}450 \text{ cm}^{-1}$ Raman shift range in solution but not in the MOF framework. 100

Figure 4-5. Oxygen-evolution data for Ru-UiO-67 (red) and $[\text{Ru}(\text{tpy})(\text{dcbpy})\text{Cl}]\text{Cl}$ (blue) in solution (soaked in water 24h before catalysis experiment). 101

Figure 5-1. X-band EPR of $[\text{Ru}^{\text{II}}(\text{bpy})(\text{bpyNO}^{\bullet-})]^{1+}$ obtained by (1-NO) reduction with ascorbate in water. The measurement was conducted at 20 K, using a modulation amplitude of 10 G and 30 mW of power. Dashed line is the simulated spectrum..... 111

Figure 5-2. The structure of some Ru with NO ligands that were mentioned in the text	114
Figure 5-3. A) Absorption spectra of 1mM (1-NO) and (1) solutions in water (pH = 7) before and after the irradiation with the different wavelenghtes (760 nm, 650 nm and 530 nm) marked by the arrows. The solutions were irradiated for 30 minutes at a room temperature. To examine the reversiblility, 20 equiv of Acs was added to reduce the sample after the irradiation with the 530 nm LED (dash blue line). Although the small absorption band around 750 nm dissapeared upon Asc addition, no absorbtion maximum shift was observed (green line). The black line is the spectrum of (1) . B) Absorption spectra of 1mM (1-NO) in water. Each spectrum was irradiated with ambient light with different exposure time.....	116
Figure 5-4. Absorption spectra of 1mM (1-NO) -orange-, (1-NO) exposed to 670 nm for 30 minutes -gray-, and (1) -blue- in water . The green spectrum consists of 70% of the blue and 11% of the orange. The yellow spectrum is the difference between gray and green.....	117
Figure 5-5. NMR spectra of (1) , (1-NO) and (1-NO) illuminated with 650 nm light in D ₂ O... 117	117
Figure 5-6. Resonance Raman spectrum of 3 mM solution of (1-NO) in water (pH= 7) before (orange curve) and after (blue curve) exposure to an ambient light. Spectrum was recorded with 442 nm laser excitation at a room temperature. The measurement took 100 seconds to minimize the laser damage. The second measurement occurred after 30 minutes of the ambient light exposure of the sample. The insert is focused on 827 cm ⁻¹ band and corresponding fits.	118
Figure 5-7. X-band EPR spectra (20 K) of illuminated and oxidized (1-NO) and (1) . Green and red curves represent (1-NO) irradiated with 530 nm and 650 nm light. Black curve is (1-NO) oxidized with 1 equiv Ce ^{IV} in the dark. Blue curve is (1-NO) oxidized with 20 equiv of Ce ^{IV} after an exposure to an ambient light for three days. The inserted structures are added to depict a closed and open configuration. pH for Ce ^{IV} mixture was set 1 and for the rest of samples it was 7.....	119
Figure 5-8. Possible pathways of conversion of (1-NO) to (1) upon light irradiation. S ₀ and S ₁ are the singlet ground and excited states, T ₁ is the excited triplet state. The spin density of the triplet state is at the top and shows the electron localization on the bpyNO ligand. The triplet state could transform into two main structures initiating different pathways.	123
Figure 5-9. Oxygraph data of (1-NO) solution exposed with light. No changes in oxygen concentration have been detected during the irradiation. The experiments have been repeated for 3 times for each concentration of Ru(bpy) ₂ (bpyNO)(PF ₆) ₂ and demonstrated the similar results.	124
Figure 5-10. Emission spectra of 0.08 mM of (1) , (1-NO) , and light exposed (1-NO) in water. (1-NO) is approximately redshifted by 4 nm. The excitation light was 350 nm.....	124
Figure 5-11. Absorption spectra of 1mM (1-NO) and illuminated (1-NO) in different solvents. All the light induced samples are illuminated with 670 nm LED for 30 minutes.	125

LIST OF ABBREVIATIONS

BD	Blue Dimer
CW	continuous wavelength
DFT	density functional theory
EPR	Electron Paramagnetic Resonance
ET	Electron transfer
FTIR	Fourier transform infra-red
HF	Hartree-Fock
HOMO	Highest Occupied Molecular Orbital
LUMO	Lowest Unoccupied Molecular Orbital
MT	Mega Tone
Mtoe	Mega Tone of Oil Equivalent
MOF	Metal organic framework
OPT	Optical Parametric Oscillators
OEC	Oxygen Evolving Complex
PEM	Proton-Exchange Membrane
PS I	Photosystem I
PS II	Photosystem II
PCET	Proton-coupled electron transfer
RC	radical coupling
RRaman	Resonance Raman
TPES	Total Primary Energy Supply
WNA	water nucleophilic attack
WOC	water oxidation complex

ABSTRACT

Climate change and the energy crisis are substantial challenges facing the human species, and they are projected to threaten life on our planet. For millions of years, the sun has been the main source of energy for life on Earth; this inspires ongoing research efforts focusing on a “sunlight to fuel” energy solution. Photosynthesis is nature’s tool to derive energy from the sun. Hence, scientists focus on the biochemistry of this phenomenon to employ photosynthesis in a man-made device. Such a device is able to convert solar energy to chemical energy through a light-driven cycle of the chemical reactions which produce hydrogen gas, later used as fuel. This process, often called “artificial photosynthesis,” needs efficient catalysts which can be incorporated into a molecular assembly and other microscopic structures or immobilized on an electrode surface.⁴⁻¹⁰

Additionally, evolution, in the course of billions of years, chose manganese as an abundant and effective metal to facilitate the process of photosynthesis. These manganese atoms formed a cluster and an optimized ligand field to maximize efficiency. The photochemistry and photo-physics process behind photosynthesis is yet to be fully understood and implemented in a man-made apparatus with comparable efficiency and durability.

Photosynthesis requires a source of electrons. Water is an abundant molecule on earth that can provide the electrons needed for the photosynthesis. Although water is ubiquitous, it is one of the most stable molecules; hence, splitting it demands a well-designed system with strong oxidizing capability. Because a single atom of oxygen is highly reactive, there should be at least four oxidation states in the system to remove four electrons and release molecular oxygen: O₂. The O-O bond formation is one of the most important steps in photosynthesis to fully understand. Lacking a thorough knowledge of this step prevents design and fabrication of robust and active water oxidizing catalysts. To fully understand O-O formation, one should perform a comprehensive study of each of the intermediates of the system. In other words, we need an understanding of the structure and electronic configuration of the system (natural or artificial) from the moment that a water molecule attaches to the catalyst (usually a metal core, central in the complex), until the moment that oxygen released as an O₂ molecule.

There are multiple possible mechanisms to explain O-O formation. Two mechanisms that were extensively studied in this thesis are water nucleophilic attack and radical coupling. The prevailing view about oxygen formation in the catalysts that we study here explains the O-O bond

formation by nucleophilic attack of a water molecule to a highly oxidized ruthenium ($\text{Ru}^{\text{V}}=\text{O}$) species. In this hypothesis, all polypyridine ligands that are coordinated to ruthenium remain neutral during the water oxidation process, while the formation of $\text{Ru}^{\text{V}}=\text{O}$ (the key intermediate) would require a relatively high free energy (about 1.8 to 2 eV¹¹); use of computational (numerical) calculations determine this to be thermodynamically inaccessible.^{12, 13} Furthermore, the failure of spectroscopic techniques to confirm the presence of $\text{Ru}^{\text{V}}=\text{O}$ calls the validity of this model into question.¹⁴)

Alternatively, radical coupling hypothesis considers another pathway to oxygen bond formation. Here, one of the nitrogen atoms coordinated to ruthenium in polypyridine plays a crucial role. We hypothesize that after formation of $\text{Ru}^{\text{IV}}=\text{O}$ (which is spectroscopically observed), one nitrogen decoordinates from the metallic core (ruthenium) and oxidizes to form Ru-ON species. This N-oxide ligand can be further oxidized to form a ligand cation radical. It has been shown that $[\text{ligand-NO}]^+$ can have almost no energy barrier for O-O bond formation via spin alignment.¹¹ The study of the role of N-oxide is one of the main focuses of this work. Since this hypothesis does not require $\text{Ru}^{\text{V}}=\text{O}$ nor water nucleophilic attack, it explains the process of water oxidation and opens further avenues for the design of future catalysts.

To confirm our hypothesis, I employed several spectroscopic methods and computational calculations. This new pathway predicts new intermediates exclusive to this model. Our objective is to prove their presence by *in situ* spectroscopy and test the possibility of formation of each intermediate computationally, to see if their formation is thermodynamically feasible.

In chapter one, I try to expand the basics of my research. Included is a brief explanation on photosynthesis and the role of photosystem II protein. The artificial photosynthesis and the reason we study ruthenium-based water oxidation catalysts concludes this chapter.

In chapter two, a description of all the major experimental and theoretical methods that I used in my research is presented. Raman and EPR spectroscopy are extensively studied. Raman, a vibrational spectroscopy, is used to study the atomic bonds. This technique is especially useful when vibrational frequency can be assigned to the crucial species such as $\text{Ru}^{\text{IV}}=\text{O}$ and Ru-O-N. Substitutions of an oxygen isotope (¹⁸O) causes the vibrational frequency to shift, indicating bond assignment and the intermediate predicted by this hypothesis. Raman spectroscopy is a powerful spectroscopic tool that can help us to have a better understanding of the geometry of the catalyst and its intermediates.

EPR is another useful technique that enables us to determine the electronic configuration of the catalyst. Knowing the oxidation state and spin state of the catalyst and its intermediates can shed light on the mechanism of oxygen evolution. For example, EPR can show us if there is Ru^{V} present as an intermediate. EPR is also sensitive to the geometry of the orbital that unpaired electrons occupy. EPR can tell us about the ligand environment, as well as oxidation state of the metal core of the catalyst.

Density functional theory (DFT) as a computational method can augment our hypothesis in many different ways. For example, the optimized geometry of an intermediate can be used to validate an X-ray study and vice versa. Calculating the free energy and vibrational frequencies are two examples that I used DFT for in my thesis. DFT is significantly useful for determining the thermodynamics and feasibility of intermediates for the reactions that our model hypothesized. Like any other simulation technique, DFT is an approximation, but knowing some experimental parameters would help to certify our theory. Also, DFT comes in handy when some of the intermediates are short lived and very difficult or impossible to trap in experiment to study with our spectroscopical tools.

In chapter three, I present some evidence on the radical coupling mechanism for the most studied Ru-based water oxidation catalyst, $[\text{Ru}^{\text{II}}(\text{tpy})(\text{bpy})(\text{H}_2\text{O})]^{2+}$. We study this catalyst and other forms from the same family, and first show that water nucleophilic attack is not a viable mechanism by the spectroscopic and theoretical information that we have on this family. Later we hypothesize that a redox active ligand plays a major role in the catalytic activity. We show by synthesizing this catalyst with N-oxide bpy ligand instead of bpy ligand the water oxidation enhances more than hundred times. We also hypothesize that ligand redox potential can inversely be correlated to the rate of oxygen evolution. This is a fundamental step in rational design of a new catalyst from this family or with similar mechanism.

In chapter four, I show how to stabilize $[\text{Ru}^{\text{II}}(\text{tpy})(\text{bpy})(\text{H}_2\text{O})]^{2+}$ by modifying bpy ligand to dcbpy and incorporating it in UiO-67 MOF, a zirconium-based MOF which has many applications because of its high surface area through a network of pores and channels. I showed that the oxygen evolution mechanism for this complex does not require dimerization. Resonance Raman helped us to selectively look at the Ru complex incorporated in MOF and making sure the MOF signal does not overwhelm the signal from Ru, even though Ru complex is a small portion of the volume of the sample.

In chapter five, we focused on the role of redox active ligands. $[\text{Ru}(\text{bpy})_2(\text{bpyNO})]^{2+}$ will be studied as a case to investigate N-oxide bpy ligand. Although this complex is not a water oxidizer, it was previously used as a model to show the feasibility of radical coupling mechanism in Ru-ON systems. The N-oxide bpy ligand in this ruthenium complex and similar complexes is light sensitive. I studied the extent of light sensitivity of N-oxide in this complex. This complex and similar complexes to this can have many applications outside of the field of artificial photosynthesis. They can be used as photo oxidizers like $[\text{Ru}(\text{bpy})_3]^{2+}$. I confirmed that this complex would transform to $[\text{Ru}(\text{bpy})_3]^{2+}$ upon light exposure.

CHAPTER 1. PHOTOSYNTHESIS

1.1 Motivation.

According to the first law of thermodynamics, the entire energy in the universe is conserved, but that doesn't mean we have unlimited energy to use. Second law of thermodynamics states that the entropy of any isolated system always increases. In other words, the "free energy" in the universe is constantly decreasing. "Free energy" is needed to run any engine. In everyday life we call this "free energy" fuel. Coal, diesel, gas, etc. are the examples of "fuels," and almost all of these energies ultimately come from the sun. The process of formation of fossil fuel occurs over millions of years, and the rate of consumption of these fossil fuels far exceeds the rate of their formation; hence, fossil fuels are not sustainable in the long term. To further complicate the energy scene, the pace of worldwide energy consumption has increased dramatically over the last few years. From 1973 to 2015, the Total Primary Energy Supply (TPES) increased from 6101 Mtoe (Mega Tone of Oil Equivalent) to 13647 Mtoe.¹⁵ In this period the oil, coal, and natural gas share of TPES reduced from 86.7% to 81.4% percent which is not very significant. The nuclear share increased from 0.9% to 4.9%. Finally, the increase in the renewable energy such as solar, wind, and hydropower was only about 2%.¹⁵ The resulting CO₂ emissions increased from 15458 Mt (mega tone) to 32294 Mt.¹⁵ Doubling the emission of carbon dioxide in about 42 years expedites global warming and climate change.

Although consumption reforms are major ways of changing the situation, finding cheap CO₂-neutral energy sources are the ultimate solution for the energy crisis, global warming, and even the world economy. Looking at the sun as an infinite source of energy (on the human life time scale), one can argue harvesting the energy of the sun, like plants do, could put an end to our dependence on fossil fuel resources. To achieve this goal, first we should know the fundamental physics and chemistry of photosynthesis with complete details to be able to recreate that in a man-made device aka artificial photosynthesis. To achieve this goal, we must strive for a fundamental understanding of the physical and chemical details of photosynthesis, to mimic the process in a man-made device, known as artificial photosynthesis.

1.2 Photosynthesis and the role of photosystem II.

Photosynthesis is the process of capturing sunlight and using its energy to produce sugar from carbon dioxide and water, **Figure 1-1**. During this process, oxygen is released as a byproduct into the atmosphere. While carbon dioxide only consists of 0.04 percent of the gas in our atmosphere, it is enough to provide the carbon atoms of glucose in the plants.

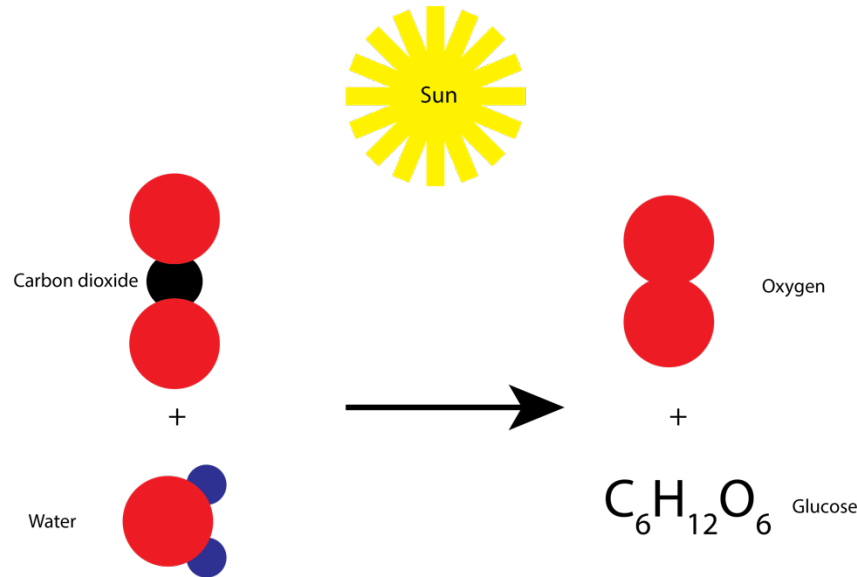


Figure 1-1. Schematic of photosynthesis reaction. Carbon dioxide and water are reactants; oxygen and glucose are the products. Solar energy provides the essential energy to run this reaction.

To have a better understanding of photosynthesis, one should have a closer look at green leaves (or cyanobacteria). **Figure 1-2** shows a cross section of a thylakoid membrane and its components. The thylakoid resides inside chloroplasts and its membrane separates the inside fluid (lumen) from the outside (stroma). Across the thylakoid, a concentration gradient is maintained for several molecules and ions. The protein complexes Photosystem I (PS I) and Photosystem II (PSII) are essential parts in driving the photosynthetic process. Since sunlight is required for reactions in both PSI and PSII, these reactions are called light-dependent reactions. As part of these reactions, the Oxygen Evolving Complex (OEC) in PS II extracts electrons from its nearby water molecules. Two oxygen atoms form a molecule and are released after the oxidizing two water molecules and removing four electrons. The electrons then going through the b_6f protein into the lumen with a

mobile electron carrier (not shown in **Figure 1-2** for simplicity). As mentioned, Photosystem I (PS I) is also driven by sunlight. Electrons will be excited at PS I and will reduce NADP^+ to NADPH. Protons (H^+) at the same time will go to ATP synthase which uses a proton-motive force to make ATP from ADP. The rest of the process is “light independent” since there is no direct sunlight’s energy to drive the reactions. The energy is already stored in ATP and NADPH, and by reducing carbon dioxide, the final product --sugar-- is created. This process is called the Calvin cycle, and details can be found elsewhere. ⁹

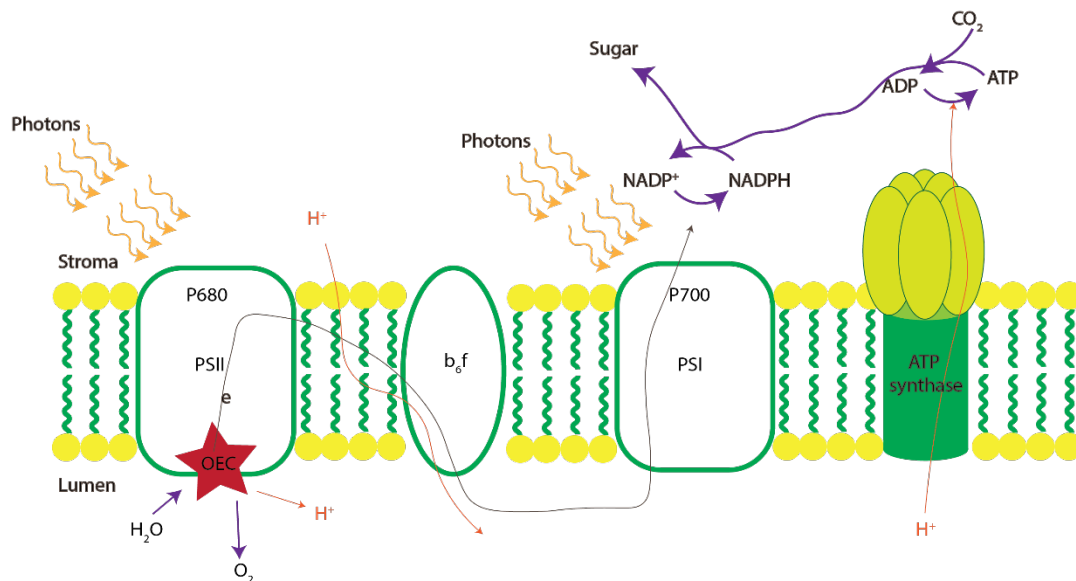


Figure 1-2. Thylakoid membrane is shown with the essential components for the electron transport chain path and its reactions.

Since this study is mainly about the process of evolving oxygen, we delve into details of PS II and the OEC a little bit more. PS II is the only protein known in nature able to evolve oxygen from water. In PS II, after a photon is captured by chlorophyll and the energy is channeled down to P680, it transfers an electron to an acceptor. In result, P680 becomes P680^{++} and gets an electron from the OEC to become P680 again. The OEC, an inorganic manganese cluster ($\text{Mn}_4\text{O}_5\text{Ca}$), becomes oxidized. This manganese cluster goes through a five-state cycle known as “Kok cycle”, or “S-state cycle”, before two water molecules are fully oxidized and return to its original oxidation state, **Figure 1-3**.

The Kok cycle, as was mentioned, refers to a photoinduced cycle which was proposed by Kok in 1970. ¹⁶ According to Kok cycle dark adapted purified PS II would release oxygen after

every four pulses of light which suggest the WOC should go through a cycle with at least four steps. It is believed that there are actually five steps (S0 to S4) but the last step in the cycle is a transient intermediate that doesn't require a photon to proceed, **Figure 1-3**. Determining the exact dynamic of Kok cycle is still a hot topic among scientists because of two reasons. First, water splitting is such an important step in evolution that there is a lot of interest in understanding of photo physics of this process; second, it is essential to understand the chemistry of manganese cluster to design an effective Water Oxidation Catalyst (WOC) aka artificial photosynthesis.

1.3 Artificial Photosynthesis

The need to understand the importance of photosynthesis leads scientists in the direction of reproducing what nature does, in a lab. The results of these efforts are called artificial photosynthesis. It's important to note here that artificial photosynthesis, as is mentioned here, only refers to a synthetic replication of water splitting. The ultimate goal is to run the following reaction as "efficient" as possible.

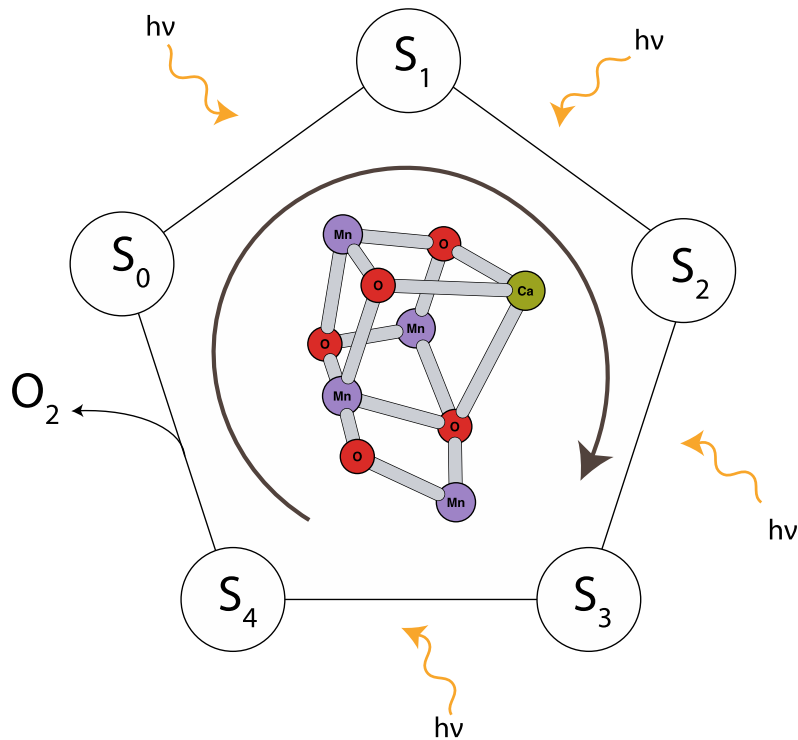
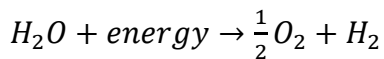


Figure 1-3. Kok's cycle. S₁ is the dark-adapted state and each photon drives the cluster one step ahead. The exact dynamics of the process is still debated.



Equation 1-1

Equation 1-1 has $\Delta G = 237 \text{ KJ/mol}$; This is the energy required to make one mole of hydrogen at standard conditions (**Figure 1-4**). This free energy can be provided by a battery with a minimum potential difference of 1.23 V (1.23 eV is the energy needed per electron in **Equation 1-1**, 1.23 eV is equivalent to the energy of a photon with 1100 nm wavelength). Although this is an endergonic reaction, the free energy of the system is not the major problem, the activation energy is. Splitting the O-H bond, however, has 500 KJ/mol .¹⁷ The presence of a catalyst will lower this barrier and make the process more efficient, **Figure 1-4**. For example, in manganese cluster in PSII, the absorbed photon which provides the energy to split water has the wavelength of 680 nm which is equivalent to 350 KJ/mol . The efficiency of this reaction would be higher if the activation energy was lower. 100% efficient reaction is a reaction with no activation energy.

Photo-induced reactions aren't the only way to split water. Water electrolysis is the current method that is used in industrial scale to split water.

In water electrolysis, two half reactions occur on each electrode to complete **Equation 1-1**. If two electrodes with potential difference of 1.23 V (plus a few hundred meV overpotential) are immersed in water (with some ions in water to act as electrolyte), oxygen molecules start to evolve on the positive electrode, or anode, and hydrogen molecules on the negative electrode, or cathode. A gold electrode was used for the first time to electrolyze water in 1789¹⁸. Since that time, many inert metals such as iridium, platinum, and stainless steel have been used as mentioned above. Depending on the electrodes, the overpotential (the potential which is above 1.23 V) could be different. For example, platinum alloys are state of art with excellent efficiency, but platinum is very expensive. Other elements such as iridium, nickel, carbon, and molybdenum are examples of materials that have been used to produce cheap efficient electrodes. A typical overpotential could be a few hundreds of mV.

Proton-exchange membrane (PEM) is also an important method to electrolyze water and is worth mentioning here. The PEM technology that is used in electrolysis is similar to fuel cell PEM: a solid membrane is used as a proton conductor. In the state of art PEM, metals such as platinum or palladium are used at the cathode where hydrogen evolves, and iridium oxides or ruthenium oxides are used at the anode where oxygen evolves. In these areas, the focus of the research is to make sustainable electrode. For example, iridium loading is a very important factor and should be as low as 0.4 mg/cm² for an electrode, without negatively effecting the catalytic performance of the process. The loading factor for the current systems is about 1 to 3 mg/cm².¹⁹

Equation 1-3 and **Equation 1-4** are half reactions which complete reaction in **Equation 1-1** on anode and cathode respectively at pH 0 with the minimum of potential of 1.23 V on anode, and 0 on the cathode



To make this process economically viable in an industrial scale, the price of electricity should be competitive with other methods such as steam reforming which is a hydrogen production process from natural gas.

Now that we introduced the electrolysis, let's step back and revisit the photo-induced water splitting reactions. Another way of providing energy to run the reaction **Equation 1-1** is to use photoinduced electromagnetic waves: the same method that nature uses in photosynthesis. 1.23eV is equivalent to the energy of a photon with 1008 nm wavelength. Theoretically, by using NIR light one can split water in a reaction with 100% efficiency, but this never occurs. If water is exposed to deep UV, eventually it starts to be split at 190 nm²⁰ but NIR and visible light is not able to split water. This deep UV is energetic enough to pass the activation energy barrier. However, it is worth mentioning this mechanism (splitting water with deep UV) is a photo ionization process, not a photo oxidation -- the main topic of this report. Since 1008 nm photons have the minimum energy needed to split water, if a catalyst can be created that can lower the activation barrier and absorb photons of that wavelength, then photons in the visible region, or even of lesser energy, could become useful in water oxidation.²¹ One approach to this problem is to produce a catalyst that reduces the activation energy of the reaction without changing the energy gap needed to run the reaction, **Figure 1-4**. The biggest problems with these catalysts are efficiency, durability, and price. We try to explain some solutions to these issues in the rest of this thesis.

1.4 Non-ruthenium-based catalysts and important concepts

Before highlighting ruthenium-based catalysts, the main subject of this study, an overview of other catalysts and an introduction to the terminology is needed.

Water oxidation reaction is endogeneric and the Gibbs free energy associated to this reaction is 237 kJ/mol. This is the energy required to make one mole of hydrogen molecules at standard conditions, **Figure 1-4**.

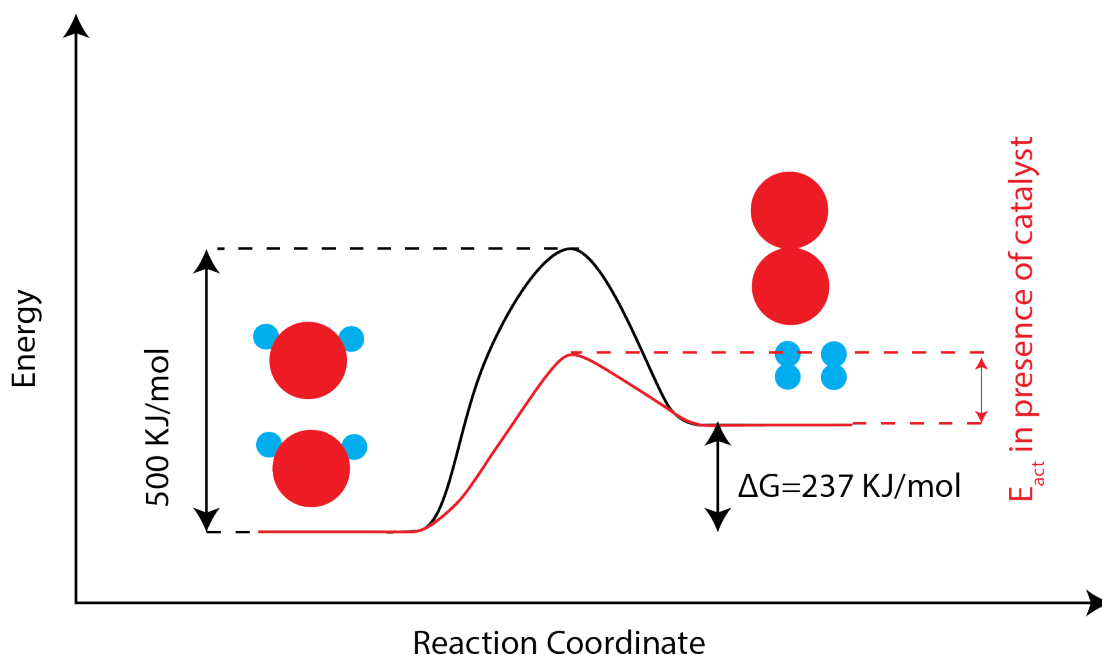


Figure 1-4. Gibbs free energy of water splitting reaction is shown. The role of a catalyst is to lower the activation energy barrier.

Platinum-based catalysts are used due to their high efficiency and durability.²² Platinum-based catalysts are also versatile, being common in fuel cells, where the opposite reaction of splitting water occurs. While these catalysts are effective, platinum is one of the most expensive metals on earth due to its scarcity. Iridium-based catalysts were used for the first time in 2008 as single site complexes.²³ Both iridium and platinum are rare metals. The abundant metals with rich redox chemistry (a system with rich redox chemistry is a system that can go through multiple oxidation states) can be found in the first-row transition metals in periodic table. Two such metals studied extensively are iron and manganese. These two are very cheap to mine and have little to no side effects from toxicity. Manganese is especially interesting because of its usage in the natural photosynthesis. In 1994, a manganese dimer was synthesized for the first time to oxidize water.²⁴ Like manganese, iron is another first row transition metal that has been incorporated into many water oxidation catalysts (WOCs).²⁴ A very comprehensive list of WOCs can be found in the reference.⁹

One of the major difficulties that WOCs have to overcome is the high activation energy barrier to evolve one molecule of oxygen from two water molecules. It requires four electron

transfer events. This means the catalyst should have the ability to convert across four oxidation states with comparable energy to 1.23 eV for each intermediate. The ultimate goal of WOC research is the formation of a stable catalyst which can cycle through these oxidation states quickly and repeatedly.²⁵ For each catalyst, the total number of cycles achieved before catalyst degradation is called the turnover number (TON). This value is experimentally measured, where the higher the TON, the more robust the catalyst. For example, the manganese cluster that naturally oxidize water can go through 10^6 Kok cycles.²⁶ The other concept that should be introduced is turnover frequency (TOF), which is basically the number of oxygen molecules evolved per unit of time for each WOC.

A WOC has many electron transfers in each cycle which are often accompanied by a proton transfer at the same time, to prevent charge buildup. This is the so-called “proton-coupled electron transfer,” or PCET. In each cycle, there are steps with PCET or electron transfer (ET), causing oxidation state changes. Understanding PCET is critical for realizing the path and the dynamics of different intermediate species created during the reaction.

To study the dynamics of a catalyst with different oxidation states, the oxidation state of the catalyst can be studied one step at a time to measure all the intermediates. To achieve this, there are some commonly used chemical oxidants. The most famous oxidant is Ce^{IV} in cerium ammonium nitrate (CAN), with chemical formula $\text{Ce}(\text{NH}_4)_2(\text{NO}_3)_6$. Ce^{IV} has the redox potential of 1.70 V vs NHE. This one-electron oxidant will extract only one electron from the complex and become Ce^{III} . The advantage of CAN is that it's almost colorless in solution (light yellow color), so it is compatible with spectroscopic studies, as it will not interfere with techniques that use visible light. The disadvantage of using CAN is that it should be used in acidic condition to work ($\text{pH} < 1$).²⁷ Potassium peroxydisulfate (Oxone) is a two-electron oxidant. Oxone has redox potential of 1.82 V vs. NHE and can work in less acidic conditions (pH up to 6) compared to CAN.^{28,29} Sodium periodate (NaIO_4) is yet another two-electron oxidant that is used and has a redox potential of 1.60 V vs. NHE and can be used for solutions with pH up to 7.5.^{30,31}

1.5 Ru-based WOCs

Ruthenium is a second-row transition metal with a standard atomic weight of 101.07 u. It has been found in several oxidation states including -4, -2, +1, +2, +3, +4, +5, +6, +7, +8. It also has 10 isotopes; six of which are stable.

In 1982, a binuclear μ -oxo-bridged ruthenium complex known as blue dimer was reported,³² **Figure 1--5A**.

It was long assumed that there must be more than one metal atom for WOCs to function, especially since the manganese cluster in PSII has four manganese atoms and the fact that oxygen evolution is a four-electron transfer process; researchers believed that single site WOC is not feasible. This rationale started to change when $[\text{Ru}(\text{bpy})_3]^{2+}$ (ruthenium polypyridyl) was reported as a new photosynthesizer in 1970³³, **Figure 1--5B**. This single site complex has been extensively studied, and although it's not capable of water splitting, it paved the way for single site catalysts such as $[\text{Ru}^{\text{II}}(\text{tpy})(\text{bpy})(\text{H}_2\text{O})]^{2+}$. $[\text{Ru}^{\text{II}}(\text{tpy})(\text{bpy})(\text{H}_2\text{O})]^{2+}$ is the most studied Ru-based catalyst and the main topic of chapter 3 and 4 in this thesis. Other generations of single site WOC with higher catalytic activity were discovered later³⁴. A complete list of WOCs with different variation of ligands can be found in a recent review.⁹

Ruthenium has pros and cons when it comes to WOCs. Although it is one of rare elements in earth crust and has potential toxicity and high price, it has features that some of the abundant elements on earth, such as iron and copper, don't have. Ruthenium with polypyridine or similar ligands demonstrates a very rich photo chemistry (with the right ligand field design, it can go through different oxidation states by photo redox reactions) that most of other elements don't. Ruthenium WOCs are usually colorful in homogeneous solution which makes them capable of absorption of visible light. Other earth-abundant-based WOCs are mainly transparent to visible light and absorb light in the UV range (although it depends on the ligand field as well). Though ruthenium is one of the more expensive metals on earth, it is still cheaper than the gold and platinum often used in water splitting systems. Finally, the toxicity and environmental effects of ruthenium, which are important to consider, can be dealt with if regulations and safety measures put in place. I should add that the final goal is to make a long-lasting and durable WOC which means there shouldn't be a lot of waste in industrial scale.

Though ruthenium may not be the final solution (it is inevitable to look towards earth abundant metals), learning about the chemistry of Ru-based WOCs can help and guide us in our journey to make an efficient, long lasting, fast, and environment friendly WOC.

Before concluding this chapter, the geometry of six-coordinate ruthenium complexes and its possible mechanisms are needed to be mentioned. The first column of **Figure 1--5C** shows the basic geometry of a complex with octahedral geometry. Although in reality, the geometry of most

complexes would be slightly different because of different ligands they have, it can show us a road map toward a basic understanding of the spin, symmetry, orbital energy splitting, and etc. Ruthenium systems are usually low spin in Ru^{II} state. Upon water coordination to the core metal (The middle column of **Figure 1--5C**), the symmetry of the system changes and can be described by a C_{4v} point group. The energy level for d_{z^2} goes lower due to change in symmetry and also the water ligand is a weaker donor compare to a nitrogen in a polypyridine ligand.³⁵ In both first and middle column in **Figure 1--5C** all the ligands are neutral with the assumption that every ligand is either a water or nitrogen in a polypyridine ligand. Later in chapter three, we show that in a higher oxidation state of ruthenium the ligand could be unneutral and go through a redox process. Finally, the last column in **Figure 1--5C** is a crucial species that its existance is vital for almost any WOC. This spicies ($\text{Ru}=\text{O}$) is at spin state one ($S = 1$) and the ruthenium oxidation state is IV. $\text{Ru}^{\text{IV}}=\text{O}(\text{L}_5) - \text{L}$ stands for ligand - is usually obtained by two consequent oxidation via PCET mechanism from $\text{Ru}^{\text{II}}(\text{H}_2\text{O})(\text{L}_5)$.

Oxygen bond formation is a crucial step in the water oxidation reaction. WNA and RC both can explain O-O formation. **Figure 1--5D**, depicts these two mechanisms. In WNA a water molecule reacts with a highly oxidized species (here $\text{Ru}^{\text{V}}=\text{O}$, notice $\text{Ru}^{\text{IV}}=\text{O}$ is not energetic enough for WNA). In WNA a pair of electrons from water transfers to oxygen coordinated to ruthenium and consequently to ruthenium and change the oxidation state of Ru^{V} to Ru^{III} . RC is another possibility for the water oxidation reaction. In this mechanism two highly active radicals react and form O-O. Since radicals are usually very energetic and unstable, O-O formation could be barrierless without activation energy.¹¹ Although in **Figure 1--5D** two ruthenium is needed to complete the mechanism; it is not always the case. In chapter three we extensively talk about RC between the oxygen in an N-oxide ligand and an oxygen coordinated to the same ruthenium core.

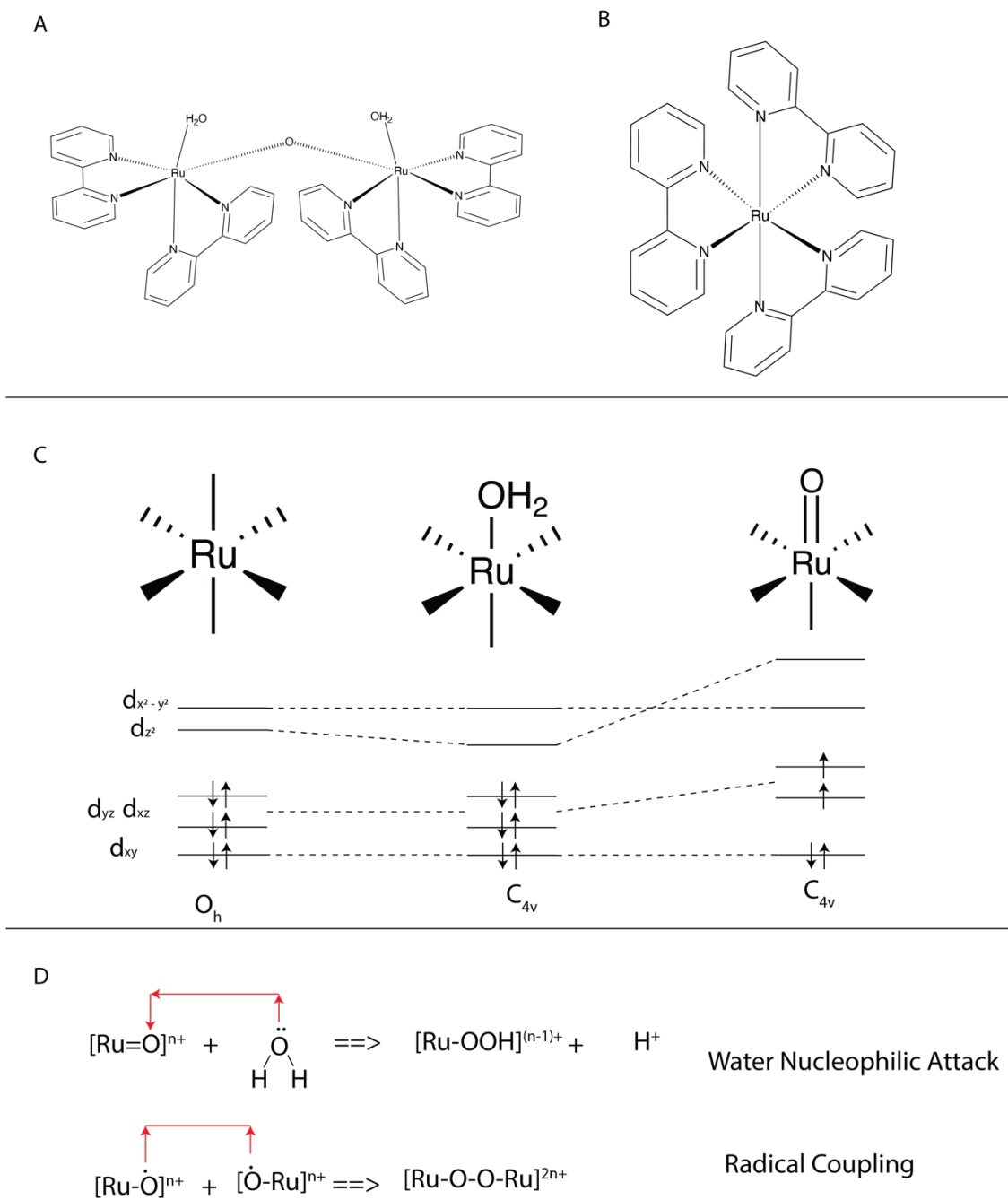


Figure 1-5. Blue dimer (A) and $[Ru(bpy)_3]^{2+}$ (B), two of the most studied catalysts in the field of artificial photosynthesis. (C) common geometries in Ru-based WOC and their corresponding orbital energies. (D) Depiction of two possible mechanisms for water splitting that are studied in this thesis

CHAPTER 2. INTRODUCTION TO METHODS

2.1 The Theory of Raman Scattering

2.1.1 Why Raman Spectroscopy

Raman spectroscopy, as well as Fourier transform infra-red (FTIR), are very powerful tools in vibrational spectroscopy. The main application of Raman scattering is to detect the atomic bonds in molecules and crystals. Detecting the existence of atomic bonds by their characteristic vibrations provides a road map to confirming or discovering the geometry of a molecular structure. I used the Raman spectroscopy technique in this report because water oxidation is a process which requires four electron removal, and a WOC would go through at least four different geometries; hence, it is a very advanced technique to distinguish the change in the geometry. Specifically, the use of isotope substitution of a specific atom to confirm a change in vibrational frequency of that atomic bond is used multiple times in this study. Another example is bond formation or ligand disassociation, which can be detected by Raman spectroscopy. Although analytical calculation of a specific vibration by solving a Hamiltonian is extremely difficult, numerical calculations such as density functional theory (DFT) can approximately compute vibrational modes of a molecules.

2.1.2 The classical description of Raman Scattering

Raman scattering could be simplified as the inelastic collision of light and matter. In this section, the classical effect (classical electromagnetic theory) of inelastic light scattering is reviewed; a non-classical and quantum version of the theory will be explained later.

Maxwell's equations show that light is electromagnetic wave and follow the wave equations. An electromagnetic wave interaction with the surface of a matter will change the distribution of surface charge density due to boundary conditions imposed by Maxwell's equations. This interaction can be in the form of absorptions, reflection, scatter, or transmittance. With a closer classical microscopic look, one can see that interactions between light and a surface is the interaction between a wave and molecule. Depending on the type of molecule, the light can produce or disrupt an already existing dipole moment of the molecule. The induced dipole moment itself radiates a secondary electromagnetic wave as inelastic scattered light. Each type of molecule has a specific electronic charge distribution with an associated induced dipole moment; thus, the

inelastic scattering light is characteristic for different molecules. To explain how the light and matter interaction can be expressed mathematically, we will use classic electromagnetism and simple harmonic oscillator.

The induced dipole moment, \vec{P} , can be related to electric field with **Equation 2-1**:

$$\vec{P} = \alpha \vec{E} \quad \text{Equation 2-1}$$

Here the tensor α is the polarizability (for the sake of simplicity, we imagine α is just a scalar, but in the most general form, it is a rank two tensor) and \vec{E} is the electric field. Since the source of the electric field is the incident light, using the results of Maxwell's equations, the electric field has wave-like behavior:

$$\vec{E} = \vec{E}_0 \cos(\omega_0 t) \quad \text{Equation 2-2}$$

ω_0 is the angular frequency of the incident light (assuming the incident light has single frequency such as a narrow-band laser). By substituting **Equation 2-1** into **Equation 2-2** the following is obtained:

$$\vec{P} = \alpha \vec{E}_0 \cos(\omega_0 t) \quad \text{Equation 2-3}$$

As α and the electric field increase, the dipole moment also increases. α is not only characteristic for each molecular structure but is also a function of the distance of the nucleus of atoms in the molecules. If x shows the distance between two atoms, then α is a function of X . In **Figure 2-1**, X_0 is the distance between atoms before the electric field interacts with a molecule (i.e. at its equilibrium) and $X_0 + \delta$ is the distance after the interaction. In general, δ is a vector that can have any direction and magnitude. If one assumes that after the interaction between light and the molecule the distance x will oscillate around the value X_0 , then the distance between the two atoms can be written as a function of time as:

$$X = X_0 + \delta \cos \omega_x \quad \text{Equation 2-4}$$

where ω_x is the angular frequency of oscillation. As was mentioned above, if α is a function of distance of the nuclear of atoms in molecules, it is convenient to write α in terms of Taylor expansion:

$$\alpha(X) = \alpha_0 + (\partial_x \alpha)|_{x_0} \cdot X_0 \cdot \cos(\omega_x t) + \dots \quad \text{Equation 2-5}$$

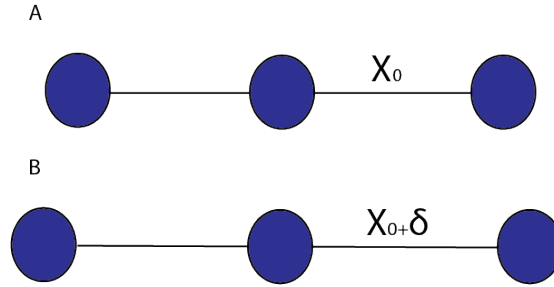


Figure 2-1. An example of a linear molecule shown in the equilibrium state(A); and an electric field induced stretched state, (B)

Plugging **Equation 2-4** and **Equation 2-5** into **Equation 2-1** would give the following equation

$$\vec{P}(t) = \alpha_0 \vec{E}_0 \cos(\omega_0 t) + (\partial_x \alpha)|_{x_0} \cdot x_0 \cdot \cos(\omega_x t) \vec{E}_0 \cos(\omega_0 t) + \dots \quad \text{Equation 2-6}$$

Using trigonometric identities for the second term in the **Equation 2-6**, $(\cos(a) \cdot \cos(b) = \frac{1}{2} (\cos(a + b) + \cos(a - b)))$. Keeping only the first order in the expansion, then the final form of **Equation 2-6** becomes:

$$\vec{P}(t) = \text{Const}_1 \cos(\omega_0 t) + \text{Const}_2 \{ \cos((\omega_x + \omega_0)t) + \cos((\omega_x - \omega_0)t) \} \quad \text{Equation 2-7}$$

There are three terms in **Equation 2-7**, the first, which has the same frequency as the incident light, is called the Rayleigh scattering. In reality, a large portion of scattering is Rayleigh scattering. The second term describes light with higher frequency of $\omega_x + \omega_0$. This is called anti-Stokes scattering. The third term shows the scattering light with lower frequency $\omega_x - \omega_0$, which is called Stokes scattering. As one can see, Rayleigh scattering is independent of ω_x , which means it is

independent of matter type. In contrary, Stokes and anti-Stokes are characteristic for each individual molecule. Usually the word “Raman scattering” refers to Stokes scattering, although in some occasions it can refer to anti-Stokes Raman scattering. Even though anti-Stokes is preferred in some situations, it is less common in experiments due to lower signal intensity.

2.1.3 Non-classical description of Raman spectroscopy

In the classical description, there is no restriction in the Stokes and anti-Stokes **Equation 2-7** to be discrete; in other words, frequencies are not quantized. However, we know from experiment that Raman bands are relatively sharp and discrete. Adding a quantum mechanical description to the picture resolves this issue. The simplest model to describe a molecular bond is the simple harmonic oscillator. If two atoms with mass m_1 and m_2 are connected to each other via a spring with a stiffness k , then the angular frequency ω can be calculated by:

$$\omega = \sqrt{\frac{k}{\mu}} \quad \text{Equation 2-8}$$

Where μ is the reduced mass and can be expressed as

$$\frac{1}{\mu} = \frac{1}{m_1} + \frac{1}{m_2} \quad \text{Equation 2-9}$$

The energy levels of a simple harmonic oscillator are

$$E = \hbar\omega \left(n + \frac{1}{2} \right) \quad n = 0, 1, 2, \dots \quad \text{Equation 2-10}$$

Where E is the energy, \hbar is $2\pi h$ and h is Plank’s constant. Here $n = 0$ is the ground state for vibrational energy (not to be confused with electronic state energy). Transition between $n = 0$ to $n = 1$ represents Stokes lines, and the transition between $n = 1$ to $n = 0$ represents anti-Stokes. **Figure 2-2** shows Raman scattering process. The red arrows represent the excitation process by a photon incident on the molecule that is being studied. This photon will knock an electron out of its electronic ground state to a virtual state **Figure 2-2 A**, and the electron returns to one of the vibrational states in the ground state; it is worth mentioning that this process occurs instantaneously in picosecond range. If the energy gap between two electronic states is approximately the same as the energy of the incident photon, the electron will go to the next electronic state **Figure 2-2 B**. In

this case, the energy gap plays the role of a resonator and the Raman scattering can be enhanced up to 10^6 times than normal Raman scattering. Since this is a very important achievement, this type of scattering has its own name: Resonance Raman (RRaman) scattering. We will talk about the RRaman scattering later. Finally, **Figure 2-2 C** is an illustration of fluorescence. More explanation about this comes with RRaman.

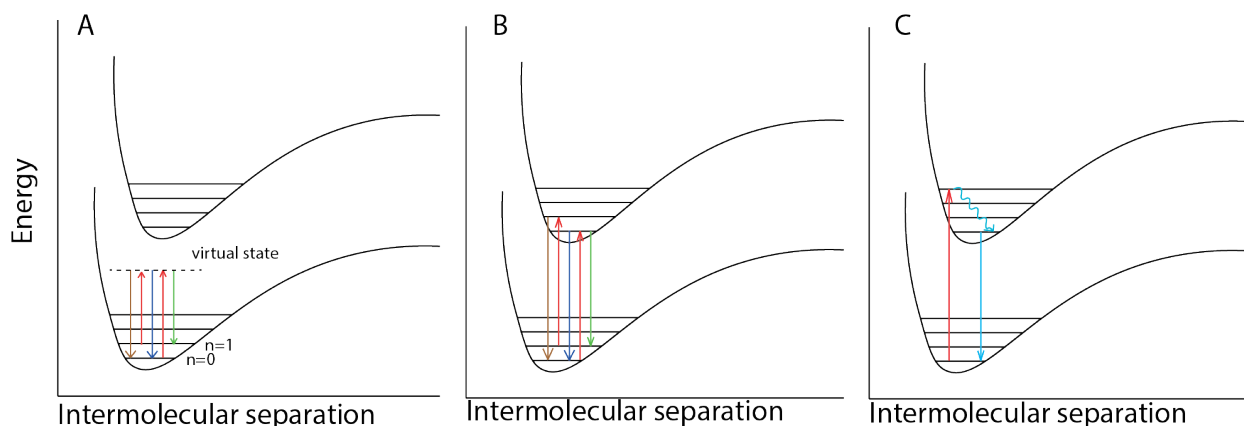


Figure 2-2. The curves represent electronic states and the horizontal lines inside the curves represent vibrational states. (A) Raman (nonresonance) scattering process; note that the energy that the electron gains is less than the energy gap between two electronic states. A virtual state is added to the figure to clarify this point. (B) RRaman scattering process; here the energy that an electron gains is close to the energy gap between two electronic states. This resonance effect enhances the signal significantly. (C) Fluorescence process; the excited electron relaxes first on the vibrational states of the electronic excited state before it decays into the electronic ground state.

The energy difference between $n = 0$ and $n = 1$ is characteristic of each bond ($\omega = \omega_x \pm \omega_0$). The angular frequency corresponding to the vibrational energy gap is proportional to the so-called “Raman shift”. More accurately, what is called Raman shift can be described as:

$$\nu = \frac{\omega}{2\pi} \quad \text{Equation 2-11}$$

ν is called the frequency of vibration. However, frequency (in Hz) is not the common unit for Raman shift; instead wavenumber (in cm^{-1}) is more widely accepted and is written as

$$\bar{\nu} = \frac{\nu}{c} = \frac{1}{\lambda} = \frac{1}{\lambda_0} \pm \frac{1}{\lambda_v} \quad \text{Equation 2-12}$$

Where c is the speed of light (in cm/sec) and λ_0 is the laser wavelength and λ_ν is Stokes or anti-Stokes wavelength (both in cm). Even though the frequency and wave number are technically different, but in the community of Raman spectroscopists they are usually used interchangeably.

The frequency of the Raman shift as mentioned above is proportional to the reduced mass and the stiffness of the spring, bond strength. As an example; consider the C-C bond and C-H bond. C-C has a reduced mass much more than C-H. The Raman frequency of C-C (in diamond) and C-H (in methane) is 1332 cm^{-1} and 2918 cm^{-1} correspondingly. There are several reasons that that the C-C frequency doesn't scale exactly as its reduced mass scale with C-H (the ratio is 6.5) as $\sqrt{\frac{1}{6.5}} = 2.55$ in this system: First, the stiffness of two bonds are not exactly the same, and secondly, the simple harmonic oscillator model isn't a perfect representation of an atomic bond. Also, the reduced mass is an approximation because atoms are bound to the rest of structure and they can't be viewed accurately in isolation. Although this could be viewed as an obvious and mundane example, it's necessary to show that quantitative analysis in this field is difficult. Later, when we use oxygen isotope substitution, we see that the change in frequency can be different even when two system are very similar. The same argument can be used to show the dependency of Raman shift on the bond strength, using C-C and C=C as an example. Both systems have the same mass but the stiffness of C=C is higher, and it has a higher frequency.

2.1.4 Raman Scattering intensity

Raman scattering is usually weak in comparison to most of optical spectroscopy such as IR spectroscopy, so it is important to know the factors that can have any effects on the signal. In the beginning of this section, it is mentioned that dipole moment radiation is a good model for Raman. Any Hertzian dipole will radiates as the following³⁶

$$I = \frac{d\Phi}{d\Omega} = \frac{\pi^2 c \bar{\nu}^4 P^2 \sin^2 \theta}{2 \epsilon_0} \quad \text{Equation 2-13}$$

Where I is the intensity, ϵ_0 is the vacuum permittivity, P is the dipole moment, and θ is the angle between the direction of the dipole moment and position of the detector. From **Equation 2-13**, we know P is proportional to the electric field of incident laser, and that is proportional to the intensity of the laser. So, the stronger the laser, the stronger the Raman signal since we see

from **Equation 2-13**, we can conclude that the Raman signal is proportional to the square of the laser power. So, to maximize Raman signal, the laser should be tuned to its highest output power. At the same time, if the laser intensity is too high, it can heat and potentially damage the signal. It's hard to have a specific recommended power for Raman, because different lasers have different absorption rates for any specific substance; additionally, most of the lasers for Raman have an output power in the range of 10 mW to 1 W. Finally, it's important to emphasize that what causes damage is the power surface density, so even a 10mW laser if focused on a very small area ($\sim\mu m^2$) can cause damage.

2.1.5 Selection Rules

There are many selection rules in quantum physics and particle physics. Selection rules are the rules imposed on the system to respect some sort of symmetry in the system. Selection rules in Raman spectroscopy refer to the rules that prevent some types of vibrations during a Raman spectroscopy measurement. A vibration is called Raman active if the vibration is allowed to happen by Raman selection rules. Usually, if a vibration is Raman inactive it is IR active. Therefore, a combination of Raman and IR spectroscopy is required to get a complete picture of all vibrational modes of a certain molecule.

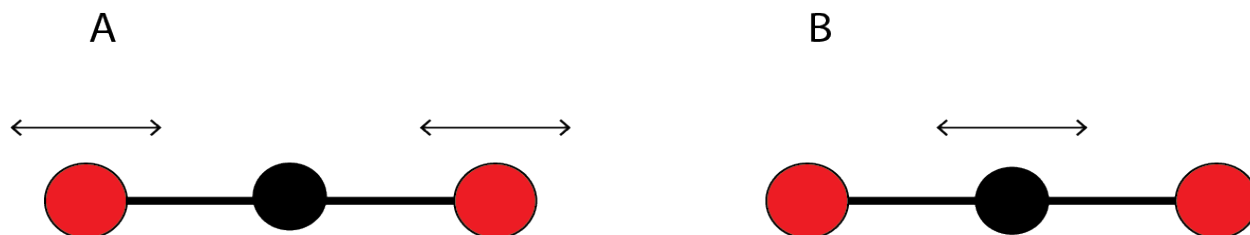


Figure 2-3. Two of the vibrational modes of CO₂. (A) represents a symmetric mode while (B) represents an anti-symmetric vibrational mode.

In the following, a simple classical description of selection rules in Raman Spectroscopy will be presented³⁷. In **Figure 2-3** two vibrational modes of a carbon dioxide (CO₂) are shown. In **Figure 2-3A** the carbon is stationary, and oxygens are moving symmetrically. In **Figure 2-3B** the oxygens are stationary, and the carbon is vibrating which indicates an asymmetry mode. From **Equation 2-6** a non-zero Raman signal in a system exists if $(\partial_X \alpha)|_{X_0} \neq 0$. So, if the derivative of polarity is non-zero in a vibration, that vibration is Raman active. Contrarily, **Figure 2-3B** has a zero $(\partial_X \alpha)|_{X_0}$ which represents a Raman inactive mode. To have an IR active mode, the dipole

derivative at the equilibrium distance should be nonzero so **Figure 2-3B** is IR active **Figure 2-3A** is IR inactive.

A vibrational mode is Raman active if the polarizability of the molecule changes during the vibration.³⁸

While the example given in the **Figure 2-3** is admittedly a simple linear example, for more complicated molecules the process of finding Raman and IR active modes can be a bit lengthier, but it still follows the same logic. For a molecule with the most general geometry, one should find the character table by analyzing the symmetry operations. By having all the symmetric elements, the point group of the molecule is known. The character table of each point group will give as all the information about the Raman and IR activity. In the table if the symmetry label of a normal mode is represented by a product term such as x^2 or yz , the vibration is Raman active. How to make a character table is beyond our discussion, but as an example, the character table of NH_3 is $3C_v$ given below in **Table 2-1**. Any irreducible representation that has basis function consist of A_1 an E has a Raman active vibration. So, in the case of ammonia, all the vibrational modes are Raman active.

Table 2-1. The Character table for point group T_d . E and C_n and S_n are symmetry elements.

C_{3v}	E	$2C_3$	$3\sigma_v$	Quadratic functions
A_1	1	1	1	x^2+y^2, z^2
A_2	1	1	-1	-
E	2	-1	0	$(x^2-y^2, xy) (xz, yz)$

2.1.6 Resonance Raman Scattering

In the “Non-classical description” section, resonance Raman Scattering mechanism was briefly described. But RRaman demands more explanation since it has been used extensively in this study.

The technical and instrumentation of the conventional and resonance Raman spectroscopy is generally the same, and the main distinction is the wavelength of the coherent light source aka the laser wavelength(see **Figure 2-2**). Electronic excitation energy levels are central to resonance

Raman spectroscopy. Electronic energy levels represent the energy of an electron in different orbitals.

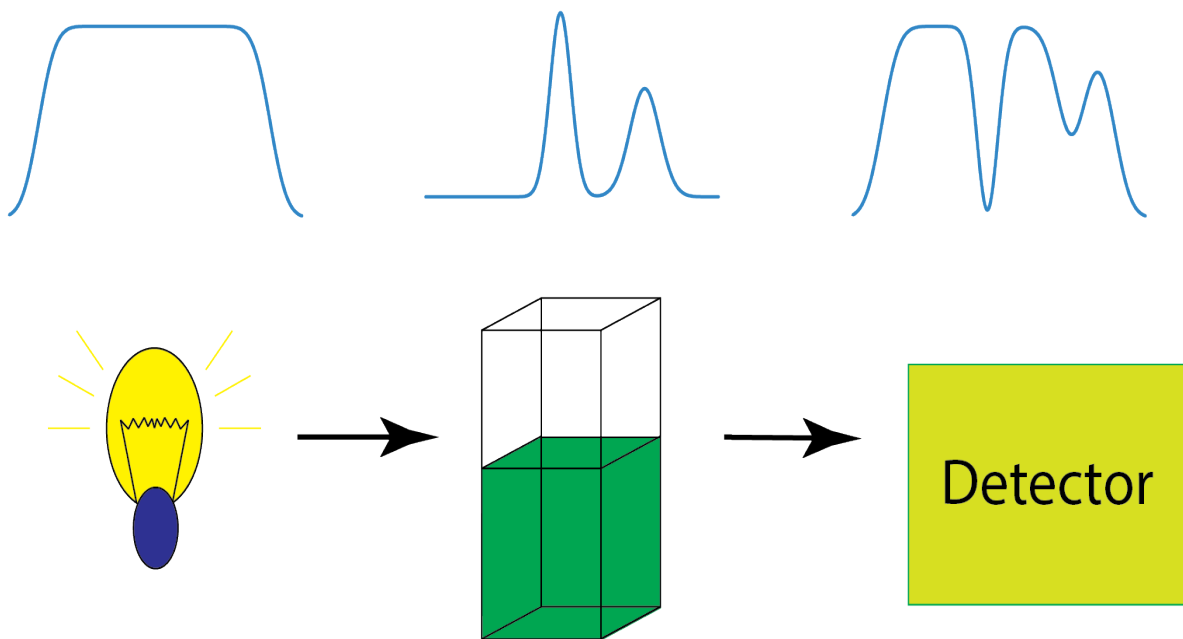


Figure 2-4. Schematic explanation of absorption spectroscopy. The top left is the spectrum of white light. The middle top curve is the absorption spectrum which is calculated from the subtraction of the top right spectrum (the portion of the light that went through the sample) and the white light spectrum

The energy difference between the Highest Occupied Molecular Orbital (HOMO) and Lowest Unoccupied Molecular Orbital (LUMO) is essentially responsible for the color of a substance. When white light (light with broad spectrum in the visible spectrum and may include ultraviolet, near infra-red etc.) illuminates a molecule, only the portion of the light will transmit through the molecule that doesn't correspond to an electronic transition. The energy between HOMO and LUMO is not always the only electronic transition; there could be several electronic transitions in the spectrum of white light. Usually, the absorption spectroscopy is used to find these electronic transitions. A spectrum of white light typically from 200nm to 900nm (different instruments have different ranges for their source) will compare the incident and transmitted spectrum to find which wavelengths were absorbed. **Figure 2-4** shows this process schematically.

After obtaining the absorption spectrum, which usually is called UV-Vis spectrum, one can tune the laser wavelength (or select a laser with a wavelength close to it) to the wavelength correspondence to an absorption peak. Each peak in absorption spectrum (to be more accurate a peak could be the convolution of several transitions) corresponds to an electronic transition and represents a different excitation and a whole new set of vibrational modes. One of the advantages of RRaman spectroscopy is the focus on a specific set of vibrations. In the case of non-resonant Raman, all vibrations will be present in the spectrum, but when tuned to a specific electronic transition, the vibrational modes correspond to that electronic transition will enhance. Depending on the intensity of absorption and vibrational mode that are being investigated and on how close the laser wavelength to the absorption peak is, the enhancement could be up to 10^6 times stronger than non-resonant Raman. This enhancement factor comes to play when a solution is being investigated and the concentration of the molecule that RRaman is intended for is less than millimolar. In non-resonance Raman, typically, the lowest concentration is in the 10^{-2} M range. In contrast, the concentration in resonance Raman can go down to 10^{-8} M. One should keep in mind Raman scattering is a very weak scattering, and only one out of every million incident photons will scatter as Raman signal.

Because in resonance Raman only some vibrational modes are enhanced, a resonance Raman spectrum has fewer bands than non-resonance Raman. This feature is especially important when big molecules with tens of atoms are investigated. The following is the formula to calculate the number of vibrational modes

$$\text{number of vibrational modes} = 3N - 6 \qquad \text{Equation 2-14}$$

This equation works only for nonlinear molecules; for linear molecules **Equation 2-14** will be modified to: *number of vibrational modes* = $3N - 5$. Here, N is the number of atoms. Thus, inorganic complexes or proteins that contain tens to hundreds of atoms, have hundreds to thousands of vibrational modes and very complicated Raman spectra which are almost impossible to interpret. By using resonance Raman and focusing on a specific electronic transition, one can enhance only a handful of relevant vibrations.

2.1.7 Fluorescence

With all the advantages that was mentioned above for RRaman, there are some disadvantages as well. One of the major problems with RRaman is fluorescence, **Figure 2-2 C**. Tuning the laser wavelength or selecting a laser with a wavelength close to the electronic transition energy gap could have the risk of electron relaxation between the vibrational states of the electronic state. Since the vibrational states are very close together, as compared to electronic states, the relaxation of the electron to its ground state will include several lines that obscure any resonance data. There are a few ways to fight fluorescence; the easiest way is to change the wavelength. For example, one of the complexes that was studied was $[\text{Ru}(\text{bpy})_3]^{2+}$. It has significant fluorescence effect with the 532 nm excitation wavelength but no fluorescence at the 442 nm excitation wavelength. This change in wavelength excitation is not always possible due to instrumentation and it will reduce the resonant enhancement if the new wavelength is not very close to the electronic transition energy. Another way of suppressing the fluorescence effect is to use anti-stokes, since the anti-stoke photons are more energetic than the exciting laser and fluorescence photons are always less energetic than the laser. The disadvantage of anti-stokes lines is the intensity of the signal. **Equation 2-15** shows the ratio of stokes lines to anti-stokes

$$\frac{\text{Anti-Stokes}}{\text{Stokes}} = e^{-\frac{\hbar\omega}{K_B T}} \quad \text{Equation 2-15}$$

Here $\hbar\omega$ is the energy gap between two consecutive vibrational states in the ground state. K_B is the Boltzmann's constant and T is the temperature. As we see in cryogenic temperatures, which are often used in samples with short lifetimes, the anti-stokes intensity will be significantly lower than stoke lines. The third way to reject the fluorescence effect in Raman spectroscopy is shifted excitation difference³⁹; in this way two Raman spectra with very close excitation wavelength (for example 532 and 533 nm) will be measured and later the two spectra will be subtracted from each other, the florescence effect which is almost independent from this small change in laser wavelength will cancel each other, but Raman signals will shift accordingly and do not cancel each other. There are other ways to suppress the fluorescence that you can find in the reference section^{40, 41}.

2.1.8 Raman experiment

In this section, I briefly review the instruments of the Raman setup. Because this setup has been extensively used in the next few chapters. **Figure 1-2** shows the setup that I collected my data schematically. In this figure there are three laser sources: one tunable, pulsed laser and two continuous wavelength (CW) lasers. The Optical Parametric Oscillators (OPT) are pumped with an Nd:YAG Q-switch nanosecond pulse laser with average power 6W and repetition of 10 Hz. Each pulse has 5 ns duration. The laser has its first and second harmonic generators (532 and 355 nm). The pump is not shown in the figure. OPO has the ability to provide the monochromatic light, from 190nm to 2.1 μ m. OPO has internal structure similar to a laser. It has a resonator and crystals with non-linear optical effects. The optical gain in OPO is based on parametric amplification, not stimulated emission. There are two output apertures on the OPO, one for emission from 190 nm to 400 nm and the other is from 400 nm to 2.1 μ m. The average output power of the OPO is dependent on the wavelength, but it won't exceed 200 mW. Although the average power is not very intense, it is a pulse laser, and the peak power can go up to megawatt. The positive side of having OPO is that it is a tunable laser source, and it makes it perfect for resonance Raman. The other advantage of having a pulse laser is that it can drive a photoinduced reaction, like those observed photosystem II. The downside of OPO is the peak power of the laser; for some complexes that power is higher than the damage threshold. Prisms were used for reflection purposes because the peak power is strong enough to damage a mirror. There are several flip mounts to use several lasers with very little modification to the setup. Nd:YAG CW laser emits 532nm (first harmonic generator), and its power can be as high as 3W. However, for the measurement, the power is usually kept below 0.5 W. HeCd laser is the other CW laser source with the wavelength of 442 nm. A band pass clean filter is used to clean the laser from some extra emission lines from the laser.

Spectral resolution of Raman spectra depends on many factors, including the slit size for input light, the number of lines per length in the grating, the pixel size in the camera, and the focal length of the light in the spectrometer. By increasing the groove density in the grating, the resolution would be higher because the light disperses with a bigger angle. This effect is linear, so the resolution of 1200 *line/mm* is twice bigger than the resolution of 600 *line/mm*. The groove density cannot be an arbitrary number. For example, for UV the groove density can be as high as 2400 *line/mm*, but the same grating would not work for NIR. The other factor which has an effect

is the focal length of the light in the spectrometer. If the focal length becomes twice bigger the resolution is twice better. But to increase this distance the spectrometer should physically become bigger.

Two lenses are used to collect signal from a point source. The lens shown at the right side of **Figure 2-5** is focused on the sample. This lens has 10 cm focal length and the lens on the left has a 20 cm focal length. The diameter of the lenses is 5.08 cm. Right before light gets into the spectrometer, there are multiple edge pass filters mounted on a wheel to filter the laser line (Rayleigh scattering). After this point, the light gets into spectrometer to be dispersed.

Figure 2-6 shows the architecture of a spectrometer. The white light first gets into the spectrometer. The first mirror will collimate the light, and then the grating disperses the light; the second mirror shines the light on the CCD to be recorded. There are two inputs for light, but only one is required for our experiments. There are also two options for the location of the camera.

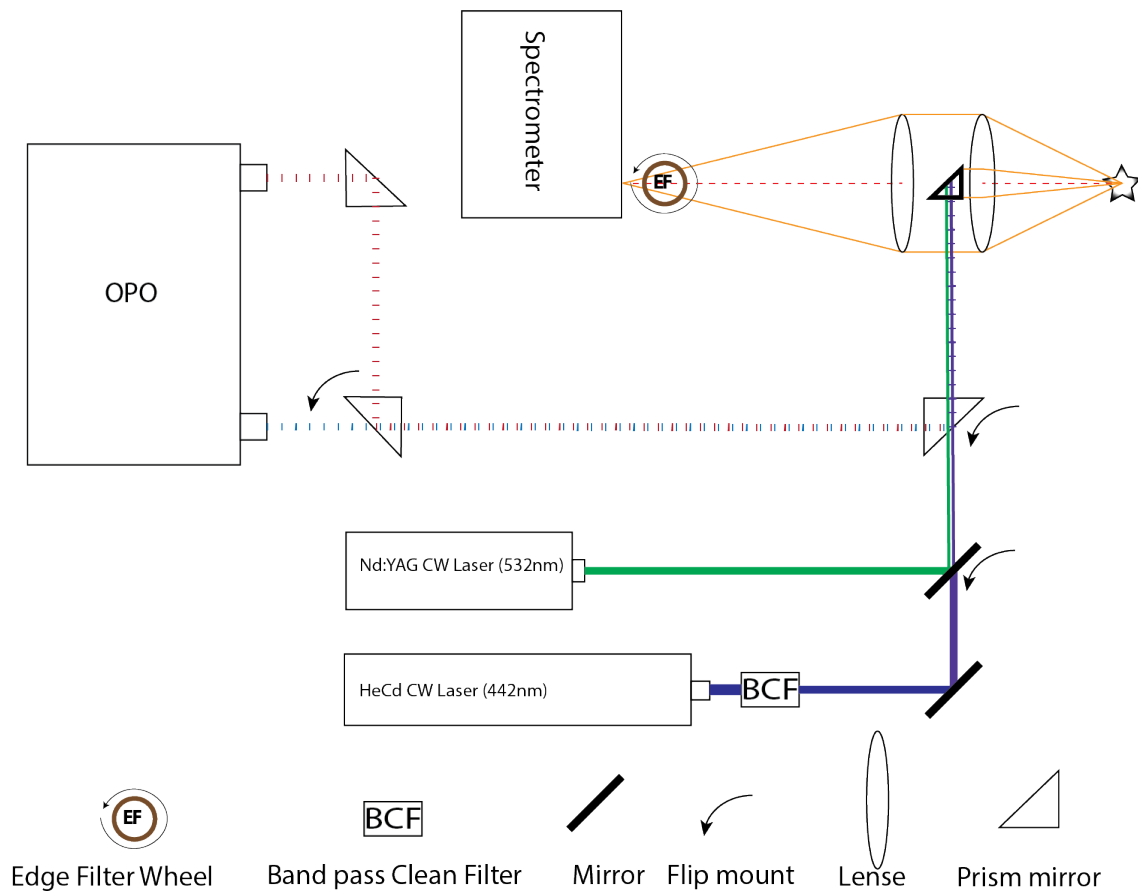


Figure 2-5. Setup of Raman spectrometer and its laser sources.

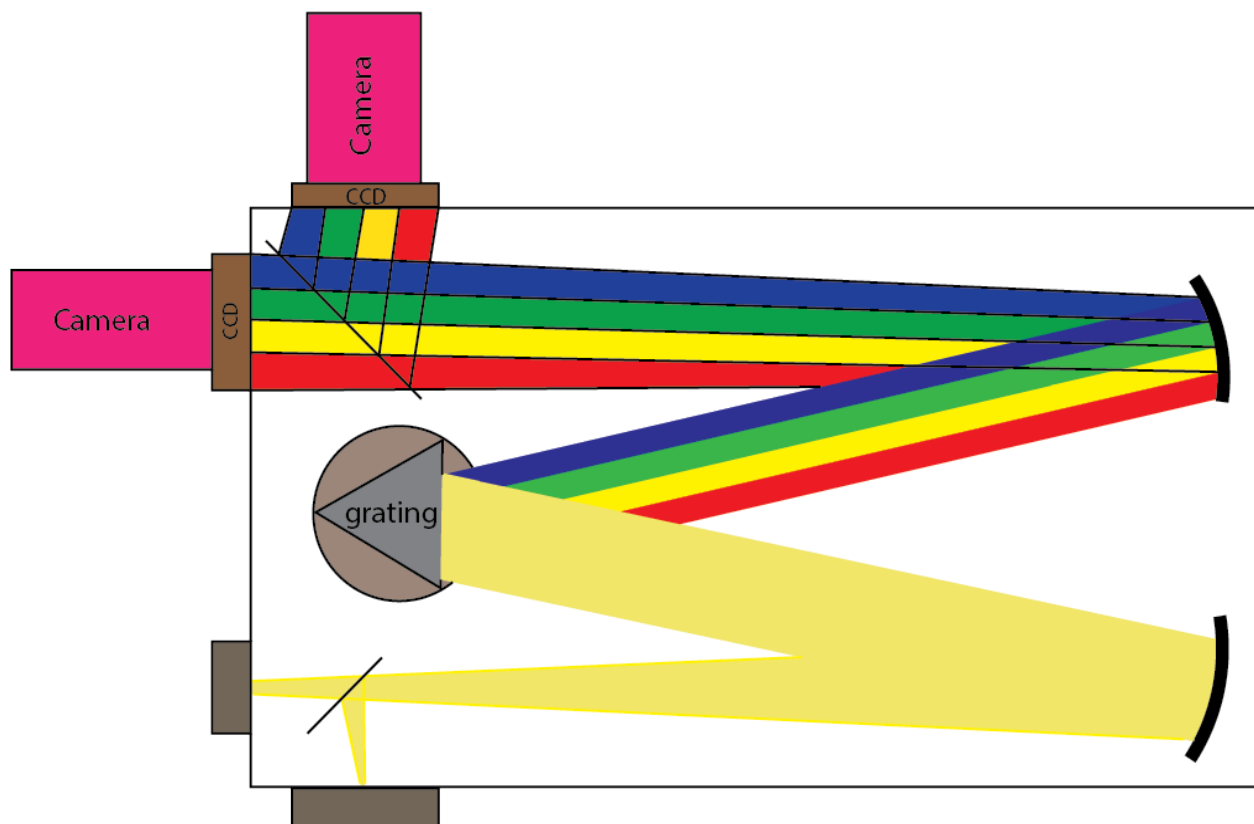


Figure 2-6. internal structure of the spectrometer that is used in the setup of this report.

2.2 An introduction to Electron Paramagnetic Resonance (EPR) spectroscopy

2.2.1 Why EPR

In this chapter, a quick review of the theory of EPR is presented. Also, I will establish the need for this technique in my research. EPR investigates paramagnetic materials by measuring the interaction of external magnetic field and the spin of unpaired electrons. EPR helps to determine the electronic structure. Later in the next section, we show that by going from higher symmetry (6-coordinate) to lower symmetry (7-coordinate) the g-factors change. The g-factors of a specific catalyst can reveal the oxidation state and the spin state. Computational calculations, on the other hand, will predict and test the models that are proposed and analyzed by EPR. For example, if a model doesn't need to have Ru^{V} , we can verify that such species isn't present, or is short lived and impossible to trap and measure by EPR.

2.2.2 Theory of EPR

Just like any other type of spectroscopy, EPR spectroscopy is about the interaction of matter and electromagnetic radiation. The electromagnetic radiation which is used in EPR is in the microwave range. In EPR spin of an electron interacts with external magnetic field. Since EPR is mostly used with samples that have an unpaired electron, it has some restrictions. For example, Ru^{II} in [Ru(tpy)(bpy)]²⁺ is EPR silent since there is no unpaired electron. However, by extracting one electron and forming Ru^{III}, the complex now has an EPR signal. The same goes for Ru^{IV}, Ru^V, and Ru^{VI}, which are EPR silent, active, and silent respectively (this argument is oversimplified because even Ru^{IV} can go to a triplet state and become EPR active).

In a nutshell, EPR measures the energy gap between two spin states of a paramagnetic material in presence of an external magnetic field. To explain this phenomenon, one can imagine a single electron which doesn't have a spin-spin interaction with another electron. If there is no external magnetic field, the spin can be either up or down direction, and there is no difference between the energy of these two orientations. In other words these two states are degenerate, **Figure 2-7**. However, as soon as an external magnetic field is applied, the spin of the electron generates two different energy levels corresponding to either a parallel or antiparallel spin, relative to the magnetic field. The change in the energy level of the system due to this interaction can be expressed as ⁴²

$$E = \pm \frac{1}{2} g_e \beta B_0 \quad \text{Equation 2-16}$$

Where g_e is spectroscopic g-factor of free electron, β is Bohr magneton, and B_0 is the external magnetic field. The interaction of an electron and an external magnetic field is called the Zeeman effect.

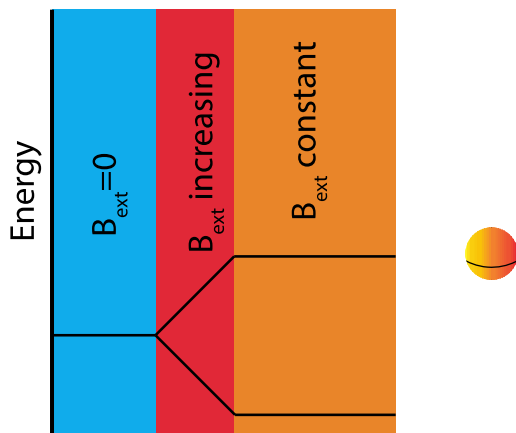


Figure 2-7. Energy splitting of an electron in the presence of an external magnetic field.

The energy gap between spin up and down states can be simply written as

$$\Delta E = g_e \beta B_0 \quad \text{Equation 2-17}$$

Naturally, the electron will transition to its lowest potential energy state but can be excited to upper state, when sufficient energy (**Equation 2-17**) is provided to cause a spin flip. This energy can be delivered by a photon with energy of

$$E = h \nu \quad \text{Equation 2-18}$$

The transition will occur if **Equation 2-17** and **Equation 2-18** are equal. In a more general case, if the electron is not free and bound to an atom or molecule, one can replace g_e with g

$$h \nu = g \beta B_0 \quad \text{Equation 2-19}$$

g is specific for each molecule and can be used as a fingerprint for that specific molecule. For any molecule with an unpaired electron, one can fix the magnetic field and vary the frequency of electromagnetic radiation or vice versa. Practically, the microwave radiation is usually kept constant and the magnetic field varies because the waveguide in the EPR instrument won't allow the change in microwave wavelength.

2.2.3 EPR spectrum

As was mentioned above, whenever the energy of the electromagnetic wave matches the energy gap between the two spin states in the presence of an external magnetic field, an absorption peak will appear. What is referred as the EPR spectrum is usually the derivative of the absorption, not the absorption itself (**Figure 2-8**). **Figure 2-8 A** can be the spectrum of a free electron or an orbital which has spherical symmetry; this is called an “isotropic” orbital, since the absorption is independent from the direction of the external magnetic field. In general, these types of orbitals are called “orient independent”. Orbitals are 3-D geometries and they have three axis such as X, Y, and Z, or the principle axes; in this example, the absorption along each axis is the same, and hence, $g_{xx} = g_{yy} = g_{zz}$. In **Figure 2-8 B**, the orbital is “orient dependent” and absorption is more spread in the Z direction but is invariant under X-Y rotation. Thus, giving $g_{xx} = g_{yy} \neq g_{zz}$. This type of orbital is called an “axial” orbital. Finally, in the most general geometry which doesn't have the same symmetries as in two mentioned cases (**Figure 2-8C**), the absorption is different along each principle axis such that $g_{xx} \neq g_{yy} \neq g_{zz}$. This last class of orbitals are called “rhombic”.

The EPR measurement of an anisotropic orbital in a solution with low viscosity will average out the anisotropy; on the other hand, for a crystal with paramagnetic molecules in the same orientation, the anisotropy would not be averaged out.

Since the g factor is measured along principal axis, the final measurement will give us three g factors: g_{xx} , g_{yy} , and g_{zz} (**Figure 2-8**). If the sample is frozen, then the issue of low viscosity is not the problem since molecules are not allowed to rotate freely. This is also different from a crystal, since in a crystal one need to rotate the crystal to see the orientation of the molecules in a specific direction but in a frozen solution of sample all orientations are randomly frozen. The EPR spectrum of a frozen sample colloquially known as the “powder spectrum” since it depicts the summation of all orientation which is effectively the same as a fine powder of a crystal.

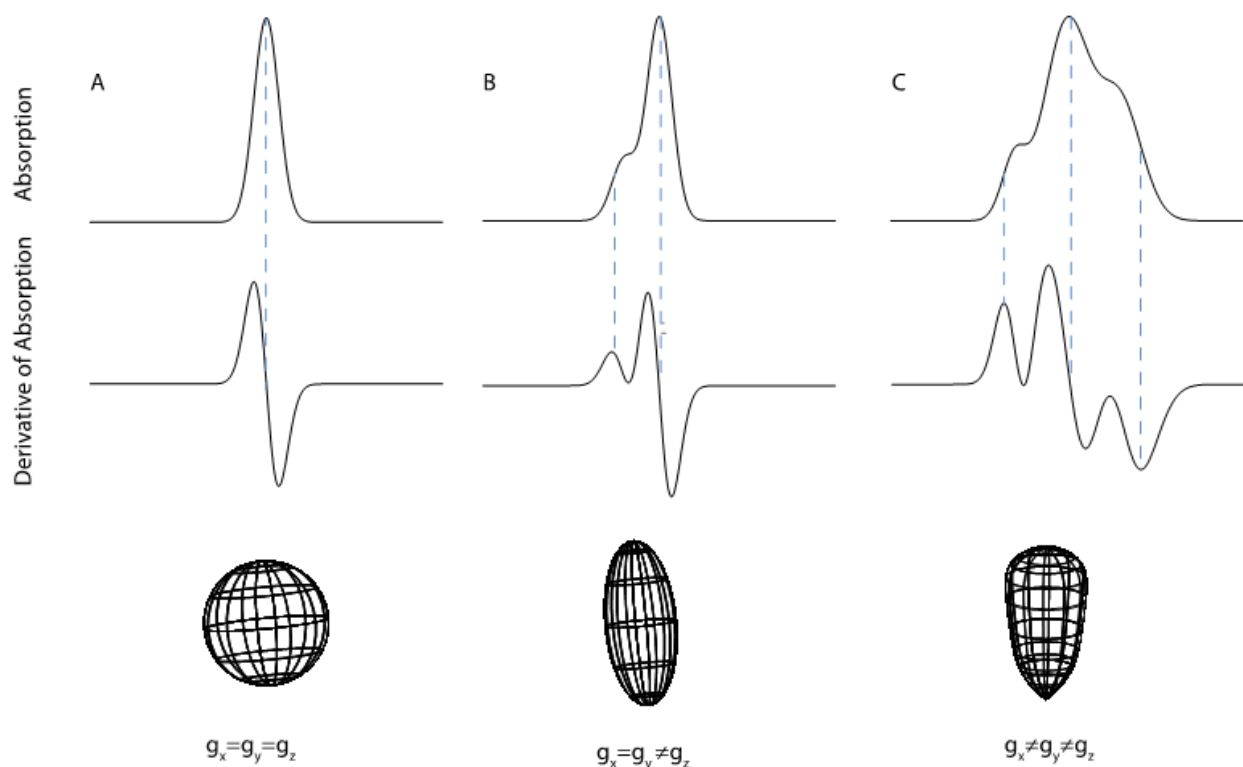


Figure 2-8. Different orbitals with different shape and orientation and their correspondence absorption and derivative of the absorption.

2.2.4 More on the g-factor with an example

In this section, we see how the g-factors can help us have a better understanding of the geometry of a molecule with an example. Daniel et al.⁴³ report a full description of a $[\text{Ru}(\text{bda})\text{L}_2]^{2+}$ catalyst (check the reference for more details on the type of the ligands and the geometry). This catalyst is initially in Ru^{II} 6-coordinate, but by addition of an excessive amount of sacrificial oxidant, it can form different states, such as a Ru^{III} 6-coordinate, Ru^{V} 6-coordinate, Ru^{III} 7-coordinate, and Ru^{V} 7-coordinate (oxidation states are listed in the same order that they form). All Ru^{III} and Ru^{V} states, regardless of their geometry, are EPR active since they all are paramagnetic. This complex will go undergo several proton-coupled electron transfer (PCET) steps to get to Ru^{V} . Other oxidation states of Ru, such as Ru^{II} and Ru^{IV} complexes, are present in the mixture, but as it was said they are EPR silent. The g tensor for Ru^{III} compound was reported $g_x=2.341$; $g_y=2.187$; $g_z=1.853$, which is in agreement with similar Ru^{III} 6-coordinates with pseudo-octahedral geometry. The other complex (Ru^{III} 7-coordinate) shows a g-tensor with values $g_x=2.58$; $g_y=2.30$; $g_z=1.675$.

By reducing the symmetry from octahedral to pentagonal bipyramidal, the splitting for orbitals increases, and the energy difference between orbitals reduces (less degeneracy); that usually leads to larger g-anisotropy ($\Delta g = g_x - g_y$). In other words, lower symmetries have wider range for in their g-tensor and vice versa, and that is what we see in the g-tensor values above.

2.2.5 Hyperfine interaction.

Conventional EPR relies on an external magnetic field and some unpaired electrons. Hyperfine interactions, on the other hand, is the interaction of an unpaired electrons and another nucleus in its singlet, triple, etc. state.

There are three types of interaction for an unpaired electron that are used in EPR. The first one is the interaction between an unpaired electron and a nucleus which is called the “hyperfine” interaction. The second type is the interaction between the wavefunction of an unpaired electron and a nucleus from a neighbor molecule, which is called “super hyperfine”. There is a third type and is the interaction between an unpaired electron and another unpaired electron from another atom, and it is called “spin-spin” interaction. The focus would be on hyperfine among the aforementioned types.

To formulate the hyperfine effect, the Hamiltonian should be modified and considering the hyperfine effect, the formula (19) will be modified to the following

$$h\nu = g\beta B_0 + hAm_I s \quad \text{Equation 2-20}$$

where A is the hyperfine coupling constant, m_I is magnetic quantum number of nucleus, and s is the spin. The magnetic quantum number of nucleus can take on values of $m_I = I, I - 1, \dots, 0, \dots, -I + 1, -I$, with $2I + 1$ being the total possible values for m_I . For example, for $I = 1/2$ there are two possible values for the magnetic quantum number which will split the absorption into twice as many lines, **Figure 2-9**. We looked at an isotope of oxygen with 17 atomic mass unit (^{17}O) to observe the super hyperfine effect (unpublished data). The spin state of ^{17}O is $= 5/2$, and $2(5/2) + 1 = 6$ would result in six distinct levels from each of the conventional absorption lines.

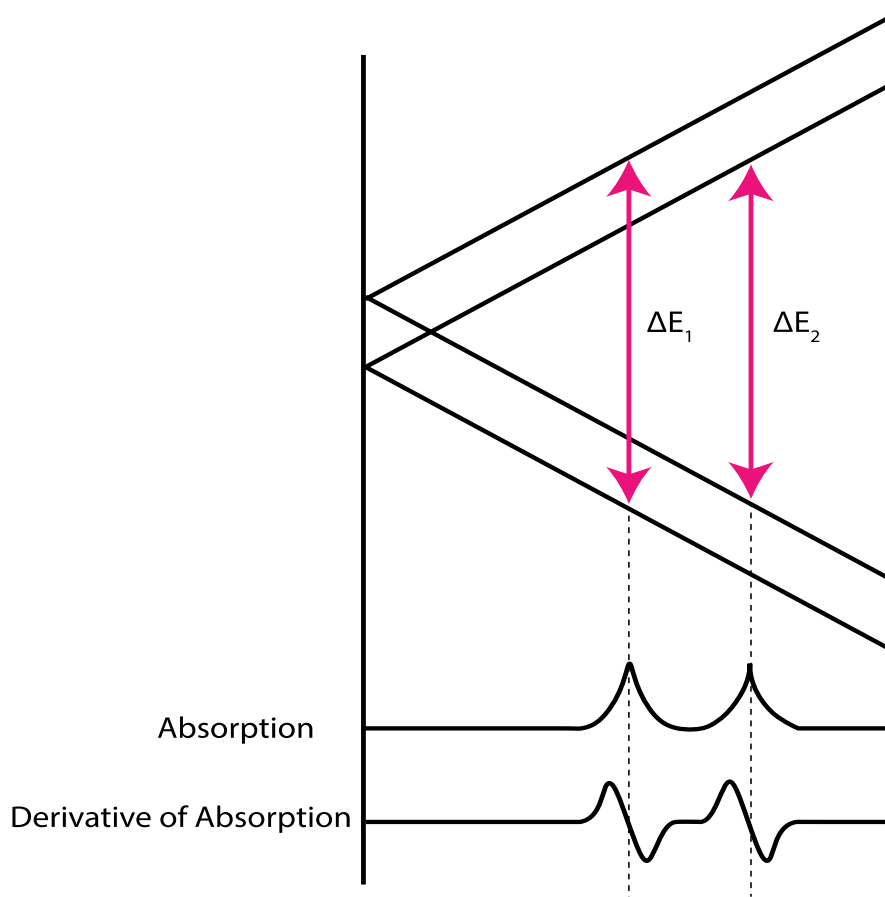


Figure 2-9. hyperfine effect cause splitting in the absorption spectrum.

2.2.6 Instrumentation.

In EPR measurements, several factors should be monitored, such as saturation, Q-factor, strength of signal, etc. The user should be familiar with these concepts and instrumentation in order to control and modify the system to get the optimum signal.

Saturation: After excreting the external magnetic field, electrons naturally go to the spin state with lower energy. A soon as the energy difference between states matches the energy that is provided by the microwave, the electron will move to spin state with higher energy. Saturation occurs when not enough electrons are in the lower energy state. This causes broadening in the EPR spectrum. This phenomenon depends on the time scale that electrons go back to the lower energy, which is called relaxation time. The relaxation time for transition metals is typically short

compared to free radicals. Depending on the temperature, the relaxation time for transition metals can be in the microsecond regime, while for radicals can be from millisecond to second. To prevent saturation, one can tune the radiation power for the best results. Lowering the power will reduce the effect of saturation, but at the same time reducing microwave power leads to a loss in signal, so one should run several measurements with different power to get to the optimum situation

Q-factor: Each cavity would have some energy losses, and the more the energy loss, the lower the Q-factor. The general definition of Q-factor is the ratio of stored energy to the dissipated energy in the cavity ($Q = \nu / \Delta\nu$ where ν being the frequency). Q-factor is especially important because it is related to sensitivity. Every time that the machine tunes itself, the resonance frequency will be displayed on the screen. The sharper the frequency (from the baseline) the higher the Q-factor; the best coupling is so-called critically coupled frequency with the cavity. In contrast, over-coupled and under-coupled are not good for highest sensitivity.

Signal: The signal is directly proportional to the Q-factor and another constant which is called the filling factor (usually showed in the literature with η). Filling factor is the ratio of the volume of the sample to the cavity.

Resolution: the shortest distance between two peaks that could be resolved without distortion is dependent on several factors such as the modulation amplitude, which modulates the external magnetic field (can go up to 40 G but in the instrument that I access, the highest value is 25 G, with typical modulation frequency of 100kHz), Q-factor, filling factor, and square root of the power. The resolution comes into play especially when someone wants to study the hyperfine effect, and the features in the spectrum are very close to each other.

All EPR measurements were taken using a “Bruker EMX EPR” spectrometer. This machine radiates in the X band which has the center frequency of 9.5 GHz and resonates with magnetic field of $B_{\text{res}} = 3389$ G for a g-factor of 2. Other bands that exist but can't be reached by this machine are L (1.1 GHz), S (3.0GHz), Q (35GHz), W (90 GHz), and J (270 GHz). This machine can work in a wide range of temperatures, varying from 5 to 300 K. For the cooling mechanism, liquid helium in a closed loop.

2.3 Computational calculations

2.3.1 Why Computational calculations

All the spectroscopic techniques that were mentioned and explained can be categorized in one of two classes: Measurements on samples with known spectroscopic signatures; in this case, the measurements are to confirm a known state or geometry. Second, are measurements on new chemical complexes with no prior knowledge on the spectroscopic signatures. One solution to this problem is to solve analytically the quantum mechanical equations – Schrodinger’s equation – for the system, find the wave function and compare the experimental data with the analytical data; however, for very simple systems, such as hydrogen atom, the exact analytical solution is impossible to calculate. The alternative to this method is computational chemistry calculations which are methods that approximately calculate the wave function by providing a numerical solution to the Hamiltonian of the system. There are multiple methods such as *Ab initio* methods, semi-empirical methods, molecular dynamics methods, density functional theories, etc. In this study, our main tool to calculate the wavefunction, geometry, energy, vibrational modes, spin density, etc. was DFT, so a brief description of DFT and its features are presented below.

2.3.2 DFT

Kohm-Sham DFT was introduced in the 60’s by Walter Kohn and Pierre Hohenberg⁴⁴ and a year later followed by another paper by Lu Jeu Sham and Walter Kohn⁴⁵. Amongst different methods, DFT is one the most successful methods to compute the electronic structure of a system because of the balnce between the accuracy and computational cost. This system can be anything from isolated atoms and molecules to solids and nuclei and even fluids. One of the advantages of DFT is the large number of the properties that it can calculate. Geometry optimization, vibrational frequencies, energies, magnetic properties, electric properties, reaction paths can be calculated.

The system’s Hamiltonian and Schrodinger’s equation for a system of atoms can be written as described in **Equation 2-21**

$$\hat{H}\Psi = [\hat{T} + \hat{V}]\Psi = \left[-\sum_{i=1}^N \frac{1}{2} \nabla_i^2 - \sum_{i=1}^N \sum_{A=1}^M \frac{Z_A}{r_{iA}} + \sum_{i=1}^N \sum_{j>i}^N \frac{1}{r_{ij}} \right] \Psi = E_{elec} \Psi$$

Equation 2-21

Here, the first term in the square bracket is the kinetic energy of the electrons, the second term is the columbic potential energy between the nuclei and the electrons, and the last term is the potential energy between electrons. This equation is simplified because some terms like the kinetic and potential energy of the nuclei are ignored because of a reasonable assumption which states the nuclei move much slower than electrons due to the mass difference, so the kinetic energy of the nuclei is effectively zero and the potential energy of the nuclei is constant. This approximation is called Born-Oppenheimer approximation. Note that the energy is only the electronic energy. This Hamiltonian is non-relativistic and does not account for electronic or nuclei spins and interactions between them. We stick to electronic Hamiltonian for the rest of the discussion for the sake of simplicity.

To find the energy of the system when the system is in the state Ψ **Equation 2-22** can be used

$$E[\Psi] = \frac{\langle \Psi | \hat{H} | \Psi \rangle}{\langle \Psi | \Psi \rangle} = \frac{\int \Psi^* \hat{H} \Psi d\vec{r}}{\int \Psi^* \Psi d\vec{r}} \quad \text{Equation 2-22}$$

Any guessed wave function plugged in this equation provides an upper limit to the real ground state, according to variational principle.

The Slater determinant consists of N (the number of electrons in the system) spin orbitals (contains both the spatial and spin function) $\psi_i(\vec{x})$; **Equation 2-23**

$$\Psi \approx \frac{1}{\sqrt{N!}} \begin{vmatrix} \psi_1(\vec{x}_1) & \psi_2(\vec{x}_1) & \dots & \psi_N(\vec{x}_1) \\ \psi_1(\vec{x}_2) & \psi_2(\vec{x}_2) & \dots & \psi_N(\vec{x}_2) \\ \vdots & \vdots & \ddots & \vdots \\ \psi_1(\vec{x}_N) & \psi_2(\vec{x}_N) & \dots & \psi_N(\vec{x}_N) \end{vmatrix} \quad \text{Equation 2-23}$$

The Ψ in this equation is antisymmetric and a product of N orthonormal $\psi_i(\vec{r})$.

The Hartree-Fock (HF) is an approximate method and tries to find the $\psi_i(\vec{r})$ to minimize the energy of Ψ . The Hartree-Fock energy is written as **Equation 2-24**

$$E_{HF} = \sum_{i=1}^N H_i + \frac{1}{2} \sum_{i,j=1}^N (J_{ij} - K_{ij}) \quad \text{Equation 2-24}$$

Where H_i , J_{ij} , K_{ij} can be defined as **Equation 2-25**, **Equation 2-26**, **Equation 2-27** respectively.

$$H_i = \int \psi_i^*(\vec{r}) \left[-\frac{1}{2} \nabla_i^2 - \sum_{A=1}^N \sum_{a=1}^M \frac{Z_A}{r_{iA}} \right] \psi_i(\vec{r}) d\vec{r} \quad \text{Equation 2-25}$$

$$J_{ij} = \iint \psi_i(\vec{r}_1) \psi_i^*(\vec{r}_1) \frac{1}{r_{12}} \psi_j^*(\vec{r}_2) \psi_j(\vec{r}_2) d\vec{r}_1 d\vec{r}_2 \quad \text{Equation 2-26}$$

$$K_{ij} = \iint \psi_i(\vec{r}_1) \psi_j^*(\vec{r}_1) \frac{1}{r_{12}} \psi_i^*(\vec{r}_2) \psi_j(\vec{r}_2) d\vec{r}_1 d\vec{r}_2 \quad \text{Equation 2-27}$$

J_{ij} are referred to as coulomb integrals and K_{ij} the exchange integrals. Both of these two integrals are real and positive with $J_{ij} \geq K_{ij}$.

The Hartree-Fock energy of the system is an approximate energy, and the method which is used to calculate this energy is called Hartree-Fock. HF finds ψ_i that satisfy **Equation 2-23** and minimize **Equation 2-24**.

Fock operator which is a Hermitian operator can be defined as **Equation 2-28**

$$\hat{O} = -\frac{1}{2} \nabla_i^2 - \sum_A^M \frac{Z_A}{r_{iA}} + V_{HF}(i) \quad \text{Equation 2-28}$$

This is similar to **Equation 2-21**, but for only one electron. $V_{HF}(i) = \sum_j^{N/2} (2J_{ji} - K_{ji})$ is the HF potential and can be defined as the average repulsive potential of the $N - 1$ electron on the i - th electron. HF is a non-local potential with spin dependency.

The electron density to be fed into **Equation 2-28** can be described by **Equation 2-29**

$$\hat{\rho}(\vec{r}) = N \int \cdots \int |\psi(\vec{r}_1, \vec{r}_2, \dots, \vec{r}_N)|^2 ds_1 dr_2 \dots dr_N \quad \text{Equation 2-29}$$

In this equation the integral is over all the spin coordinates, as well as all spatial coordinates from all the electrons except one.

Electron density can be interpreted as the probability of finding any of the N electron in a differential element of volume. Consequently, the integral of $\hat{\rho}(\vec{r})$ over $d\vec{r}$ has to be N .

Kohn and Hohenberg showed that the ground state energy of a system is

$$E = E[\hat{\rho}(\vec{r})]$$

This energy is unique and square brackets represent the functional nature of the problems. The only problem remains is to find the density of electrons. The energy is unique and any $\hat{\rho}(\vec{r})$ that is different from the true density function of the system would give an energy above the unique energy of the system. So, to find the true electron density of the system, one can start with a guess. Using the guessed electron density, the energy of the system can be calculated and from the energy, the wavefunction can be calculated. The calculated wavefunction can result in a new electron density and that electron density is used to calculate the new energy and wavefunction. This loop continues until the electron density almost doesn't change any more. This is so-called self-consistency condition. To present a more intuitive picture of this scenario, one can look at the geometry of a system. **Figure 2-10A** shows the potential surface energy of a two-atom system. The self-consistency conditions would be used for different geometries and find the r with the optimum geometry. In **Figure 2-10B**, potential surface energy is a 2-D surface, but the logic is the same. In both cases **Equation 2-30** can describe where on potential surface energy an optimized geometry stands.

$$\left. \frac{\partial E}{\partial r} \right|_{r_0} = 0 \quad \text{and} \quad \left. \frac{\partial^2 E}{\partial r^2} \right|_{r_0} > 0 \quad \text{Equation 2-30}$$

Although we mentioned the energy of a satisfied self-consistency is unique, if the initial guess is far off, the geometry can converge to a local minimum and hence it's not a representation of the most stable form of the system, **Figure 2-10C**. The local minimum in **Figure 2-10C** is still unique, but it is not desired geometry that we expect.

Before concluding this section, it is worth mentioning the computational cost of solving the DFT equations. Solving an equation like **Equation 2-31** by computers could be challenging. First of all, the system scales by N^3 . This means a system with 2 electrons will converge 125000 times faster than a system with 100 electrons. In reality, the systems that researchers need to solve by DFT can have thousands of electrons, so it requires infrastructure such as supercomputers for efficient and pragmatic calculations. Second, the type of basis set plays a similar role in terms of calculation cost. A basis set is a set of functions that can describe the wavefunction of the system. Usually, a bigger basis set gives a better presentation of the system, but at the same time would impose a greater computational cost to the user. Some basis sets are minimal like STO-3G some are more comprehensive such as 6-311+G* which can add the polarization and diffusion of some orbitals to the solution. The convention of naming the basis sets can be easily found in any textbook.

I used Gaussian16 in my thesis.⁴⁶ In the next two chapters whenever DFT has been employed, the basis set and further methods has been explained.

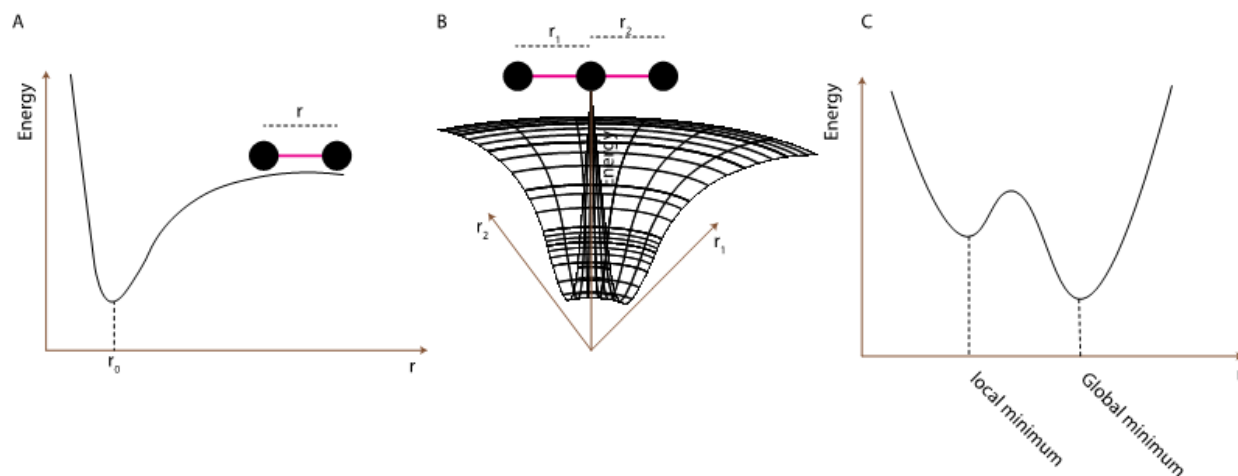


Figure 2-10. (A) the potential energy of a diatomic molecule. (B) the potential surface energy of two molecule bonds. (C) a local and global minimum for a potential surface energy

CHAPTER 3. UNRAVELING THE MECHANISM OF CATALYTIC WATER OXIDATION VIA DE NOVO SYNTHESIS OF REACTIVE INTERMEDIATE

This chapter is published in whole or part in the Journal of American Chemical Society with DOI: 10.1021/jacs.9b10265

3.1 Abstract

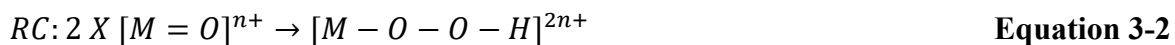
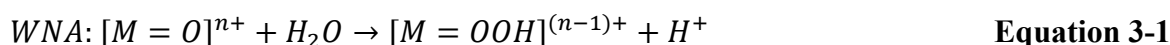
Artificial photosynthesis could promise abundant, carbon-neutral energy, but implementation is currently limited by a lack of control in multi-electron catalysis of water oxidation. Discoveries of the most active catalysts still rely heavily on serendipity. $[(\text{tpy})(\text{bpy})\text{Ru}(\text{H}_2\text{O})]^{2+}$ (**1**) (bpy = 2,2'-bipyridine, tpy = 2,2';6',2''-terpyridine) is representative of the largest known class of water oxidation catalysts. We undertook an extensive spectroscopic analysis of the prototypical (**1**) water oxidation catalyst and its fastest known analog $[(\text{EtO-tpy})(\text{bpy})\text{Ru}(\text{H}_2\text{O})]^{2+}$ (**2**), capable of ten times faster water oxidation, to investigate the mechanism of action and factors controlling catalytic activity. EPR and resonance Raman did not detect the proposed $[\text{Ru}^{\text{V}}=\text{O}]$ intermediate in (**1**) and (**2**) but indicated the possible formation of N-oxides. A lag phase was observed prior to O_2 evolution, suggesting catalyst modification before the onset of catalysis. The reactive intermediate $[\text{Ru}(\text{tpy})(\text{bpy-NO})(\text{H}_2\text{O})]^{2+}$ (**1-NO**) (bpy-NO = 2,2'-bipyridine-N-oxide) proposed by combined spectroscopic and DFT analysis was *de novo* synthesized and demonstrated hundredfold greater catalytic activity than (**1**). Thus, *in situ* transient formation of small amounts of the Ru complex with N-oxide ligands can significantly activate single site Ru-based catalysts. Furthermore, the rate of O_2 evolution was found to correlate with the redox potential of the ligand: an observation critical for rational design of new catalysts.

3.2 Introduction

The growing amount of greenhouse gases, especially CO_2 , in the atmosphere has been connected with climate change and higher incidence of severe weather events. Significant increase in generation of renewable, CO_2 neutral energy is required to satisfy growing energy demands world-wide.⁴⁷ The creation of a man-made device mimicking the light-induced water splitting which occurs during natural photosynthesis⁴⁸⁻⁵² would enable solar energy to fuel conversion

schemes.^{10, 53-55} Intermittent electricity from solar and wind can potentially be converted into fuels via water splitting, but such processes are currently expensive. Development of artificial photosynthesis as well as the optimization of modern electrolyzers hinges on the understanding water oxidation mechanisms in both the natural Oxygen Evolving Complex of Photosystem II^{48-51, 56, 57} and in man-made catalysts.^{58, 59}

O-O bond formation can proceed via two main mechanisms: water nucleophilic attack (WNA) **Equation 3-1** and radical coupling (RC) **Equation 3-2**.



Both mechanisms require formation of highly oxidized metal-oxo (M=O) species which are typically achieved from M-H₂O via proton coupled electron transfer (PCET). Molecular catalysts of water oxidation provide a convenient system for detailed mechanistic analysis.⁶⁰ While such catalysts have been reported for multiple metal ions, Ru-based complexes remain the most stable and the most studied.^{10, 12, 53-55, 61, 62} Mechanistic analysis with spectroscopic identification of reactive intermediates is available for the first discovered molecular water oxidation catalyst - Blue Dimer (BD)⁶³, where the formation of the [Ru^{IV},Ru^V=O] intermediate was confirmed by X-ray spectroscopy and Electron Paramagnetic Resonance (EPR), **Figure 3-1A**.^{2, 64} [Ru^{IV},Ru^V=O] is expected to react with water via WNA. However, resulting peroxo intermediates have not been yet unambiguously identified.⁶⁵ [(bpy)₂Ru^V=O(OH)]²⁺ was identified by EPR and can react via both WNA and RC.^{66, 67} Its high activity, however, subsides to quick de-activation via dimer formation.⁶⁷

Introduction of negatively charged bda (H₂bda=2,2'-bipyridine-6,6'-dicarboxylic acid) ligand resulted in family of fast Ru^{II}(L)₂(bda) catalysts, **Figure 3-1B**.^{68, 69} These react quickly in solution via RC as evident by rate of O₂ evolution that is second order on catalyst. Immobilization of the Ru^{II}(L)₂(bda) complex on the electrode surface allowed first spectroscopic characterization of the key 7-coordinate [Ru^V=O(L)₂(bda)]⁺ intermediate.⁶¹ bda family of catalysts currently demonstrate highest rate of water oxidation in acidic solutions. However, surface immobilization significantly lowers the catalytic rate as it disrupts RC pathway. Neutral polypyridine ligands can

also support formation of 7-coordinate $[\text{Ru}^{\text{V}}=\text{O}(\text{L})_2(\text{dpp})]^{3+}$ intermediate under oxidizing conditions, **Figure 3-1C**. Increased lifetime of this species was attributed to the protective effect of ligand environment.⁷⁰

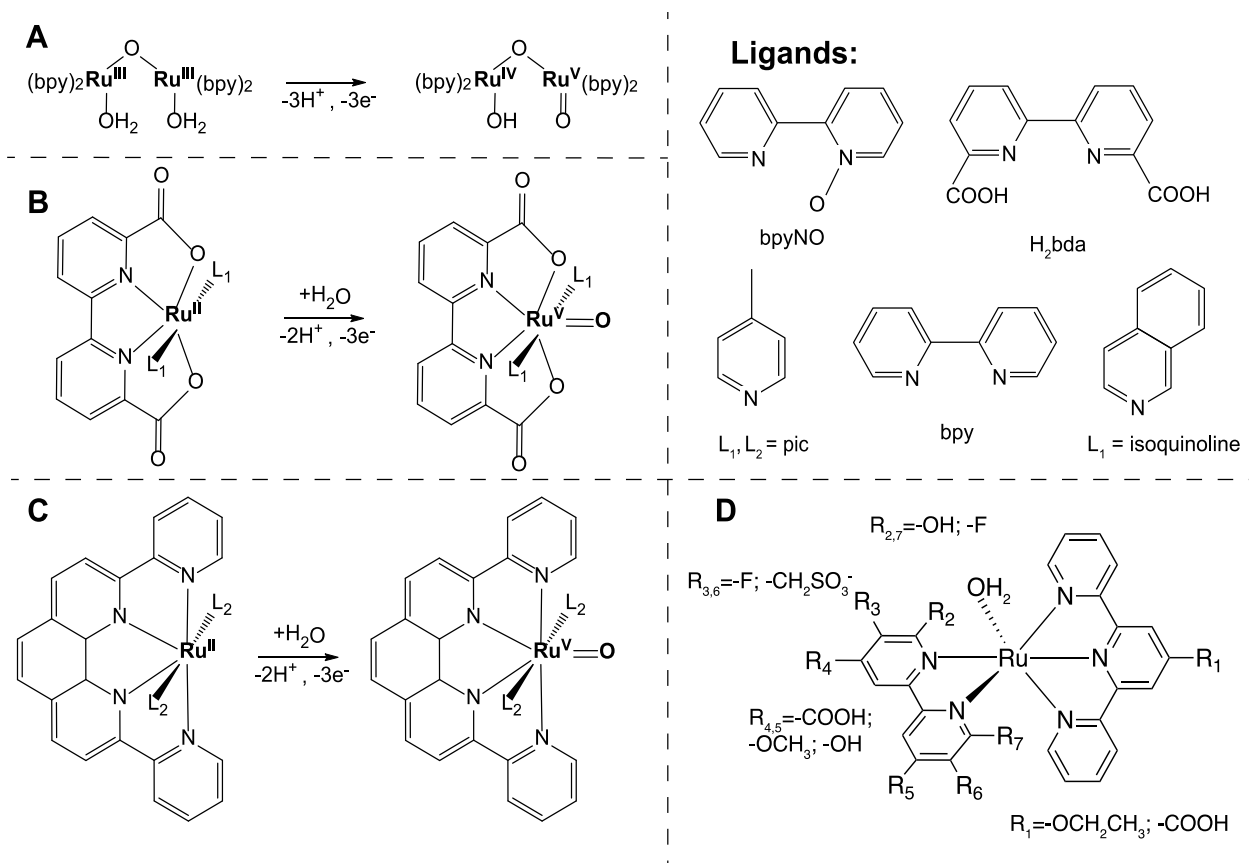


Figure 3-1. Activated Ru-based species capable of O-O bond formation and oxygen atom transfer. A) Formation of the activated $[\text{Ru}^{\text{IV}}, \text{Ru}^{\text{V}}=\text{O}]$ intermediate in the blue dimer is achieved via PCET. B) $\text{Ru}^{\text{II}}(\text{L})_2(\text{bda})$ class of WOCs form 7-coordinate $\text{Ru}^{\text{V}}=\text{O}$ intermediate via coordination sphere expansion and PCET. Catalysts with variety of axial ligands were investigated, two typical axial ligands (L_1) are shown. C) 7-coordinate $[\text{Ru}^{\text{V}}=\text{O}(\text{L})_2(\text{dpp})]^{3+}$ intermediate with neutral dpp ligand is stable in solutions on a minute time scale due to ligand protection of the $\text{Ru}^{\text{V}}=\text{O}$ fragment. Activation occurs via oxygen atom transfer with formation of dpp-N-oxides. D) Overview of ligand modifications in $[\text{Ru}^{\text{II}}(\text{bpy})(\text{tpy})(\text{H}_2\text{O})]^{2+}$ family of catalysts. It has been shown that ethoxy (EtO-) and methoxy (MeO-) substituents increase the rate of O_2 evolution.

Despite recent spectroscopic advances, there remains the largest class of Ru complexes with currently unexplained mechanism of action. These complexes utilize neutral polypyridine ligands and single water as a direct ligand to Ru, **Figure 3-1D**. In this study, we focus on the basic catalyst family of $[\text{Ru}^{\text{II}}(\text{bpy})(\text{tpy})(\text{H}_2\text{O})]^{2+}$ (**1**) (tpy = 2,2';6',2''-terpyridine, bpy = 2,2'-bipyridine), the framework of which was used extensively for ligand modification to uncover structure-activity relationships, **Figure 3-1D**. Following ligand modifications were reported: $\text{R}_{2,4} = -\text{OMe}$, $-\text{COOH}$; ⁷¹ $\text{R}_{2,7} = -\text{OH}$, $\text{R}_{4,5} = -\text{OH}$, $\text{R}_{2,4} = -\text{OMe}$; ⁷² $\text{R}_{2,7} = -\text{F}$, $\text{R}_{3,6} = -\text{F}$; ⁷³ $\text{R}_{3,6} = -\text{CH}_2\text{SO}_3^-$; ⁷⁴ $\text{R}_1 = -\text{OEt}$, $-\text{OMe}$, $-\text{Me}$, $-\text{Cl}$. ⁷⁵ Extensive studies have shown that introduction of the ethoxy (EtO-) and methoxy (MeO-) substituents on tpy or bpy ligands increase the rate of O₂ evolution as much as a factor of ten. Other modifications were moderately activating or moderately de-activating. Faster O₂ evolution was attributed to the decrease in redox potential of the $[\text{Ru}^{\text{V}}=\text{O}(\text{bpy})(\text{EtO-tpy})]^{3+}$ formation. ^{75, 76} Catalysts of this type are also widely tested for incorporation in functional assemblies but, so far, with limited success. ^{77, 78}

Our quest for an alternative mechanism was driven by an apparent controversy in the field of catalytic water oxidation. While multiple PCET accessible $\text{Ru}^{\text{V}}=\text{O}$ (S=1/2) intermediates critical for O-O bond formation were detected (**Figure 3-1A-C**)^{2, 61, 64, 67, 70}, $[(5\text{N-ligands})\text{Ru}^{\text{V}}=\text{O}]^{3+}$ intermediates^{14, 71, 79} and products of its reaction with water have never been observed (blue path in **Figure 3-2**).^{12, 62} Here, catalyst activation proceeds via PCET to $\text{Ru}^{\text{IV}}=\text{O}$ steady state species characterized *in situ* by XAS and resonance Raman (green box, **Figure 3-2**)^{12, 60, 62, 80} However, $\text{Ru}^{\text{IV}}=\text{O}$ does not have enough energy to react with water via WNA or RC. The PCET channel to form a $\text{Ru}^{\text{V}}=\text{O}$ state is not available and direct oxidation (without PCET) appears thermodynamically prohibitive, see **Figure 3-2**, insert.^{12, 62} For Ru complexes with neutral polypyridine ligands, WNA on a $\text{Ru}^{\text{V}}=\text{O}$ species to form O-O bond adds second (~0.6-1.1 eV) barrier.⁸¹⁻⁸⁶ In total, two significant, consecutive activation barriers must be overcome first to generate the $\text{Ru}^{\text{V}}=\text{O}$ and then for its reaction with water. Some studies proposed direct involvement of Ce^{IV} (via hydroxo- Ce^{IV} fragment) to facilitate O-O bond formation^{71, 87} and to bind with Ru complexes^{65, 71}. While we recently characterized $\text{Mn}^{\text{IV}}=\text{O}\cdots\text{Ce}^{\text{IV}}$ adduct⁸⁸, our earlier EXAFS of Ru-based WOCs did not reveal structural signatures of the $\text{Ru}^{\text{IV}}=\text{O}\cdots\text{Ce}^{\text{IV}}$ or other adducts with Ce^{IV} .

Thus, there is a need for a new hypothesis on how such molecular catalysts can be transformed to achieve water oxidation reaction. All these catalysts commonly use polypyridine

ligands. Recently, we have shown that both 6-coordinate $\text{Ru}^{\text{IV}}=\text{O}$ and 7-coordinate $\text{Ru}^{\text{V}}=\text{O}$ can efficiently transfer oxygen to nitrogen atoms in polypyridine ligands, with the formation of N-oxides.^{62, 70, 89} Computationally, the $[\text{Ru}^{\text{IV}}=\text{O}(\text{tpy})(\text{L})]^{2+}$ was shown to convert to intermediates with coordinated N-oxide.⁹⁰

Here, using the combination of the *in situ* spectroscopy and *de novo* synthesis of the reactive intermediate, we were able to establish that formation of the complex with N-oxide ligand has a key activating role for $[(5\text{N-ligands})\text{Ru}(\text{H}_2\text{O})]^{2+}$ class of catalysts. This discovery resulted from detailed spectroscopic analysis and identification of transient reactive intermediates. Direct synthesis of the reactive intermediate $[\text{Ru}^{\text{II}}(\text{bpy-NO})(\text{tpy})(\text{H}_2\text{O})]^{2+}$ (**1-NO**) validated a multitude of *in situ* spectroscopic observations and computational predictions. Overall, single atom modification of the ligand resulted in a hundredfold increase in catalytic activity.

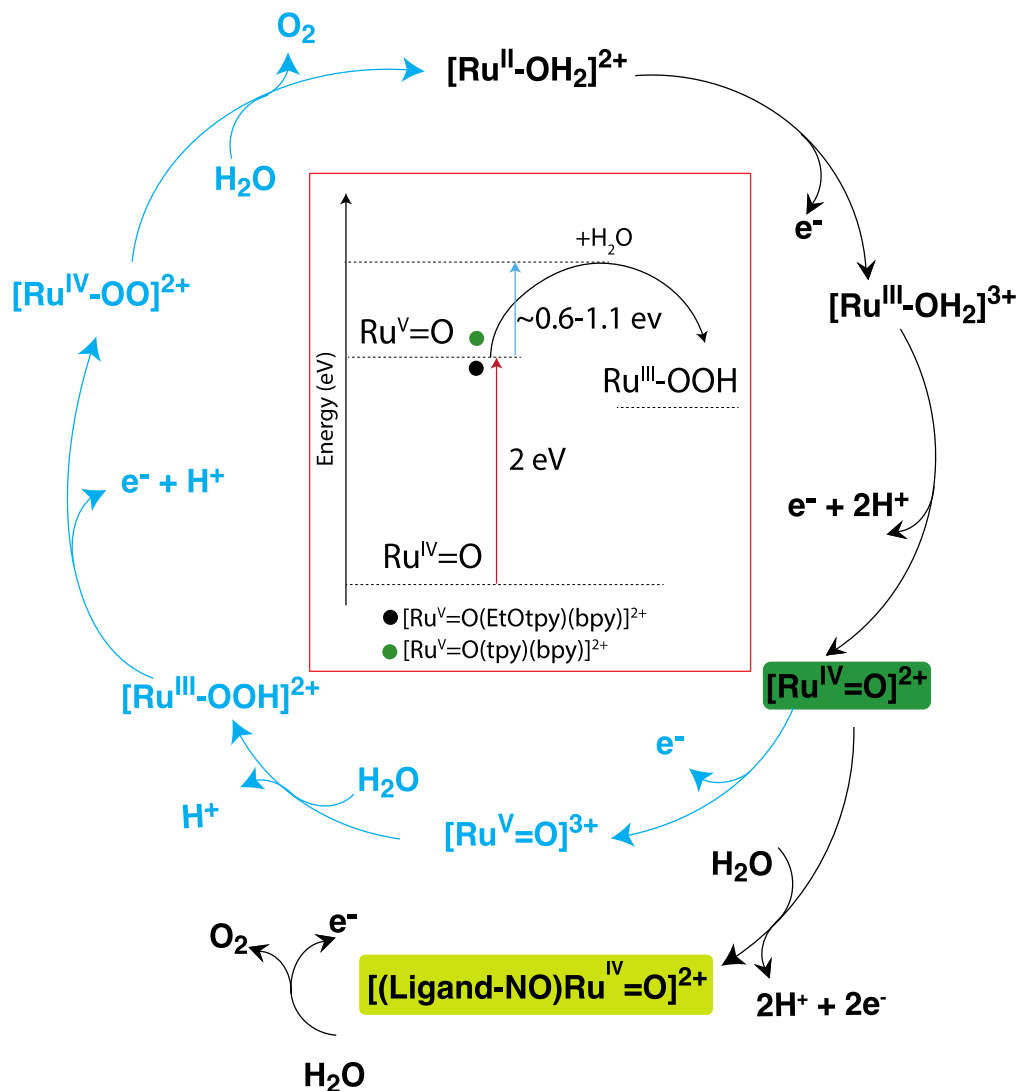


Figure 3-2. Catalytic cycle of $[\text{Ru}^{\text{II}}(\text{5N-ligands})\text{H}_2\text{O}]^{2+}$ family of catalysts, **Figure 3-1D**. There is $\sim 95\%$ of $[\text{Ru}^{\text{IV}}=\text{O}(\text{bpy})(\text{tpy})]^{2+}$ in the catalytic steady state. Involvement of the $\text{Ru}^{\text{V}}=\text{O}$ and proposed O-O bond formation via WNA (blue arrows) currently lacks reaction with water (middle insert). The lag phase in the onset of O_2 evolution indicates an additional step of catalyst activation (yellow box).

3.3 Results and discussion

1. Spectroscopic characterization of water oxidation using $[Ru^{II}(bpy)(tpy)(H_2O)]^{2+}$ (1) and $[Ru(bpy)(EtO-tpy)(H_2O)]^{2+}$ (2). Upon addition of one equivalent of Ce^{IV} to (1) and (2), Ru^{III} ($S=1/2$) forms with $g_{xx}=2.60$ $g_{yy}=2.4$ and $g_{zz}=1.66$ in (1) and $g_{xx} = 2.78$ $g_{yy}= 2.33$ and $g_{zz} = 1.53$ in (2), **Figure 3-3A**. Such Ru^{III} ($S=1/2$) EPR signals are well-known.^{12, 62, 80, 91} Under catalytic conditions, modeled here by adding 20 equiv of Ce^{IV} , the majority of the (1) and (2) is in the EPR silent $[Ru^{IV}=O]$ state ($S=1$), see decrease in EPR intensity in Figure 3A. Residual (~5%) EPR signals in Figure 3B ($g_{xx}=2.31$, $g_{yy}=2.20$ and $g_{zz}=1.91$ for (1)^{12, 80} and $g_{xx}=2.33$, $g_{yy}=2.18$ and $g_{zz}=1.90$ for (2)) do not match expected g-factors of the $Ru^V=O$ ($S=1/2$) species, Table S1.^{34, 61, 66, 67, 92} Reported $Ru^V=O$ g-factors show g_{xx} range from 2.05 to 2.08 and g_{yy} from 1.98 to 2.01 and g_{zz} from 1.85 to 1.91, Table S1. For (1) using a combination of EPR and X-ray absorption spectroscopy, we demonstrated earlier that 95% of the Ru complex in the catalytic steady state is in the form of $[Ru^{IV}=O(bpy)(tpy)]^{2+}$.¹² According to literature reports, the $Ru^V=O$ state should be more accessible in $[Ru(bpy)(EtO-tpy)(H_2O)]^{2+}$ (2).^{75, 76} However, similar to (1), a low intensity EPR signal with $g_{xx}=2.33$, $g_{yy}=2.18$ and $g_{zz}=1.90$ is detected here instead of the expected EPR associated with $[Ru^V=O(bpy)(EtO-tpy)]^{3+}$. The EPR signals in **Figure 3-3B** form quickly and are not sensitive to the nature of acid ruling out their origin as anation products. Since our 2014 report,¹² EPR spectra with similar g-tensors were found for Ru complex $[Ru^{III}(NPM-NO)(4-pic)_2(H_2O)]^{3+}$ and $[Ru^{III}(NPM-NO,NO)(4-pic)_2]^{3+}$ (where (NPM = 4-t-butyl-2,6-di(1',8'-naphthyrid-2'-yl)-pyridine, pic = 4-picoline) $g_{xx}=2.30$, $g_{yy} = 2.18$, and $g_{zz} = 1.83$ ⁶² and in the $[Ru^{III}(pic)_2(dpp-NO)]^{3+}$ ($g_{xx}=2.39$, $g_{yy}=2.16$, $g_{zz}=1.86$) and $[Ru^{III}(pic)_2(dpp-NO,NO)]^{3+}$ ($g_{xx}=2.23$, $g_{yy}=2.16$, $g_{zz}=1.92$) catalytic intermediates which all featured the N-oxide ligands.⁷⁰

Table 3-1. g-factors comparison for Ru^V=O species.

<i>Species</i>	<i>g_{xx}</i>	<i>g_{yy}</i>	<i>g_{zz}</i>	<i>Ref.</i>
<i>5-coordinate</i> [ⁿ Pr ₄ N][Ru ^V (O)(2-hydroxy-2-thylbutyrato) ₂]	2.08	1.98	1.91	92
<i>7-coordinate</i> [Ru ^V =O(bpy) ₂ (H ₂ O) ₂] ³⁺	2.05	1.99	1.85	67, 66
<i>7-coordinate</i> [Ru ^V =O(bda)(isoq) ₂] ³⁺	2.07	2.00	-	61
<i>7-coordinate</i> [Ru ^V =O(pic) ₂ (dpp)] ³⁺	2.08	2.01	1.90	70

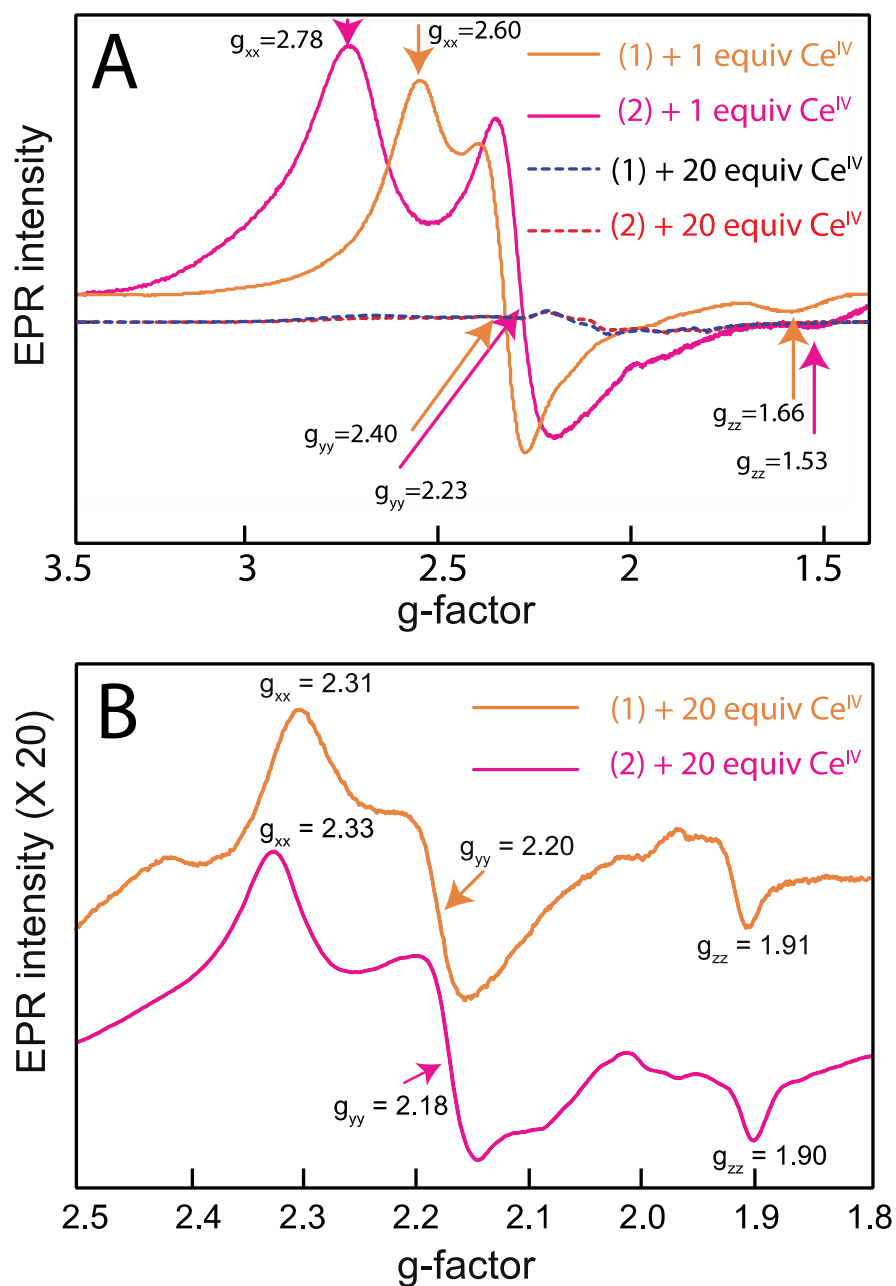


Figure 3-3. A) EPR spectra of **(1)** (orange) and **(2)** (magenta) in 0.1 M HNO₃ after addition of one equiv of Ce^{IV} (solid lines) and after addition of 20 equiv of Ce^{IV} (dash lines) B) Zoom (×20) into low intensity EPR signals from solutions generated by adding 20 equiv of Ce^{IV} in 0.1 M HNO₃ to **(1)** (orange) and to **(2)** (magenta). All samples were frozen within 30 s.

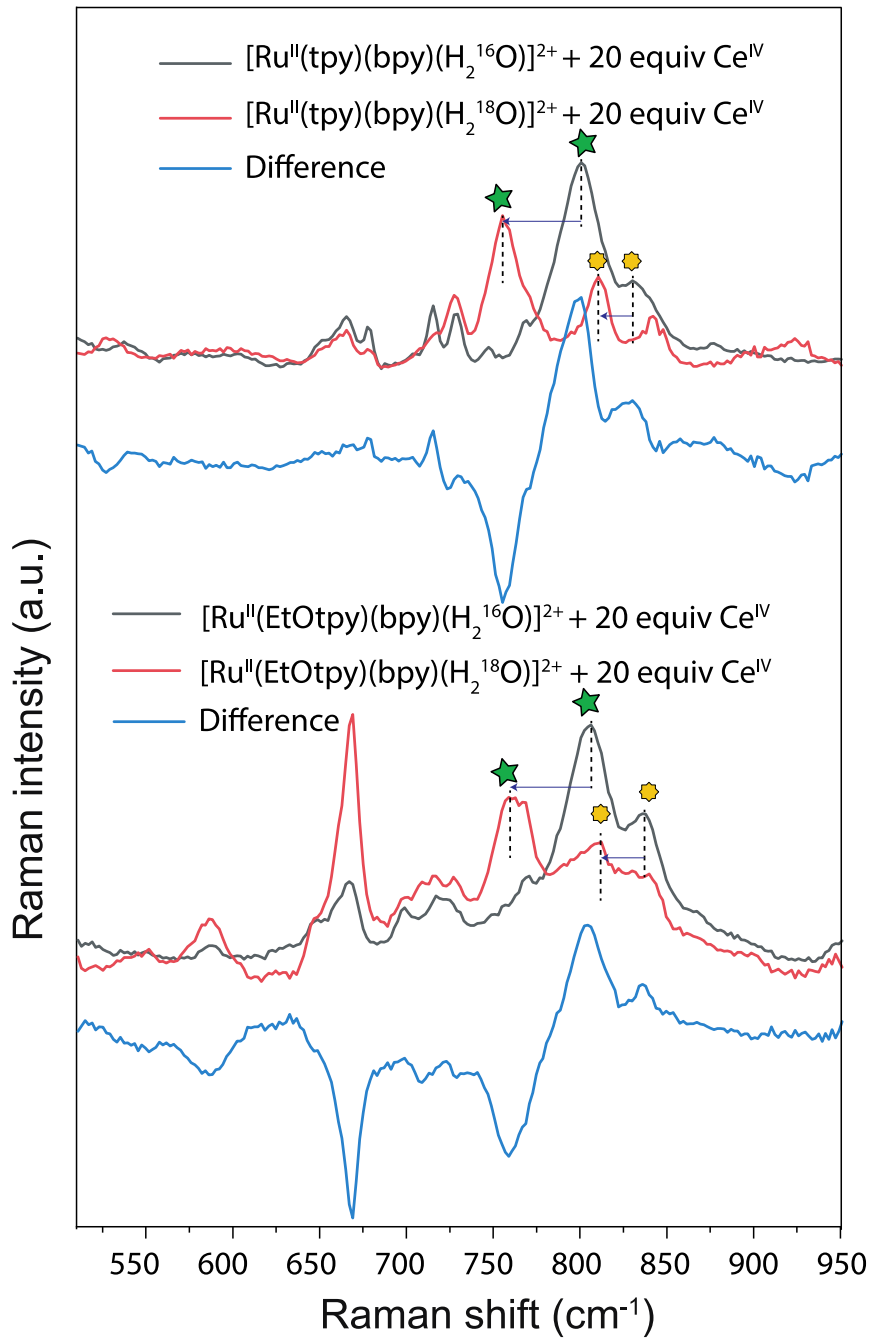


Figure 3-4. The selected frequency range of resonance Raman (532 nm) of (1) and (2) 1mM solutions in 0.1 M HNO₃ mixed with 20 equiv of Ce^{IV} (one minute after oxidation) in H₂¹⁶O and H₂¹⁸O, Figure S1, Table S2. Two isotope sensitive vibrations were assigned to Ru^{IV}=O (~800 cm⁻¹) and Ru-O-N (~830 cm⁻¹).

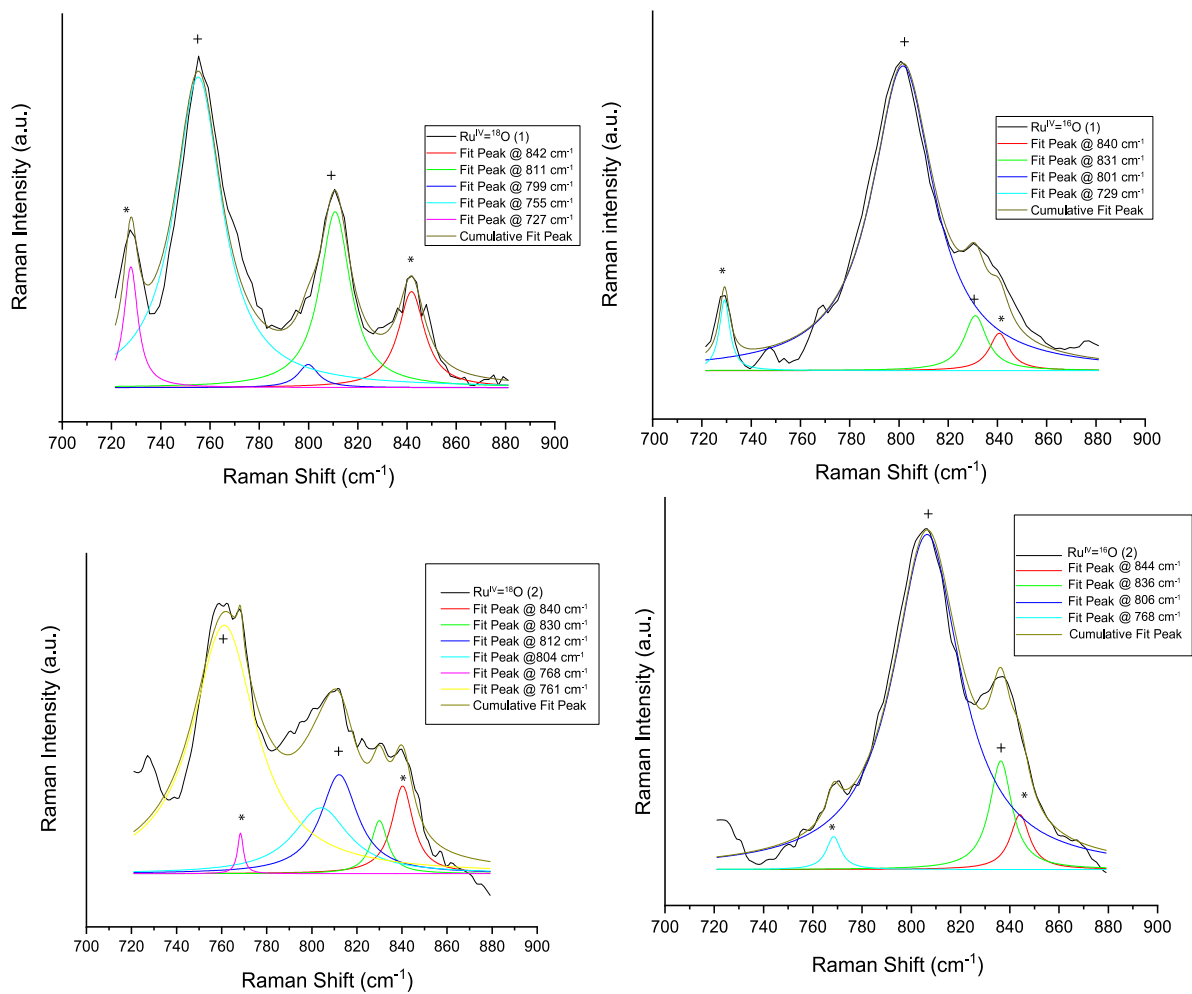


Figure 3-5 Fits to the room temperature RR spectra (532 nm) of (1) and (2) 1 mM dissolved in H₂¹⁸O (final H₂¹⁸O content ~85%) and H₂¹⁶O in 0.1 M HNO₃ upon oxidation with 20 equiv of Ce^{IV}. Bands marked with ‘*’ did not shift after isotope substitution while those marked with ‘+’ and are oxygen isotope sensitive.

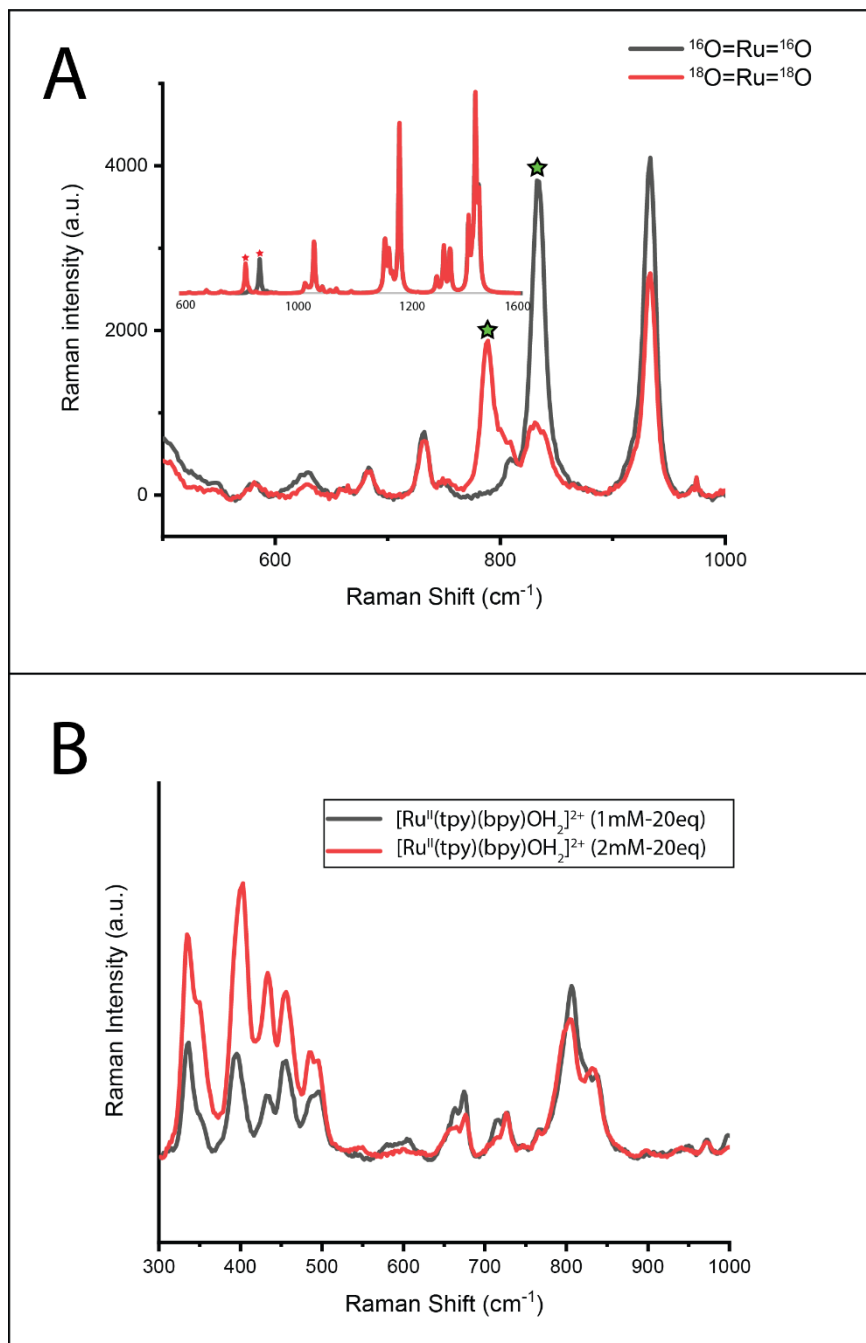


Figure 3-6. A Raman spectrum of $[(\text{tpy})\text{Ru}^{\text{VI}}=\text{O},=\text{O},(\text{OH})]^+$ with ^{18}O and ^{16}O . The insert is the Raman calculated by DFT. B Raman spectra of **(1)**, concentration of 1 mM and 2 mM in 0.1 M HNO_3 recorded 30 min after oxidation with 20 equiv of Ce^{IV} . Two spectra are normalized to the same height for bands around 800 cm^{-1} . Formation of dimeric species is evident by new bands at $300\text{-}400\text{ cm}^{-1}$ corresponding to Ru-O-Ru bridging unit.¹⁻³ Increase in concentration stimulates dimer formation, a second order process. Loss or partial de-coordination of bpy ligand might facilitate formation of dimeric species

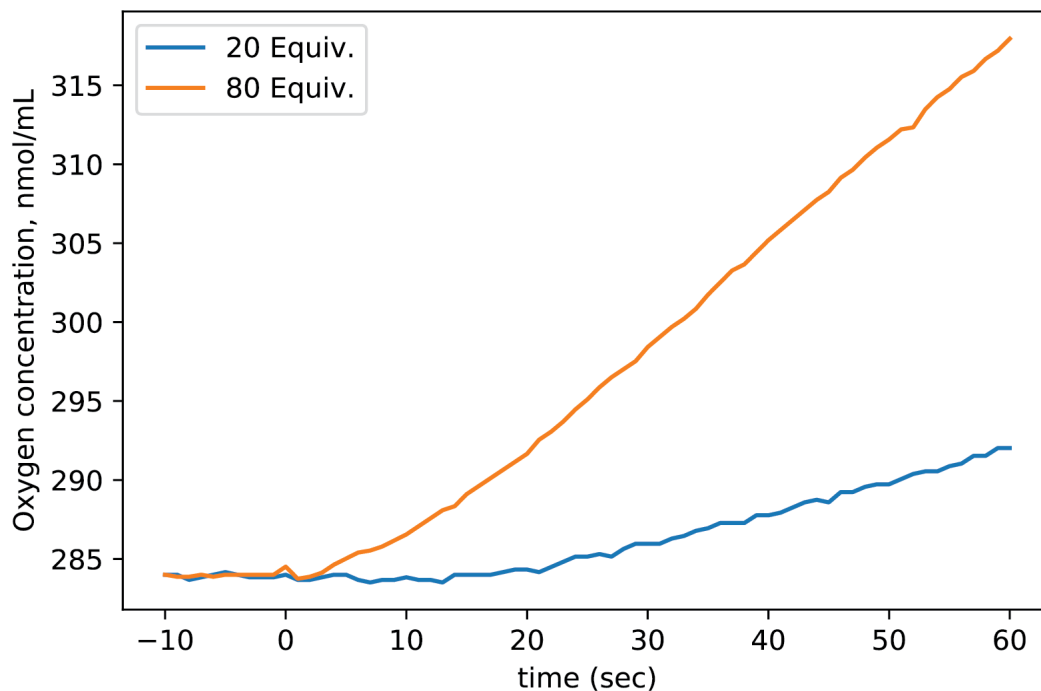
Table 3-2. Lorentzian fit parameters for resonance Raman spectra of **(1)** and **(2)**. H₂¹⁸O and H₂¹⁶O are presented in separate sections and peaks sensitive to oxygen isotope substitution are highlighted by dark gray (Ru=O) and light gray (Ru-N-O)

Position (cm ⁻¹)	FWHM (cm ⁻¹)	normalized amplitude
841.8	12.9	0.17
810.8	14.9	0.36
799.8	10	0.032
755.2	23	1
727.8	6.8	0.11
H ₂ ¹⁶ O		
840.7	9.8	0.04
831	11.2	0.07
801	30.5	1
729	5.1	0.04
H ₂ ¹⁶ O		
840	11.4	0.12
830	9	0.06
812.1	20	0.23
804	30	0.23
768.3	3.1	0.015
761.1	34.3	1
H ₂ ¹⁶ O		
844	9.5	0.05
836.3	10.9	0.11
806.4	33.1	1
768.5	7.2	0.02

Table 3-3. Delay (lag phase) (seconds) in O₂ evolution in 0.1 M HNO₃.

Number of Ce ^{IV} equiv	0.1 mM [Ru ^{II} (bpy)(tpy-EtO)(H ₂ O)] ²⁺	1 mM [Ru ^{II} (bpy)(tpy)(H ₂ O)] ²⁺
20	20	99
40	12	61
60	2	52
80	0	42

A



B

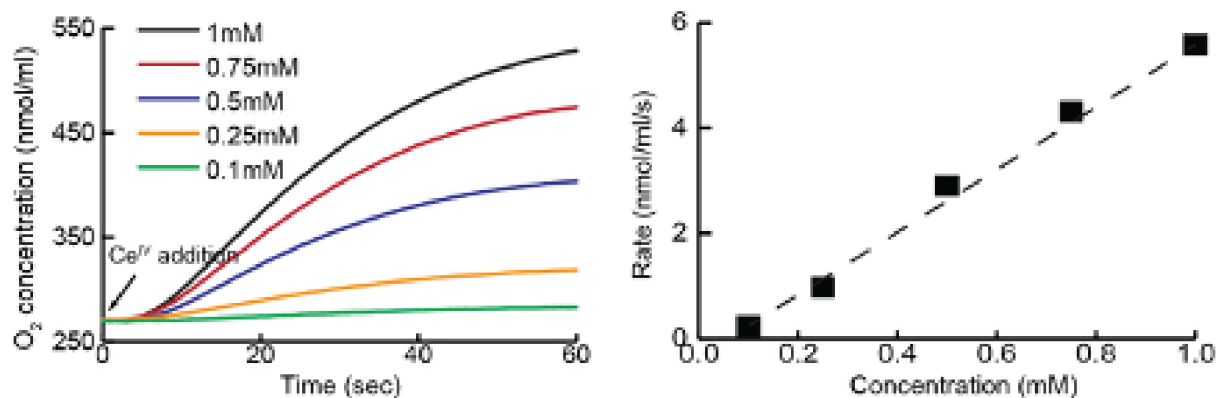


Figure 3-7. A) Representative oxygen evolution profiles for 0.1mM $[\text{Ru}^{\text{II}}(\text{bpy})(\text{tpy-EtO})(\text{H}_2\text{O})]^{2+}$ in 0.1 M HNO_3 with different equiv of Ce^{IV} added at $t = 0$ s. B) Oxygen evolution after addition of indicated amount of 10% $[\text{Ru}(\text{tpy})(\text{bpyNO})(\text{H}_2\text{O})]^{2+}$ / 90% $[\text{Ru}(\text{tpy})(\text{bpy})(\text{H}_2\text{O})]^{2+}$ at $t = 0$ to 20 mM solution of Ce^{IV} oxidant in 0.1 M HNO_3 . Rate was determined over the linear slope and was shown to be first order in catalyst.

Resonance Raman (RR)spectroscopy: resonance Raman with $^{16}\text{O}/^{18}\text{O}$ isotope labeling is particularly helpful with identification of key Ru=O, Ru-O and possibly O-O bonds, **Figure 3-4**. In **Figure 3-5** the spectra of **(1)** and **(2)** after oxidation are fitted for both oxygen isotope to get a better estimation for the shift of oxygen sensitive peaks. The fit parameters are summarized in **Table 3-2**. In **(1)** and **(2)** oxidized with 20 equiv of Ce^{IV} in 0.1 M $\text{HNO}_3/\text{H}_2^{16}\text{O}$ or H_2^{18}O , the major band at 800 cm^{-1} undergoes a -45 cm^{-1} shift. This band was previously assigned to $\text{Ru}^{\text{IV}}=\text{O}$ and similar isotope shifts were reported.^{62, 93} Interestingly, the 800 cm^{-1} band was accompanied by the $^{16}\text{O}/^{18}\text{O}$ isotope sensitive band (-20 cm^{-1}) at $\sim 831\text{ cm}^{-1}$ detected previously¹ and assigned to $[(\text{tpy})\text{Ru}^{\text{VI}}=\text{O},=\text{O},\text{OH}]^+$. The RRaman spectrum of the $[(\text{tpy})\text{Ru}^{\text{VI}}=\text{O},=\text{O},\text{OH}]^+$, prepared as a reference compound, showed an isotope shift of -44 cm^{-1} for its symmetric $\text{Ru}^{\text{VI}}=\text{O},=\text{O}$ vibration at 833 cm^{-1} , **Figure 3-6A**. While a -44 cm^{-1} shift is consistent with the $\text{Ru}^{\text{VI}}=\text{O}$ nature of the bond, a -20 cm^{-1} shift is more appropriate for a single Ru-O bond. To the best of our knowledge, only the Ru-O-N vibration of N-oxide's coordinated to Ru is known to be at $\sim 830\text{ cm}^{-1}$.^{70, 94}

Figure 3-6B is RRaman on the **(1)** with different concentration. As low frequency peaks (below 500 cm^{-1}) suggest that they correspond to dimer formation. Dimer formation is a second order reaction and predicts the change in intensity of the peaks we see them.

We also obtained a lag phase (delay in O_2 evolution after addition of Ce^{IV} oxidant) on the order of 2-20 sec for 0.1 mM solution of the **(2)** and 40-100 sec for the 1.0 mM solution of less active **(1)**, **Table 3-3**, **Figure 3-7**. The lag phase is shorter for more active **(2)**. An increase in Ce^{IV} concentration results in the shortening of the lag phase. From this result, we believe both complexes undergo an additional activation step in agreement with earlier reports⁸⁵ for **(1)**. The classical mechanism of O-O bond formation via water nucleophilic attack (**Figure 3-2**) is inconsistent with experimental observations of the lag phase. An activation period on the order of minutes was observed in Ru-based water oxidation catalysts with quaterpyridine ligands, and it was attributed to $\text{qpy-N,N}''$ -dioxide formation as a key step in catalyst activation.^{70, 89} Dimer formation was noted for **(1)** and its analogs under prolonged oxidation, **Figure 3-6B**. It has been reported that prolonged bulk electrolysis or prolonged oxidation (several days to 1 week) with excess of Ce^{IV} of **(1)** and its analogs might result in dimerization of this complex with formation of more stable but less active $[(\text{tpy})(\text{bpy})\text{Ru}^{\text{IV}}-\text{O}-\text{Ru}^{\text{IV}}(\text{tpy})=\text{O}(\text{OH})]^{4+}$.^{95, 96} Analog with bpym s = 2,2'-bipyridine-5,5'-bis(methanesulfonate) delivered crystals with $[(\text{tpy})(\text{bpym})\text{Ru}^{\text{III}}-\text{O}-\text{Ru}^{\text{III}}(\text{tpy})(\text{bpym})]^{4+}$ dimer after 3 weeks with Ce^{IV} .⁷⁴ Formation of the bpy N-oxide and its

consecutive de-coordination might be responsible for the reported $[(\text{tpy})(\text{bpy})\text{Ru}^{\text{IV}}\text{-O-Ru}^{\text{IV}}(\text{tpy})=\text{O}(\text{OH})]^{4+}$ dimer formation. We demonstrated that catalysts de-activation via dimerization can be effectively prevented for catalyst immobilized in metal organic frameworks.⁷⁷ ⁹³ XRD analysis of late dimeric products deliver limited information on *in situ* processes at early times and, in particular, on catalysts activation at the onset of catalytic current. Formation of free bpy-NO was noted under catalytic conditions.⁷¹ Thus, we reasoned that while dimer formation cannot account for the lag phase, ligand N-oxide formation can happen quickly at the $\text{Ru}^{\text{IV}}=\text{O}$ level ($\sim 95\%$ in catalytic steady state)¹² and result in catalyst activation. This hypothesis is tested below via *de novo* synthesis of proposed reactive intermediate.

2. De novo synthesis of the $[(\text{tpy})(\text{bpy-NO})\text{Ru}(\text{H}_2\text{O})]^{2+}$ (1-NO**).** The catalytic intermediate $[(\text{tpy})(\text{bpy-NO})\text{Ru}(\text{H}_2\text{O})]^{2+}$ (**1-NO**) was prepared and its performance in O_2 evolution was investigated, **Figure 3-8**. To the best of our knowledge, few Ru complexes with N-oxide ligands have been described.^{89, 94, 97, 98} Earlier we⁹⁴ and others⁹⁷ were able to synthesize $[\text{Ru}^{\text{II}}(\text{bpy})_2(\text{bpy-NO})]^{2+}$. However, this compound is extremely light sensitive. $[\text{Ru}(\text{tpy})(\text{bpy-NO})\text{Cl}]\text{Cl}$ was prepared using a procedure similar to the synthesis of $[\text{Ru}^{\text{II}}(\text{bpy})(\text{tpy})\text{Cl}]\text{Cl}$ with some modifications.⁹⁹ All preparations were handled in the dark due to its unknown properties. (**1-NO**) turned out to be a reactive compound with tendency to convert to (**1**) under conditions of the synthesis. Regardless of the precautions and explored alternative synthetic routes, mixtures of $(\text{tpy})(\text{bpy})\text{RuCl}_2$ and $(\text{tpy})(\text{bpy-NO})\text{RuCl}_2$ were obtained. Facile conversion of $[\text{Ru}(\text{tpy})(\text{bpy-NO})(\text{X})]$ to $[\text{Ru}(\text{tpy})(\text{bpy})(\text{X})]$ happens under condition of synthesis, in stark contrast to properties of $[\text{Ru}^{\text{II}}(\text{bpy})_2(\text{bpy-NO})]^{2+}$, which was prepared with good yields.⁹⁴ We attributed this dramatic difference to the much higher reactivity of $[(\text{tpy})(\text{bpy-NO})\text{Ru}(\text{X})]^{2+}$. We noted that decrease of the water content from 25% to 5% in the reaction mixture helps to increase the (**1-NO**) content. We also noted that in $[(\text{tpy})(\text{bpy-NO})\text{RuCl}]\text{Cl}$ ligand exchanges faster than in (**1**). Thus, we can speculate that presence of the liable Ru-Cl and/or Ru- H_2O ligand is responsible for conversion of the (**1-NO**) to (**1**) especially when heated.

Despite the mixed content, such catalysts preparations already demonstrated a tenfold increase in the rate of catalytic water oxidation using Ce^{IV} (**Figure 3-7**). Separation on silica gel allowed us to purify *trans* and *cis* (**1-NO**). UV-vis and FTIR data (, **Figure 3-8A,B**) show distinct spectroscopic signatures of the (**1-NO**) which include a purple color and distinct $\sim 830\text{ cm}^{-1}$

vibration also noted in the $[\text{Ru}^{\text{II}}(\text{bpy})_2(\text{bpy-NO})]^{2+}$ complex⁹⁴. *cis* (**1-NO**) demonstrated high catalytic activity, **Figure 3-8C, D**. To the best of our knowledge this is the highest O₂ evolution activity reported for a single site Ru-based catalyst in acid and with first order rate dependence on the catalyst complex. Note that some faster catalysts are accessible via a radical coupling mechanism^{68, 100} but these cannot currently be integrated into devices as at pH=1 their activity decreases upon immobilization. *trans*(**1-NO**) isomer forms in unpractically small amounts and was not investigated beyond UV-Vis and NMR characterization.

cis (**1-NO**) electrochemical properties were investigated by cyclic voltammetry, **Figure 3-8C**. Redox events at ~0.8-0.9 V vs NHE is likely the oxidation of the Ru^{II} to Ru^{III} and later to Ru^{IV} predicted by DFT at ~1 V (**Table 3-1**). An onset of catalytic current at ~1.4 V is the lowest known for Ru-based complexes outside the Ru-bda family.⁶⁸ Overall high catalytic activity of the *cis* (**1-NO**) intermediate shows that formation of such or analogous tpy-NO intermediates at a level of few percent might be fully responsible for all observed catalytic activity of $[(\text{tpy})(\text{bpy})\text{Ru}(\text{H}_2\text{O})]^{2+}$ and its large family of analogs.

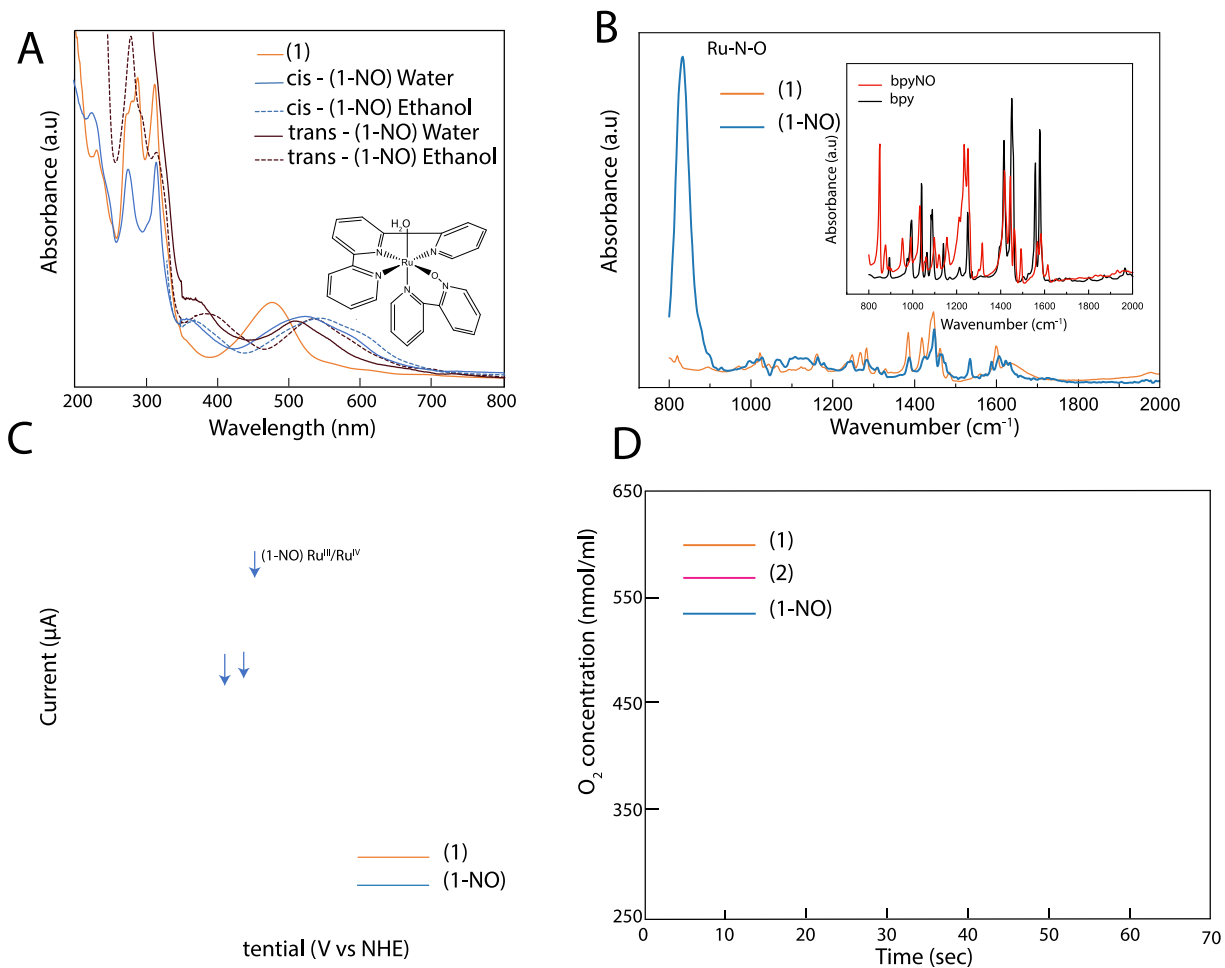


Figure 3-8 Spectroscopic and catalytic properties of the $[\text{Ru}(\text{tpy})(\text{bpy-NO})(\text{H}_2\text{O})]^{2+}$ (1-NO) intermediate. A) UV-Vis absorption of (1), *trans*-(1-NO) and *cis*-(1-NO). Ethanol solutions contain *trans*- and *cis*- $[\text{Ru}(\text{tpy})(\text{bpy-NO})\text{Cl}]^+$ correspondingly. In $[\text{Ru}(\text{tpy})(\text{bpy-NO})\text{Cl}]^+$ Cl undergoes fast exchange in water. B) FTIR of (1) and (1-NO) powders. Insert shows FTIR of pure ligands. C) Cyclic voltammetry of 0.5 mM (1) and *cis*-(1-NO) in 0.1 M HNO_3 , scan rate 0.1 V/sec. The insert shows the $\text{Ru}^{\text{II}}/\text{Ru}^{\text{III}}$ and $\text{Ru}^{\text{III}}/\text{Ru}^{\text{IV}}$ couples. D) Oxygen evolution of (1), (2) and *cis*-(1-NO) prepared by mixing of 1 mL of 0.2 mM of the solution and 40 equiv of Ce^{IV} in 0.1 M HNO_3 .

DFT analysis of catalytic mechanism. DFT was used here to support the analysis of redox properties, spectroscopic signatures, and chemical reactivity of Ru-based catalysts, **Table 3-4**, **Table 3-5**, **Table 3-6**, **Table 3-7**, **Table 3-8**. Latimer-Frost diagrams for variety of possible intermediates and reactivity pathways give better understanding of the feasibility of catalysts activation via formation of N-oxide ligands and their further reactivity, **Figure 3-9**, **Figure 3-10**, **Figure 3-11**, **Figure 3-12**. Calculations for the redox potentials of the **(1)**, **(1-NO)** and **(2)** (**Table 3-4**) agree well with the literature reports^{75, 76} and measurements for **(1-NO)**.

The redox potential for the $[\text{Ru}^{\text{V}}=\text{O}(\text{bpy})(\text{EtO-tpy})]^{3+}$ formation was found to be ~ 1.98 V, which is slightly lower than ~ 2.15 V computed for $[\text{Ru}^{\text{V}}=\text{O}(\text{bpy})(\text{tpy})]^{3+}$, and ~ 2.12 for $[\text{Ru}^{\text{V}}=\text{O}(\text{bpy-NO})(\text{tpy})]^{3+}$, **Table 3-4**. Neither potential is accessible to the Ce^{IV} oxidant (~ 1.7 V).

We also analyzed the reactivity of $\text{Ru}^{\text{IV}}=\text{O}$ in **(1)** and **(2)** in the oxygen atom transfer to bpy, tpy and EtO-tpy ligands with the formation of ligand-N-oxides, **Table 3-4**. The free energies in both paths are small (~ 0.1 eV) and transfers to tpy and EtO-tpy are more favorable compared to the transfer to bpy. Preliminary computational analysis by other groups⁹⁰ has shown similar results. Both bpy-NO and tpy-NO ligand modifications could exist under reaction conditions.

It has been long noted that the redox potentials of the Ru complexes correlate poorly with catalytic activity in water oxidation.¹⁰⁰ With three molecularly highly similar catalysts spanning two orders of magnitude in catalytic activity, we searched for a molecular property which correlates with O_2 evolution rates. Formation of the $\text{Ru}^{\text{V}}=\text{O}$ state is considered key to both pathways of the O-O bond formation via radical coupling and via water nucleophilic attack. In all cases, when $\text{Ru}^{\text{V}}=\text{O}$ species were thermodynamically accessible via PCET, presence of these species was verified by spectroscopy.^{2, 61, 64, 70} However, despite the assumed accessibility of the $[\text{Ru}^{\text{V}}=\text{O}(\text{bpy})(\text{EtO-tpy})]^{3+}$ state, the corresponding EPR was not detected, **Figure 3-3**. Moreover, the calculated $\text{Ru}^{\text{V}}=\text{O}$ potentials for the three analyzed complexes (**Table 3-4**) do not correlate with the rate of O_2 evolution. At the same time, we noted that onset of catalytic current (~ 1.6 V and ~ 1.4 V for **(1)** and **(1-NO)**, **Figure 3-8C**) happens at a potential higher than formation of the Ru^{IV} state. This was earlier interpreted as a wave for Ru^{IV} to Ru^{V} oxidation.⁷¹ However, it can also correspond to a ligand oxidation. For instance, the most oxidatively potent bio-inorganic compound, Complex I, is known to contain a $\text{Fe}^{\text{IV}}=\text{O}$ unit and oxidized ligand in a cation radical form.¹⁰¹ Computed redox potentials for the ligand cation radicals listed in **Table 3-4** correlate significantly better with O_2 evolution activity, **Figure 3-13**. Frontier orbitals (HOMO) of the

$[\text{Ru}^{\text{IV}}=\text{O}]^{2+}$ states show delocalization onto EtO-tpy and bpy-NO ligands (**Figure 3-14**) suggesting that electron removal can happen from a ligand localized orbital or oxidized species can have a multi-configurational character. Alternatively, ligands with lower oxidation potentials can acquire N-oxides more readily causing increase in catalytic activity. For complexes with bpy-NO, tpy-NO and EtO-tpy-NO ligands NO group de-coordination i) opens PCET channel via recruitment of the additional water ligand into the first coordination sphere of Ru; ii) results in $[\text{Ru}^{\text{IV}}=\text{O}(\text{ligandNO}^{\bullet+})]$ states which carry three holes but are significantly more accessible (~ 1.5 V, **Table 3-4**) than $[\text{Ru}^{\text{V}}=\text{O}]^{3+}$ states at (~ 2.0 eV); iii) have redox potential above the +1.23 V required for water oxidation. Thus, we can suggest that if $\text{Ru}^{\text{V}}=\text{O}$ formation is prohibitively high thermodynamically (due to the lack of the PCET), the catalytically competent $[\text{Ru}^{\text{IV}}=\text{O}(\text{cation radical}^{\bullet+})]$ state might form ensuring activity in the water oxidation. More experiments are underway to elucidate the pathway for O-O bond formation and results will be reported in a follow up paper.

3.4 Conclusions

Overall, *de novo* synthesis and isolation of the reactive catalytic intermediate $[(\text{tpy})(\text{bpy-NO})\text{Ru}(\text{H}_2\text{O})]^{2+}$ resulted in material with high catalytic potency. Thus, the mere presence of such intermediate or similar tpy-NO in the reaction mixtures at a level of few percent can account for the entire catalytic activity of the most studied $[(\text{tpy})\text{Ru}(\text{bpy})(\text{H}_2\text{O})]^{2+}$ family of Ru-based water oxidation catalysts. A difference of two orders of magnitude in catalytic activity was correlated with the redox property of the ligand toward formation of the cation radical.

Table 3-4. Key thermodynamic parameters computed using DFT.

Reaction*	$\Delta G^0/$ eV	E^0/V^{**}
<i>Redox reactions</i>		
(2) $[\text{Ru}^{\text{III}}(\text{EtO-tpy})(\text{bpy})(\text{H}_2\text{O})]^{3+}/2\text{H}_2\text{O} + \text{e}^- = [\text{Ru}^{\text{II}}(\text{EtO-tpy})(\text{bpy})(\text{H}_2\text{O})]^{2+}/2\text{H}_2\text{O}$		+1.03 (+0.98 ⁷⁵)
(2) $[\text{Ru}^{\text{IV}}=\text{O}(\text{EtO-tpy})(\text{bpy})]^{2+}/2\text{H}_2\text{O} + \text{e}^- + 2\text{H}^+ = [\text{Ru}^{\text{III}}(\text{EtO-tpy})(\text{bpy})(\text{H}_2\text{O})]^{3+}/2\text{H}_2\text{O}$		+1.14 (+1.24 ⁷⁵)
(1) $[\text{Ru}^{\text{III}}(\text{tpy})(\text{bpy})(\text{H}_2\text{O})]^{3+}/2\text{H}_2\text{O} + \text{e}^- = [\text{Ru}^{\text{II}}(\text{tpy})(\text{bpy})(\text{H}_2\text{O})]^{2+}/2\text{H}_2\text{O}$		+1.10 (+1.04 ⁷¹)
(1) $[\text{Ru}^{\text{IV}}=\text{O}(\text{tpy})(\text{bpy})]^{2+}/2\text{H}_2\text{O} + \text{e}^- + 2\text{H}^+ = [\text{Ru}^{\text{III}}(\text{tpy})(\text{bpy})(\text{H}_2\text{O})]^{3+}/2\text{H}_2\text{O}$		+1.12 (+1.23 ⁷¹)
(1-NO) $[\text{Ru}^{\text{III}}(\text{tpy})(\text{bpy-NO})(\text{H}_2\text{O})]^{3+}/2\text{H}_2\text{O} + \text{e}^- = [\text{Ru}^{\text{II}}(\text{tpy})(\text{bpy-NO})(\text{H}_2\text{O})]^{2+}/2\text{H}_2\text{O}$		+1.01 (+0.82)
(1-NO) $[\text{Ru}^{\text{IV}}=\text{O}(\text{tpy})(\text{bpy-NO})]^{2+}/2\text{H}_2\text{O} + \text{e}^- + 2\text{H}^+ = [\text{Ru}^{\text{III}}(\text{tpy})(\text{bpy-NO})(\text{H}_2\text{O})]^{3+}/2\text{H}_2\text{O}$		+0.89 (+0.86)
<i>Ru^V=O formation</i>		
(2) $[\text{Ru}^{\text{V}}=\text{O}(\text{EtO-tpy})(\text{bpy})]^{3+}/2\text{H}_2\text{O} + \text{e}^- = [\text{Ru}^{\text{IV}}=\text{O}(\text{EtO-tpy})(\text{bpy})]^{2+}/2\text{H}_2\text{O}$		+1.98
(1) $[\text{Ru}^{\text{V}}=\text{O}(\text{tpy})(\text{bpy})]^{3+}/2\text{H}_2\text{O} + \text{e}^- = [\text{Ru}^{\text{IV}}=\text{O}(\text{tpy})(\text{bpy})]^{2+}/2\text{H}_2\text{O}$		+2.15
(1-NO) $[\text{Ru}^{\text{V}}=\text{O}(\text{tpy})(\text{bpy-NO})]^{3+}/\text{H}_2\text{O} + \text{e}^- = [\text{Ru}^{\text{IV}}=\text{O}(\text{tpy})(\text{bpy-NO})]^{2+}/\text{H}_2\text{O}$		+2.12
<i>Ru^{IV}=O(ligand •+) formation</i>		
(1-NO) $[\text{Ru}^{\text{IV}}=\text{O}(\text{tpy})(\text{bpy-NO}_{\text{out}}^{\bullet+})(\text{OH})]^{2+} + \text{e}^- + \text{H}^+ = [\text{Ru}^{\text{IV}}=\text{O}(\text{tpy})(\text{bpy-NO}_{\text{out}})(\text{H}_2\text{O})]^{2+}$		+1.51
<i>Oxygen atom transfer to ligand with formation of N-oxide</i>		
(2) $[\text{Ru}^{\text{IV}}=\text{O}(\text{EtO-tpy})(\text{bpy})]^{2+}/2\text{H}_2\text{O} = [\text{Ru}^{\text{II}}(\text{EtO-tpy-NO})(\text{bpy})(\text{H}_2\text{O})]^{2+}/\text{H}_2\text{O}$	-0.09	

Table 3-4 continued

(2) $[\text{Ru}^{\text{IV}}=\text{O}(\text{EtO-tpy})(\text{bpy})]^{2+}/2\text{H}_2\text{O} = [\text{Ru}^{\text{II}}(\text{EtO-tpy})(\text{bpy-NO})(\text{H}_2\text{O})]^{2+}/\text{H}_2\text{O}$	+0.14	
(1) $[\text{Ru}^{\text{IV}}=\text{O}(\text{tpy})(\text{bpy})]^{2+}/2\text{H}_2\text{O} = [\text{Ru}^{\text{II}}(\text{tpy-NO})(\text{bpy})(\text{H}_2\text{O})]^{2+}/\text{H}_2\text{O}$	-0.13	
(1) $[\text{Ru}^{\text{IV}}=\text{O}(\text{tpy})(\text{bpy})]^{2+}/2\text{H}_2\text{O} = [\text{Ru}^{\text{II}}(\text{tpy})(\text{bpy-NO})(\text{H}_2\text{O})]^{2+} + \text{H}_2\text{O}$	+0.09	
<i>Oxidation of the ligand with formation of cation radical</i>		
$\text{tpy} + \text{e}^- = \text{tpy}^{\bullet+}$		+1.86
$\text{EtO-tpy} + \text{e}^- = \text{EtO-tpy}^{\bullet+}$		+1.70
$\text{bpyNO} + \text{e}^- = \text{bpyNO}^{\bullet+}$		+1.31

* /H₂O denotes explicit solvent molecule used in DFT calculations. ** Experimental values are in parentheses.

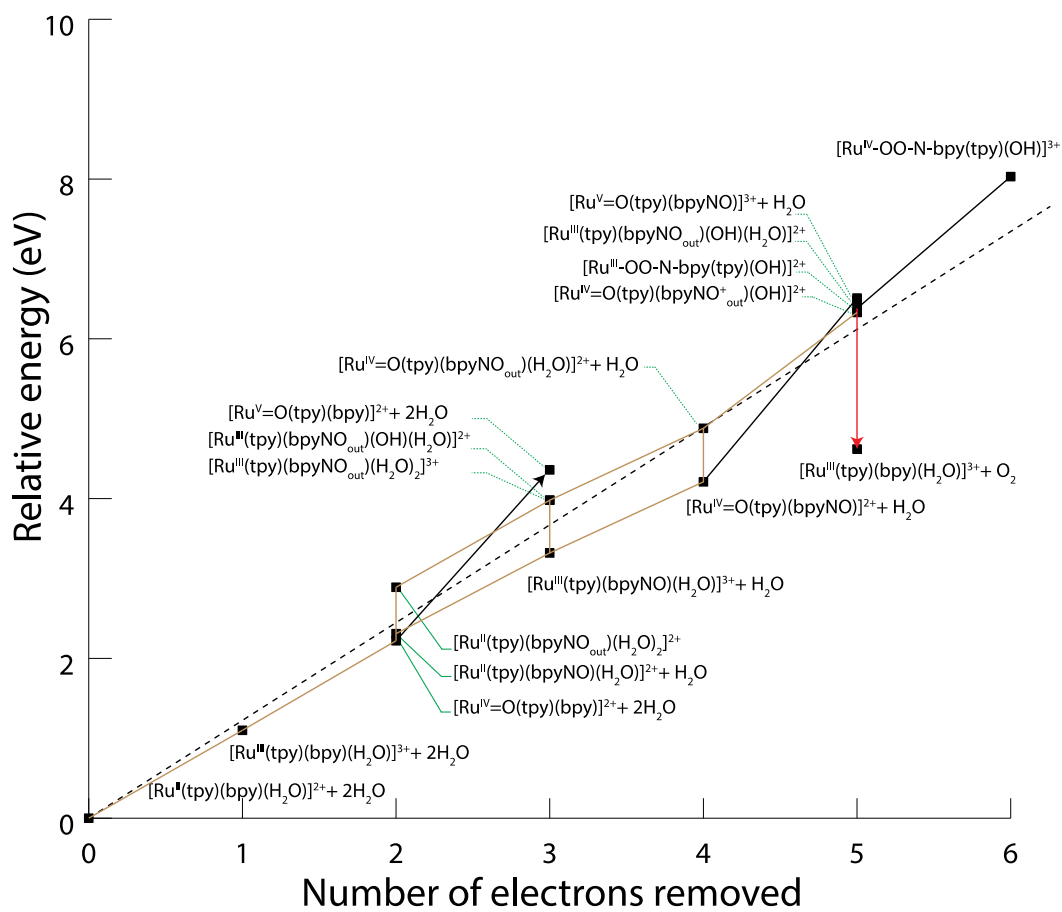


Figure 3-9. Latimer Frost diagram of $[\text{Ru}^{\text{II}}(\text{tpy})(\text{bpy})(\text{H}_2\text{O})]^{2+}$. This diagram is focused on bpy ligand oxidation.

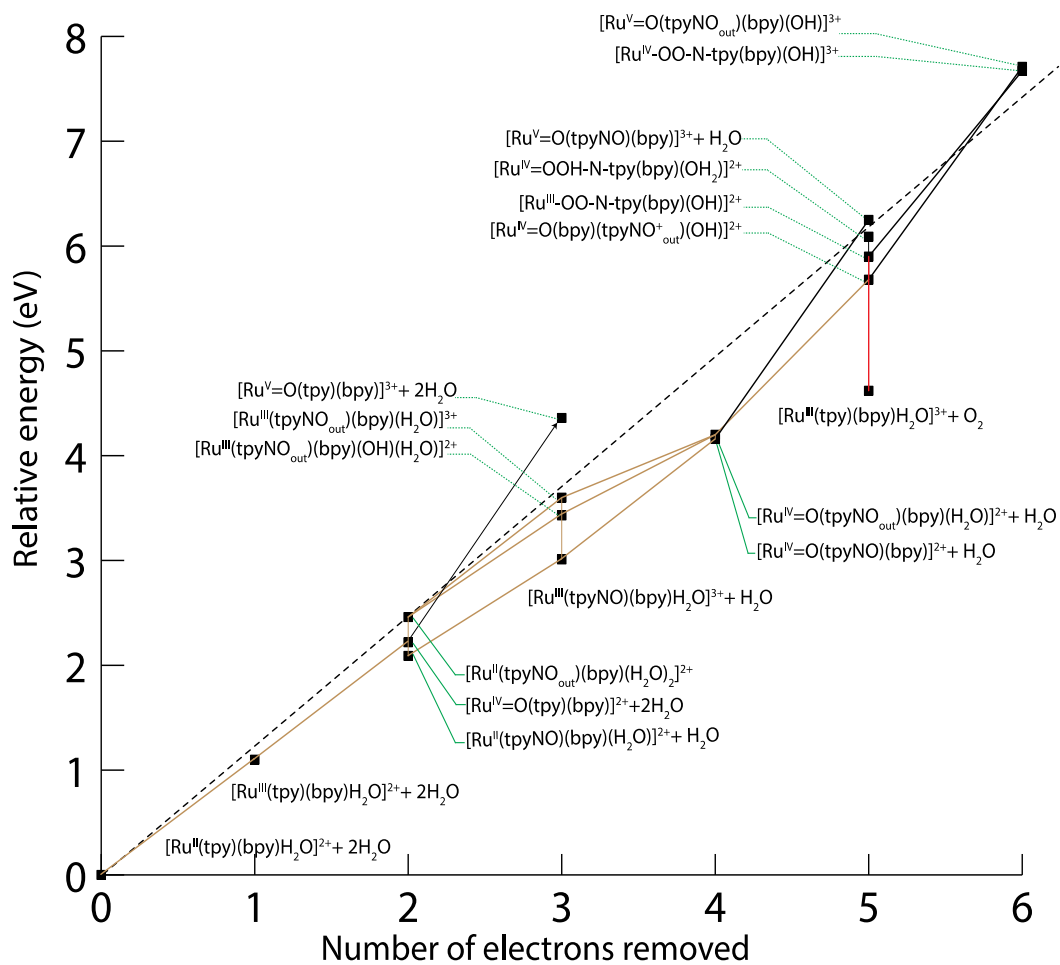


Figure 3-10. Latimer Frost diagram of $[\text{Ru}^{\text{II}}(\text{tpy})(\text{bpy})(\text{H}_2\text{O})]^{2+}$. This diagram is focused on tpy ligand oxidation.

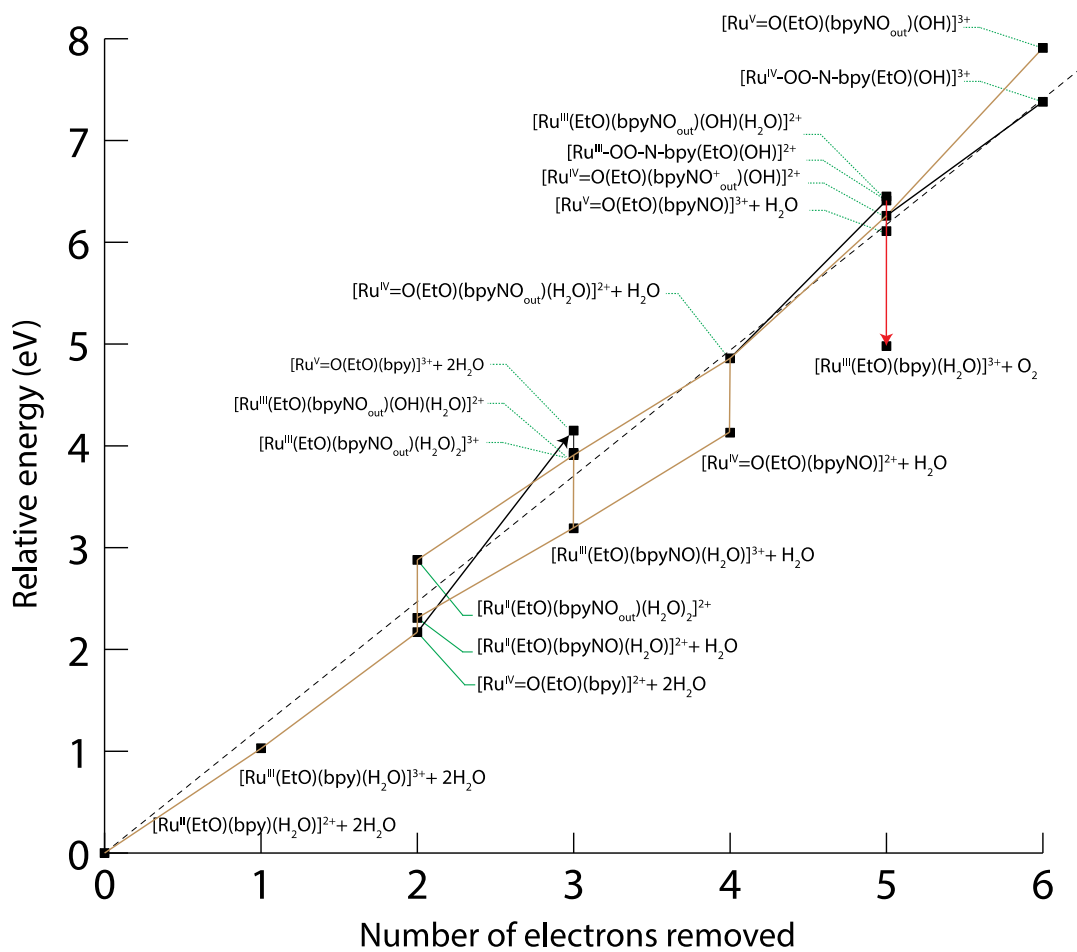


Figure 3-11. Latimer Frost diagram of $[\text{Ru}^{\text{II}}(\text{EtO-tpy})(\text{bpy})(\text{H}_2\text{O})]^{2+}$. This diagram is focused on bpy ligand oxidation.

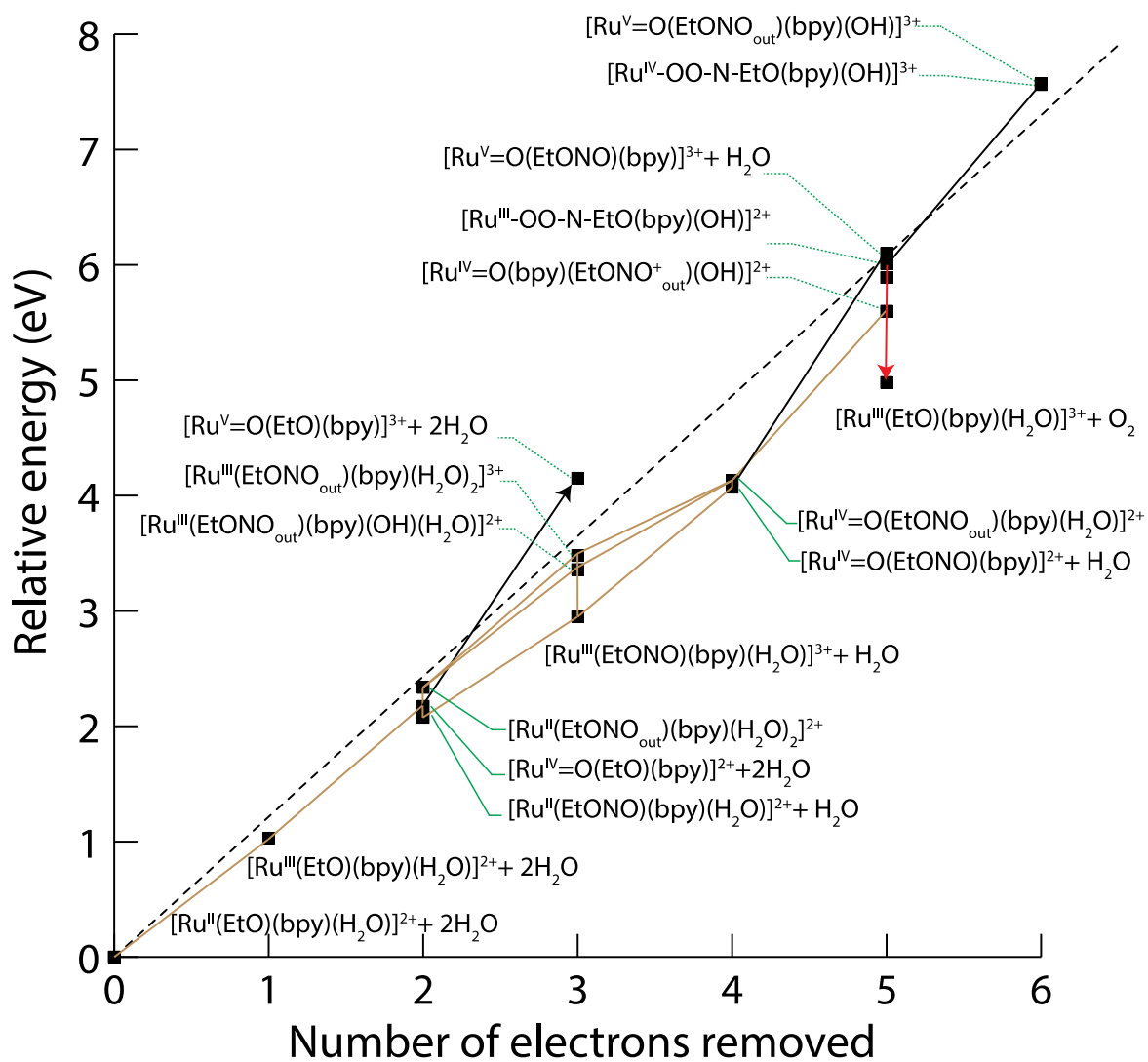


Figure 3-12. Latimer Frost diagram of $[\text{Ru}^{\text{II}}(\text{tpy})(\text{bpy})(\text{H}_2\text{O})]^{2+}$. This diagram is focused on EtO-tpy ligand oxidation.

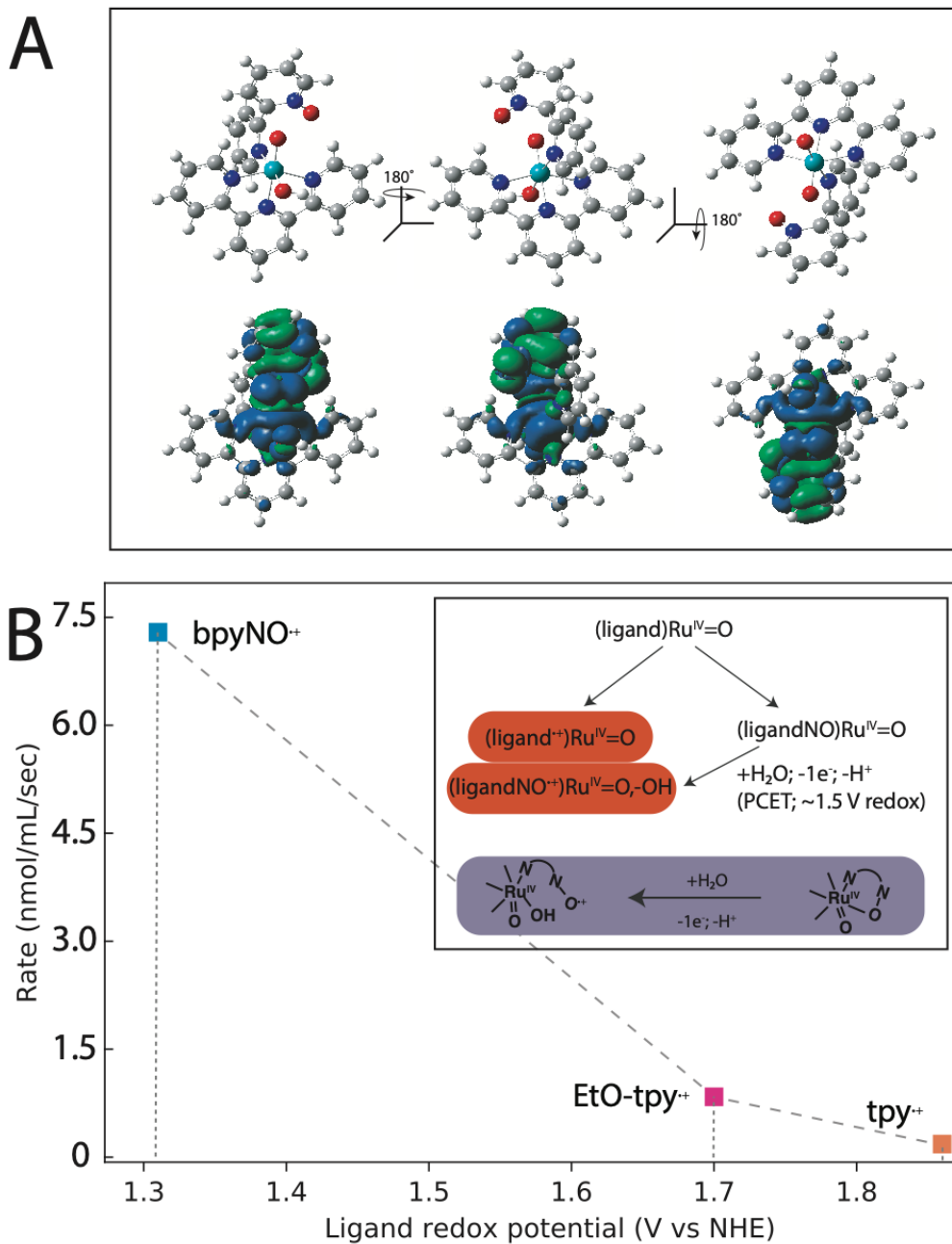


Figure 3-13. (A) Spin density of $[\text{Ru}^{\text{IV}}=\text{O}(\text{tpy})(\text{bpyNO}^+_{\text{out}})(\text{OH})]^{2+}$ in three different views. (B) DFT computed $\text{Ru}^{\text{V}}=\text{O}$ redox potentials (**Table 3-1**) do not correlate with the rate of O_2 evolution. We found that redox potentials for ligand oxidation (dashed lines) correlate better with O_2 evolution rates. Transient ligand oxidation with the formation of the ligand-N-oxide lowers the oxidation potential of the ligand, allowing it to store the third hole needed for water activation.

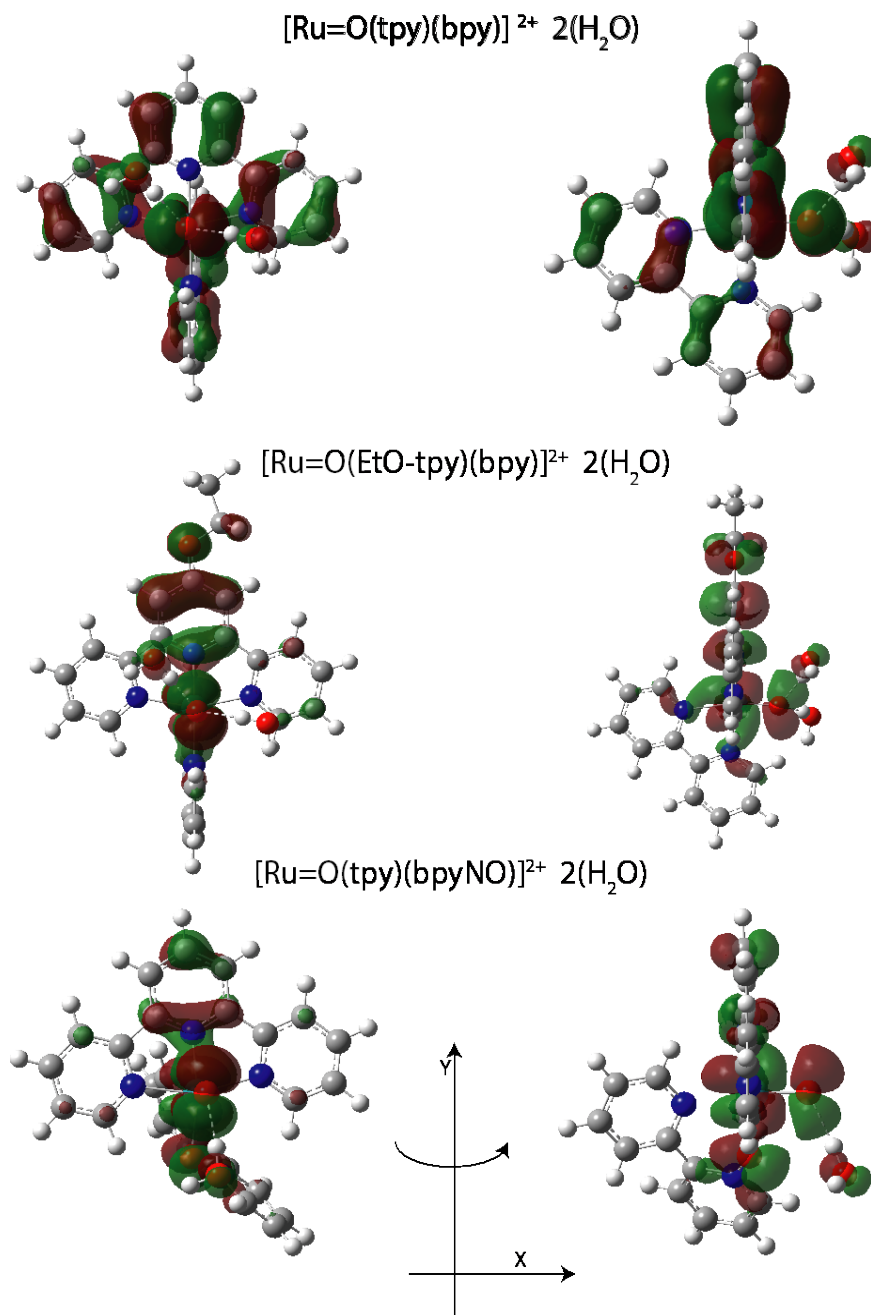
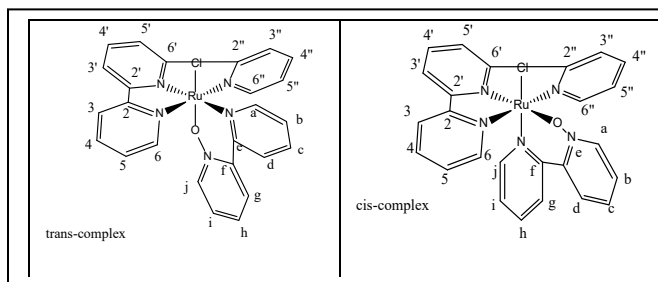


Figure 3-14. HOMO orbitals of the (1); (2) and (1-NO) in $[\text{Ru}^{\text{IV}}=\text{O}]^{2+}$ state. Delocalization to EtO-tpy and bpyNO ligands is evident. Thus, these ligands can delocalize hole upon oxidation.

3.5 Materials and methods

Ultra-pure nitric acid was used (Catalog No. 225711 from Sigma Aldrich). Commercially available ligands and precursors were used such as bpy, tpy, bpy-NO and 4'-chloro-terpyridine. Aqueous solutions were



prepared using ultrapure (Type 1) water (resistivity 18.2 M Ω .cm at 25°C, TOC 4 μ g/L), Millipore.

[Ru^{II}(bpy)(tpy)Cl]Cl and [Ru^{II}(bpy)(4'-EtO-tpy)Cl]Cl (tpy = 2,2';6',2''-terpyridine, bpy = 2,2'-bipyridine) were synthesized and characterized as described in the literature.^{75, 99} Synthesis of [Ru(tpy)(C₂O₄)(H₂O)]*2H₂O reference compound was performed according to procedure described previously.¹⁰² bpy-NO ligand was obtained from Sigma-Aldrich. [Ru(tpy)(bpy-NO)Cl]Cl was prepared by procedure similar to synthesis of the [Ru^{II}(bpy)(tpy)Cl]Cl¹⁰² with following details:

150 mg of Ru(tpy)Cl₃ (0.34 mmol) and 58 mg of bpy-NO (1 equiv), 0.1 ml of trimethylamine and 30 mg of LiCl were mixed in solution of 40 ml of ethanol and 2 ml of water and refluxed for 1 hour at temperature not exceeding 100° C. After cooling to room temperature all solvents were evaporated at reduced pressure to dryness. ¹H NMR of a residue was taken showing the presence of 61% of [Ru(tpy)(bpy-NO)Cl]Cl. The residue was separated using 100% ethanol on a silica gel column (Sorbtech, 200*400mesh), collecting 3-4 ml fractions. Products in the fractions were monitored by UV-vis and NMR. All steps of the synthesis were completed under the dim red light due to suspected light sensitivity. Elution from silica gel column with ethanol resulted in first purple fraction of *trans*- isomer with very low content of compound; later [Ru(bpy)(tpy)Cl]⁺ was eluted followed by fractions enriched with *cis*-[Ru(bpy-NO)(tpy)Cl]⁺. Later fractions allowed to isolate pure *cis*-Ru(bpyNO)(tpy)Cl₂ for catalytic tests and spectroscopy.

Table 3-5. $[\text{Ru}^{\text{II}}(\text{EtO-tpy})(\text{bpy})\text{H}_2\text{O}]^{2+}$ theoretical free energy and other intermediates and molecules that are necessary to explain our ligand oxidation model. All the theoretical energies are calculated by DFT

Compound name	Energy (Hartree)	Charge	Spin
$[\text{Ru}^{\text{II}}(\text{EtO-tpy})(\text{bpy})(\text{H}_2\text{O})]^{2+} + 2\text{H}_2\text{O}$	-6063.1936	2	1
$[\text{Ru}^{\text{III}}(\text{EtO-tpy})(\text{bpy})(\text{H}_2\text{O})]^{3+} + 2 \text{H}_2\text{O}$	-6062.9926	3	2
$[\text{Ru}^{\text{IV}}=\text{O}(\text{EtO-tpy})(\text{bpy})]^{2+} + 2\text{H}_2\text{O}$	-6061.9319	2	3
$[\text{Ru}^{\text{II}}(\text{EtO-tpyNO})(\text{bpy})(\text{H}_2\text{O})]^{2+} + \text{H}_2\text{O}$	-6061.9354	2	1
$[\text{Ru}^{\text{II}}(\text{EtO-tpyNO}_{\text{out}})(\text{bpy})(\text{H}_2\text{O})_2]^{2+}$	-6061.9259	2	1
$[\text{Ru}^{\text{III}}(\text{EtO-tpyNO})(\text{bpy})(\text{H}_2\text{O})]^{3+} + \text{H}_2\text{O}$	-6061.7401	3	2
$[\text{Ru}^{\text{III}}(\text{EtO-tpyNO}_{\text{out}})(\text{bpy})(\text{H}_2\text{O})_2]^{3+}$	-6061.720665	3	2
$[\text{Ru}^{\text{V}}=\text{O}(\text{EtO-tpy})(\text{bpy})]^{3+} + 2\text{H}_2\text{O}$	-6061.696071	3	2
$[\text{Ru}^{\text{IV}}=\text{O}(\text{EtO-tpyNO})(\text{bpy})]^{2+} + \text{H}_2\text{O}$	-6060.680218	2	3
$[\text{Ru}^{\text{IV}}=\text{O}(\text{EtO-tpyNO}_{\text{out}})(\text{bpy})(\text{H}_2\text{O})]^{2+} + \text{H}_2\text{O}$	-6060.678033	2	3
$[\text{Ru}^{\text{V}}=\text{O}(\text{EtO-tpyNO})(\text{bpy})]^{3+} + \text{H}_2\text{O}$	-6060.442537	3	2
$[\text{Ru}^{\text{IV}}=\text{O}(\text{EtO-tpyNO}^*_{\text{out}})(\text{bpy})(\text{OH})]^{2+}$	-6060.033192	2	2
$[\text{Ru}^{\text{III}}\text{-OO-N-EtO-tpy}(\text{bpy})(\text{OH})]^{2+}$	-6060.022448	2	2
$[\text{Ru}^{\text{IV}}\text{-OO-N-EtO-tpy}(\text{bpy})(\text{OH})]^{3+}$	-6059.797853	3	3
$[\text{Ru}^{\text{III}}(\text{EtO-tpy})(\text{bpy})(\text{H}_2\text{O})]^{3+}$	-5910.163554	3	2
$[\text{Ru}^{\text{III}}(\text{EtO-tpyNO}_{\text{out}})(\text{bpy})(\text{OH})(\text{H}_2\text{O})]^{2+}$	-6061.297377	2	2
$[\text{Ru}^{\text{V}}=\text{O}(\text{EtO-tpyNO}_{\text{out}})(\text{bpy})(\text{OH})]^{3+}$	-6059.797511	3	3
$[\text{Ru}^{\text{III}}\text{-OO-N-EtO-tpy}(\text{bpy})(\text{OH})(\text{H}_2\text{O})]^{2+}$	-6136.431179	2	2
$[\text{Ru}^{\text{II}}(\text{EtO-tpy})(\text{bpyNO})(\text{H}_2\text{O})]^{2+} + \text{H}_2\text{O}$	-6061.926853	2	1

Table 3-5 continued

$[\text{Ru}^{\text{II}}(\text{EtO-tpy})(\text{bpyNO}_{\text{out}})(\text{H}_2\text{O})_2]^{2+}$	-6061.90599	2	1
$[\text{Ru}^{\text{III}}(\text{EtO-tpy})(\text{bpyNO})(\text{H}_2\text{O})]^{3+} + \text{H}_2\text{O}$	-6061.731287	3	2
$[\text{Ru}^{\text{III}}(\text{EtO-tpy})(\text{bpyNO}_{\text{out}})(\text{H}_2\text{O})_2]^{3+}$	-6061.704895	3	2
$[\text{Ru}^{\text{V}}=\text{O}(\text{EtO-tpy})(\text{bpy})]^{3+} + 2\text{H}_2\text{O}$	-6061.696071	3	2
$[\text{Ru}^{\text{IV}}=\text{O}(\text{EtO-tpy})(\text{bpyNO})]^{2+} + \text{H}_2\text{O}$	-6060.678003	2	3
$[\text{Ru}^{\text{IV}}=\text{O}(\text{EtO-tpy})(\text{bpyNO}_{\text{out}})(\text{H}_2\text{O})]^{2+}$	-6060.651182	2	3
$[\text{Ru}^{\text{V}}=\text{O}(\text{EtO-tpy})(\text{bpyNO})]^{3+} + \text{H}_2\text{O}$	-6060.442187	3	2
$[\text{Ru}^{\text{IV}}=\text{O}(\text{EtO-tpy})(\text{bpyNO}^{*+}_{\text{out}})(\text{OH})]^{2+}$	-6060.008901	2	2
$[\text{Ru}^{\text{III}}\text{-OO-N-bpy}(\text{EtO-tpy})(\text{OH})]^{2+}$	-6060.003355	2	2
$[\text{Ru}^{\text{IV}}\text{-OO-N-bpy}(\text{EtO-tpy})(\text{OH})]^{3+}$	-6059.784984	3	3
$[\text{Ru}^{\text{III}}(\text{EtO-tpy})(\text{bpy})(\text{H}_2\text{O})]^{3+}$	-5910.163554	3	2
$[\text{Ru}^{\text{III}}(\text{EtO-tpy})(\text{bpyNO}_{\text{out}})(\text{OH})(\text{H}_2\text{O})]^{2+}$	-6061.276355	2	2
$[\text{Ru}^{\text{III}}\text{-OO-N-bpy}(\text{EtO-tpy})(\text{H}_2\text{O})]^{2+}$	-6136.414861	2	2
H_2O	-76.413	0	1
O_2	-150.320134	0	3

Table 3-6. Theoretical Analysis of Oxidation, Oxygen Atom Transfer and O-O bond formation in $[\text{Ru}^{\text{II}}(\text{EtO-tpy})(\text{bpy})(\text{H}_2\text{O})]^{2+}$ water oxidation catalyst. Number in parenthesis are the experimental values

			$\Delta G/\text{eV}$	E_0/eV
	$[\text{Ru}^{\text{III}}(\text{EtO-tpy})(\text{bpy})(\text{H}_2\text{O})]^{3+} + 2\text{H}_2\text{O} + \text{e}$	\rightarrow	$[\text{Ru}^{\text{II}}(\text{EtO-tpy})(\text{bpy})(\text{H}_2\text{O})]^{2+} + 2\text{H}_2\text{O}$	(0.98 ⁷⁵) 1.03
	$[\text{Ru}^{\text{IV}}=\text{O}(\text{EtO-tpy})(\text{bpy})]^{2+} + 2\text{H}_2\text{O} + \text{e} + 2\text{H}^+$	\rightarrow	$[\text{Ru}^{\text{III}}(\text{EtO-tpy})(\text{bpy})(\text{H}_2\text{O})]^{3+} + 2\text{H}_2\text{O}$	(1.24 ⁷⁵) 1.14
	$[\text{Ru}^{\text{V}}=\text{O}(\text{EtO-tpy})(\text{bpy})]^{3+} + 2\text{H}_2\text{O} + \text{e}$	\rightarrow	$[\text{Ru}^{\text{IV}}=\text{O}(\text{EtO-tpy})(\text{bpy})]^{2+} + 2\text{H}_2\text{O}$	1.98
EtO-tpy Path	$[\text{Ru}^{\text{IV}}=\text{O}(\text{EtO-tpy})(\text{bpy})]^{2+} + 2\text{H}_2\text{O}$	\rightarrow	$[\text{Ru}^{\text{II}}(\text{EtO-tpyNO})(\text{bpy})(\text{H}_2\text{O})]^{2+} + \text{H}_2\text{O}$	-0.09
	$[\text{Ru}^{\text{III}}(\text{EtO-tpyNO})(\text{bpy})(\text{H}_2\text{O})]^{3+} + \text{H}_2\text{O} + \text{e}$	\rightarrow	$[\text{Ru}^{\text{II}}(\text{EtO-tpyNO})(\text{bpy})(\text{H}_2\text{O})]^{2+} + \text{H}_2\text{O}$	0.87
	$[\text{Ru}^{\text{IV}}=\text{O}(\text{EtO-tpyNO})(\text{bpy})]^{2+} + \text{H}_2\text{O} + \text{e} + 2\text{H}^+$	\rightarrow	$[\text{Ru}^{\text{III}}(\text{EtO-tpyNO})(\text{bpy})(\text{H}_2\text{O})]^{3+} + \text{H}_2\text{O}$	1.12
	$[\text{Ru}^{\text{V}}=\text{O}(\text{EtO-tpyNO})(\text{bpy})]^{3+} + \text{H}_2\text{O} + \text{e}$	\rightarrow	$[\text{Ru}^{\text{IV}}=\text{O}(\text{EtO-tpyNO})(\text{bpy})]^{2+} + \text{H}_2\text{O}$	2.03
	$[\text{Ru}^{\text{II}}(\text{EtO-tpyNO})(\text{bpy})(\text{H}_2\text{O})]^{2+} + \text{H}_2\text{O}$	\rightarrow	$[\text{Ru}^{\text{II}}(\text{EtO-tpyNO}_{\text{out}})(\text{bpy})(\text{H}_2\text{O})_2]^{2+}$	0.26
	$[\text{Ru}^{\text{III}}(\text{EtO-tpyNO})(\text{bpy})(\text{H}_2\text{O})]^{3+} + \text{H}_2\text{O}$	\rightarrow	$[\text{Ru}^{\text{III}}(\text{EtO-tpyNO}_{\text{out}})(\text{bpy})(\text{H}_2\text{O})_2]^{3+}$	0.53
	$[\text{Ru}^{\text{IV}}=\text{O}(\text{EtO-tpyNO}_{\text{out}})(\text{bpy})(\text{H}_2\text{O})]^{2+} + \text{e} + 2\text{H}^+$	\rightarrow	$[\text{Ru}^{\text{III}}(\text{EtO-tpyNO}_{\text{out}})(\text{bpy})(\text{H}_2\text{O})_2]^{3+}$	0.65
	$[\text{Ru}^{\text{IV}}=\text{O}(\text{EtO-tpyNO}_{\text{out}})(\text{bpy})(\text{OH})]^{2+} + \text{e} + \text{H}^+$	\rightarrow	$[\text{Ru}^{\text{IV}}=\text{O}(\text{EtO-tpyNO}_{\text{out}})(\text{bpy})(\text{H}_2\text{O})]^{2+}$	1.47
	$[\text{Ru}^{\text{IV}}=\text{O}(\text{EtO-tpyNO}_{\text{out}})(\text{bpy})(\text{OH})]^{2+}$	\rightarrow	$[\text{Ru}^{\text{III}}-\text{OO}-\text{N}-\text{EtO-tpy}(\text{bpy})(\text{OH})]^{2+}$	0.29
	$[\text{Ru}^{\text{IV}}-\text{OO}-\text{N}-\text{EtO-tpy}(\text{bpy})(\text{OH})]^{3+} + \text{e}$	\rightarrow	$[\text{Ru}^{\text{III}}-\text{OO}-\text{N}-\text{EtO-tpy}(\text{bpy})(\text{OH})]^{2+}$	1.67
	$[\text{Ru}^{\text{III}}-\text{OO}-\text{N}-\text{EtO-tpy}(\text{bpy})(\text{OH})]^{2+} + \text{H}^+$	\rightarrow	$[\text{Ru}^{\text{III}}(\text{EtO-tpy})(\text{bpy})(\text{H}_2\text{O})]^{3+} + \text{O}_2$	-0.91
	$[\text{Ru}^{\text{III}}(\text{EtO-tpyNO}_{\text{out}})(\text{bpy})(\text{OH})(\text{H}_2\text{O})]^{2+} + \text{e} + \text{H}^+$	\rightarrow	$[\text{Ru}^{\text{II}}(\text{EtO-tpyNO}_{\text{out}})(\text{bpy})(\text{H}_2\text{O})]^{2+}$	1.02
	$[\text{Ru}^{\text{V}}=\text{O}(\text{EtO-tpyNO}_{\text{out}})(\text{bpy})(\text{OH})]^{3+} + \text{e}$	\rightarrow	$[\text{Ru}^{\text{IV}}=\text{O}(\text{EtO-tpyNO}_{\text{out}})(\text{bpy})(\text{OH})]^{2+}$	1.97
	$[\text{Ru}^{\text{III}}-\text{OO}-\text{N}-\text{EtO-tpy}(\text{bpy})(\text{OH})]^{2+} + \text{H}_2\text{O}$	\rightarrow	$[\text{Ru}^{\text{III}}-\text{OO}-\text{N}-\text{EtO-tpy}(\text{bpy})(\text{H}_2\text{O})]^{2+}$	0.41
bpy Path	$[\text{Ru}^{\text{IV}}=\text{O}(\text{EtO-tpy})(\text{bpy})]^{2+} + 2\text{H}_2\text{O}$	\rightarrow	$[\text{Ru}^{\text{II}}(\text{EtO-tpy})(\text{bpyNO})(\text{H}_2\text{O})]^{2+} + \text{H}_2\text{O}$	0.14
	$[\text{Ru}^{\text{III}}(\text{EtO-tpy})(\text{bpyNO})(\text{H}_2\text{O})]^{3+} + \text{H}_2\text{O} + \text{e}$	\rightarrow	$[\text{Ru}^{\text{II}}(\text{EtO-tpy})(\text{bpyNO})(\text{H}_2\text{O})]^{2+} + \text{H}_2\text{O}$	0.88
	$[\text{Ru}^{\text{IV}}=\text{O}(\text{EtO-tpy})(\text{bpyNO})]^{2+} + \text{H}_2\text{O} + \text{e} + 2\text{H}^+$	\rightarrow	$[\text{Ru}^{\text{III}}(\text{EtO-tpy})(\text{bpyNO})(\text{H}_2\text{O})]^{3+} + \text{H}_2\text{O}$	0.94
	$[\text{Ru}^{\text{V}}=\text{O}(\text{EtO-tpy})(\text{bpyNO})]^{3+} + \text{H}_2\text{O} + \text{e}$	\rightarrow	$[\text{Ru}^{\text{IV}}=\text{O}(\text{EtO-tpy})(\text{bpyNO})]^{2+} + \text{H}_2\text{O}$	1.98
	$[\text{Ru}^{\text{II}}(\text{EtO-tpy})(\text{bpyNO})(\text{H}_2\text{O})]^{2+} + \text{H}_2\text{O}$	\rightarrow	$[\text{Ru}^{\text{II}}(\text{EtO-tpy})(\text{bpyNO}_{\text{out}})(\text{H}_2\text{O})_2]^{2+}$	0.57
	$[\text{Ru}^{\text{III}}(\text{EtO-tpy})(\text{bpyNO})(\text{H}_2\text{O})]^{3+} + \text{H}_2\text{O}$	\rightarrow	$[\text{Ru}^{\text{III}}(\text{EtO-tpy})(\text{bpyNO}_{\text{out}})(\text{H}_2\text{O})_2]^{3+}$	0.72
	$[\text{Ru}^{\text{IV}}=\text{O}(\text{EtO-tpy})(\text{bpyNO}_{\text{out}})(\text{H}_2\text{O})]^{2+} + \text{H}_2\text{O} + \text{e} + 2\text{H}^+$	\rightarrow	$[\text{Ru}^{\text{III}}(\text{EtO-tpy})(\text{bpyNO}_{\text{out}})(\text{H}_2\text{O})_2]^{3+}$	0.95
	$[\text{Ru}^{\text{IV}}=\text{O}(\text{EtO-tpy})(\text{bpyNO}_{\text{out}})(\text{OH})]^{2+} + \text{e} + \text{H}^+$	\rightarrow	$[\text{Ru}^{\text{IV}}=\text{O}(\text{EtO-tpy})(\text{bpyNO}_{\text{out}})(\text{H}_2\text{O})]^{2+}$	1.40
	$[\text{Ru}^{\text{IV}}=\text{O}(\text{EtO-tpy})(\text{bpyNO}_{\text{out}})(\text{OH})]^{2+}$	\rightarrow	$[\text{Ru}^{\text{III}}-\text{OO}-\text{N}-\text{bpy}(\text{EtO-tpy})(\text{OH})]^{2+}$	0.15
	$[\text{Ru}^{\text{IV}}-\text{OO}-\text{N}-\text{bpy}(\text{EtO-tpy})(\text{OH})]^{3+} + \text{e}$	\rightarrow	$[\text{Ru}^{\text{III}}-\text{OO}-\text{N}-\text{bpy}(\text{EtO-tpy})(\text{OH})]^{2+}$	1.50
	$[\text{Ru}^{\text{III}}-\text{OO}-\text{N}-\text{bpy}(\text{EtO-tpy})(\text{OH})]^{2+} + \text{H}^+$	\rightarrow	$[\text{Ru}^{\text{III}}(\text{EtO-tpy})(\text{bpy})(\text{H}_2\text{O})]^{3+} + \text{O}_2$	-1.43
	$[\text{Ru}^{\text{III}}(\text{EtO-tpy})(\text{bpyNO}_{\text{out}})(\text{OH})(\text{H}_2\text{O})]^{2+} + \text{e} + \text{H}^+$	\rightarrow	$[\text{Ru}^{\text{II}}(\text{EtO-tpy})(\text{bpyNO}_{\text{out}})(\text{H}_2\text{O})]^{2+}$	1.05
	$[\text{Ru}^{\text{III}}-\text{OO}-\text{N}-\text{bpy}(\text{EtO-tpy})(\text{OH})]^{2+} + \text{H}_2\text{O}$	\rightarrow	$[\text{Ru}^{\text{III}}-\text{OO}-\text{N}-\text{bpy}(\text{EtO-tpy})(\text{H}_2\text{O})]^{2+}$	0.19

Table 3-7. $[\text{Ru}^{\text{II}}(\text{tpy})(\text{bpy})(\text{H}_2\text{O})]^{2+}$ theoretical free energy and other intermediates and molecules that are necessary to explain our ligand oxidation model. All the theoretical energies are calculated by DFT

	Energy (Hartree)	Charge	Spin
$[\text{Ru}^{\text{II}}(\text{tpy})(\text{bpy})(\text{H}_2\text{O})]^{2+} + 2\text{H}_2\text{O}$	-5909.40469	2	1
$[\text{Ru}^{\text{III}}(\text{tpy})(\text{bpy})(\text{H}_2\text{O})]^{3+} + 2\text{H}_2\text{O}$	-5909.20128	3	2
$[\text{Ru}^{\text{IV}}=\text{O}(\text{tpy})(\text{bpy})]^{2+} + 2\text{H}_2\text{O}$	-5908.14137	2	3
$[\text{Ru}^{\text{II}}(\text{tpyNO})(\text{bpy})(\text{H}_2\text{O})]^{2+} + \text{H}_2\text{O}$	-5908.14612	2	1
$[\text{Ru}^{\text{II}}(\text{tpyNO}_{\text{out}})(\text{bpy})(\text{H}_2\text{O})_2]^{2+}$	-5908.1323	2	1
$[\text{Ru}^{\text{III}}(\text{tpyNO})(\text{bpy})(\text{H}_2\text{O})]^{3+} + \text{H}_2\text{O}$	-5907.94891	3	2
$[\text{Ru}^{\text{III}}(\text{tpyNO}_{\text{out}})(\text{bpy})(\text{H}_2\text{O})_2]^{3+}$	-5907.92728	3	2
$[\text{Ru}^{\text{V}}=\text{O}(\text{tpy})(\text{bpy})]^{3+} + 2\text{H}_2\text{O}$	-5907.89932	3	2
$[\text{Ru}^{\text{IV}}=\text{O}(\text{tpyNO})(\text{bpy})]^{2+} + \text{H}_2\text{O}$	-5906.88805	2	3
$[\text{Ru}^{\text{IV}}=\text{O}(\text{tpyNO}_{\text{out}})(\text{bpy})(\text{H}_2\text{O})]^{2+} + \text{H}_2\text{O}$	-5906.88663	2	3
$[\text{Ru}^{\text{V}}=\text{O}(\text{tpyNO})(\text{bpy})]^{3+} + \text{H}_2\text{O}$	-5906.64827	3	2
$[\text{Ru}^{\text{IV}}=\text{O}(\text{tpyNO}^+_{\text{out}})(\text{bpy})(\text{OH})]^{2+}$	-5906.24119	2	2
$[\text{Ru}^{\text{III}}-\text{OO}-\text{N}-\text{tpy}(\text{bpy})(\text{OH})]^{2+}$	-5906.2332	2	2
$[\text{Ru}^{\text{IV}}-\text{OO}-\text{N}-\text{tpy}(\text{bpy})(\text{OH})]^{3+}$	-5906.0052	3	3
$[\text{Ru}^{\text{III}}(\text{tpy})(\text{bpy})(\text{H}_2\text{O})]^{3+}$	-5756.37159	3	2
$[\text{Ru}^{\text{III}}(\text{tpyNO}_{\text{out}})(\text{bpy})(\text{OH})(\text{H}_2\text{O})]^{2+}$	-5907.50568	2	2
$[\text{Ru}^{\text{V}}=\text{O}(\text{tpyNO}_{\text{out}})(\text{bpy})(\text{OH})]^{3+}$	-5906.00357	3	3
$[\text{Ru}^{\text{III}}-\text{OO}-\text{N}-\text{tpy}(\text{bpy})(\text{H}_2\text{O})]^{2+}$	-5982.63938	2	2
$[\text{Ru}^{\text{II}}(\text{tpy})(\text{bpyNO})(\text{H}_2\text{O})]^{2+} + \text{H}_2\text{O}$	-5908.137992	2	1
$[\text{Ru}^{\text{II}}(\text{tpy})(\text{bpyNO}_{\text{out}})(\text{H}_2\text{O})_2]^{2+}$	-5908.116543	2	1
$[\text{Ru}^{\text{III}}(\text{tpy})(\text{bpyNO})(\text{H}_2\text{O})]^{3+} + \text{H}_2\text{O}$	-5907.937806	3	2
$[\text{Ru}^{\text{III}}(\text{tpy})(\text{bpyNO}_{\text{out}})(\text{H}_2\text{O})_2]^{3+}$	-5907.913232	3	2
$[\text{Ru}^{\text{V}}=\text{O}(\text{tpy})(\text{bpy})]^{3+} + 2\text{H}_2\text{O}$	-5907.899321	3	2
$[\text{Ru}^{\text{IV}}=\text{O}(\text{tpy})(\text{bpyNO})]^{2+} + \text{H}_2\text{O}$	-5906.88637	2	3
$[\text{Ru}^{\text{IV}}=\text{O}(\text{tpy})(\text{bpyNO}_{\text{out}})(\text{H}_2\text{O})]^{2+}$	-5906.861787	2	3
$[\text{Ru}^{\text{V}}=\text{O}(\text{tpy})(\text{bpyNO})]^{3+} + \text{H}_2\text{O}$	-5906.645237	3	2

Table 3-7 continued

$[\text{Ru}^{\text{IV}}=\text{O}(\text{bpyNO}^{\bullet+}_{\text{out}})(\text{tpy})(\text{OH})]^{2+}$	-5906.215415	2	2
$[\text{Ru}^{\text{III}}-\text{OO}-\text{N}-\text{bpy}(\text{tpy})(\text{OH})]^{2+}$	-5906.210938	2	2
$[\text{Ru}^{\text{IV}}-\text{OO}-\text{N}-\text{bpy}(\text{tpy})(\text{OH})]^{3+}$	-5905.991693	3	3
$[\text{Ru}^{\text{III}}(\text{tpy})(\text{bpy})(\text{H}_2\text{O})]^{3+}$	-5756.371589	3	2
$[\text{Ru}^{\text{III}}(\text{tpy})(\text{bpyNO}_{\text{out}})(\text{OH})(\text{H}_2\text{O})]^{2+}$	-5907.485559	2	2
$[\text{Ru}^{\text{III}}-\text{OO}-\text{N}-\text{bpy}(\text{tpy})(\text{H}_2\text{O})]^{2+}$	-5982.625022	2	2

Table 3-8. Theoretical Analysis of Oxidation, Oxygen Atom Transfer and O-O bond formation in $[\text{Ru}^{\text{II}}(\text{tpy})(\text{bpy})\text{H}_2\text{O}]^{2+}$ water oxidation catalyst.

			$\Delta\text{G}/\text{eV}$	E_0/eV	
	$[\text{Ru}^{\text{III}}(\text{tpy})(\text{bpy})(\text{H}_2\text{O})]^{3+} + 2\text{H}_2\text{O} + \text{e}$	\rightarrow	$[\text{Ru}^{\text{II}}(\text{tpy})(\text{bpy})(\text{H}_2\text{O})]^{2+} + 2\text{H}_2\text{O}$	1.10	
	$[\text{Ru}^{\text{IV}}=\text{O}(\text{tpy})(\text{bpy})]^{2+} + 2\text{H}_2\text{O} + \text{e} + 2\text{H}^+$	\rightarrow	$[\text{Ru}^{\text{III}}(\text{tpy})(\text{bpy})(\text{H}_2\text{O})]^{3+} + 2\text{H}_2\text{O}$	1.12	
	$[\text{Ru}^{\text{V}}=\text{O}(\text{tpy})(\text{bpy})]^{3+} + 2\text{H}_2\text{O} + \text{e}$	\rightarrow	$[\text{Ru}^{\text{IV}}=\text{O}(\text{tpy})(\text{bpy})]^{2+} + 2\text{H}_2\text{O}$	2.15	
tpy Path	$[\text{Ru}^{\text{IV}}=\text{O}(\text{tpy})(\text{bpy})]^{2+} + 2\text{H}_2\text{O}$	\rightarrow	$[\text{Ru}^{\text{II}}(\text{tpyNO})(\text{bpy})]^{2+} + 2\text{H}_2\text{O}$	-0.13	
	$[\text{Ru}^{\text{III}}(\text{tpyNO})(\text{bpy})(\text{H}_2\text{O})]^{3+} + \text{H}_2\text{O} + \text{e}$	\rightarrow	$[\text{Ru}^{\text{II}}(\text{tpyNO})(\text{bpy})(\text{H}_2\text{O})]^{2+} + \text{H}_2\text{O}$		0.93
	$[\text{Ru}^{\text{IV}}=\text{O}(\text{tpyNO})(\text{bpy})]^{2+} + \text{H}_2\text{O} + \text{e} + 2\text{H}^+$	\rightarrow	$[\text{Ru}^{\text{III}}(\text{tpyNO})(\text{bpy})(\text{H}_2\text{O})]^{3+} + \text{H}_2\text{O}$		1.15
	$[\text{Ru}^{\text{V}}=\text{O}(\text{tpyNO})(\text{bpy})]^{3+} + \text{H}_2\text{O} + \text{e}$	\rightarrow	$[\text{Ru}^{\text{IV}}=\text{O}(\text{tpyNO})(\text{bpy})]^{2+} + \text{H}_2\text{O}$		2.08
	$[\text{Ru}^{\text{II}}(\text{tpyNO})(\text{bpy})(\text{H}_2\text{O})]^{2+} + \text{H}_2\text{O}$	\rightarrow	$[\text{Ru}^{\text{II}}(\text{tpyNO}_{\text{out}})(\text{bpy})(\text{H}_2\text{O})_2]^{2+}$	0.38	
	$[\text{Ru}^{\text{III}}(\text{tpyNO})(\text{bpy})(\text{H}_2\text{O})]^{3+} + \text{H}_2\text{O}$	\rightarrow	$[\text{Ru}^{\text{III}}(\text{tpyNO}_{\text{out}})(\text{bpy})(\text{H}_2\text{O})_2]^{3+}$	0.59	
	$[\text{Ru}^{\text{IV}}=\text{O}(\text{tpyNO}_{\text{out}})(\text{bpy})(\text{H}_2\text{O})]^{2+} + \text{e} + 2\text{H}^+$	\rightarrow	$[\text{Ru}^{\text{III}}(\text{tpyNO}_{\text{out}})(\text{bpy})(\text{H}_2\text{O})]^{3+}$		0.60
	$[\text{Ru}^{\text{IV}}=\text{O}(\text{tpyNO}^{*\text{out}})(\text{bpy})(\text{OH})]^{2+} + \text{e} + \text{H}^+$	\rightarrow	$[\text{Ru}^{\text{IV}}=\text{O}(\text{tpyNO}_{\text{out}})(\text{bpy})(\text{H}_2\text{O})]^{2+}$		1.48
	$[\text{Ru}^{\text{IV}}=\text{O}(\text{tpyNO}^{*\text{out}})(\text{bpy})(\text{OH})]^{2+}$	\rightarrow	$[\text{Ru}^{\text{III}}-\text{OO}-\text{N}-\text{tpy}(\text{bpy})(\text{OH})]^{2+}$	0.22	
	$[\text{Ru}^{\text{IV}}-\text{OO}-\text{N}-\text{tpy}(\text{bpy})(\text{OH})]^{3+} + \text{e}$	\rightarrow	$[\text{Ru}^{\text{III}}-\text{OO}-\text{N}-\text{tpy}(\text{bpy})(\text{OH})]^{2+}$		1.76
	$[\text{Ru}^{\text{III}}-\text{OO}-\text{N}-\text{tpy}(\text{bpy})(\text{OH})]^{2+} + \text{H}^+$	\rightarrow	$[\text{Ru}^{\text{III}}(\text{tpy})(\text{bpy})(\text{H}_2\text{O})]^{3+} + \text{O}_2$	-1.28	
	$[\text{Ru}^{\text{III}}(\text{tpyNO}_{\text{out}})(\text{bpy})(\text{OH})(\text{H}_2\text{O})]^{2+} + \text{e} + \text{H}^+$	\rightarrow	$[\text{Ru}^{\text{II}}(\text{tpyNO}_{\text{out}})(\text{bpy})(\text{H}_2\text{O})_2]^{2+}$		0.97
	$[\text{Ru}^{\text{V}}=\text{O}(\text{tpyNO}_{\text{out}})(\text{bpy})(\text{OH})]^{3+} + \text{e}$	\rightarrow	$[\text{Ru}^{\text{IV}}=\text{O}(\text{tpyNO}^{*\text{out}})(\text{bpy})(\text{OH})]^{2+}$		2.03
	$[\text{Ru}^{\text{III}}-\text{OO}-\text{N}-\text{tpy}(\text{bpy})(\text{OH})]^{2+} + \text{H}_2\text{O}$	\rightarrow	$[\text{Ru}^{\text{III}}-\text{OO}-\text{N}-\text{tpy}(\text{bpy})(\text{H}_2\text{O})]^{2+}$	-0.40	0.40
bpy Path	$[\text{Ru}^{\text{IV}}=\text{O}(\text{tpy})(\text{bpy})]^{2+} + 2\text{H}_2\text{O}$	\rightarrow	$[\text{Ru}^{\text{II}}(\text{tpy})(\text{bpyNO})(\text{H}_2\text{O})]^{2+} + \text{H}_2\text{O}$	0.09	
	$[\text{Ru}^{\text{III}}(\text{tpy})(\text{bpyNO})(\text{H}_2\text{O})]^{3+} + \text{H}_2\text{O} + \text{e}$	\rightarrow	$[\text{Ru}^{\text{II}}(\text{tpy})(\text{bpyNO})(\text{H}_2\text{O})]^{2+} + \text{H}_2\text{O}$		1.01
	$[\text{Ru}^{\text{IV}}=\text{O}(\text{tpy})(\text{bpyNO})]^{2+} + \text{H}_2\text{O} + \text{e} + 2\text{H}^+$	\rightarrow	$[\text{Ru}^{\text{III}}(\text{tpy})(\text{bpyNO})(\text{H}_2\text{O})]^{3+} + \text{H}_2\text{O}$		0.89
	$[\text{Ru}^{\text{V}}=\text{O}(\text{tpy})(\text{bpyNO})]^{3+} + \text{H}_2\text{O} + \text{e}$	\rightarrow	$[\text{Ru}^{\text{IV}}=\text{O}(\text{tpy})(\text{bpyNO})]^{2+} + \text{H}_2\text{O}$		2.12
	$[\text{Ru}^{\text{II}}(\text{tpy})(\text{bpyNO})(\text{H}_2\text{O})]^{2+} + \text{H}_2\text{O}$	\rightarrow	$[\text{Ru}^{\text{II}}(\text{tpy})(\text{bpyNO}_{\text{out}})(\text{H}_2\text{O})_2]^{2+}$	0.58	
	$[\text{Ru}^{\text{III}}(\text{tpy})(\text{bpyNO})(\text{H}_2\text{O})]^{3+} + \text{H}_2\text{O}$	\rightarrow	$[\text{Ru}^{\text{III}}(\text{tpy})(\text{bpyNO}_{\text{out}})(\text{H}_2\text{O})_2]^{3+}$	0.67	
	$[\text{Ru}^{\text{IV}}=\text{O}(\text{tpy})(\text{bpyNO}_{\text{out}})(\text{H}_2\text{O})]^{2+} + \text{e} + 2\text{H}^+$	\rightarrow	$[\text{Ru}^{\text{III}}(\text{tpy})(\text{bpyNO}_{\text{out}})(\text{H}_2\text{O})_2]^{3+}$		0.89
	$[\text{Ru}^{\text{IV}}=\text{O}(\text{tpy})(\text{bpyNO}^{*\text{out}})(\text{OH})]^{2+} + \text{e} + \text{H}^+$	\rightarrow	$[\text{Ru}^{\text{IV}}=\text{O}(\text{tpy})(\text{bpyNO}_{\text{out}})(\text{H}_2\text{O})]^{2+}$		1.51
	$[\text{Ru}^{\text{IV}}=\text{O}(\text{tpy})(\text{bpyNO}^{*\text{out}})(\text{OH})]^{2+}$	\rightarrow	$[\text{Ru}^{\text{III}}-\text{OO}-\text{N}-\text{bpy}(\text{tpy})(\text{OH})]^{2+}$	0.12	
	$[\text{Ru}^{\text{IV}}-\text{OO}-\text{N}-\text{bpy}(\text{tpy})(\text{OH})]^{3+} + \text{e}$	\rightarrow	$[\text{Ru}^{\text{III}}-\text{OO}-\text{N}-\text{bpy}(\text{tpy})(\text{OH})]^{2+}$		1.53
	$[\text{Ru}^{\text{III}}-\text{OO}-\text{N}-\text{bpy}(\text{tpy})(\text{OH})]^{2+} + \text{H}^+$	\rightarrow	$[\text{Ru}^{\text{III}}(\text{tpy})(\text{bpy})(\text{H}_2\text{O})]^{3+} + \text{O}_2$	-1.88	
	$[\text{Ru}^{\text{III}}(\text{tpy})(\text{bpyNO}_{\text{out}})(\text{OH})(\text{H}_2\text{O})]^{2+} + \text{e} + \text{H}^+$	\rightarrow	$[\text{Ru}^{\text{II}}(\text{tpy})(\text{bpyNO}_{\text{out}})(\text{H}_2\text{O})_2]^{2+}$		1.09
	$[\text{Ru}^{\text{IV}}=\text{O}(\text{tpy})(\text{bpyNO}^{*\text{out}})(\text{OH})]^{2+} + \text{H}_2\text{O}$	\rightarrow	$[\text{Ru}^{\text{III}}-\text{OOH}-\text{Nbpy}(\text{tpy})(\text{H}_2\text{O})]^{2+}$	-0.092	0.092

$[\text{Ru}^{\text{II}}(\text{bpy})(\text{tpy})(\text{H}_2\text{O})]\text{Cl}_2$; $[\text{Ru}^{\text{II}}(\text{bpy})(4'\text{-EtO-tpy})(\text{H}_2\text{O})]\text{Cl}_2$ and $[\text{Ru}^{\text{II}}(\text{bpy-NO})(\text{tpy})(\text{H}_2\text{O})]\text{Cl}_2$ were prepared by aging corresponding chlorides in pure water for 24 hrs. After that 2 equiv of silver nitrate were added to solution, which then was filtered, in order to remove Cl^- ions. When Ce^{IV} is used as oxidant, it is prepared freshly daily. O_2 evolution activity using Ce^{IV} was in agreement with earlier reports.^{12, 75, 79, 103} Oxygen evolution was measured with a PC operated Clark type polarographic oxygen electrode from Oxygraph System (Hansatech Instruments Ltd.). The sample was housed within a hermetic borosilicate glass reaction vessel. Calibration was carried out by measurements of the signal from O_2 -saturated water in an open reaction vessel. Sodium dithionite, an oxygen depleting agent, was added to the water, and the drop in the signal was related to the solubility of oxygen in water at room temperature (262 $\mu\text{mol/L}$). The glass vessel was thoroughly washed with water and 0.6 mL of Ru complex solution in 0.1M HNO_3 was added. A defined number of Ce^{IV} equivalents were carefully added into the chamber and oxygen evolution was measured as a function of time.

To prepare EPR samples, 200 μl of 1 mM solution of Ru complex in 0.1 M HNO_3 were oxidized with a defined number of Ce^{IV} equivalents, transferred in EPR tube and frozen in liquid nitrogen within 30 sec. Low-temperature X-band EPR spectra were recorded with a Bruker EMX X-band spectrometer equipped with a X-Band CW microwave bridge. The sample temperature was maintained at 20 K using ColdEdge closed cycle cryostat. For EPR signal quantitation, the standard EPR sample tubes were filled with sample through all of the resonator space and signal intensities were measured on the same day and in the same conditions to allow direct comparison of the signal intensities.

The resonance Raman was collected using a HeCd CW laser with the wavelength of 420 nm and 20 mW power and second-harmonic wave of Nd:YAG (532nm). The sample is held in a Teflon custom design electrochemical cell with clear polypropylene thin film window for bulk electrolysis resonance Raman measurement. For the Ce^{IV} treatment a drop of sample directly was exposed to laser. The diameter of the laser beam at the sample is about 0.5 mm. The orientation of the laser beam, the sample, and the detector was held in zero degrees. Two fused silica lenses were used to collect the Raman signal and focus it at the Shamrock 303i spectrometer input slit. The width of slit was 50 μm . The Semrock edge pass filter eliminated the Rayleigh scattering to get into the spectrometer. The holographic grating with 1800 l/mm for 442 nm laser and a 1200 l/mm

(grating blaze 500) for 532 nm laser were used to disperse the light and later collimated light exposed on iDus 420 Andor camera.

The DFT calculations were performed with Gaussian09 using the B3LYP exchange-correlation (XC) functional. The 6-31G* basis was set for all organic atoms (C, O, N, H), and the all electron DGDZVP basis was set for the Ru atom. The CPCM polarizable conductor model was used to model water solvation. The value of the reference potential (NHE) was assigned value to 4.44 V and the solvation free energy of a proton to -11.64 V. Earlier we demonstrated that this computational technique reproduces bond distances and redox potentials of the Ru complexes.^{12, 61, 62, 67, 104} With our calculation protocol we have historically achieved match (within expected 0.2 eV) to all unambiguously known redox potentials for all analyzed by our group Ru complexes as outlined in our earlier publications.^{12, 61, 62}

A Thermo Nicolet Nexus FTIR Spectrometer conducted FTIR measurements. OMNIC software, a MCT detector, and a KBr beam splitter are some of specification of the spectrometer. The spectrometer was continuously purged with nitrogen gas before and during measurements. For data collection, the powder sample was pressed against an attenuated total reflectance (ATR) diamond crystal. The measurement was conducted in the dark, at room temperature and dim ambient light to make sure the light will not cause the unintended reactions. The graph consists of 36 scans with 4 cm^{-1} resolution.

UV-Vis absorptions spectroscopy was conducted by using a Cary 300 UV-Vis spectrometer. All solutions were measured in a quartz cuvette with path line 1 mm.

All of the electrochemistry experiments were conducted with BASi Epsilon potentiostat with a platinum counter electrode, and Ag/AgCl (saturated KCl) as the reference electrode. The reference electrode was calibrated against the $\text{Fe}(\text{CN})_6^{3-}/\text{Fe}(\text{CN})_6^{4-}$ redox couple in 0.5 M NaCl, which should be 0.208 V versus Ag/AgCl (saturated KCl). Bulk electrolysis experiments were performed in a three-compartment electrochemical cell with each compartment separated by porous glass frits. For cyclic voltammetry a polished platinum electrode with Ag/AgCl (saturated KCl) as reference electrode was used. The scan rate in CV was 0.1 V/S. All the solutions were in 0.1 M HNO_3 and all the presented measurements are already subtracted by pure platinum and 0.1M HNO_3 as background.

CHAPTER 4. INSIGHTS INTO MOF REACTIVITY: CHEMICAL WATER OXIDATION CATALYSIS BY A [RU(TPY)(DCBPY)OH₂]²⁺ MODIFIED METAL-ORGANIC FRAMEWORK

This chapter is published in whole or part in the ChemSusChem Journal with DOI: 10.1002/cssc.201701644

4.1 Abstract

Incorporating WOCs in metal organic frameworks (MOFs) is one of the ways to stabilize the system and increase the TON. [Ru(tpy)(bpy)(OH₂)]²⁺ was studied in the previous chapter. By modifying the bpy ligand to dcbpy the complex would become [Ru(tpy)(dcbpy)(OH₂)]²⁺. [Ru(tpy)(dcbpy)(OH₂)]²⁺ doped UiO-67 MOF. The MOF catalyst exhibited a single-site reaction pathway with kinetic behavior similar to that of a homogeneous Ru complex. The reaction was first order with respect to both the concentration of the Ru catalyst and ceric ammonium nitrate (CAN), with $k_{\text{cat}} = 3(\pm 2) \times 10^{-3} \text{ M}^{-1} \text{ s}^{-1}$ in HNO₃ (pH 0.5).⁹³ The common degradation pathways of ligand dissociation and dimerization were precluded by MOF incorporation, which led to sustained catalysis and greater reusability as opposed to the molecular catalyst in homogeneous solution. Lastly, at the same loading (ca. 97 nmol mg⁻¹), samples of different particle sizes generated the same amount of oxygen (ca. 100 nmol), indicative of in-MOF reactivity. The results suggest that the rate of redox-hopping charge transport is sufficient to promote chemistry throughout the MOF particulates.

4.2 Introduction

Metal organic frameworks (MOFs) have emerged as a promising class of porous catalysts due to many favorable properties.¹⁰⁵⁻¹⁰⁸ MOFs exhibit extremely high surface areas accessible through a network of pores or channels. The pore size can be tuned to enable size selective catalysis and the surface area enables a large number of active sites to be placed in a small geometric area. With the multi-component nature of MOFs, dual functionality and cooperative catalysis has been exhibited between linker and node, linker and linker, and node/linker and an encapsulated guest.¹⁰⁹⁻¹¹² Moreover, MOFs can lock known molecular catalysts into defined geometries, leading to enhanced stability, and confirmed single site reactivity.¹¹³⁻¹¹⁶

Recently, MOFs have been used to promote the electrochemical transformation of protons, carbon dioxide, and water, the critical components of artificial photosynthetic chemistry.¹¹⁷⁻¹²⁷ The primary mechanism for the reduction or oxidation of MOF bound catalytic active moieties is one of redox hopping, akin to that observed in linear polymers decorated with redox active inorganic or organic species.¹²⁷⁻¹³¹ In a redox hopping process, electrons and counter balancing ions diffuse through the framework limited by the rate of catalyst self-exchange and/or the diffusion of ions. The current observed in an electrochemical experiment is then diffusion limited and follows the classic Randles-Sevcik relationship $\text{current} \propto (\text{scan rate})^{1/2}$. Even considering such non-metallic transport, higher catalytic activity as compared to a monolayer of catalyst in the same geometric area has been observed. Specifically, the electrochemical oxidation of water by ruthenium-catalyst doped MOF was near 120 times that of the purely molecular approach. The enhancement was possible even considering only ~30% of the catalytic sites were electrochemically accessible.¹²⁷

While the demonstration of diffusion-limited current indicated that the chemistry extended beyond the surface of the electrode. True in-MOF reactivity was not exclusively confirmed. A key question that persists through the MOF literature remains. Does the observed catalysis occur on the surface or inside the MOF crystallites? Or more direct to electrochemical methods, is the rate of redox hopping sufficient to promote in-MOF reactivity? Unfortunately, due to the polycrystalline and polydisperse nature of the solvothermally deposited MOF films it is difficult to design experiments to directly address this concern. The common support for in-MOF reactivity comes from size-dependent studies or surface modification studies carried out on crystalline MOF powders.

Herein, we provide insight into the ability of redox hopping electron transport to promote in-MOF reactivity by $[\text{Ru}(\text{tpy})(\text{dcbpy})(\text{OH}_2)]^{2+}$ (tpy = 2,2':6',2''-terpyridine; dcbpy = 5,5'-dicarboxybipyridine) doped MOF, termed Ru-UiO-67. As a substitute to electrochemical methods, chemical oxidation by cerium ammonium nitrate (CAN) was carried out on pre-formed MOF crystallites. Modifications of the synthetic procedure, namely, adjusting the amount of modulator during the MOF synthesis, allowed for direct control of particle size. Therefore, in-MOF reactivity could be directly probed under pseudo-electrochemical conditions. In addition, two approaches for incorporation of $[\text{Ru}(\text{tpy})(\text{dcbpy})(\text{OH}_2)]^{2+}$ into UiO-67 structure were carried out: in situ synthesis and post-synthetic ligand exchange (PSE) of existing framework. Finally, Ru-UiO-67 presents an

opportunity to validate the single-site water oxidation reaction mechanism proposed in the literature.¹³²⁻¹³⁵ While inside the MOF structure, the catalysts are physically separated from each other by the structural Zr-oxo clusters and the pore space. Therefore, the bimolecular pathway and common deactivation pathways^{136, 137} are inoperative, as was confirmed with Raman studies. The results presented provide the guidelines for next iteration of MOF- based catalyst design with improved catalytic efficiency and higher turnover rates.

4.3 Results and Discussion

Among all single-site Ru-based water oxidation catalysts, $[\text{Ru}(\text{tpy})(\text{bpy})(\text{OH}_2)]^{2+}$ is a representative example, which was subjected to extensive mechanistic studies in the past.^{134, 135, 138-142} This complex can be readily functionalized with carboxylic acid groups on 5 and 5' positions of bipyridine ligand to serve as a linker in many MOF structures. For the present study, the modified catalyst was doped into the well-known UiO-67 structure^{143, 144} through replacement of the native biphenyldicarboxylate linker. The catalyst-doped UiO-67, termed Ru-UiO-67, was prepared via a previously reported procedure.¹²⁷ The acetic acid in the synthesis play the role of the modulator. In MOF synthesis, modulators are used to competitively bind to the inorganic nodes, slow particle growth, and aid in crystallization.

To probe the formation of the active catalytic state of the catalysts under chemical oxidation, Raman spectroscopy was carried out on UiO-67, Ru-UiO-67 and $[\text{Ru}(\text{tpy})(\text{dcbpy})\text{Cl}]\text{Cl}$. In **Figure 4-1**, a comparison between the Fourier Transform Raman (FTRaman) of the pure UiO-67, Ru-UiO-67, and $[\text{Ru}(\text{tpy})(\text{dcbpy})\text{Cl}]\text{Cl}$ complex is demonstrated. The spectrum of the Ru-UiO-67 is primarily a combination of the spectra of the pure UiO-67 and the Ru complex as one would expect. The signals attributed to the UiO-67 backbone are dominant in comparison to the Ru complex. This is simply a consequence of concentration.

By using different excitation wavelengths, different parts of Ru-UiO-67 can be probed. For example, upon excitation at 1064 nm, where both the Ru complex and the MOF are not resonant, the MOF structure is the main contributor to the Raman spectrum, In **Figure 4-1**. Upon excitation at 532 nm excitation was used, the signals from the Ru complex are noticeably enhanced, **Figure 4-2**. At this wavelength the excitation source is resonant with the absorption spectrum of the $[\text{Ru}(\text{tpy})(\text{bpy})\text{OH}_2]^{2+}$. By the combination of wavelengths/techniques, non-resonance Raman (FTRaman) and resonance Raman (RRaman), one can selectively monitor MOF components.

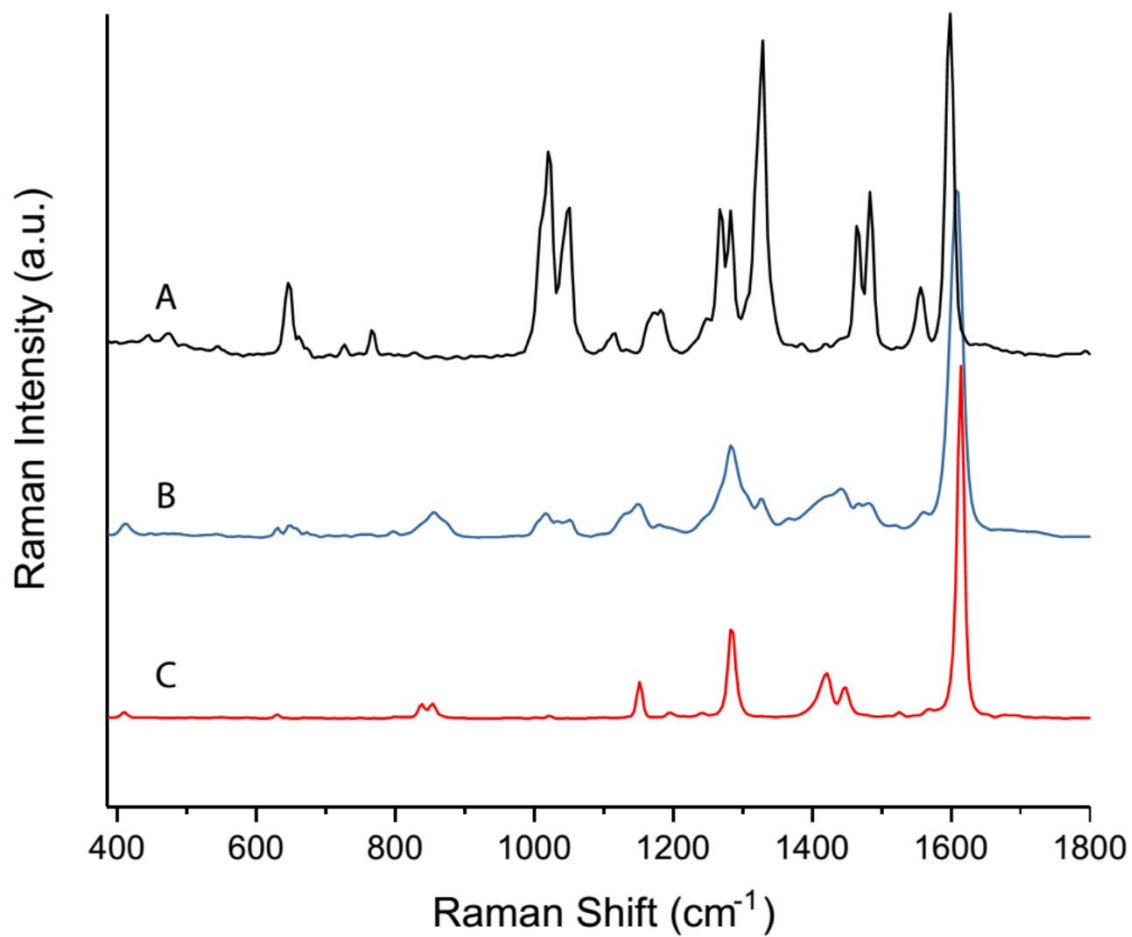


Figure 4-1. FTRaman ($\lambda_{\text{ex}} = 1064 \text{ nm}$) of (A, black) $[\text{Ru}(\text{tpy})(\text{dcbpy})\text{Cl}]\text{Cl}$, (B, blue) Ru-UiO-67 and (C, red) UiO-67.

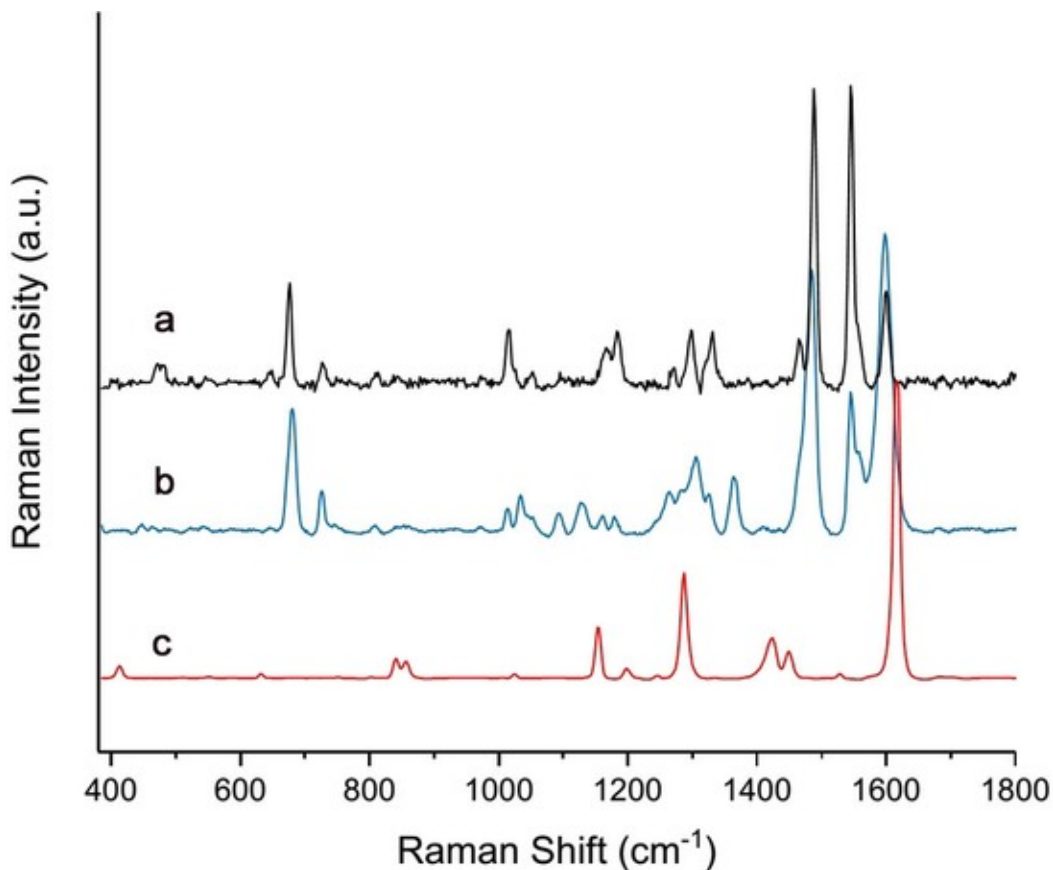


Figure 4-2. Raman ($\lambda_{\text{ex}}=532$ nm) spectra of a) $[\text{Ru}(\text{tpy})(\text{bpy})\text{Cl}]\text{Cl}$, b) Ru-UiO-67, and c) UiO-67.

The changes to the Raman spectrum of $[\text{Ru}(\text{tpy})(\text{bpy})(\text{H}_2\text{O})]^{2+}$ after treatment with a chemical oxidant, cerium ammonium nitrate (CAN) was monitored as a function of time, **Figure 4-3**. The Raman spectra of Ru-UiO-67 after CAN treatment show significant changes consistent with a change in oxidation state from Ru^{II} to Ru^{IV} and change of the Ru ligand environment from $\text{Ru}^{\text{II}}\text{-H}_2\text{O}$ to $\text{Ru}^{\text{IV}}\text{=O}$. Different peaks also experienced different resonance enhancement due to change of sample colour from light violet for initial material to brown for oxidized crystallites.

The most common deactivation pathway for $[\text{Ru}(\text{tpy})(\text{bpy})\text{OH}_2]^{2+}$ is the loss of the bipyridine ligand.^{134, 136, 137} If this process were to occur inside the framework, it would lead to the detachment of the putative $[\text{Ru}(\text{tpy})(\text{O}_2)(\text{H}_2\text{O})]^{2+}$ product from the MOF backbone and its presence in the surrounding solution. ICP-MS conducted on the reaction mixture after Ru-UiO-67 catalysis

experiments, found that only 1.2 ± 0.3 % of starting Ru inside the MOF leached out. Thus, immobilization of Ru catalyst inside the MOF appears to suppress this deactivation pathway.

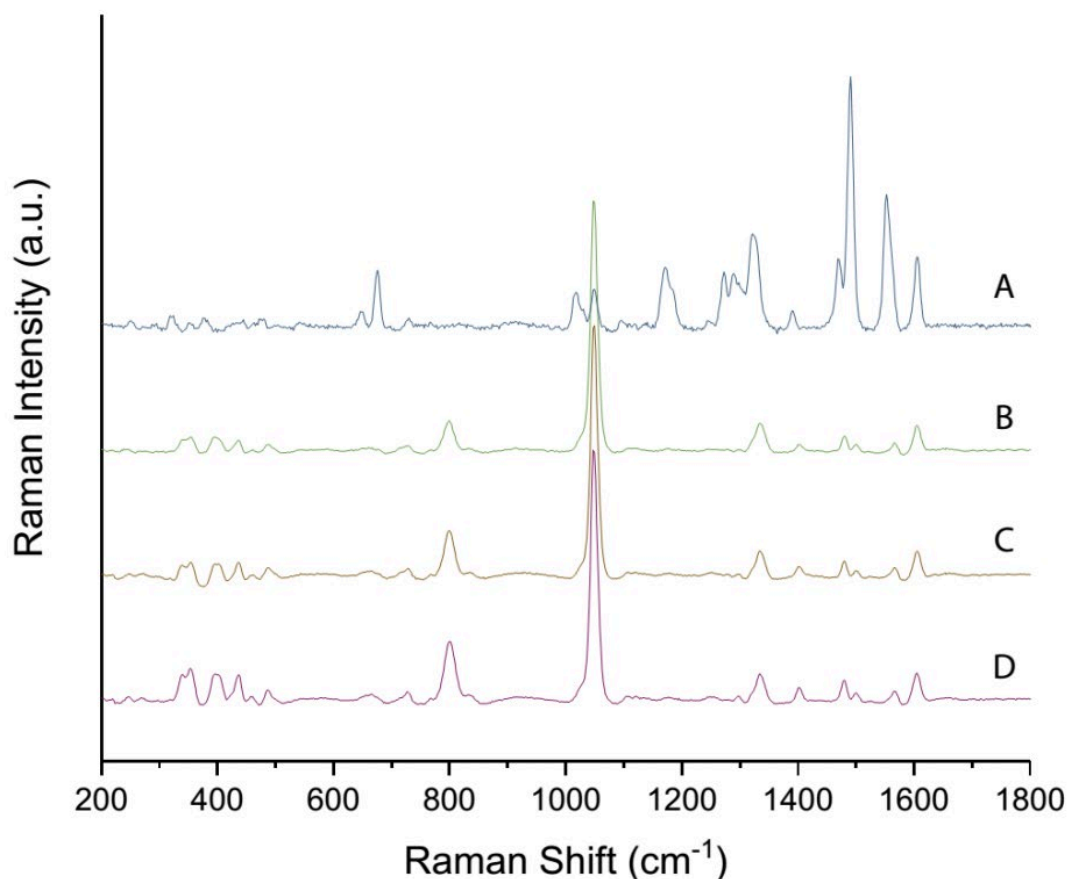


Figure 4-3. RRaman ($\lambda_{\text{ex}}=532$ nm) of Ru complex under CAN treatment (100 equivalents of CAN in nitric acid pH 1) at (A) the beginning, (B) 30 minutes, (C) 1 hour and (D) 2 hours later.

MOFs supports also prevent intermolecular side reactions between catalytic centres.^{115, 145, 146} Llobet et al. reported that after losing bipyridine ligand, Ru-OH₂ complex is susceptible to dimerization, resulting in $[(\text{tpy})(\text{bpy})\text{Ru}^{\text{IV}}(\mu\text{-O})\text{Ru}^{\text{IV}}(\text{tpy})(\text{O})(\text{H}_2\text{O})]^{4+}$ WOC.^{136, 137} Interestingly, in the RRaman spectrum of the molecular catalyst after CAN treatment in solution clear vibrations can be seen due to the formation of this dimeric species at low frequency (**Figure 4-4**). The stretching frequencies assigned to the dimer were confirmed by comparison to previously reported values.^{137, 147, 148} In the RRaman spectrum of Ru-UiO-67 after CAN treatment, the dimer is not observed. Therefore, in addition to the suppression of ligand dissociation, MOF incorporation

limited the dimerization pathway. The diffusion of the $[\text{Ru}(\text{tpy})(\text{O}_2)(\text{H}_2\text{O})]^{2+}$ fragment may be limited due to the confinement effect of the MOF pores, increasing possibility of recombination with parent bipyridine ligand and therefore, regeneration of the catalyst.¹¹⁰

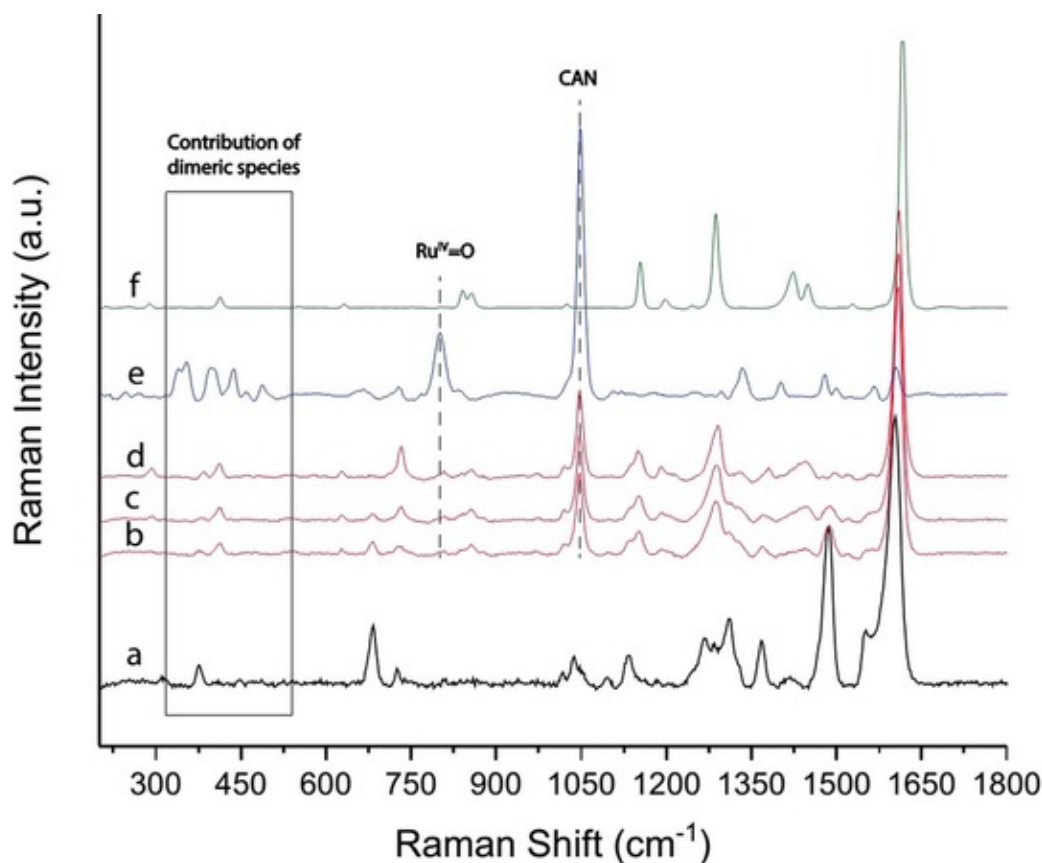


Figure 4-4. RRaman ($\lambda_{\text{ex}}=532$ nm) spectra of Ru-UiO-67 at a) $t=0$ min and after 100 mM CAN treatment (in nitric acid, pH 1): b) 0–20 min, c) 20–40 min, and d) 2 h. e) $[\text{Ru}(\text{tpy})(\text{bpy})(\text{OH}_2)]^{2+}$ solution incubated with CAN (100 equiv.) for 2 h. f) Untreated UiO-67. Spectral signatures of the Ru–O–Ru bridges were observed in 300–450 cm^{-1} Raman shift range in solution but not in the MOF framework.

The catalytic activity of Ru-UiO-67 for chemical water oxidation was confirmed and directly compared to $[\text{Ru}(\text{tpy})(\text{dcbpy})(\text{OH}_2)]^{2+}$ in solution by oxygen production studies (**Figure 4-5**). The amount of catalyst used in control reaction was matched with the Ru content in Ru-UiO-67 (2 μmol), as determined by ICP-MS. The time-dependent oxygen production showed that the initial oxygen generation rate of the ligand in solution is lower than that in the MOF. The initial O_2 production rate for Ru-UiO-67 was 0.43 nmol/s, while the production from the homogeneous catalyst was 0.25 nmol/s. Additionally, for the ligand control reaction, the oxygen production

ceased after 10 min, indicating deactivation of the dissolved Ru complex. In comparison, oxygen production from Ru-UiO-67 was observed for over 50 minutes. The maximum amount of oxygen produced during the experiment reached 110 ± 58 nmol for the soluble ligand, compared to 212 ± 25 nmol for the Ru-UiO-67 framework.

Based on these results, it was proposed that the prime mechanism for water oxidation inside Ru-UiO-67 is mononuclear. Therefore, reaction kinetics should exhibit first order relationship between evolved oxygen and the concentration of Ru catalyst. Berlinguette et al. showed that in 0.1 M HNO₃ the reaction is first order with respect to [Ru], while in 1 M HNO₃ the reaction is first order to both [Ru] and [CAN].¹⁴² In the present oxygen generation studies, the reaction was carried out at pH 0.5 (HNO₃). Thus, either kinetic regimes were possible. It was found that at constant MOF amount (and as a consequence constant [Ru]), the reaction is first order with respect to the concentration of CAN. On the other hand, when [CAN] is held constant, the reaction becomes first order to the [Ru]. Thus, water oxidation follows the following rate expression, Rate = $k_{cat}[CAN][Ru]$, where $k_{cat} = 3 (\pm 2) \times 10^{-3} \text{ M}^{-1} \text{ s}^{-1}$ for Ru-UiO-67. These findings provided further evidence for the single-site reaction pathway mechanism of this type of catalyst.

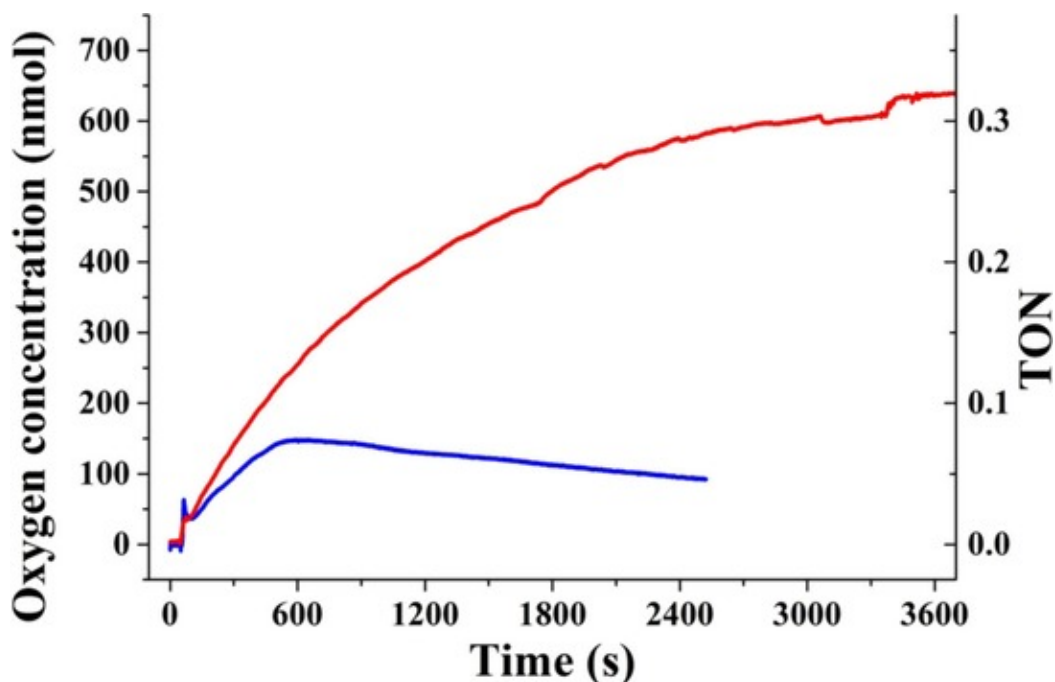


Figure 4-5. Oxygen-evolution data for Ru-UiO-67 (red) and [Ru(tpy)(dcbpy)Cl]Cl (blue) in solution (soaked in water 24h before catalysis experiment).

4.4 Experimental Section

4.4.1 Materials

All chemicals and solvents were used as obtained without further purification, including $\text{RuCl}_3 \cdot x\text{H}_2\text{O}$ (Acros, 35–40% Ru), 2,2'-bipyridyl-5,5'-dicarboxylic acid (dcbpy, Ark Pharm, Inc., 95%+), 2,2':6,2''-terpyridine, (tpy, Alfa Aesar, 97%), 4,4'-biphenyldicarboxylic acid (BPDC, TCI, 97%), zirconium chloride, (ZrCl_4 , Sigma-Aldrich, 98%), N,N-dimethylformamide (DMF, Fisher Scientific, HPLC grade > 99%), acetonitrile (Fisher Scientific, HPLC grade), Acetic acid (Fisher Chemical, glacial), sodium hydroxide (NaOH, Spectrum, 97%), cerium ammonium nitrate (CAN, Alfa Aesar, 99+%), sulfuric acid, (H_2SO_4 , Spectrum, ACS reagent), acetone, (Spectrum, HPLC grade).

Synthesis of $[\text{Ru}(\text{tpy})(\text{dcbpy})\text{Cl}]\text{Cl}$ (tpy = 2,2':6,2''-terpyridine, dcbpy=5,5'-dicarboxy-2,2'-bipyridine), and $[\text{Ru}(\text{tpy})(\text{dcbpy})\text{OH}_2](\text{ClO}_4)_2$

$[\text{Ru}(\text{tpy})(\text{dcbpy})\text{Cl}]\text{Cl}$ was synthesized using method adapted from published procedures.[45] $\text{Ru}(\text{tpy})\text{Cl}_3$ (300.0 mg, 0.68 mmol) and dcbpy (168.5 mg, 0.68 mmol) were refluxed in 100 mL of EtOH/water (v/v, 3:1) for 16 h. The reaction mixture was filtered hot and the filtrate was reduced to 25 mL by rotary evaporation. 3 mL of 1 M HCl was added and the solution was chilled in fridge for 1 day. The solid product was collected by filtration, washed with cool water and dried under air. To synthesize $[\text{Ru}(\text{tpy})(\text{dcbpy})\text{OH}_2](\text{ClO}_4)_2$, $[\text{Ru}(\text{tpy})(\text{dcbpy})\text{Cl}]\text{Cl}$ (162.3 mg, 0.25 mmol) and excess AgClO_4 (518.3 mg, 2.5 mmol) were refluxed in 100 mL acetone/water (v/v, 3:1) for 16 h. The AgCl precipitate was filtered off and the filtrate reduced to 25 mL by rotary evaporation. 3 mL of 1 M HClO_4 was added and the solution chilled in fridge for 1 day. The solid product was collected by filtration, washed with cool water and dried under air.

4.4.2 Fabrication of Ru-UiO-67 MOF powder

0.5 mmol of ZrCl_4 , x mmol of $[\text{Ru}(\text{tpy})(\text{dcbpy})\text{Cl}]\text{Cl}$, (0.5-x) mmol of BPDC ligand and acetic acid (17.5 mmol for loading dependent samples, 5 to 35 mmol for size dependent samples) were dissolved in 20 mL DMF in 6 dram vial. The mixture was sonicated until all the starting materials dissolved. The vial was sealed and heated at 120 °C for 48 h. After cooling to room temperature, the solid material was filtered and washed with DMF and acetone. The MOF powder was air-dried followed by soaking in acetone (3 d, solvent exchanged each day) to remove the

residual DMF in MOF pore space. The acetone soaked MOFs was evacuated at R. T. The MOF powder was soaked in water (pH ~ 3, adjusted with HNO₃) for 24 h. The powder was collected by centrifugation, washed with acetone and dried under vacuum at R. T.

4.4.3 FTRaman

FTRaman was performed with a Thermo Nicolet 6700 FTIR/FT-Raman Spectrophotometer at an excitation wavelength of 1064nm, and a power of 1 W. Spectral resolution was 8 cm⁻¹ and samples were housed in NMR tubes (MANUFACTURER AND ITEM # (get from chemistry store)). Each spectrum consists of approximately 1000 scans.

4.4.4 RRaman

RRaman was performed to have the advantage of suspending the sample in liquid (HNO₃ 0.1 M) to watch the dynamics in situ. The Laser wavelength was 532 nm (Second harmonic generator of Nd: YAG CW laser). Laser intensity has a power of 50mW. The orientation of the Laser and sample and detector was 0 degree. Spectrometer and CCD detector were both from Andor (spectrometer Shamrock 303i and camera was iDus 420). The exposure time was 20 seconds per scan, and each spectrum consists of 20 scans. Grating Groove Density was (line/mm):1199.2 with 500nm blazed. The slit aperture size was 80 μm.

4.4.5 Oxygen evolution measurement

In a typical experiment, ~15 mg of Ru-UiO-67 powder was added to 5 ml of HNO₃ solution (pH 0.5), while 0.15 mmol of CAN dissolved in 5 ml of HNO₃ solution (pH 0.5) in two separate vials. Both vials were sealed with rubber septa and the solution was purged with Argon for at least 30 min before each catalysis experiment. The CAN solution was transferred to the vial with MOF suspension using a 10 ml syringe. The headspace of the vial with Ru-UiO-67 was continuously purged with Argon until the completion of the CAN injection. The amount of oxygen evolved was measured by Unisense oxygen sensor OX-NP. After the reaction completion, the mixture was centrifuged at 3000 rpm for 5 min recovering the MOF catalysts, which was washed with water. The collected powder was soaked in acetone for 3 d to exchange the solvent. The MOF powder was isolated by centrifugation and dried on air.

4.5 Conclusions

In conclusion, $[\text{Ru}(\text{tpy})(\text{dcbpy})(\text{OH}_2)]^{2+}$ (tpy=2,2':6',2''-terpyridine, dcbpy=5,5'-dicarboxy-2,2'-bipyridine) catalyst embedded inside the UiO-67 backbone was found to catalyze water oxidation through a single-site catalytic pathway, exhibiting kinetics similar to those of its homogeneous counterpart. The lifetime of the catalytically active species in the hybrid Ru-UiO-67 system was enhanced relative to that of the molecular complex, and the MOF catalyst also demonstrated superior recyclability. This is most likely due to the ability of metal-organic framework (MOF) incorporation to shut-off common degradation pathways, including ligand release and dimerization.

CHAPTER 5. FACILE LIGHT INDUCED TRANSFORMATION OF $[\text{Ru}^{\text{II}}(\text{BPY})_2(\text{BPYNO})]^{2+}$ TO $[\text{Ru}^{\text{II}}(\text{BPY})_3]^{2+}$

This chapter is published in whole or part in the Inorganic Chemistry Journal with DOI: 10.1021/acs.inorgchem.0c01446

5.1 Abstract

In previous chapter we introduced and studied radical coupling as an alternative to water nucleophilic attack. In RC the N-oxide ligand plays a major role; here we study the properties and photo chemistry of this ligand in a similar ruthenium complex to $[\text{Ru}(\text{tpy})(\text{bpy})(\text{H}_2\text{O})]^{2+}$. Although a different complex, it can still reveal a lot about the properties of N-oxides in polypyridine ligands. Ru-based coordination compounds have important applications as photosensitizers and catalysts. $[\text{Ru}^{\text{II}}(\text{bpy})_2(\text{bpyNO})]^{2+}$ (bpy = 2,2'-bipyridine and bpyNO = 2,2'-bipyridine-N-oxide) was reported to be extremely light sensitive, but its light induced transformation pathways have not been analyzed. Here, we elucidated a mechanism of the light-induced transformation of $[\text{Ru}^{\text{II}}(\text{bpy})_2(\text{bpyNO})]^{2+}$ using UV-Vis, EPR, resonance Raman, and NMR spectroscopic techniques. The spectroscopic analysis was augmented with the DFT calculations. We concluded that upon 530-650 nm light excitation, $^3[\text{Ru}^{\text{III}}(\text{bpyNO}^\cdot)(\text{bpy})_2]^{2+}$ is formed similarly to the $^3[\text{Ru}^{\text{III}}(\text{bpy}^\cdot)(\text{bpy})_2]^{2+}$ light induced state of the well-known $[\text{Ru}^{\text{II}}(\text{bpy})_3]^{2+}$ photosensitizer. An electron localization on the bpyNO ligand was confirmed by obtaining a unique EPR signal of reduced $[\text{Ru}^{\text{II}}(\text{bpy})_2(\text{bpyNO}^\cdot)]^+$ ($g_{xx} = 2.02$, $g_{yy} = 1.99$, and $g_{zz} = 1.87$ and ^{14}N hfs $A_{xx} = 12$ G, $A_{yy} = 34$ G and $A_{zz} = 11$ G). $^3[\text{Ru}^{\text{III}}(\text{bpyNO}^\cdot)(\text{bpy})_2]^{2+}$ may evolve via breaking of the Ru-O-N fragment at two different positions resulting in $[\text{Ru}^{\text{IV}}=\text{O}(\text{bpy})_2(\text{bpy}_{\text{out}})]^{2+}$ for breakage at O-|N bond and $[\text{Ru}^{\text{II}}(\text{H}_2\text{O})(\text{bpy})_2(\text{bpyNO}_{\text{out}})]^{2+}$ for breakage at Ru-|O bond. These pathways were found to have comparable ΔG . A reduction of $[\text{Ru}^{\text{IV}}=\text{O}(\text{bpy})_2(\text{bpy}_{\text{out}})]^{2+}$ may result in water elimination and formation of $[\text{Ru}^{\text{II}}(\text{bpy})_3]^{2+}$. The expected intermediates, $[\text{Ru}^{\text{III}}(\text{bpy})_2(\text{bpyNO})]^{3+}$ and $[\text{Ru}^{\text{III}}(\text{bpy})_3]^{3+}$, were detected by EPR. In addition, a new signal with $g_{xx} = 2.38$, $g_{yy} = 2.10$, and $g_{zz} = 1.85$ was observed and tentatively assigned to a complex with the dissociated ligand, such as $[\text{Ru}^{\text{III}}(\text{H}_2\text{O})(\text{bpy})_2(\text{bpyNO}_{\text{out}})]^{3+}$. The spectroscopic signatures of $[\text{Ru}^{\text{IV}}=\text{O}(\text{bpy})_2(\text{bpy}_{\text{out}})]^{2+}$ were not observed, although, DFT analysis and $[\text{Ru}^{\text{II}}(\text{bpy})_3]^{2+}$ formation suggest this intermediate. Thus, $[\text{Ru}^{\text{II}}(\text{bpy})_2(\text{bpyNO})]^{2+}$ has a potential as a light-induced oxidizer.

5.2 Introduction

The Ru based coordination compounds were developed as catalysts¹⁴⁹⁻¹⁵³, photo-sensitizers^{154, 155}, and anti-cancer drugs.^{156, 157} Multiple Ru-based polypyridine complexes draw considerable attention as they are easily modifiable, stable catalysts and sensitizers in the processes with the harsh reaction conditions, such as the oxidation reactions.^{59, 158, 159} Their analogues, the Ru coordination compounds with polypyridyl N-oxides, were noted in the multiple Ru based catalytic systems under the conditions of water oxidation.^{62, 70, 94, 160} The polypyridyl N-oxides are the reactive compounds with applications in chemical synthesis, catalysis, and drug design.^{161, 162} Their combination with the photo-active Ru catalytic centers may result in novel, unusual properties particularly suitable for the oxidation reactions.^{98, 163} Out of these considerations, we studied the photochemical transformations of $[\text{Ru}^{\text{II}}(\text{bpy})_2(\text{bpyNO})]^{2+}$ (**1-NO**), a compound with pronounced light- sensitivity.^{94, 97} Its structural predecessor, $[\text{Ru}(\text{bpy})_3]^{2+}$ (**1**), is widely known as a photosensitizer with well understood photochemistry and has wide-ranging applications in a photo-redox catalysis.¹⁶⁴⁻¹⁶⁶ The analogs of this compound are also used in dye-sensitized solar cells.¹⁶⁷ This compound appears as a single product of (**1-NO**) irradiation. Previously, (**1-NO**) behavior was analyzed in oxidation.⁹⁴ For instance, the oxidation of (**1-NO**) in the dark with Ce(IV) ammonium nitrate (Ce^{IV}) resulted in a majority conversion to $[\text{Ru}^{\text{III}}(\text{bpy})_2(\text{bpyNO})]^{3+}$. A minority, assigned to an open form, $[\text{Ru}^{\text{II}}(\text{H}_2\text{O})(\text{bpy})_2(\text{bpyNO}_{\text{out}})]^{2+}$, is capable of O-O bond formation and O_2 evolution via proposed $[\text{Ru}^{\text{IV}}=\text{O}(\text{bpy})_2(\text{bpyNO}^+_{\text{out}})]^{3+}$ intermediate.⁹⁴ After oxidation with Ce^{IV} in the dark, the $\text{Ru}^{\text{IV}}=\text{O}$ moiety vibration was detected at $\sim 799 \text{ cm}^{-1}$.⁹⁴ Here, we describe the behavior of (**1-NO**) under the illumination with visible light (530-650 nm). Relatively short (5 – 30 minutes) exposure of (**1-NO**) solution in water or acetonitrile to ambient light resulted in irreversible changes in its UV-Vis absorption spectrum. We were able to characterize a final product of the light induced transformation as (**1**). We propose that light induced $^3[\text{Ru}^{\text{III}}(\text{bpyNO}^*)(\text{bpy})_2]^{2+}$ is capable of dissociating the N-oxide group with formation of $[\text{Ru}^{\text{IV}}=\text{O}(\text{bpy})_2(\text{bpy}_{\text{out}})]^{2+}$ intermediate, which later reduces to (**1**) and water.

5.3 Experimental section

5.3.1 Synthesis:

Complex (**1-NO**) was prepared and synthesized using the published procedure.⁹⁴

5.3.2 Sample illumination:

All samples were exposed to LED lamps with 530 nm (10W), 650 nm (10W), and 760 nm (15W). The spectrum of each LED was measured, and FWHM of each LED was less than 15 nm. Each sample was exposed to intense LED light (15 cm away from the light source) for 30 minutes in a heat bath, to keep the temperature constant (room temperature) during the experiment. No change in the neutral pH was observed while irradiating samples in water.

5.3.3 Raman Spectroscopy:

A HeCd CW laser (442 nm and ~15 mW) was employed for the resonance Raman. The measurement was conducted at room temperature and hence the sample was in liquid form. To minimize background, measurements were done on a hanging drop, partially extruded from a syringe pre-filled with sample solution. The sample area directly exposed to the laser beam was a circle with a diameter of ~ 0.5 mm. The laser beam was focused on the sample with fused silica lens with 10 cm focal length. The light (Raman signal) collecting system consisted of two fused silica lenses, the first lens was the same lens which focused the laser beam on the sample, the second lens focused the collected signal on the monochromator slit. The slit width during the measurement was 70 μm . A Semrock edge pass filter prevented Rayleigh scattering to get into the monochromator. A holographic grating with 1800 l/mm was used. An iDus 420 Andor camera was used.

5.3.4 EPR Spectroscopy:

200 μl of sample with 1 mM concentration in 0.1 M HNO_3 was added to EPR tubes and frozen in liquid nitrogen (in less than 30 sec). Low-temperature (20 K using ColdEdge closed cycle cryostat) X-band EPR spectra were recorded with a Bruker EMX X-band spectrometer and X-Band CW microwave bridge. For EPR signal quantitation, the standard EPR sample tubes were filled with the samples through all of the resonator space. The signal intensities were measured on the same day, also in the same conditions, to allow direct comparison of the signal intensities. For the spectrum simulation SimFonia software from Bruker was used.

UV-Vis absorption spectroscopy: A Cary 300 UV-Vis spectrometer was used for the absorption measurements. The sample was held in a quartz cuvette with 1 mm light path at room temperature.

5.3.5 Oxygen-evolution measurement:

Oxygen-evolution measurements of 1 mM and 4 mM Ru(bpy)₂(bpyNO)(PF₆)₂ water solutions were performed under irradiation with visible light. In a typical experiment, 0.5 ml of (**1-NO**) solution was added to an Oxygraph System (Hansatech Instruments Ltd.) chamber and constantly stirred, followed by illumination with a 150 Watt halogen lamp, covering the entire visible range, for 30 minutes. The oxygen concentration was recorded as a function of time. Calibration was performed by measuring a signal in oxygen-saturated deionized water (284 μM/L at 20° C), followed by an addition of the oxygen-depleted reagent (sodium dithionite).

5.3.6 DFT:

Gaussian16 software with the B3LYP exchange-correlation (XC) functional was used for DFT calculations. The 6-31G* basis was set for all organic atoms (C, O, N, H), and the all electron DGDZVP basis was set for the Ru atom. To model water solvation, the CPCM polarizable conductor model was used. The value of the reference potential (NHE) was assigned to 4.44 V and the solvation free energy of a proton was set to -11.64 V.

5.3.7 Nuclear magnetic resonance spectroscopy:

NMR spectra were recorded on a Bruker AV-III-HD-400 400MHz spectrometer and chemical shifts were referenced to solvent residual peaks.

¹H NMR of (**1-NO**) (400 MHz, CD₃CN) σ/ppm: 8.98 (d, 1H), 8.70 (d, 1H), 8.57-8.50 (m, 2 H), 8.38 (dd, 2H), 8.25 (t, 1H), 8.09 – 8.05 (m, 4 H), 7.98 - 7.88 (m, 4 H), 7.84 (d, 1 H), 7.75 – 7.69 (m, 2 H), 7.48 (d, 1 H), 7.41 (t, 1 H), 7.31-7.26 (m, 2 H), 7.22 – 7.15 (m, 2 H).

¹H NMR of (**1-NO**) (400 MHz, D₂O) σ/ppm: 8.96 (d, 1 H), 8.74 (d, 1 H), 8.60-8.58 (m, 2 H), 8.46-8.42 (m, 2 H), 8.26 (t, 1 H), 8.19 (s, 1 H), 8.15 (s, 1 H), 8.10 – 8.03 (m, 2 H), 8.01 – 7.88 (m, 5 H), 7.69 (t, 1 H), 7.55 (d, 1 H), 7.40-7.33 (m, 3 H), 7.26 (t, 1 H), 7.21 – 7.13 (m, 2 H).

In-situ NMR experiments were performed in D₂O (> 99,8 atom % D) and CD₃CN (> 99,8 atom % D) by irradiating of D₂O and CD₃CN solutions with LEDs at 520 nm and 659 nm.

¹H NMR (400 MHz, D₂O) σ /ppm after irradiation: 8.55 (d, 6 H), 8.05 (t, 6 H), 7.82 (d, 6 H), 7.38 (t, 6 H).

¹H NMR (400 MHz, CD₃CN) σ /ppm after irradiation: 8.51 (d, 6 H), 8.07 (t, 6 H), 7.74 (d, 6 H), 7.41 (t, 6 H).

5.4 Results

5.4.1 Redox behavior:

In the previous report, we outlined the main spectroscopic and redox properties of [Ru^{II}(bpy)₂(bpyNO)]²⁺ (**1-NO**).⁹⁴ (**1-NO**) is EPR silent with Ru²⁺ in the d⁶ electronic configuration, a singlet (S = 0) low spin state and the neutral ligands. A singlet state allows a convenient investigation of (**1-NO**) by NMR. Upon addition of one equiv of an oxidant or reductant, it converts into S=1/2 species [Ru^{III}(bpy)₂(bpyNO)]³⁺⁹⁴ (will be discussed later in the EPR studies section) and [Ru^{II}(bpy)₂(bpyNO^{•-})]¹⁺, correspondingly. An EPR spectrum of the reduced (**1-NO**) (**Figure 5-1**) was generated by addition of one equiv of sodium ascorbate (Asc). The EPR spectrum was simulated with g-factors g_{xx} = 2.02, g_{yy} = 1.99, and g_{zz} = 1.87 and A_{xx} = 12 G, A_{yy} = 34 G and A_{zz} = 11 G. The signal shape and g-factor of reduced (**1**) [Ru^{II}(bpy)₂(bpy^{•-})]¹⁺, were reported previously¹⁶⁸ and are significantly different from the reduced (**1-NO**) in **Figure 5-1**. Note that Asc is a mild reductant with estimated ~ -0.3 V redox potential.¹⁶⁹ Earlier, it was found that the N-oxides of pyridine origin were difficult to reduce in the aprotic solvents.¹⁷⁰ An interaction of a polypyridine N-oxide ligand with the Ru^{II} center is likely to lower the reduction potential. The redox potential for the reduction of (**1-NO**) was measured as -0.4 V vs. NHE by cyclic voltammetry in acetonitrile solution with 0.1 M Et₄NClO₄ as an electrolyte.

Table 5-1 shows the DFT estimated redox potentials. A one electron oxidation allows conversion of the Ru center to a paramagnetic [Ru^{III}(bpy)₂(bpyNO)]³⁺, while further oxidation to [Ru^{IV}(bpy)₂(bpyNO)]⁴⁺ is thermodynamically prohibitive, **Table 5-1**. The reduction is ligand-centered and produces the bpyNO^{•-} ligand. A closed configuration, where bpyNO^{•-} is a bidentate ligand to Ru atom, is a predominant state since the reaction occurs in the dark and also previous published data has shown that closed configuration is thermodynamically more favorable.^{94, 171}

Nevertheless, a possibility of an open configuration should not be excluded. Regardless of the configuration, a reductive potential of the $[\text{Ru}^{\text{II}}(\text{bpy})_2(\text{bpyNO}^{\bullet})]^{1+}$ species is estimated to be significantly more negative than for the Asc used to generate the unique $[\text{Ru}^{\text{II}}(\text{bpy})(\text{bpyNO}^{\bullet})]^{1+}$ EPR signal, **Table 5-1**. Previously, it was shown that DFT results for the Ru complexes can deviate up to ~ -0.5 eV for the reduction reactions.¹⁷² The calculations presented in **Table 5-1** for the $[\text{Ru}^{\text{II}}(\text{bpy})_2(\text{bpyNO}^{\bullet})]^{1+}$ and $[\text{Ru}^{\text{II}}(\text{bpy})_2(\text{H}_2\text{O})(\text{bpyNO}^{\bullet}\text{H}_{\text{out}})]^{1+}$ correctly predict the localization of an unpaired electron on the bpyNO ligand. We conducted the DFT calculations for multiple possible configurations of the reduced $[\text{Ru}^{\text{II}}(\text{bpy})_2(\text{bpyNO}^{\bullet})]^{1+}$ species and found that only the $[\text{Ru}^{\text{II}}(\text{bpy})(\text{bpyNO}^{\bullet})]^{1+}$ and $[\text{Ru}^{\text{II}}(\text{H}_2\text{O})(\text{bpy})(\text{bpyNO}^{\bullet}\text{H}_{\text{out}})]^{2+}$ species were energetically viable and provide reasonable ^{14}N hyperfine splitting (hfs), **Table 5-2**. The EPR signal in **Figure 5-1** resembles the EPR spectrum of Ru^{II} complexes with NO^{\bullet} such as *trans*- $[\text{Ru}^{\text{II}}\text{Cl}(\text{NO}^{\bullet})(\text{cyclam})]^+$ with $g_{xx} = 2.03$, $g_{yy} = 1.99$, $g_{zz} = 1.88$ and ^{14}N ($I = 1$), hfs $A_{xx} = 17$ G, $A_{yy} = 32$ G, $A_{zz} = 15$ G¹⁷³ and *trans*- $[\text{Ru}^{\text{II}}(\text{NO}^{\bullet})((\text{CH}_3\text{CH}_2)_2\text{PCH}_2\text{CH}_2\text{P}(\text{CH}_2\text{CH}_3)_2)\text{Cl}]^+$ with $g_{xx} = 2.01$, $g_{yy} = 1.98$, $g_{zz} = 1.88$, hfs $A_{xx} = 18$ G, $A_{yy} = 35$ G, $A_{zz} = 19$ G¹⁷³. Following redox potentials were reported for other Ru complexes with $[\text{Ru}^{\text{II}}(\text{NO})(\text{L})_5]^{2+}$ structures, such as *trans*- $[\text{Ru}(\text{NO})\text{Cl}(\text{cyclam})]^{2+}$ with -0.37 V vs. Ag/AgCl¹⁷⁴, *trans*- $[\text{Ru}(\text{NO})\text{Cl}(1-(3\text{-propylammonium})\text{cyclam})]^{3+}$ with -0.34 V vs. Ag/AgCl¹⁷⁵, *trans*- $[\text{Ru}(\text{NO})\text{Cl}(15\text{aneN}_4)]^{2+}$ with -0.28 V vs. Ag/AgCl¹⁷⁶ and *fac*- $[\text{Ru}(\text{NO})\text{Cl}_2(\text{k}^3\text{N}^4, \text{N}^8, \text{N}^{11}(1\text{-carboxypropyl})\text{cyclam})]^+$ with -0.39 V vs. Ag/AgCl¹⁷⁷. (See **Figure 4-2** for the structures)

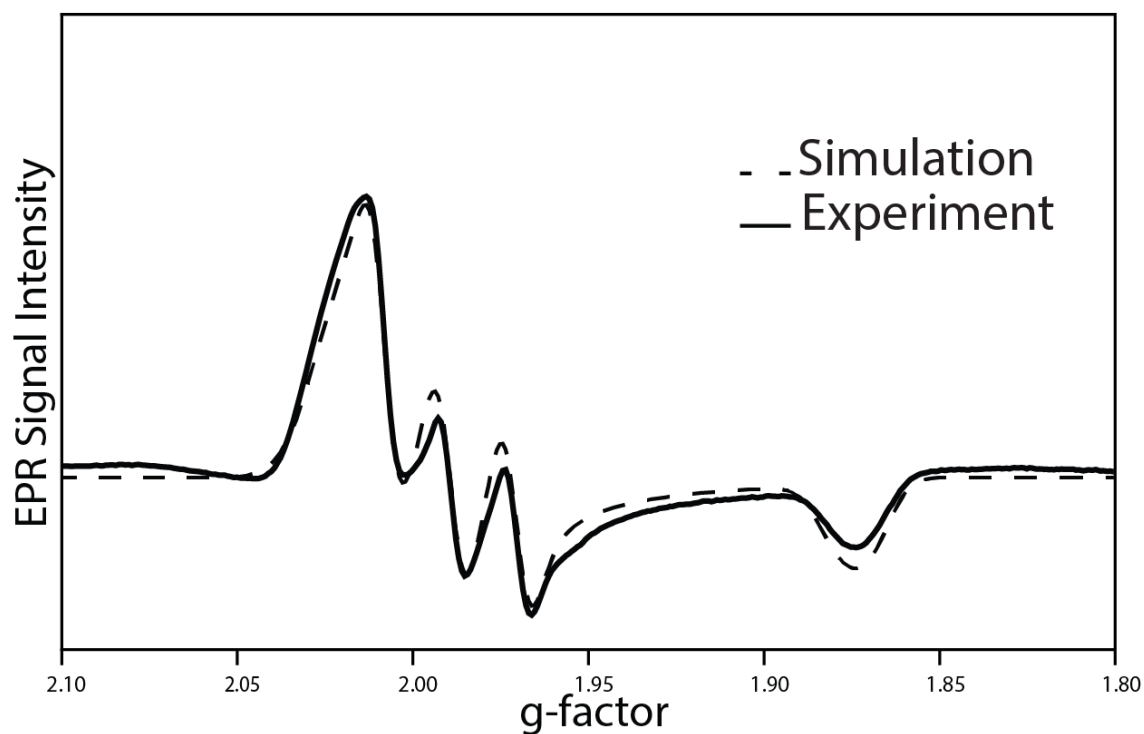


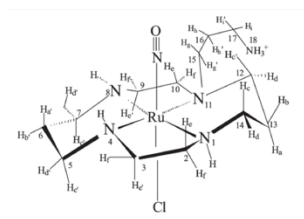
Figure 5-1. X-band EPR of $[\text{Ru}^{\text{II}}(\text{bpy})(\text{bpyNO}^{\bullet-})]^{1+}$ obtained by **(1-NO)** reduction with ascorbate in water. The measurement was conducted at 20 K, using a modulation amplitude of 10 G and 30 mW of power. Dashed line is the simulated spectrum.

Table 5-1. Redox properties of $[\text{Ru}^{\text{II}}(\text{bpy})_2(\text{bpyNO})]^{2+}$ and $[\text{Ru}^{\text{II}}(\text{bpy})_3]^{2+}$ from DFT analysis^a

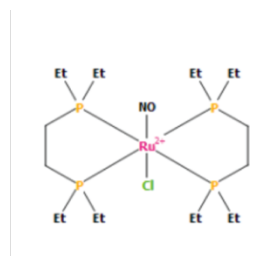
	E^0/V
$\text{Asc}^- \rightarrow \text{Asc}^{\bullet-} + e^- + \text{H}^+$	-0.01
$[\text{Ru}^{\text{II}}(\text{bpy})_2(\text{bpyNO}^{\bullet-})]^{1+} \rightarrow [\text{Ru}^{\text{II}}(\text{bpy})_2(\text{bpyNO})]^{2+} + e^-$	-1.39
$[\text{Ru}^{\text{II}}(\text{bpy})_2(\text{H}_2\text{O})(\text{bpyNO}^{\bullet}\text{H}_{\text{out}})]^{2+} \rightarrow [\text{Ru}^{\text{II}}(\text{bpy})_2(\text{H}_2\text{O})(\text{bpyNO}_{\text{out}})]^{2+} + e^- + \text{H}^+$	-1.45
$[\text{Ru}^{\text{II}}(\text{bpy})_2(\text{bpyNO})]^{2+} \rightarrow [\text{Ru}^{\text{III}}(\text{bpy})_2(\text{bpyNO})]^{3+} + e^-$	+1.00
$[\text{Ru}^{\text{III}}(\text{bpy})_2(\text{bpyNO})]^{3+} \rightarrow [\text{Ru}^{\text{IV}}(\text{bpy})_2(\text{bpyNO})]^{3+} + e^-$	+2.88
$[\text{Ru}^{\text{II}}(\text{bpy})_3]^{2+} \rightarrow [\text{Ru}^{\text{III}}(\text{bpy})_3]^{3+} + e^-$	+1.29 (1.27 ¹⁷⁸)
$[\text{Ru}^{\text{I}}(\text{bpy})_3]^{1+} \rightarrow [\text{Ru}^{\text{II}}(\text{bpy})_3]^{2+} + e^-$	-1.71 (- 1.31 ¹⁷⁸)
^a The values in the parenthesis are from the experiment	

Table 5-2. Relative energies and ^{14}N hfs for selected configuration of $[\text{Ru}(\text{bpy})_2(\text{bpyNO})]^{1+}$ species.

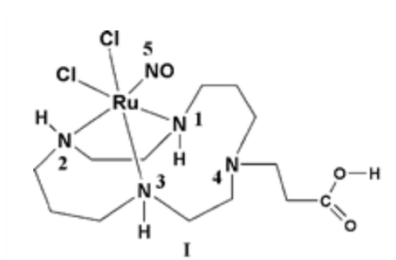
Species:	^{14}N hfs, G ($A_{yy}; A_{xx}; A_{zz}$)	Free Energy, Hartree	Relative energy, eV	N-O distance, Å
$[\text{Ru}^{\text{II}}(\text{bpy})(\text{bpyNO}^{\bullet-})]^{1+}$	13; 2; 2	- 6003.667367	0	1.354 (836 cm^{-1})
5-coordinate $[\text{Ru}^{\text{II}}(\text{bpy})(\text{bpyNO}^{\bullet-}_{\text{out}})]^{1+}$		- 6003.642298	+0.68	1.292
5-coordinate $[\text{Ru}^{\text{II}}(\text{bpy})(\text{bpyNOH}^{\bullet}_{\text{out}})]^{2+}$	20.3; 8.6; 8	- 6004.073328	+0.59	1.423
$[\text{Ru}^{\text{II}}(\text{H}_2\text{O})(\text{bpy})(\text{bpyNO}^{\bullet-}_{\text{out}})]^{1+}$		- 6080.048229	+0.87	1.316
$[\text{Ru}^{\text{II}}(\text{H}_2\text{O})(\text{bpy})(\text{bpyNOH}^{\bullet}_{\text{out}})]^{2+}$	30.62; 17.6; 19.63	- 6080.478178	+0.82	1.477
$[\text{Ru}^{\text{II}}(\text{OH})(\text{bpy})(\text{bpyNO}^{\bullet-}_{\text{out}})]$		- 6079.566980	+2.33	1.296
$[\text{Ru}^{\text{II}}(\text{OH})(\text{bpy})(\text{bpyNOH}^{\bullet}_{\text{out}})]^{1+}$	26.2; 14.4; 15.5	- 6080.014961	+1.78	1.441



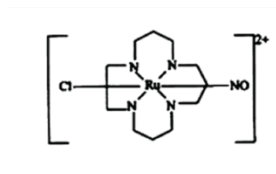
trans-[Ru(NO)Cl(1-(3-propylammonium)cyclam)]³⁺



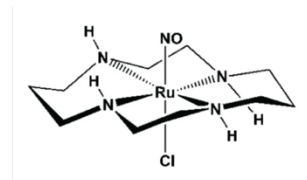
trans-[Ru(NO)((CH₃CH₂)₂PCH₂CH₂P(CH₂CH₃)₂)₂Cl]⁺



fac-[Ru(NO)Cl₂(κ³N⁴,N⁸,N¹¹(1-carboxypropyl)cyclam)]⁺



trans-[Ru(NO)Cl(15aneN₄)]²⁺



trans-[Ru(NO)Cl(cyclam)]²⁺

Figure 5-2. The structure of some Ru with NO ligands that were mentioned in the text

5.4.2 Spectroscopic Study

Spectroscopic characterization of the final product of light induced (**1-NO**) transformation: Previously, our group⁹⁴ and others⁹⁷ have noted an extreme light sensitivity of (**1-NO**). To gain further insight, the light induced changes were monitored using UV-Vis, NMR, and resonance Raman spectroscopy, **Figure 5-3**, **Figure 5-4**, **Figure 5-5**, **Figure 5-6**, **Figure 5-7**. We have compared spectroscopic properties of (**1-NO**) after a light irradiation with spectra of (**1**). It was found that the product of (**1-NO**) irradiation resembles (**1**). The irradiation for 30 minutes was performed using three LED monochromatic light sources at 760, 650 and 530 nm. We recorded absorption spectra of irradiated (**1-NO**) with different irradiation times (**Figure 5-3B**) and found that 30 minutes light exposure is sufficient to achieve the end of photo reactivity under the experimental condition. 760 nm light was not effective in changing (**1-NO**) because of the lack of (**1-NO**) absorption at that wavelength. Despite the low absorption at 650 nm, a conversion of (**1-NO**) to (**1**) occurs, which shows an extent of (**1-NO**) light sensitivity. As a result of the illumination, the main MLCT peak in (**1-NO**) is blue-shifted for about 10 nm to coincide with the main MLCT of (**1**) while the broad peak at ~560 nm largely disappeared. It was observed that (**1-NO**) transforms to (**1**) by the illumination with both 650 and 530 nm light, **Figure 5-3A**. The deconvolution of UV-Vis at 650 nm shows that 70% of (**1-NO**) converted to (**1**), 11% remained intact, and 9% formed other intermediates, **Figure 5-4**. In UV-Vis absorption spectra, a greater effect was observed under illumination with the 530 nm light. In this case, a new absorption band around 750 nm appeared. This band could be assigned to the Ru^{III} species since the Ru^{III} complexes have an absorption band in the 750 nm region. Asc caused this absorption band to disappear which also supports the assignment of the 750 nm band to the Ru^{III}.

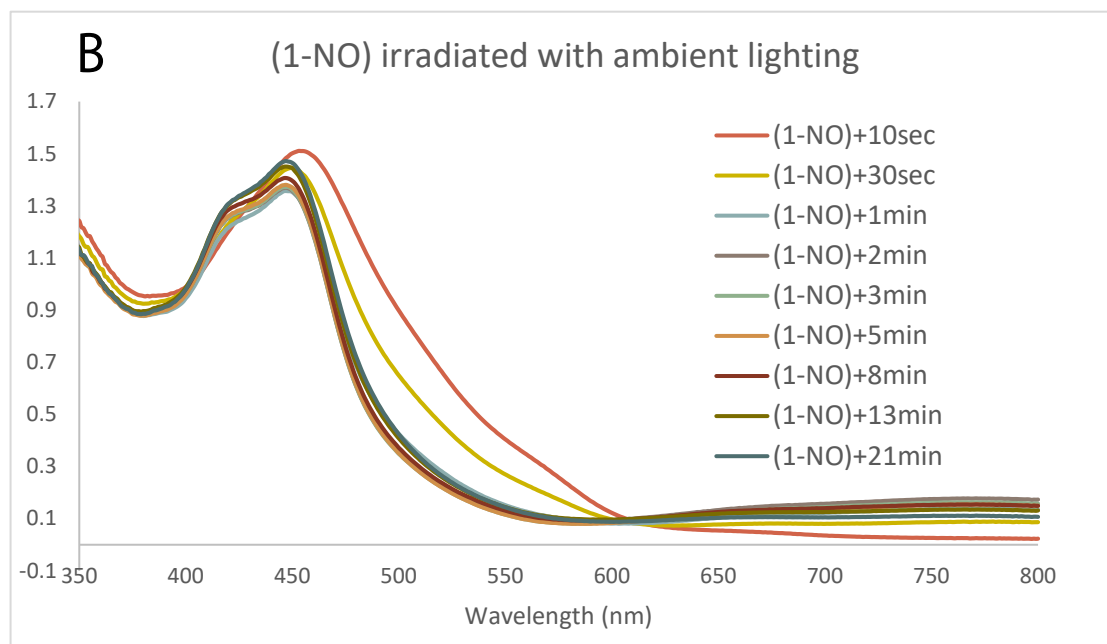
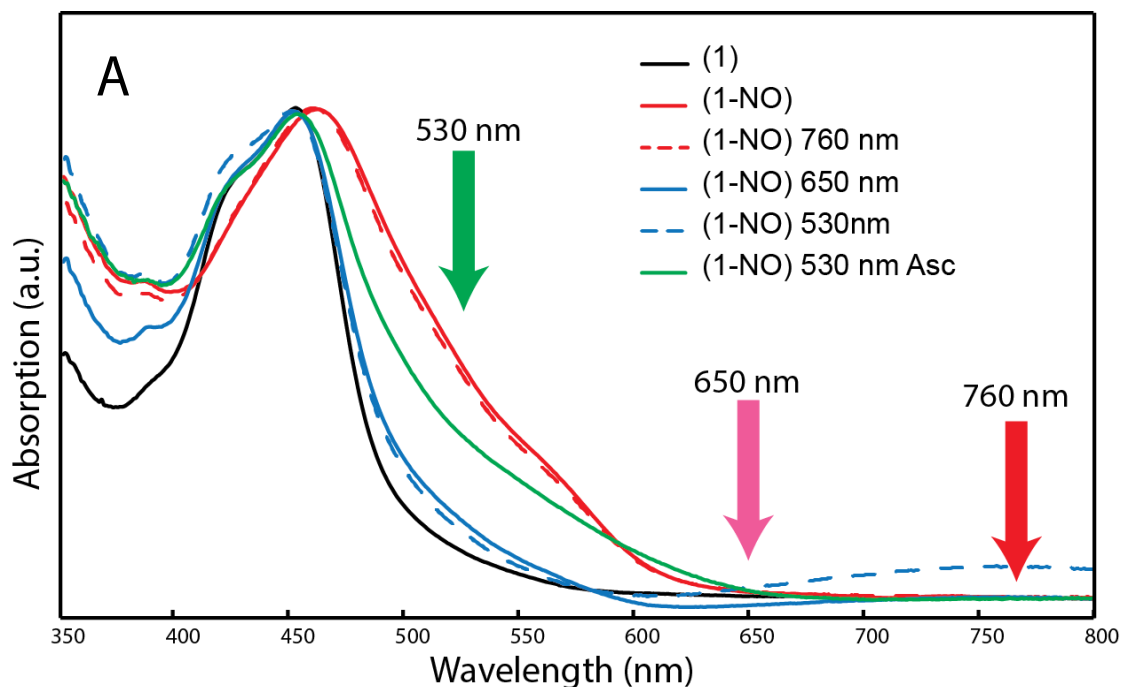


Figure 5-3. A) Absorption spectra of 1mM (1-NO) and (1) solutions in water (pH = 7) before and after the irradiation with the different wavelngthes (760 nm, 650 nm and 530 nm) marked by the arrows. The solutions were irradiated for 30 minutes at a room temperature. To examine the reversiblility, 20 equiv of Acs was added to reduce the sample after the irradiation with the 530 nm LED (dash blue line). Although the small absorption band around 750 nm dissapeared upon Asc addition, no absorbtion maximum shift was observed (green line). The black line is the spectrum of (1). B) Absorption spectra of 1mM (1-NO) in water. Each spectrum was irradiated with ambient light with different exposure time

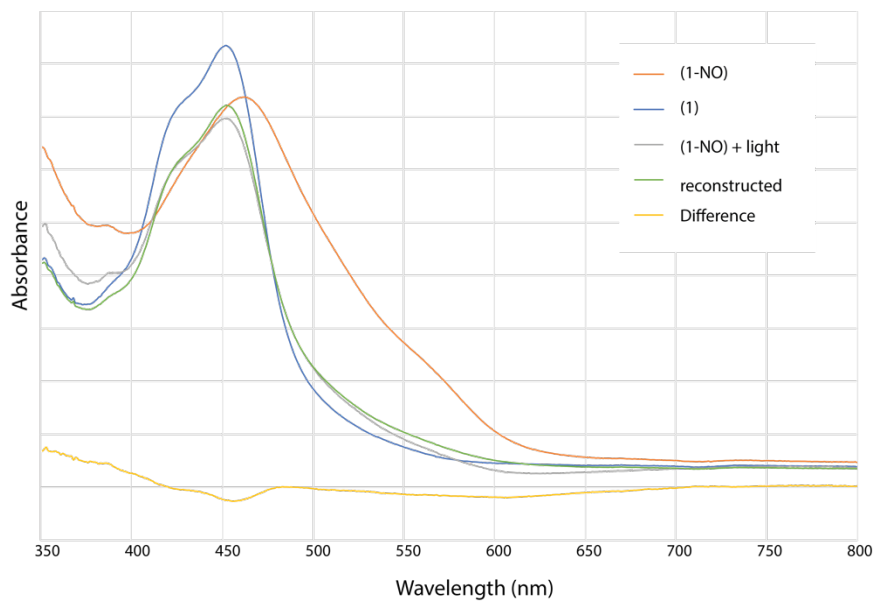


Figure 5-4. Absorption spectra of 1mM (1-NO) -orange-, (1-NO) exposed to 670 nm for 30 minutes -gray-, and (1) -blue- in water . The green spectrum consists of 70% of the blue and 11% of the orange. The yellow spectrum is the difference between gray and green.

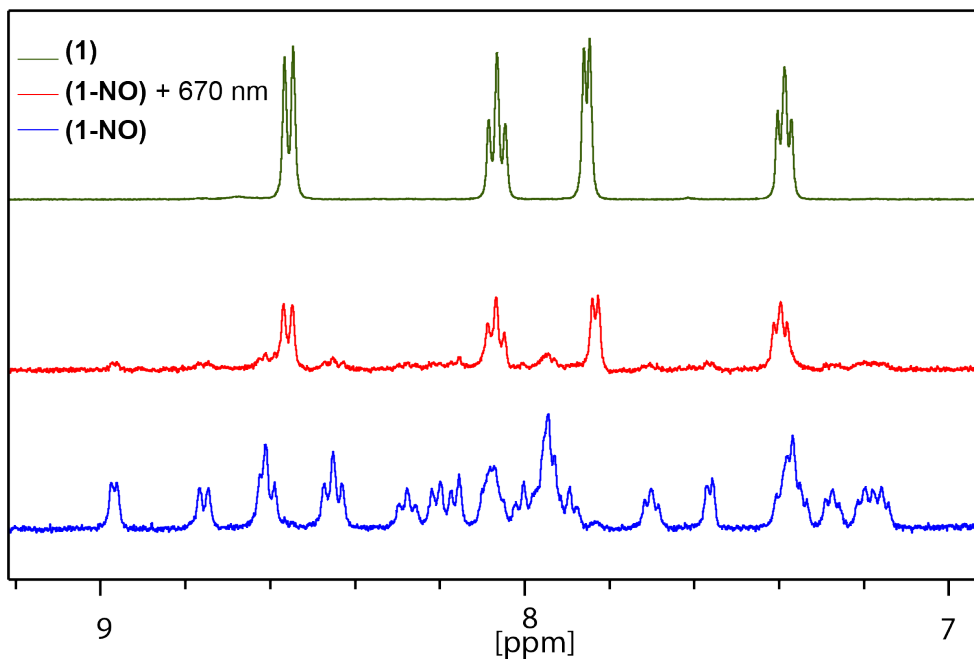


Figure 5-5. NMR spectra of (1), (1-NO) and (1-NO) illuminated with 650 nm light in D₂O.

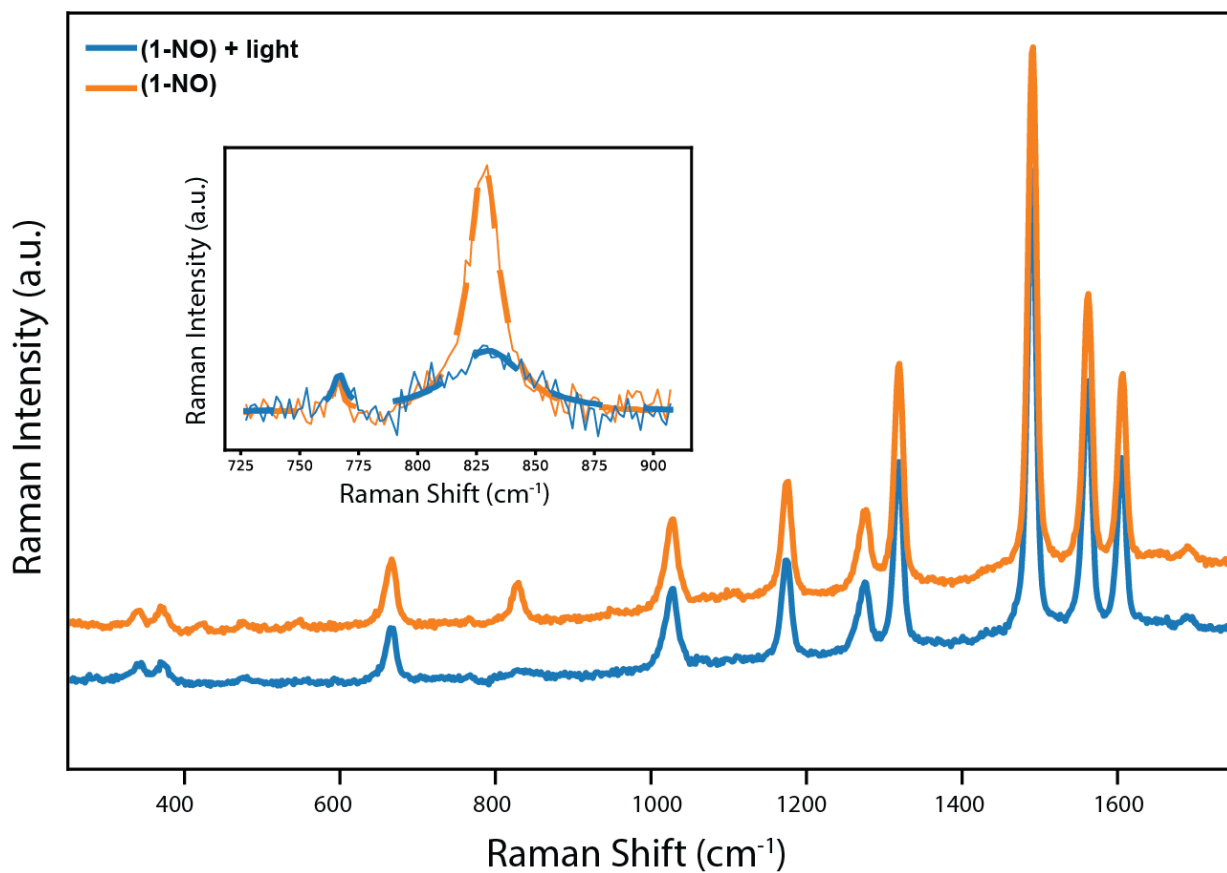


Figure 5-6. Resonance Raman spectrum of 3 mM solution of (1-NO) in water (pH= 7) before (orange curve) and after (blue curve) exposure to an ambient light. Spectrum was recorded with 442 nm laser excitation at a room temperature. The measurement took 100 seconds to minimize the laser damage. The second measurement occurred after 30 minutes of the ambient light exposure of the sample. The insert is focused on 827 cm⁻¹ band and corresponding fits.

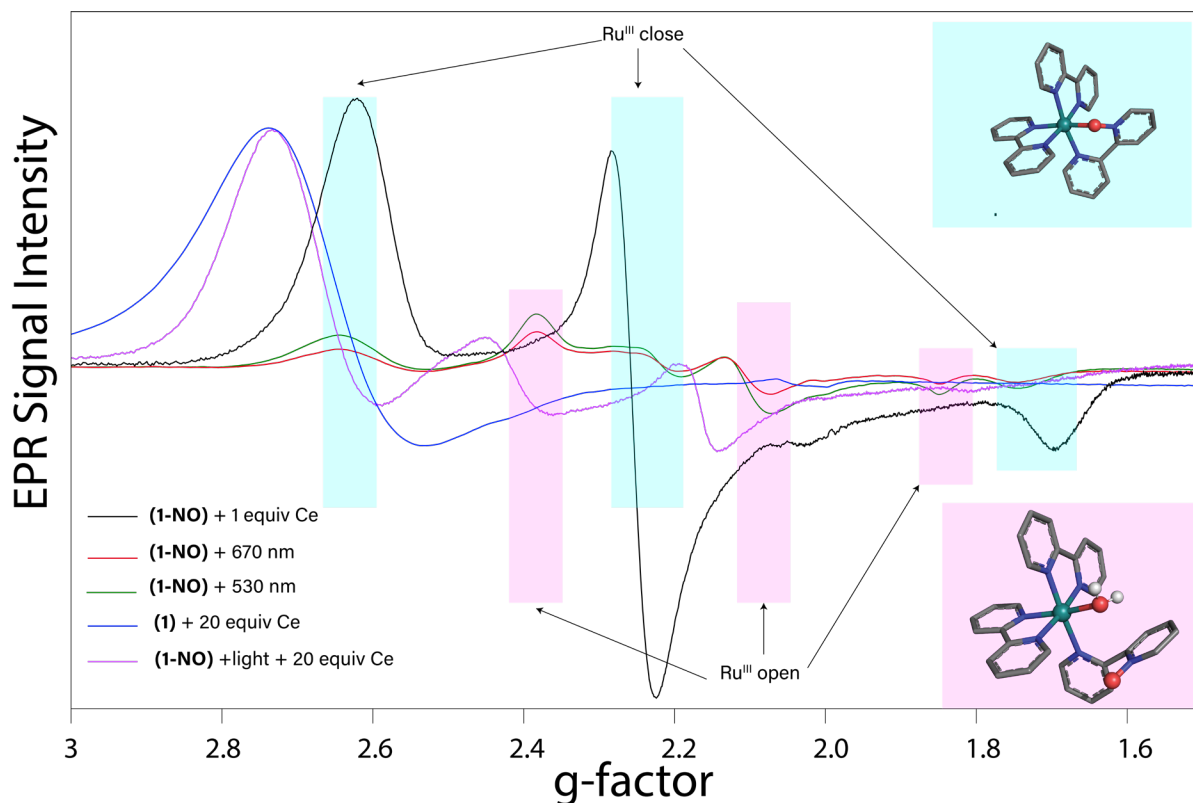


Figure 5-7. X-band EPR spectra (20 K) of illuminated and oxidized **(1-NO)** and **(1)**. Green and red curves represent **(1-NO)** irradiated with 530 nm and 650 nm light. Black curve is **(1-NO)** oxidized with 1 equiv Ce^{IV} in the dark. Blue curve is **(1-NO)** oxidized with 20 equiv of Ce^{IV} after an exposure to an ambient light for three days. The inserted structures are added to depict a closed and open configuration. pH for Ce^{IV} mixture was set 1 and for the rest of samples it was 7.

NMR spectroscopy showed evidence of **(1-NO)** to **(1)** conversion, **Figure 5-5**. NMR spectrum of **(1)** is well known¹⁷⁹ and has a distinct signal because of its D_3 point group symmetry. The majority of the **(1-NO)** converts to **(1)** in D_2O after 30 minutes of 650 nm illumination, **Figure 5-5**. A spectrum after irradiation with the 530 nm light is not shown because the peaks are less resolved due to a presence of paramagnetic Ru^{III} in the reaction mixture. This result is in agreement with the UV-Vis spectroscopic data of the Ru^{III} at 530 nm. A presence of the Ru^{III} species was later confirmed by EPR, **Figure 5-7**.

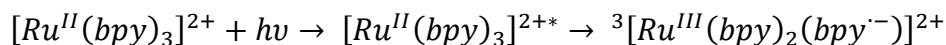
A resonance Raman spectroscopy with an excitation by the 442 nm laser was used to analyze the structural changes in **(1-NO)**, **Figure 5-6**. The band at 827 cm^{-1} is typical for the Ru-O-N vibration.^{94, 160, 180} After the illumination all the vibrational bands of **(1-NO)** remain,

except the 827 cm⁻¹ band, which loses its intensity. In **Figure 5-6** insert, the fitted data show that the intensity of the Ru-N-O band reduced by more than 76%.

EPR studies were used to investigate the paramagnetic intermediates and products of illuminated **(1-NO)**. Both Ru^{II} and Ru^{IV} are EPR silent, while Ru^{III} and Ru^V are paramagnetic with S=1/2. Ru^V complexes with polypyridine ligands are scarce and also may be thermodynamically inaccessible in some complexes.^{94, 160} The characteristic g-factors of Ru^V^{92, 180} have not been observed in EPR spectra in this study. Light exposed **(1-NO)** solutions showed a formation of at least two coexisting Ru^{III} species. One intermediate has g-factor, g_{xx} = 2.64, g_{yy} = 2.22, and g_{zz} = 1.74, while the second has g_{xx} = 2.38, g_{yy} = 2.10, and g_{zz} = 1.85 (**Figure 5-7**, red and green spectra). We assigned the first one to a Ru^{III} complex with the oxygen atom in bpyNO ligand coordinated to the Ru center of ([Ru^{III}(bpy)₂(bpyNO)]³⁺), which is also referred to as “closed form”. Addition of one equivalent of Ce^{IV} to **(1-NO)** in the dark produces the same signal (**Figure 5-7**, black line). The EPR signal of illuminated **(1-NO)** in **Figure 5-7** (green and red spectra) is significantly less intense than **(1-NO)** mixed with 1 equiv of Ce^{IV} (black spectrum) which confirms the UV-Vis deconvolution assessment that the majority of illuminated **(1-NO)** is not in the form of Ru^{III}. In addition a new signal with g_{xx} = 2.38, g_{yy} = 2.10, and g_{zz} = 1.85 was observed and tentatively assigned to a complex with the dissociated ligand such as [Ru^{III}(H₂O)(bpy)₂(bpyNO_{out})]³⁺. Ru^{III} N-oxide g-factors similar to the observed g-factors in this study have been reported previously.^{62, 160, 180} For example, g_{xx} = 2.31, g_{yy} = 2.2, and g_{zz} = 1.91 have been assigned to oxidized [Ru^{II}(bpyNO)(tpy)(H₂O)]²⁺ compound. Another study¹⁸¹ on *trans*-[Ru^{III}(bpy)₂(H₂O)₂]³⁺ reported g_{xx} = 2.38, g_{yy} = 2.27, and g_{zz} = 1.88. Lastly, to test **(1-NO)** to **(1)** conversion hypothesis, Ce^{IV} was added to the prolong light exposed **(1-NO)** and followed by a comparison with the Ce^{IV}-oxidized **(1)** (**Figure 5-7**, blue and magenta). This comparison indicates that the final products of the oxidized illuminated **(1-NO)** and the oxidized **(1)** are similar.

5.4.3 Discussion of the mechanism of the light induced transformation

Ru polypyridine complexes are well known for their distinct photo-physical properties.^{182, 183} **(1)** and the similar Ru-based complexes are among the most studied systems since they are widely used as photosensitizers.^{154, 155} Absorption of a photon in **(1)** followed by an intersystem crossing results in a triplet state of **(1)**:



The lifetime of the charge separated state is solvent dependent, but on average is $\sim 1 \mu s$.
¹⁸⁴ **(1-NO)** system may undergo similar light excitation and charge separation processes:

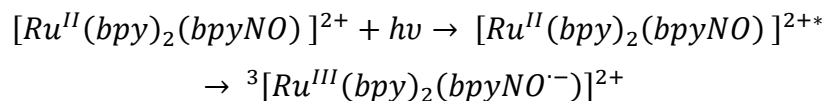


Figure 5-8 red arrows represent this path. In **(1)**, due to its D_3 point group symmetry, any of the ligands can be reduced, while for **(1-NO)** the bpyNO ligand becomes reduced due to higher electronegativity of its N-O moiety. **Figure 5-8** depicts a spin density distribution for the **(1-NO)** triplet state to illustrate an electron localization on the bpyNO ligand. We compared well known photoluminescence of **(1)** ¹⁸⁵, **(1-NO)** and **(1-NO)** exposed to a light, **Figure 5-9**. The intensity of the spectrum is lower in **(1-NO)** compared to **(1)**. A ~ 4 nm redshift in the emission spectrum of **(1-NO)** indicates the smaller energy band gap between the singlet ground and excited state in **(1-NO)**.

As experimental data strongly supports **(1-NO)** to **(1)** conversion, we proposed several viable pathways for this conversion, **Figure 5-8**. Since no O_2 evolution was observed for this system under light illumination (**Figure 5-9**), the oxygen from the bpyNO ligand would be released either as water or as $O^{\cdot}H$ radical. In **Figure 5-8**, one pathway proceeds with the $Ru^{IV}=O$ formation. First, the Ru^{IV} intermediate would be reduced to Ru^{III} followed by a conversion to the Ru^{II} species with the release of H_2O . DFT calculations predict a negative free energy for Ru^{IV} to Ru^{III} and Ru^{III} to Ru^{II} reductions. **Table 5-3** presents possible reactions and their corresponding energies. Although this path is thermodynamically favorable, two electrons and protons are needed for its completion. The initial Ru^{II} complex can serve as a reductant to achieve the Ru^{III} state. $[Ru^{III}(bpy)_3]^{3+}$ is known to spontaneously decay in the basic solutions with $[Ru^{II}(bpy)_3]^{2+}$ formation. ¹⁸⁶ Some literature reports indicate a possibility of a hydroxyl radical production from reduced N-oxides via protonation ¹⁸⁷. De-coordinated bpy-N-oxide ligand can potentially engage in such a pathway (**Figure 5-9**) producing highly reactive hydroxyl radical, which may have potential in the biomedical applications, such as

cancer treatments.^{156, 157, 188} However, it is an energetically more demanding pathway (**Table 5-3**) and we did not observe any indication of O•H radical formation (data not shown). In both pathways, we assumed that (**1-NO**) is in water solution, where the protons needed for the transformation are readily available. In an attempt to determine the solvent dependency of the (**1-NO**) conversion to (**1**), we illuminated (**1-NO**) dissolved in trifluoroethanol, which is a non-coordinating solvent, **Figure 5-11**. Although, to a lesser extent, the conversion still occurs in trifluoroethanol. Other possible pathway, that may be solvent-independent, is oxygen atom transfer from $[\text{Ru}^{\text{IV}}=\text{O}(\text{bpy})_2(\text{bpy}_{\text{out}})]^{2+}$ to the solvent, organic impurities or bpy ligand with consecutive degradation.

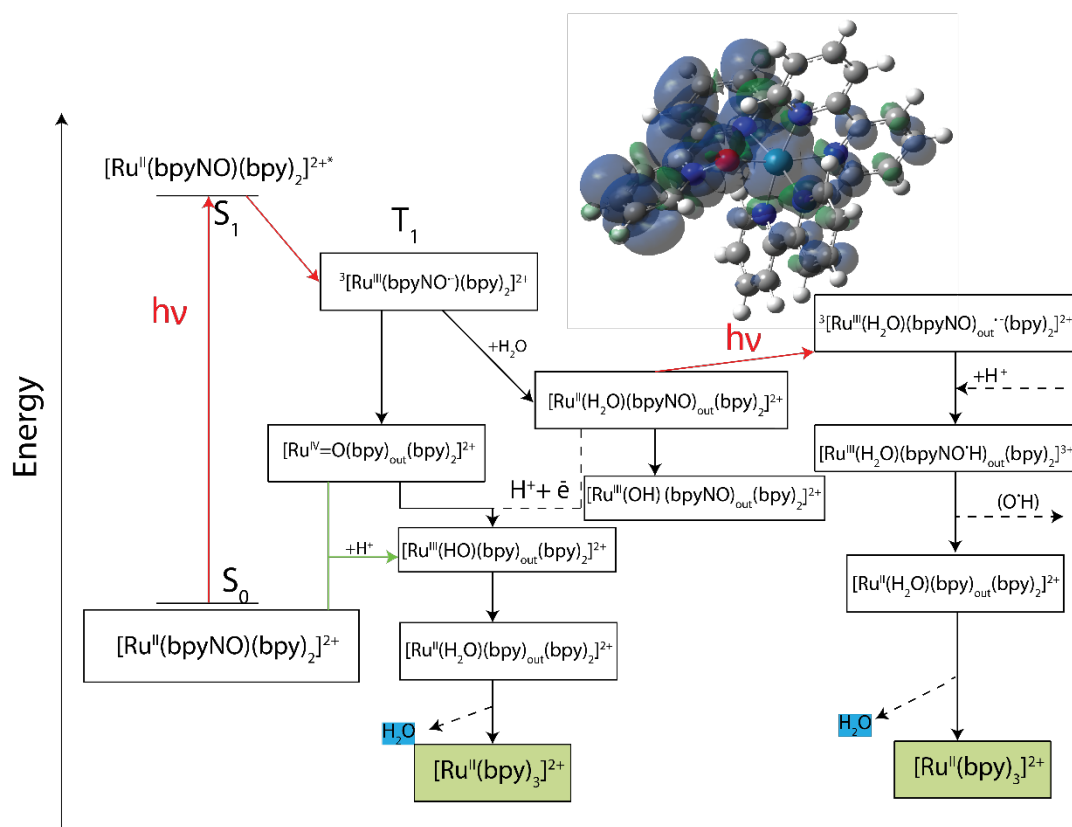


Figure 5-8. Possible pathways of conversion of (1-NO) to (1) upon light irradiation. S_0 and S_1 are the singlet ground and excited states, T_1 is the excited triplet state. The spin density of the triplet state is at the top and shows the electron localization on the bpyNO ligand. The triplet state could transform into two main structures initiating different pathways.

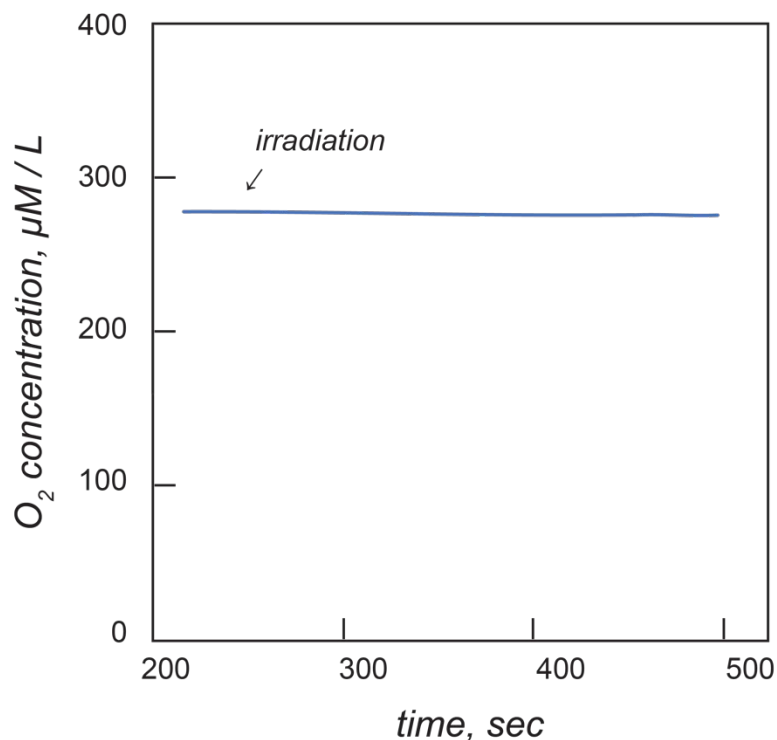


Figure 5-9. Oxygraph data of (1-NO) solution exposed with light. No changes in oxygen concentration have been detected during the irradiation. The experiments have been repeated for 3 times for each concentration of Ru(bpy)₂(bpyNO)(PF₆)₂ and demonstrated the similar results.

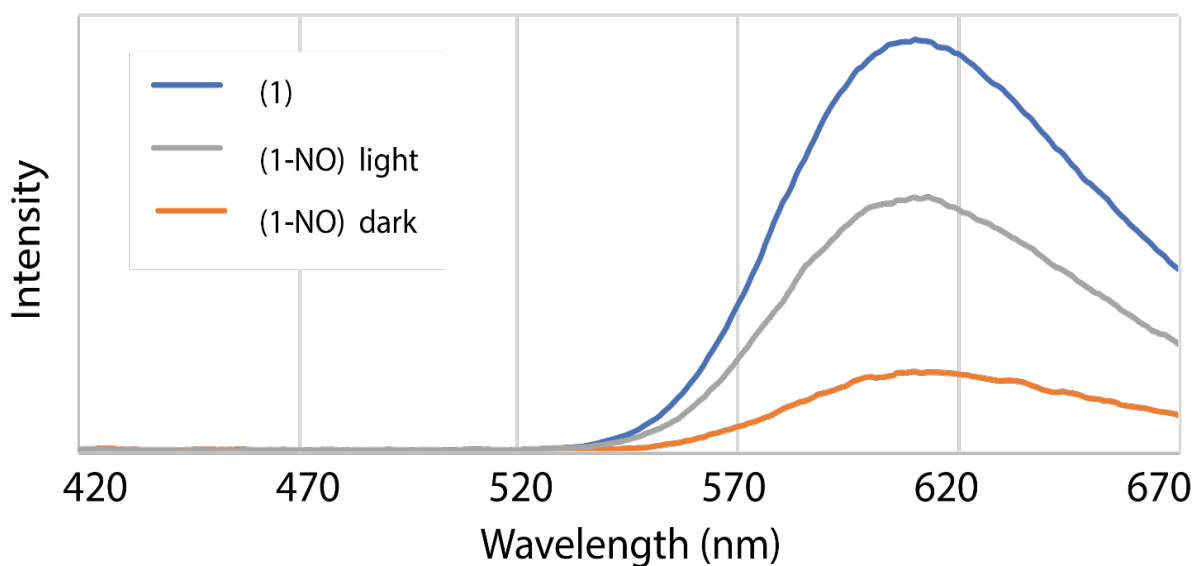


Figure 5-10. Emission spectra of 0.08 mM of (1), (1-NO), and light exposed (1-NO) in water. (1-NO) is approximately redshifted by 4 nm. The excitation light was 350 nm

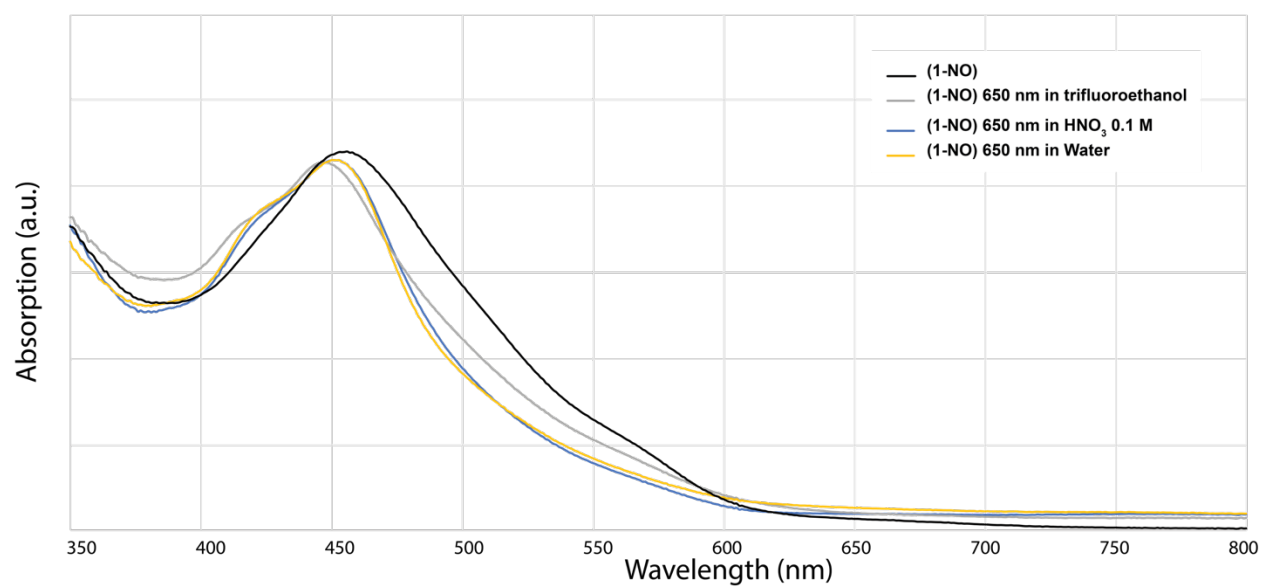


Figure 5-11. Absorption spectra of 1mM (1-NO) and illuminated (1-NO) in different solvents. All the light induced samples are illuminated with 670 nm LED for 30 minutes.

Table 5-3. Calculated energies of light driven reactions with DFT (the photon energy is not explicitly entered in the calculations) ^a

Reaction	Energy (eV)
$[\text{Ru}^{\text{II}}(\text{bpyNO})(\text{bpy})_2]^{2+} + h\nu = {}^3[\text{Ru}^{\text{III}}(\text{bpyNO}^{\bullet})(\text{bpy})_2]^{2+}$	+1.71
$[\text{Ru}^{\text{II}}(\text{bpyNO})(\text{bpy})_2]^{2+} + h\nu = 5\text{-coord } {}^3[\text{Ru}^{\text{II}}(\text{bpyNO}_{\text{out}})(\text{bpy})_2]^{2+}$	+1.69
${}^3[\text{Ru}^{\text{III}}(\text{bpyNO}^{\bullet})(\text{bpy})_2]^{2+} = [\text{Ru}^{\text{IV}}=\text{O}(\text{bpy})_2(\text{bpy}_{\text{out}})]^{2+}$	-1.02
${}^3[\text{Ru}^{\text{III}}(\text{bpyNO}^{\bullet})(\text{bpy})_2]^{2+} + \text{H}_2\text{O} = [\text{Ru}^{\text{II}}(\text{H}_2\text{O})(\text{bpy})_2(\text{bpyNO}_{\text{out}})]^{2+}$	-0.77
$[\text{Ru}^{\text{II}}(\text{bpyNO})(\text{bpy})_2]^{2+} + [\text{Ru}^{\text{IV}}=\text{O}(\text{bpy})_2(\text{bpy}_{\text{out}})]^{2+} + \text{H}^+ = [\text{Ru}^{\text{III}}(\text{bpyNO})(\text{bpy})_2]^{3+} + [\text{Ru}^{\text{III}}(\text{OH})(\text{bpy})_2(\text{bpy}_{\text{out}})]^{2+}$	0.04
$[\text{Ru}^{\text{II}}(\text{bpyNO})(\text{bpy})_2]^{2+} + [\text{Ru}^{\text{III}}(\text{OH})(\text{bpy})_2(\text{bpy}_{\text{out}})]^{2+} + \text{H}^+ = [\text{Ru}^{\text{III}}(\text{bpyNO})(\text{bpy})_2]^{3+} + [\text{Ru}^{\text{II}}(\text{H}_2\text{O})(\text{bpy})_2(\text{bpy}_{\text{out}})]^{2+}$	0.21
$[\text{Ru}^{\text{II}}(\text{H}_2\text{O})(\text{bpy})_2(\text{bpy}_{\text{out}})]^{2+} = [\text{Ru}^{\text{II}}(\text{bpy})_3]^{2+} + \text{H}_2\text{O}$	-1.31
$[\text{Ru}^{\text{II}}(\text{bpyNO})(\text{bpy})_2]^{2+} + [\text{Ru}^{\text{IV}}=\text{O}(\text{bpy})_2(\text{bpy}_{\text{out}})]^{2+} + 2\text{H}^+ = [\text{Ru}^{\text{III}}(\text{bpyNO})(\text{bpy})_2]^{3+} + [\text{Ru}^{\text{III}}(\text{bpy})_3]^{3+} + \text{H}_2\text{O}$	-0.79
$[\text{Ru}^{\text{IV}}=\text{O}(\text{bpy})_2(\text{bpy}_{\text{out}})]^{2+} + [\text{Ru}^{\text{II}}(\text{H}_2\text{O})(\text{bpy})_2(\text{bpyNO}_{\text{out}})]^{2+} + \text{H}^+ = [\text{Ru}^{\text{III}}(\text{OH})(\text{bpy})_2(\text{bpy}_{\text{out}})]^{2+} + [\text{Ru}^{\text{III}}(\text{H}_2\text{O})(\text{bpy})_2(\text{bpyNO}_{\text{out}})]^{3+}$	-0.16
$[\text{Ru}^{\text{II}}(\text{bpyNO})(\text{bpy})_2]^{2+} + h\nu + \text{H}_2\text{O} = [\text{Ru}^{\text{III}}(\text{OH})(\text{bpy})_2(\text{bpyNO}^{\bullet}\text{H}_{\text{out}})]^{2+}$	+3.06
$[\text{Ru}^{\text{II}}(\text{bpyNO})(\text{bpy})_2]^{2+} + h\nu + \text{H}^+ \square 5 \text{ coord } -[\text{Ru}^{\text{III}}(\text{bpy})_2(\text{bpyNO}^{\bullet}\text{H}_{\text{out}})]^{3+}$	+2.03
^a The energy of the complexes can be found in Table 5-4	

Table 5-4. (1-NO) and possible intermediates theoretical free energy by DFT

Chemical formula	Charge, Spin multiplicity	Energy (Hartree)
$[\text{Ru}^{\text{II}}(\text{bpyNO})(\text{bpy})_2]^{2+}$	2, 1	-6003.5559
$^3[\text{Ru}^{\text{III}}(\text{bpyNO}^{\bullet-})(\text{bpy})_2]^{2+}$	2 3	-6003.4931
$[\text{Ru}^{\text{IV}}=\text{O}(\text{bpy}_{\text{out}})(\text{bpy})_2]^{2+}$	2 3	-6003.5306
$[\text{Ru}^{\text{III}}(\text{OH})(\text{bpy}_{\text{out}})(\text{bpy})_2]^{2+}$	2 2	-6004.1567
$[\text{Ru}^{\text{II}}(\text{H}_2\text{O})(\text{bpy}_{\text{out}})(\text{bpy})_2]^{2+}$	2 1	-6004.7759
$[\text{Ru}^{\text{II}}(\text{bpy})_3]^{2+}$	2 1	-5928.4111
$[\text{Ru}^{\text{II}}(\text{H}_2\text{O})(\text{bpyNO}_{\text{out}})(\text{bpy})_2]^{2+}$	2 1	-6079.9343
$[\text{Ru}^{\text{III}}(\text{OH})(\text{bpyNO}_{\text{out}})(\text{bpy})_2]^{2+}$	2 2	-6079.3175
$[\text{Ru}^{\text{III}}(\text{H}_2\text{O})(\text{bpy})_2(\text{bpyNO}^{\bullet}_{\text{out}})]^{2+}$	2 3	-6079.8925
$[\text{Ru}^{\text{III}}(\text{H}_2\text{O})(\text{bpy})_2(\text{bpyNOH}^{\bullet}_{\text{out}})]^{3+}$	3 3	-6080.3074

5.5 Conclusions

I have investigated the photochemical and redox behavior of very light sensitive (**1-NO**) complex. The bpyNO ligand in (**1-NO**) undergoes a reduction to bpyNO^{•-} in the presence of the mild reducing agent Asc. The UV-Vis, NMR and Raman spectroscopy confirm the formation of (**1**) as a single product of the light irradiation of (**1-NO**). EPR signals observed in the solutions of (**1-NO**) upon the irradiation were assigned to the open and closed forms of the Ru^{III} intermediates. The simulated hfs are in agreement with the EPR measurements and the previous reports of NO radicals coordinated to the Ru center. Several pathways were proposed to explain the conversion of (**1-NO**) to (**1**) and validated with DFT calculations.

REFERENCES

1. Keidel, A.; López, I.; Staffa, J.; Kuhlmann, U.; Bozoglian, F.; Gimbert-Suriñach, C.; Benet-Buchholz, J.; Hildebrandt, P.; Llobet, A., Electrochemical and Resonance Raman Spectroscopic Studies of Water-Oxidizing Ruthenium Terpyridyl–Bipyridyl Complexes. *ChemSusChem* **2017**, *10* (3), 551-561.
2. Moonshiram, D.; Jurss, J. W.; Concepcion, J. J.; Zakharova, T.; Alperovich, I.; Meyer, T. J.; Pushkar, Y., Structure and electronic configurations of the intermediates of water oxidation in blue ruthenium dimer catalysis. *Journal of the American Chemical Society* **2012**, *134* (10), 4625-36.
3. Hurst, J. K., Water oxidation catalyzed by dimeric mu-oxo bridged ruthenium diimine complexes. *Coord. Chem. Rev.* **2005**, *249* (3-4), 313-328.
4. Swierk, J. R.; Mallouk, T. E., Design and development of photoanodes for water-splitting dye-sensitized photoelectrochemical cells. *Chem. Soc. Rev.* **2013**, *42* (6), 2357-2387.
5. Osterloh, F. E., Inorganic nanostructures for photoelectrochemical and photocatalytic water splitting. *Chem. Soc. Rev.* **2013**, *42* (6), 2294-2320.
6. Singh, A.; Spiccia, L., Water oxidation catalysts based on abundant 1st row transition metals. *Coord. Chem. Rev.* **2013**, *257* (17-18), 2607-2622.
7. Gao, Y.; Ding, X.; Liu, J. H.; Wang, L.; Lu, Z. K.; Li, L.; Sun, L. C., Visible Light Driven Water Splitting in a Molecular Device with Unprecedentedly High Photocurrent Density. *Journal of the American Chemical Society* **2013**, *135* (11), 4219-4222.
8. Karkas, M. D.; Akermark, B., Water oxidation using earth-abundant transition metal catalysts: opportunities and challenges. *Dalton Trans.* **2016**, *45* (37), 14421-14461.
9. Karkas, M. D.; Verho, O.; Johnston, E. V.; Akermark, B., Artificial Photosynthesis: Molecular Systems for Catalytic Water Oxidation. *Chem. Rev.* **2014**, *114* (24), 11863-12001.
10. Blakemore, J. D.; Crabtree, R. H.; Brudvig, G. W., Molecular Catalysts for Water Oxidation. *Chem. Rev.* **2015**, *115* (23), 12974-13005.
11. Pushkar, Y.; Pineda-Galvan, Y.; Ravari, A. K.; Otroshchenko, T.; Hartzler, D. A., Mechanism for O-O Bond Formation via Radical Coupling of Metal and Ligand Based Radicals: A New Pathway. *Journal of the American Chemical Society* **2018**, *140* (42), 13538-13541.
12. Pushkar, Y.; Moonshiram, D.; Purohit, V.; Yan, L.; Alperovich, I., Spectroscopic Analysis of Catalytic Water Oxidation by [RuII(bpy)(tpy)H₂O]₂⁺ Suggests That RuV=O Is Not a Rate-Limiting Intermediate. *Journal of the American Chemical Society* **2014**, *136* (34), 11938–11945.
13. Moonshiram, D.; Pineda-Galvan, Y.; Erdman, D.; Palenik, M.; Zong, R.; Thummel, R.; Pushkar, Y., Uncovering the role of oxygen atom transfer in Ru-based Catalytic Water Oxidation. *Journal of the American Chemical Society* **2016**, *138* (48), 15605-15616.
14. Concepcion, J. J.; Tsai, M. K.; Muckerman, J. T.; Meyer, T. J., Mechanism of Water Oxidation by Single-Site Ruthenium Complex Catalysts. *Journal of the American Chemical Society* **2010**, *132* (5), 1545-1557.
15. IEA, Key World Energy Statistics 2017. 2017.

16. Kok, B.; Forbush, B.; McGloin, M., COOPERATION OF CHARGES IN PHOTOSYNTHETIC O₂ EVOLUTION–I. A LINEAR FOUR STEP MECHANISM. *Photochemistry and Photobiology* **1970**, *11* (6), 457-475.
17. Clarizia, L.; Russo, D.; Di Somma, I.; Andreozzi, R.; Marotta, R., Hydrogen Generation through Solar Photocatalytic Processes: A Review of the Configuration and the Properties of Effective Metal-Based Semiconductor Nanomaterials. *Energies* **2017**, *10* (10), 21.
18. de Levie, R., The electrolysis of water. *Journal of Electroanalytical Chemistry* **1999**, *476* (1), 92-93.
19. Ayers, K.; Danilovic, N.; Ouimet, R.; Carmo, M.; Pivovar, B.; Bornstein, M., Perspectives on Low-Temperature Electrolysis and Potential for Renewable Hydrogen at Scale. *Annual Review of Chemical and Biomolecular Engineering, Vol 10* **2019**, *10*, 219-239.
20. Coehn, A.; Becker, H., Studies concerning photochemical equilibrium III. The light equilibrium of phosgene. *Berichte Der Deutschen Chemischen Gesellschaft* **1910**, *43*, 130-133.
21. Fujishima, A.; Honda, K., ELECTROCHEMICAL PHOTOLYSIS OF WATER AT A SEMICONDUCTOR ELECTRODE. *Nature* **1972**, *238* (5358), 37-+.
22. Sakai, K.; Ozawa, H., Homogeneous catalysis of platinum(II) complexes in photochemical hydrogen production from water. *Coordination Chemistry Reviews* **2007**, *251* (21-24), 2753-2766.
23. McDaniel, N. D.; Coughlin, F. J.; Tinker, L. L.; Bernhard, S., Cyclometalated iridium(III) aquo complexes: Efficient and tunable catalysts for the homogeneous oxidation of water. *Journal of the American Chemical Society* **2008**, *130* (1), 210-217.
24. Naruta, Y.; Sasayama, M.; Sasaki, T., OXYGEN EVOLUTION BY OXIDATION OF WATER WITH MANGANESE PORPHYRIN DIMERS. *Angewandte Chemie-International Edition in English* **1994**, *33* (18), 1839-1841.
25. Inoue, H.; Shimada, T.; Kou, Y.; Nabetani, Y.; Masui, D.; Takagi, S.; Tachibana, H., The Water Oxidation Bottleneck in Artificial Photosynthesis: How Can We Get Through It? An Alternative Route Involving a Two-Electron Process. *Chemsuschem* **2011**, *4* (2), 173-179.
26. Sun, L. C.; Hammarstrom, L.; Akermark, B.; Styring, S., Towards artificial photosynthesis: ruthenium-manganese chemistry for energy production. *Chemical Society Reviews* **2001**, *30* (1), 36-49.
27. Nair, V.; Deepthi, A., Cerium(IV) ammonium nitrate - A versatile single-electron oxidant. *Chemical Reviews* **2007**, *107* (5), 1862-1891.
28. Limburg, J.; Crabtree, R. H.; Brudvig, G. W., Kinetic analysis of the O₂-forming reaction between Mn(III)(dpa)₂ (-) (dpa = dipicolinate) and potassium peroxomonosulfate. *Inorganica Chimica Acta* **2000**, *297* (1-2), 301-306.
29. **Robert, A.; Meunier, B., Oxygenation of hydrocarbons by potassium hydrogen persulfate (KHSO₅) catalyzed by manganese porphyrin complexes.** *New Journal of Chemistry*: 1988.
30. Hetterscheid, D. G. H.; Reek, J. N. H., Periodate as an Oxidant for Catalytic Water Oxidation: Oxidation via Electron Transfer or O-Atom Transfer? *European Journal of Inorganic Chemistry* **2014**, (4), 742-749.
31. Weavers, L. K.; Hua, I.; Hoffmann, M. R., Degradation of triethanolamine and chemical oxygen demand reduction in wastewater by photoactivated periodate. *Water Environment Research* **1997**, *69* (6), 1112-1119.

32. Gersten, S. W.; Samuels, G. J.; Meyer, T. J., Catalytic oxidation of water by an oxo-bridged ruthenium dimer. *J. Am. Chem. Soc.* **1982**.
33. Demas, J. N.; Adamson, A. W., NEW PHOTSENSITIZER - TRIS(2,2'-BIPYRIDINE)RUTHENIUM(II) CHLORIDE. *Journal of the American Chemical Society* **1971**, *93* (7), 1800-&.
34. Pineda-Galvan, Y.; Ravari, A. K.; Shmakov, S.; Lifshits, L.; Kaveevivitchai, N.; Thummel, R.; Pushkar, Y., Detection of the site protected 7-coordinate RuV=O species and its chemical reactivity to enable catalytic water oxidation. *Journal of Catalysis* **2019**, accepted.
35. Tong, L. P.; Thummel, R. P., Mononuclear ruthenium polypyridine complexes that catalyze water oxidation. *Chemical Science* **2016**, *7* (11), 6591-6603.
36. Vandenabeele, P., Practical Raman spectroscopy an introduction. Wiley,: Chichester, West Sussex, U.K., 2013; p. 1 online resource (163 p.).
37. Dieing, T.; Hollricher, O.; Toporski, J., Confocal Raman Microscopy. In *Springer Series in Optical Sciences*, [Online]; pp. 1 online resource (XVI, 292 p.).
38. Harris, D. C.; Bertolucci, M. D., *Symmetry and spectroscopy : an introduction to vibrational and electronic spectroscopy*. Oxford University Press: New York, 1978; p xii, 550 p.
39. Society for Applied Spectroscopy., Applied spectroscopy. Society for Applied Spectroscopy.: Baltimore, Md., p v.
40. Xie, L.; Ling, X.; Fang, Y.; Zhang, J.; Liu, Z., Graphene as a substrate to suppress fluorescence in resonance Raman spectroscopy. *J Am Chem Soc* **2009**, *131* (29), 9890-1.
41. Overall, N.; Hahn, T.; Matousek, P.; Parker, A. W.; Towrie, M., Picosecond time-resolved Raman spectroscopy of solids: Capabilities and limitations for fluorescence rejection and the influence of diffuse reflectance. *Applied Spectroscopy* **2001**, *55* (12), 1701-1708.
42. J.N.Junk, M., Assessing the Functional Structure of Molecular Transporters by EPR Spectroscopy. In *Springer Theses* [Online]; p. 1 online resource (224 p.).
43. Daniel, Q.; Huang, P.; Fan, T.; Wang, Y.; Duan, L. L.; Wang, L.; Li, F. S.; Rinkevicius, Z.; Mamedov, F.; Ahlquist, M. S. G.; Styring, S.; Sun, L. C., Rearranging from 6-to 7-coordination initiates the catalytic activity: An EPR study on a Ru-bda water oxidation catalyst. *Coordination Chemistry Reviews* **2017**, *346*, 206-215.
44. Hohenberg, P.; Kohn, W., Inhomogeneous Electron Gas. *Physical Review* **1964**, *136* (3B), B864-B871.
45. Kohn, W.; Sham, L. J., Self-Consistent Equations Including Exchange and Correlation Effects. *Physical Review* **1965**, *140* (4A), A1133-A1138.
46. Frisch, M. J.; Trucks, G. W.; Schlegel, H. B.; Scuseria, G. E.; Robb, M. A.; Cheeseman, J. R.; Scalmani, G.; Barone, V.; Petersson, G. A.; Nakatsuji, H.; Li, X.; Caricato, M.; Marenich, A. V.; Bloino, J.; Janesko, B. G.; Gomperts, R.; Mennucci, B.; Hratchian, H. P.; Ortiz, J. V.; Izmaylov, A. F.; Sonnenberg, J. L.; Williams; Ding, F.; Lipparini, F.; Egidi, F.; Goings, J.; Peng, B.; Petrone, A.; Henderson, T.; Ranasinghe, D.; Zakrzewski, V. G.; Gao, J.; Rega, N.; Zheng, G.; Liang, W.; Hada, M.; Ehara, M.; Toyota, K.; Fukuda, R.; Hasegawa, J.; Ishida, M.; Nakajima, T.; Honda, Y.; Kitao, O.; Nakai, H.; Vreven, T.; Throssell, K.; Montgomery Jr., J. A.; Peralta, J. E.; Ogliaro, F.; Bearpark, M. J.; Heyd, J. J.; Brothers, E. N.; Kudin, K. N.; Staroverov, V. N.; Keith, T. A.; Kobayashi, R.; Normand, J.; Raghavachari, K.; Rendell, A. P.; Burant, J. C.; Iyengar, S. S.; Tomasi, J.; Cossi, M.; Millam, J. M.; Klene, M.; Adamo, C.; Cammi, R.; Ochterski, J. W.; Martin, R. L.;

- Morokuma, K.; Farkas, O.; Foresman, J. B.; Fox, D. J. *Gaussian 16 Rev. C.01*, Wallingford, CT, 2016.
47. De Luna, P.; Hahn, C.; Higgins, D.; Jaffer, S. A.; Jaramillo, T. F.; Sargent, E. H., What would it take for renewably powered electrosynthesis to displace petrochemical processes? *Science* **2019**, *364* (6438), eaav3506.
 48. Suga, M.; Akita, F.; Sugahara, M.; Kubo, M.; Nakajima, Y.; Nakane, T.; Yamashita, K.; Umena, Y.; Nakabayashi, M.; Yamane, T.; Nakano, T.; Suzuki, M.; Masuda, T.; Inoue, S.; Kimura, T.; Nomura, T.; Yonekura, S.; Yu, L.-J.; Sakamoto, T.; Motomura, T.; Chen, J.-H.; Kato, Y.; Noguchi, T.; Tono, K.; Joti, Y.; Kameshima, T.; Hatsui, T.; Nango, E.; Tanaka, R.; Naitow, H.; Matsuura, Y.; Yamashita, A.; Yamamoto, M.; Nureki, O.; Yabashi, M.; Ishikawa, T.; Iwata, S.; Shen, J.-R., Light-induced structural changes and the site of O=O bond formation in PSII caught by XFEL. *Nature* **2017**, *543* (7643), 131-135.
 49. Kern, J.; Chatterjee, R.; Young, I. D.; Fuller, F. D.; Lassalle, L.; Ibrahim, M.; Gul, S.; Fransson, T.; Brewster, A. S.; Alonso-Mori, R.; Hussein, R.; Zhang, M.; Douthit, L.; de Lichtenberg, C.; Cheah, M. H.; Shevela, D.; Wersig, J.; Seuffert, I.; Sokaras, D.; Pastor, E.; Weninger, C.; Kroll, T.; Sierra, R. G.; Aller, P.; Butryn, A.; Orville, A. M.; Liang, M.; Batyuk, A.; Koglin, J. E.; Carbajo, S.; Boutet, S.; Moriarty, N. W.; Holton, J. M.; Dobbek, H.; Adams, P. D.; Bergmann, U.; Sauter, N. K.; Zouni, A.; Messinger, J.; Yano, J.; Yachandra, V. K., Structures of the intermediates of Kok's photosynthetic water oxidation clock. *Nature* **2018**, *563* (7731), 421-425.
 50. Davis, K. M.; Sullivan, B. T.; Palenik, M. C.; Yan, L.; Purohit, V.; Robison, G.; Kosheleva, I.; Henning, R. W.; Seidler, G. T.; Pushkar, Y., Rapid Evolution of the Photosystem II Electronic Structure during Water Splitting. *Phys. Rev. X* **2018**, *8* (4), 041014.
 51. Davis, K. M.; Pushkar, Y. N., Structure of the Oxygen Evolving Complex of Photosystem II at Room Temperature. *J. Phys. Chem. B* **2015**, *119* (8), 3492-3498.
 52. Katherine M. Davis; Brendan T. Sullivan; Mark Palenik; Lifen Yan; Vatsal Purohit; Gregory Robison; Irina Kosheleva; Robert W. Henning; Gerald T. Seidler; Pushkar, Y., Rapid Evolution of the Photosystem II Electronic Structure During Water Splitting. . *arXiv:1506.08862* **2015**.
 53. House, R. L.; Iha, N. Y. M.; Coppo, R. L.; Alibabaei, L.; Sherman, B. D.; Kang, P.; Brennaman, M. K.; Hoertz, P. G.; Meyer, T. J., Artificial photosynthesis: Where are we now? Where can we go? *J. Photochem. Photobiol. C-Photochem. Rev.* **2015**, *25*, 32-45.
 54. Li, J.; Guttinger, R.; More, R.; Song, F.; Wan, W.; Patzke, G. R., Frontiers of water oxidation: the quest for true catalysts. *Chem. Soc. Rev.* **2017**, *46* (20), 6124-6147.
 55. Matheu, R.; Garrido-Barros, P.; Gil-Sepulcre, M.; Ertem, M. Z.; Sala, X.; Gimbert-Surinach, C.; Llobet, A., The development of molecular water oxidation catalysts. *Nat. Rev. Chem.* **2019**, *3* (5), 331-341.
 56. Pushkar, Y.; Davis, K. M.; Palenik, M., Model of the Oxygen Evolving Complex Which is Highly Predisposed to O–O Bond Formation. *J. Phys. Chem. Lett.* **2018**, *9*, 3524-3531.
 57. Pushkar, Y.; K. Ravari, A.; Jensen, S. C.; Palenik, M., Early Binding of Substrate Oxygen Is Responsible for a Spectroscopically Distinct S2 State in Photosystem II. *The Journal of Physical Chemistry Letters* **2019**, *10* (17), 5284-5291.
 58. Ye, S.; Ding, C.; Liu, M.; Wang, A.; Huang, Q.; Li, C., Water Oxidation Catalysts for Artificial Photosynthesis. *Adv. Mater.* **2019**, *n/a* (n/a), 1902069.

59. Zhang, B.; Sun, L., Artificial photosynthesis: opportunities and challenges of molecular catalysts. *Chem. Soc. Rev.* **2019**, *48* (7), 2216-2264.
60. Garrido-Barros, P.; Gimbert-Surinach, C.; Matheu, R.; Sala, X.; Llobet, A., How to make an efficient and robust molecular catalyst for water oxidation. *Chem. Soc. Rev.* **2017**, *46* (20), 6088-6098.
61. Lebedev, D.; Pineda-Galvan, Y.; Tokimaru, Y.; Fedorov, A.; Kaeffer, N.; Copéret, C.; Pushkar, Y., The Key RuV=O Intermediate of Site-Isolated Mononuclear Water Oxidation Catalyst Detected by in Situ X-ray Absorption Spectroscopy. *Journal of the American Chemical Society* **2018**, *140* (1), 451-458.
62. Moonshiram, D.; Pineda-Galvan, Y.; Erdman, D.; Palenik, M.; Zong, R. F.; Thummel, R.; Pushkar, Y., Uncovering the Role of Oxygen Atom Transfer in Ru-Based Catalytic Water Oxidation. *Journal of the American Chemical Society* **2016**, *138* (48), 15605-15616.
63. Gersten, S. W.; Samuels, G. J.; Meyer, T. J., Catalytic oxidation of water by an oxo-bridged ruthenium dimer. *J. Am. Chem. Soc.* **1982**, *104* (14), 4029-4030.
64. Moonshiram, D.; Alperovich, I.; Concepcion, J. J.; Meyer, T. J.; Pushkar, Y., Experimental demonstration of radicaloid character in a Ru-V=O intermediate in catalytic water oxidation. *Proc. Natl. Acad. Sci. U. S. A.* **2013**, *110* (10), 3765-3770.
65. Stull, J. A.; Britt, R. D.; McHale, J. L.; Knorr, F. J.; Lymar, S. V.; Hurst, J. K., Anomalous reactivity of ceric nitrate in ruthenium "blue dimer"-catalyzed water oxidation. *Journal of the American Chemical Society* **2012**, *134* (49), 19973-6.
66. Planas, N.; Vigara, L.; Cady, C.; Miro, P.; Huang, P.; Hammarstrom, L.; Styring, S.; Leidel, N.; Dau, H.; Haumann, M.; Gagliardi, L.; Cramer, C. J.; Llobet, A., Electronic Structure of Oxidized Complexes Derived from cis-Ru(II)(bpy)(2)(H(2)O)(2)](2+) and Its Photoisomerization Mechanism. *Inorganic Chemistry* **2011**, *50* (21), 11134-11142.
67. Erdman, D.; Pineda-Galvan, Y.; Pushkar, Y., Mechanistic Analysis of Water Oxidation Catalyst cis- Ru(bpy)(2)(H2O)(2) (2+): Effect of Dimerization. *Catalysts* **2017**, *7* (2).
68. Duan, L. L.; Bozoglian, F.; Mandal, S.; Stewart, B.; Privalov, T.; Llobet, A.; Sun, L. C., A molecular ruthenium catalyst with water-oxidation activity comparable to that of photosystem II. *Nat. Chem.* **2012**, *4* (5), 418-423.
69. Duan, L. L.; Araujo, C. M.; Ahlquist, M. S. G.; Sun, L. C., Highly efficient and robust molecular ruthenium catalysts for water oxidation. *Proc. Natl. Acad. Sci. U. S. A.* **2012**, *109* (39), 15584-15588.
70. Pineda-Galvan, Y.; Ravari, A. K.; Shmakov, S.; Lifshits, L.; Kaveevivitchai, N.; Thummel, R.; Pushkar, Y., Detection of the site protected 7-coordinate RuV = O species and its chemical reactivity to enable catalytic water oxidation. *Journal of Catalysis* **2019**, *375*, 1-7.
71. Wasylenko, D. J.; Ganesamoorthy, C.; Henderson, M. A.; Koivisto, B. D.; Osthoff, H. D.; Berlinguette, C. P., Electronic Modification of the [Ru-II(tpy)(bpy)(OH2)](2+) Scaffold: Effects on Catalytic Water Oxidation. *Journal of the American Chemical Society* **2010**, *132* (45), 16094-16106.
72. Marelus, D. C.; Bhagan, S.; Charboneau, D. J.; Schroeder, K. M.; Kamdar, J. M.; McGettigan, A. R.; Freeman, B. J.; Moore, C. E.; Rheingold, A. L.; Cooksy, A. L.; Smith, D. K.; Paul, J. J.; Papish, E. T.; Grotjahn, D. B., How Do Proximal Hydroxy or Methoxy Groups on the Bidentate Ligand Affect (2,2'-6',2'-Terpyridine)Ru-(N,N)X Water-Oxidation Catalysts? Synthesis, Characterization, and Reactivity at Acidic and Near-Neutral pH. *European Journal of Inorganic Chemistry* **2014**, (4), 676-689.

73. Maji, S.; Lopez, I.; Bozoglian, F.; Benet-Buchholz, J.; Llobet, A., Mononuclear Ruthenium-Water Oxidation Catalysts: Discerning between Electronic and Hydrogen-Bonding Effects. *Inorganic Chemistry* **2013**, *52* (7), 3591-3593.
74. Yoshida, M.; Kondo, M.; Torii, S.; Sakai, K.; Masaoka, S., Oxygen Evolution Catalyzed by a Mononuclear Ruthenium Complex Bearing Pendant SO₃⁻ Groups. *Angew. Chem.* **2015**, *127* (27), 8092-8095.
75. Yagi, M.; Tajima, S.; Komi, M.; Yamazaki, H., Highly active and tunable catalysts for O₂ evolution from water based on mononuclear ruthenium(II) monoquo complexes. *Dalton Trans.* **2011**, *40* (15), 3802-3804.
76. Honta, J.; Tajima, S.; Sato, T.; Saito, K.; Yui, T.; Yagi, M., Spectroelectrochemical investigation of electrocatalytic water oxidation by a mononuclear ruthenium complex in a homogeneous solution. *J. Photochem. Photobiol. A-Chem.* **2015**, *313*, 126-130.
77. Lin, S.; Pineda-Galvan, Y.; Maza, W. A.; Epley, C. C.; Zhu, J.; Kessinger, M. C.; Pushkar, Y.; Morris, A. J., Electrochemical Water Oxidation by a Catalyst-Modified Metal-Organic Framework Thin Film. *ChemSusChem* **2017**, *10* (3), 514-522.
78. Brennaman, M. K.; Gish, M. K.; Alibabaei, L.; Norris, M. R.; Binstead, R. A.; Nayak, A.; Lapedes, A. M.; Song, W. J.; Brown, R. J.; Concepcion, J. J.; Templeton, J. L.; Papanikolas, J. M.; Meyer, T. J., Pathways Following Electron Injection: Medium Effects and Cross-Surface Electron Transfer in a Ruthenium-Based, Chromophore-Catalyst Assembly on TiO₂. *J. Phys. Chem. C* **2018**, *122* (24), 13017-13026.
79. Masaoka, S.; Sakai, K., Clear Evidence Showing the Robustness of a Highly Active Oxygen-evolving Mononuclear Ruthenium Complex with an Aqua Ligand. *Chem. Lett.* **2009**, *38* (2), 182-183.
80. Yan, L. F.; Zong, R. F.; Pushkar, Y., Unexpected ligand lability in condition of water oxidation catalysis. *Journal of Catalysis* **2015**, *330*, 255-260.
81. Hughes, T. F.; Friesner, R. A., Systematic Investigation of the Catalytic Cycle of a Single Site Ruthenium Oxygen Evolving Complex Using Density Functional Theory. *J. Phys. Chem. B* **2011**, *115* (29), 9280-9289.
82. Sala, X.; Ertem, M. Z.; Vigarà, L.; Todorova, T. K.; Chen, W. Z.; Rocha, R. C.; Aquilante, F.; Cramer, C. J.; Gagliardi, L.; Llobet, A., The cis-[Ru-II(bpy)(2)(H₂O)(2)](2+) Water-Oxidation Catalyst Revisited. *Angew. Chem.-Int. Edit.* **2010**, *49* (42), 7745-7747.
83. Vigarà, L.; Ertem, M. Z.; Planas, N.; Bozoglian, F.; Leidel, N.; Dau, H.; Haumann, M.; Gagliardi, L.; Cramer, C. J.; Llobet, A., Experimental and quantum chemical characterization of the water oxidation cycle catalysed by [Ru-II(damp)(bpy)(H₂O)](2+). *Chem. Sci.* **2012**, *3* (8), 2576-2586.
84. Privalov, T.; Akermark, B.; Sun, L. C., The O-O Bonding in Water Oxidation: the Electronic Structure Portrayal of a Concerted Oxygen Atom-Proton Transfer Pathway. *Chemistry-a European Journal* **2011**, *17* (30), 8313-8317.
85. Angeles-Boza, A. M.; Ertem, M. Z.; Sarma, R.; Ibanez, C. H.; Maji, S.; Llobet, A.; Cramer, C. J.; Roth, J. P., Competitive oxygen-18 kinetic isotope effects expose O-O bond formation in water oxidation catalysis by monomeric and dimeric ruthenium complexes. *Chem. Sci.* **2014**, *5* (3), 1141-1152.
86. Tong, L. P.; Inge, A. K.; Duan, L. L.; Wang, L.; Zou, X. D.; Sun, L. C., Catalytic Water Oxidation by Mononuclear Ru Complexes with an Anionic Ancillary Ligand. *Inorganic Chemistry* **2013**, *52* (5), 2505-2518.

87. Kimoto, A.; Yamauchi, K.; Yoshida, M.; Masaoka, S.; Sakai, K., Kinetics and DFT studies on water oxidation by Ce⁴⁺ catalyzed by [Ru(terpy)(bpy)(OH₂)]₂⁺. *Chem Commun (Camb)* **2012**, 48 (2), 239-41.
88. Karmalkar, D. G.; Sankaralingam, M.; Seo, M. S.; Ezhov, R.; Lee, Y. M.; Pushkar, Y. N.; Kim, W. S.; Fukuzumi, S.; Nam, W., A High-Valent Manganese(IV)-Oxo-Cerium(IV) Complex and Its Enhanced Oxidizing Reactivity. *Angew. Chem.-Int. Edit.* **2019**, 7.
89. Liu, Y. Y.; Ng, S. M.; Yiu, S. M.; Lam, W. W. Y.; Wei, X. G.; Lau, K. C.; Lau, T. C., Catalytic Water Oxidation by Ruthenium(II) Quaterpyridine (qpy) Complexes: Evidence for Ruthenium(III) qpy-N,N'-dioxide as the Real Catalysts. *Angew. Chem.-Int. Edit.* **2014**, 53 (52), 14468-14471.
90. Wang, Y.; Rinkevicius, Z.; Ahlquist, M. S. G., Formation of N-oxide in the third oxidation of Ru-II(tpy)(L)(OH₂) (2⁺). *Chem. Commun.* **2017**, 53 (41), 5622-5624.
91. Raynor, J. B.; Jeliaskowa, B. G., ELECTRON-SPIN RESONANCE-SPECTRA OF SOME LOW-SPIN RUTHENIUM(III) COMPLEXES - A PROBE FOR SOLVATION EFFECTS. *J. Chem. Soc.-Dalton Trans.* **1982**, (7), 1185-1189.
92. Dengel, A. C.; Griffith, W. P., Studies on transition-metal oxo and nitrido complexes. 12. Synthesis, spectroscopic properties, and reactions of stable ruthenium(V) and osmium(V) oxo complexes containing .alpha.-hydroxy carboxylate and .alpha.-amino carboxylate ligands. *Inorganic Chemistry* **1991**, 30 (4), 869-871.
93. Lin, S. Y.; Ravari, A. K.; Zhu, J.; Usov, P. M.; Cai, M.; Ahrenholtz, S. R.; Pushkar, Y.; Morris, A. J., Insight into Metal-Organic Framework Reactivity: Chemical Water Oxidation Catalyzed by a Ru(tpy)(dcbpy)(OH₂) (2⁺)-Modified UiO-67. *ChemSusChem* **2018**, 11 (2), 464-471.
94. Pushkar, Y.; Pineda-Galvan, Y.; Ravari, A. K.; Otroshchenko, T.; Hartzler, D. A., Mechanism for O-O bond formation via radical coupling of metal and ligand based radicals – a new pathway *Journal of the American Chemical Society* **2018**, 140 (42), 13538-13541.
95. Lopez, I.; Ertem, M. Z.; Maji, S.; Benet-Buchholz, J.; Keidel, A.; Kuhlmann, U.; Hildebrandt, P.; Cramer, C. J.; Batista, V. S.; Llobet, A., A Self-Improved Water-Oxidation Catalyst: Is One Site Really Enough? *Angew. Chem.-Int. Edit.* **2014**, 53 (1), 205-209.
96. Lopez, I.; Maji, S.; Benet-Buchholz, J.; Llobet, A., Oxo-Bridge Scenario behind Single-Site Water-Oxidation Catalysts. *Inorganic Chemistry* **2014**, 54 (2), 658-666.
97. Ghosh, P. K.; Brunschwig, B. S.; Chou, M.; Creutz, C.; Sutin, N., THERMAL AND LIGHT-INDUCED REDUCTION OF RU(BPY)₃(3⁺) IN AQUEOUS-SOLUTION. *Journal of the American Chemical Society* **1984**, 106 (17), 4772-4783.
98. Kojima, T.; Nakayama, K.; Sakaguchi, M.; Ogura, T.; Ohkubo, K.; Fukuzumi, S., Photochemical Activation of Ruthenium(II)-Pyridylamine Complexes Having a Pyridine-N-Oxide Pendant toward Oxygenation of Organic Substrates. *Journal of the American Chemical Society* **2011**, 133 (44), 17901-17911.
99. Takeuchi, K. J.; Thompson, M. S.; Pipes, D. W.; Meyer, T. J., Redox and spectral properties of monooxo polypyridyl complexes of ruthenium and osmium in aqueous media. *Inorganic Chemistry* **1984**, 23 (13), 1845-1851.
100. Matheu, R.; Ertem, M. Z.; Gimbert-Suriñach, C.; Sala, X.; Llobet, A., Seven Coordinated Molecular Ruthenium–Water Oxidation Catalysts: A Coordination Chemistry Journey. *Chem. Rev.* **2019**, 119 (6), 3453-3471.

101. Rittle, J.; Green, M. T., Cytochrome P450 Compound I: Capture, Characterization, and C-H Bond Activation Kinetics. *Science* **2010**, *330* (6006), 933-937.
102. Adeyemi, S. A.; Dovletoglou, A.; Guadalupe, A. R.; Meyer, T. J., REDOX AND SPECTRAL PROPERTIES OF THE 4-ELECTRON OXIDANT TRANS-RU(TPY)(O)₂(H₂O) (ClO₄)₂. *Inorganic Chemistry* **1992**, *31* (8), 1375-1383.
103. Tseng, H. W.; Zong, R.; Muckerman, J. T.; Thummel, R., Mononuclear Ruthenium(II) Complexes That Catalyze Water Oxidation. *Inorganic Chemistry* **2008**, *47* (24), 11763-11773.
104. Moonshiram, D.; Purohit, V.; Concepcion, J. J.; Meyer, T. J.; Pushkar, Y., Mechanism of Catalytic Water Oxidation by the Ruthenium Blue Dimer Catalyst: Comparative Study in D₂O versus H₂O. *Materials* **2013**, *6* (2), 392-409.
105. Farrusseng, D.; Aguado, S.; Pinel, C., Metal-organic frameworks: opportunities for catalysis. *Angewandte Chemie International Edition* **2009**, *48* (41), 7502-7513.
106. Furukawa, H.; Cordova, K. E.; O'Keeffe, M.; Yaghi, O. M., The chemistry and applications of metal-organic frameworks. *Science* **2013**, *341* (6149), 1230444.
107. Lee, J.; Farha, O. K.; Roberts, J.; Scheidt, K. A.; Nguyen, S. T.; Hupp, J. T., Metal-organic framework materials as catalysts. *Chemical Society Reviews* **2009**, *38* (5), 1450-1459.
108. Lu, W.; Wei, Z.; Gu, Z.-Y.; Liu, T.-F.; Park, J.; Park, J.; Tian, J.; Zhang, M.; Zhang, Q.; Gentle III, T., Tuning the structure and function of metal-organic frameworks via linker design. *Chemical Society Reviews* **2014**, *43* (16), 5561-5593.
109. Hou, C.-C.; Li, T.-T.; Cao, S.; Chen, Y.; Fu, W.-F., Incorporation of a [Ru (dcbpy)(bpy) 2] 2+ photosensitizer and a Pt (dcbpy) Cl 2 catalyst into metal-organic frameworks for photocatalytic hydrogen evolution from aqueous solution. *Journal of Materials Chemistry A* **2015**, *3* (19), 10386-10394.
110. Kim, D.; Whang, D. R.; Park, S. Y., Self-healing of molecular catalyst and photosensitizer on metal-organic framework: robust molecular system for photocatalytic H₂ evolution from water. *Journal of the American Chemical Society* **2016**, *138* (28), 8698-8701.
111. Wang, C.; DeKrafft, K. E.; Lin, W., Pt nanoparticles@ photoactive metal-organic frameworks: efficient hydrogen evolution via synergistic photoexcitation and electron injection. *Journal of the American Chemical Society* **2012**, *134* (17), 7211-7214.
112. Zhang, Z.-M.; Zhang, T.; Wang, C.; Lin, Z.; Long, L.-S.; Lin, W., Photosensitizing metal-organic framework enabling visible-light-driven proton reduction by a Wells-Dawson-type polyoxometalate. *Journal of the American Chemical Society* **2015**, *137* (9), 3197-3200.
113. Fei, H.; Sampson, M. D.; Lee, Y.; Kubiak, C. P.; Cohen, S. M., Photocatalytic CO₂ reduction to formate using a Mn (I) molecular catalyst in a robust metal-organic framework. *Inorganic chemistry* **2015**, *54* (14), 6821-6828.
114. Pullen, S.; Fei, H.; Orthaber, A.; Cohen, S. M.; Ott, S., Enhanced photochemical hydrogen production by a molecular diiron catalyst incorporated into a metal-organic framework. *Journal of the American Chemical Society* **2013**, *135* (45), 16997-17003.
115. Wang, C.; Wang, J.-L.; Lin, W., Elucidating molecular iridium water oxidation catalysts using metal-organic frameworks: A comprehensive structural, catalytic, spectroscopic, and kinetic study. *Journal of the American Chemical Society* **2012**, *134* (48), 19895-19908.
116. Wang, C.; Xie, Z.; Lin, W., Doping metal-organic frameworks for water oxidation, carbon dioxide reduction, and organic photocatalysis. *J. Am. Chem. Soc* **2011**, *133* (34), 13445-13454.

117. Hod, I.; Sampson, M. D.; Deria, P.; Kubiak, C. P.; Farha, O. K.; Hupp, J. T., Fe-porphyrin-based metal-organic framework films as high-surface concentration, heterogeneous catalysts for electrochemical reduction of CO₂. *ACS Catalysis* **2015**, *5* (11), 6302-6309.
118. Jahan, M.; Bao, Q.; Loh, K. P., Electrocatalytically active graphene-porphyrin MOF composite for oxygen reduction reaction. *Journal of the American Chemical Society* **2012**, *134* (15), 6707-6713.
119. Kornienko, N.; Zhao, Y.; Kley, C. S.; Zhu, C.; Kim, D.; Lin, S.; Chang, C. J.; Yaghi, O. M.; Yang, P., Metal-organic frameworks for electrocatalytic reduction of carbon dioxide. *J. Am. Chem. Soc* **2015**, *137* (44), 14129-14135.
120. Kung, C.-W.; Mondloch, J. E.; Wang, T. C.; Bury, W.; Hoffeditz, W.; Klahr, B. M.; Klet, R. C.; Pellin, M. J.; Farha, O. K.; Hupp, J. T., Metal-organic framework thin films as platforms for atomic layer deposition of cobalt ions to enable electrocatalytic water oxidation. *ACS applied materials & interfaces* **2015**, *7* (51), 28223-28230.
121. Lu, X.-F.; Liao, P.-Q.; Wang, J.-W.; Wu, J.-X.; Chen, X.-W.; He, C.-T.; Zhang, J.-P.; Li, G.-R.; Chen, X.-M., An alkaline-stable, metal hydroxide mimicking metal-organic framework for efficient electrocatalytic oxygen evolution. *J. Am. Chem. Soc* **2016**, *138* (27), 8336-8339.
122. Morozan, A.; Jaouen, F., Metal organic frameworks for electrochemical applications. *Energy & environmental science* **2012**, *5* (11), 9269-9290.
123. Shen, J.-Q.; Liao, P.-Q.; Zhou, D.-D.; He, C.-T.; Wu, J.-X.; Zhang, W.-X.; Zhang, J.-P.; Chen, X.-M., Modular and Stepwise Synthesis of a Hybrid Metal-Organic Framework for Efficient Electrocatalytic Oxygen Evolution. *Journal of the American Chemical Society* **2017**, *139* (5), 1778-1781.
124. Usov, P. M.; Ahrenholtz, S. R.; Maza, W. A.; Stratakes, B.; Epley, C. C.; Kessinger, M. C.; Zhu, J.; Morris, A. J., Cooperative electrochemical water oxidation by Zr nodes and Ni-porphyrin linkers of a PCN-224 MOF thin film. *Journal of Materials Chemistry A* **2016**, *4* (43), 16818-16823.
125. Usov, P. M.; Huffman, B.; Epley, C. C.; Kessinger, M. C.; Zhu, J.; Maza, W. A.; Morris, A. J., Study of Electrocatalytic Properties of Metal-Organic Framework PCN-223 for the Oxygen Reduction Reaction. *ACS Applied Materials & Interfaces* **2017**.
126. Johnson, B. A.; Bhunia, A.; Ott, S., Electrocatalytic water oxidation by a molecular catalyst incorporated into a metal-organic framework thin film. *Dalton Transactions* **2017**, *46* (5), 1382-1388.
127. Lin, S.; Pineda-Galvan, Y.; Maza, W. A.; Epley, C. C.; Zhu, J.; Kessinger, M. C.; Pushkar, Y.; Morris, A. J., Electrochemical Water Oxidation by a Catalyst-Modified Metal-Organic Framework Thin Film. *ChemSusChem* **2017**, *10* (3), 514-522.
128. Ahrenholtz, S. R.; Epley, C. C.; Morris, A. J., Solvothermal preparation of an electrocatalytic metalloporphyrin MOF thin film and its redox hopping charge-transfer mechanism. *Journal of the American Chemical Society* **2014**, *136* (6), 2464-2472.
129. Kaufman, F.; Schroeder, A.; Engler, E.; Kramer, S.; Chambers, J., Ion and electron transport in stable, electroactive tetrathiafulvalene polymer coated electrodes. *Journal of the American Chemical Society* **1980**, *102* (2), 483-488.
130. Kaufman, F. B.; Engler, E. M., Solid-state spectroelectrochemistry of crosslinked donor bound polymer films. *Journal of the American Chemical Society* **1979**, *101* (3), 547-549.

131. Schroeder, A. H.; Kaufman, F. B.; Patel, V.; Engler, E. M., Comparative behavior of electrodes coated with thin films of structurally related electroactive polymers. *Journal of Electroanalytical Chemistry and Interfacial Electrochemistry* **1980**, *113* (2), 193-208.
132. Concepcion, J. J.; Tsai, M.-K.; Muckerman, J. T.; Meyer, T. J., Mechanism of water oxidation by single-site ruthenium complex catalysts. *Journal of the American Chemical Society* **2010**, *132* (5), 1545-1557.
133. Tong, L.; Thummel, R. P., Mononuclear ruthenium polypyridine complexes that catalyze water oxidation. *Chemical Science* **2016**, *7* (11), 6591-6603.
134. Wasylenko, D. J.; Ganesamoorthy, C.; Koivisto, B. D.; Henderson, M. A.; Berlinguette, C. P., Insight into water oxidation by mononuclear polypyridyl Ru catalysts. *Inorganic chemistry* **2010**, *49* (5), 2202-2209.
135. Yagi, M.; Tajima, S.; Komi, M.; Yamazaki, H., Highly active and tunable catalysts for O₂ evolution from water based on mononuclear ruthenium (II) monoquo complexes. *Dalton Transactions* **2011**, *40* (15), 3802-3804.
136. López, I.; Ertem, M. Z.; Maji, S.; Benet-Buchholz, J.; Keidel, A.; Kuhlmann, U.; Hildebrandt, P.; Cramer, C. J.; Batista, V. S.; Llobet, A., A Self-Improved Water-Oxidation Catalyst: Is One Site Really Enough? *Angewandte Chemie International Edition* **2014**, *53* (1), 205-209.
137. López, I.; Maji, S.; Benet-Buchholz, J.; Llobet, A., Oxo-bridge scenario behind single-site water-oxidation catalysts. *Inorganic chemistry* **2014**, *54* (2), 658-666.
138. Concepcion, J. J.; Binstead, R. A.; Alibabaei, L.; Meyer, T. J., Application of the rotating ring-disc-electrode technique to water oxidation by surface-bound molecular catalysts. *Inorganic chemistry* **2013**, *52* (19), 10744-10746.
139. Kaveevivitchai, N.; Zong, R.; Tseng, H.-W.; Chitta, R.; Thummel, R. P., Further observations on water oxidation catalyzed by mononuclear Ru (II) complexes. *Inorganic chemistry* **2012**, *51* (5), 2930-2939.
140. Pushkar, Y.; Moonshiram, D.; Purohit, V.; Yan, L.; Alperovich, I., Spectroscopic Analysis of Catalytic Water Oxidation by [RuII (bpy)(tpy) H₂O] ²⁺ Suggests That RuV □ O Is Not a Rate-Limiting Intermediate. *Journal of the American Chemical Society* **2014**, *136* (34), 11938-11945.
141. Wasylenko, D. J.; Ganesamoorthy, C.; Henderson, M. A.; Berlinguette, C. P., Unraveling the Roles of the Acid Medium, Experimental Probes, and Terminal Oxidant, (NH₄)₂ [Ce (NO₃)₆], in the Study of a Homogeneous Water Oxidation Catalyst. *Inorganic chemistry* **2011**, *50* (8), 3662-3672.
142. Wasylenko, D. J.; Ganesamoorthy, C.; Henderson, M. A.; Koivisto, B. D.; Osthoff, H. D.; Berlinguette, C. P., Electronic modification of the [RuII (tpy)(bpy)(OH₂)] ²⁺ scaffold: Effects on catalytic water oxidation. *Journal of the American Chemical Society* **2010**, *132* (45), 16094-16106.
143. Cavka, J. H.; Jakobsen, S.; Olsbye, U.; Guillou, N.; Lamberti, C.; Bordiga, S.; Lillerud, K. P., A new zirconium inorganic building brick forming metal organic frameworks with exceptional stability. *Journal of the American Chemical Society* **2008**, *130* (42), 13850-13851.
144. Schaate, A.; Roy, P.; Godt, A.; Lippke, J.; Waltz, F.; Wiebcke, M.; Behrens, P., Modulated synthesis of Zr-based metal-organic frameworks: from nano to single crystals. *Chemistry-A European Journal* **2011**, *17* (24), 6643-6651.

145. Hansen, R. E.; Das, S., Biomimetic di-manganese catalyst cage-isolated in a MOF: robust catalyst for water oxidation with Ce (IV), a non-O-donating oxidant. *Energy & Environmental Science* **2014**, *7* (1), 317-322.
146. Nepal, B.; Das, S., Sustained Water Oxidation by a Catalyst Cage-Isolated in a Metal–Organic Framework. *Angewandte Chemie International Edition* **2013**, *52* (28), 7224-7227.
147. Moonshiram, D.; Jurss, J. W.; Concepcion, J. J.; Zakharova, T.; Alperovich, I.; Meyer, T. J.; Pushkar, Y., Structure and Electronic Configurations of the Intermediates of Water Oxidation in Blue Ruthenium Dimer Catalysis. *Journal of the American Chemical Society* **2012**, *134* (10), 4625-4636.
148. Hurst, J. K.; Zhou, J.; Lei, Y., Pathways for water oxidation catalyzed by the (μ -oxo)bis[aquabis(bipyridine)ruthenium](4+) ion. *Inorganic Chemistry* **1992**, *31* (6), 1010-1017.
149. Concepcion, J. J.; Jurss, J. W.; Norris, M. R.; Chen, Z.; Templeton, J. L.; Meyer, T. J., Catalytic Water Oxidation by Single-Site Ruthenium Catalysts. *Inorganic Chemistry* **2010**, *49* (4), 1277-1279.
150. Boddien, A.; Loges, B.; Junge, H.; Gärtner, F.; Noyes, J. R.; Beller, M., Continuous Hydrogen Generation from Formic Acid: Highly Active and Stable Ruthenium Catalysts. *Advanced Synthesis & Catalysis* **2009**, *351* (14-15), 2517-2520.
151. Zhang, S. Y.; Ding, Y. B.; Wei, H., Ruthenium Polypyridine Complexes Combined with Oligonucleotides for Bioanalysis: A Review. *Molecules* **2014**, *19* (8), 11933-11987.
152. Grubbs, R. H., Olefin metathesis. *Tetrahedron* **2004**, *60* (34), 7117-7140.
153. Iglesia, E.; Soled, S. L.; Fiato, R. A., FISCHER-TROPSCH SYNTHESIS ON COBALT AND RUTHENIUM - METAL DISPERSION AND SUPPORT EFFECTS ON REACTION-RATE AND SELECTIVITY. *J. Catal.* **1992**, *137* (1), 212-224.
154. Juris, A.; Balzani, V.; Belser, P.; von Zelewsky, A., Characterization of the Excited State Properties of Some New Photosensitizers of the Ruthenium (Polypyridine) Family. *Helvetica Chimica Acta* **1981**, *64* (7), 2175-2182.
155. O'Regan, B.; Grätzel, M., A low-cost, high-efficiency solar cell based on dye-sensitized colloidal TiO₂ films. *Nature* **1991**, *353* (6346), 737-740.
156. Antonarakis, E. S.; Emadi, A., Ruthenium-based chemotherapeutics: are they ready for prime time? *Cancer Chemoth Pharm* **2010**, *66* (1), 1-9.
157. Bergamo, A.; Gaiddon, C.; Schellens, J. H. M.; Beijnen, J. H.; Sava, G., Approaching tumour therapy beyond platinum drugs: Status of the art and perspectives of ruthenium drug candidates. *Journal of Inorganic Biochemistry* **2012**, *106* (1), 90-99.
158. Meyer, T. J.; Huynh, M. H., The remarkable reactivity of high oxidation state ruthenium and osmium polypyridyl complexes. *Inorg Chem* **2003**, *42* (25), 8140-60.
159. Kamdar, J. M.; Grotjahn, D. B., An Overview of Significant Achievements in Ruthenium-Based Molecular Water Oxidation Catalysis. *Molecules* **2019**, *24* (3), 24.
160. Ravari, A. K.; Zhu, G.; Ezhov, R.; Pineda-Galvan, Y.; Page, A.; Weinschenk, W.; Yan, L.; Pushkar, Y., Unraveling the Mechanism of Catalytic Water Oxidation via de Novo Synthesis of Reactive Intermediate. *Journal of the American Chemical Society* **2020**, *142* (2), 884-893.
161. Mfuh, A. M.; Larionov, O. V., Heterocyclic N-Oxides - An Emerging Class of Therapeutic Agents. *Curr. Med. Chem.* **2015**, *22* (24), 2819-2857.

162. Li, D. L.; Wu, P. P.; Sun, N.; Lu, Y. J.; Wong, L.; Fang, Z. Y. A.; Zhang, K., The Diversity of Heterocyclic N-oxide Molecules: Highlights on their Potential in Organic Synthesis, Catalysis and Drug Applications. *Curr. Org. Chem.* **2019**, *23* (5), 616-627.
163. Petrosyan, A.; Hauptmann, R.; Pospech, J., Heteroarene N-Oxides as Oxygen Source in Organic Reactions. *Eur. J. Org. Chem.* **2018**, *2018* (38), 5237-5252.
164. Kalyanasundaram, K., Photophysics, photochemistry and solar energy conversion with tris(bipyridyl)ruthenium(II) and its analogues. *Coordination Chemistry Reviews* **1982**, *46*, 159-244.
165. Těplý, F., PHOTOREDOX CATALYSIS BY Ru(bpy)₃(2+) TO TRIGGER TRANSFORMATIONS OF ORGANIC MOLECULES. ORGANIC SYNTHESIS USING VISIBLE-LIGHT PHOTOCATALYSIS AND ITS 20th CENTURY ROOTS. *Collection of Czechoslovak Chemical Communications* **2011**, *76* (7), 859-917.
166. Young, K. J.; Martini, L. A.; Milot, R. L.; Snoeberger, R. C.; Batista, V. S.; Schmuttenmaer, C. A.; Crabtree, R. H.; Brudvig, G. W., Light-driven water oxidation for solar fuels. *Coord. Chem. Rev.* **2012**, *256* (21-22), 2503-2520.
167. Zhang, S. F.; Yang, X. D.; Numata, Y. H.; Han, L. Y., Highly efficient dye-sensitized solar cells: progress and future challenges. *Energy Environ. Sci.* **2013**, *6* (5), 1443-1464.
168. Motten, A. G.; Hanck, K.; DeArmound, M. K., ESR of the reduction products of [Fe(bpy)₃]²⁺ and [Ru(bpy)₃]²⁺. *Chemical Physics Letters* **1981**, *79* (3), 541-546.
169. Warren, J. J.; Mayer, J. M., Tuning of the Thermochemical and Kinetic Properties of Ascorbate by Its Local Environment: Solution Chemistry and Biochemical Implications. *Journal of the American Chemical Society* **2010**, *132* (22), 7784-7793.
170. Miyazaki, H.; Matsuhisa, Y.; Kubota, T., CYCLIC VOLTAMMETRY OF AROMATIC AMINE N-OXIDES IN NON-AQUEOUS SOLVENTS AND THE STABILITY OF THE FREE-RADICALS PRODUCED. *Bull. Chem. Soc. Jpn.* **1981**, *54* (12), 3850-3853.
171. Govindarajan, N.; Meijer, E. J., Modeling the Catalyst Activation Step in a Metal-Ligand Radical Mechanism Based Water Oxidation System. *Inorganics* **2019**, *7* (5), 7.
172. Baik, M.-H.; Friesner, R. A., Computing Redox Potentials in Solution: Density Functional Theory as A Tool for Rational Design of Redox Agents. *The Journal of Physical Chemistry A* **2002**, *106* (32), 7407-7412.
173. McGarvey, B. R.; Ferro, A. A.; Tfouni, E.; Bezerra, C. W. B.; Bagatin, I.; Franco, D. W., Detection of the EPR spectra of NO center dot in ruthenium(II) complexes. *Inorganic Chemistry* **2000**, *39* (16), 3577-3581.
174. Lang, D. R.; Davis, J. A.; Lopes, L. G. F.; Ferro, A. A.; Vasconcellos, L. C. G.; Franco, D. W.; Tfouni, E.; Wieraszko, A.; Clarke, M. J., A Controlled NO-Releasing Compound: Synthesis, Molecular Structure, Spectroscopy, Electrochemistry, and Chemical Reactivity of R,R,S,S-trans-[RuCl(NO)(cyclam)]²⁺(1,4,8,11-tetraazacyclotetradecane). *Inorganic Chemistry* **2000**, *39* (11), 2294-2300.
175. Ferreira, K. Q.; Doro, F. G.; Tfouni, E., Aquation reactions of RuII and RuIII dichloro complexes with 1-(3-propylammonium)cyclam: Properties of trans-[RuClL(1-(3-propylammonium)cyclam)]ⁿ⁺ complexes (L=Cl⁻, tfms⁻, H₂O). *Inorganica Chimica Acta* **2003**, *355*, 205-212.
176. Oliveira, F. d. S.; Togniolo, V.; Pupo, T. T.; Tedesco, A. C.; da Silva, R. S., Nitrosyl ruthenium complex as nitric oxide delivery agent: synthesis, characterization and photochemical properties. *Inorganic Chemistry Communications* **2004**, *7* (2), 160-164.

177. Doro, F. G.; Pepe, I. M.; Galembeck, S. E.; Carlos, R. M.; da Rocha, Z. N.; Bertotti, M.; Tfouni, E., Reactivity, photolability, and computational studies of the ruthenium nitrosyl complex with a substituted cyclam fac-[Ru(NO)Cl₂(κ³N₄,N₈,N₁₁(1-carboxypropyl)cyclam)]Cl·H₂O. *Dalton Transactions* **2011**, 40 (24), 6420-6432.
178. Rillema, D. P.; Allen, G.; Meyer, T. J.; Conrad, D., Redox properties of ruthenium(II) tris chelate complexes containing the ligands 2,2'-bipyrazine, 2,2'-bipyridine, and 2,2'-bipyrimidine. *Inorganic Chemistry* **1983**, 22 (11), 1617-1622.
179. Iranmanesh, H.; Bhadbhade, M.; De Haas, N.; Luis, E. T.; Yan, H.; Yang, J.; Beves, J. E., Badly behaving bipyridine: the surprising coordination behaviour of 5,5'-substituted-2,2'-bipyridine towards iron(II) and ruthenium(II) ions. *Supramolecular Chemistry* **2015**, 27 (11-12), 854-864.
180. Pineda-Galvan, Y.; Ravari, A. K.; Shmakov, S.; Lifshits, L.; Kaveevivitchai, N.; Thummel, R.; Pushkar, Y., Detection of the site protected 7-coordinate Ru-V = O species and its chemical reactivity to enable catalytic water oxidation. *Journal of Catalysis* **2019**, 375, 1-7.
181. Planas, N.; Vigara, L.; Cady, C.; Miró, P.; Huang, P.; Hammarström, L.; Styring, S.; Leidel, N.; Dau, H.; Haumann, M.; Gagliardi, L.; Cramer, C. J.; Llobet, A., Electronic Structure of Oxidized Complexes Derived from cis-[RuII(bpy)₂(H₂O)₂]²⁺ and Its Photoisomerization Mechanism. *Inorganic Chemistry* **2011**, 50 (21), 11134-11142.
182. Anderson, C. P.; Salmon, D. J.; Meyer, T. J.; Young, R. C., Photochemical Generation of Ru(bpy)₃⁺ and O₂. *Journal of the American Chemical Society* **1977**, 99 (6), 1980-1982.
183. Caspar, J. V.; Meyer, T. J., Photochemistry of tris(2,2'-bipyridine)ruthenium(2+) ion (Ru(bpy)₃²⁺). Solvent effects. *Journal of the American Chemical Society* **1983**, 105 (17), 5583-5590.
184. Kaizu, Y.; Ohta, H.; Kobayashi, K.; Kobayashi, H.; Takuma, K.; Matsuo, T., Lifetimes of the lowest excited state of tris(2,2'-bipyridine)ruthenium(II) and its amphiphatic derivative in micellar systems. *Journal of Photochemistry* **1985**, 30 (1), 93-103.
185. Ogawa, M.; Kuroda, K., Photofunctions of Intercalation Compounds. *Chemical Reviews* **1995**, 95 (2), 399-438.
186. Singh, W. M.; Pegram, D.; Duan, H.; Kalita, D.; Simone, P.; Emmert, G. L.; Zhao, X., Hydrogen Production Coupled to Hydrocarbon Oxygenation from Photocatalytic Water Splitting. *Angewandte Chemie International Edition* **2012**, 51 (7), 1653-1656.
187. Konev, M. O.; Cardinale, L.; Jacobi von Wangelin, A., Catalyst-Free N-Deoxygenation by Photoexcitation of Hantzsch Ester. *Organic Letters* **2020**, 22 (4), 1316-1320.
188. Nakanishi, I.; Nishizawa, C.; Ohkubo, K.; Takeshita, K.; Suzuki, K. T.; Ozawa, T.; Hecht, S. M.; Tanno, M.; Sueyoshi, S.; Miyata, N.; Okuda, H.; Fukuzumi, S.; Ikota, N.; Fukuhara, K., Hydroxyl radical generation via photoreduction of a simple pyridine N-oxide by an NADH analogue. *Org. Biomol. Chem.* **2005**, 3 (18), 3263-3265.